

Terahertz and Microwave Spectroscopy of Liquids and Hydrogen-Bonded Clusters

Thesis by
Ian Alan Finneran

In Partial Fulfillment of the Requirements for the
degree of
Doctor of Philosophy

The logo for the California Institute of Technology (Caltech), featuring the word "Caltech" in a bold, orange, sans-serif font.

CALIFORNIA INSTITUTE OF TECHNOLOGY
Pasadena, California

2017
Defended March 1, 2017

© 2017

Ian Alan Finneran

ORCID: 0000-0003-2506-4652

All rights reserved

ACKNOWLEDGEMENTS

Throughout graduate school I have been helped and supported by many wonderful people. Without these people, none of the work in this thesis would have been possible. For this support, I will be forever grateful.

First, I would like to thank my advisor Geoff Blake. From the beginning, his calm and logical approach to research helped me find my way in the lab. When times were tough and experiments weren't working, he was always willing to chat and help me work through problems. He gave me a lot of freedom to explore and find new directions in the lab, which I feel helped me grow as a scientist. And he always helped me see the bigger picture of our work when I was stuck sorting through technical details on a malfunctioning instrument.

I would also like to thank the members of my candidacy and thesis committees – Tom Miller, Jack Beauchamp, Mitchio Okumura, and Vincent McKoy – for their support and feedback on my thesis work and propositions.

Learning ultrafast THz spectroscopy has been challenging, but fortunately I had many excellent teachers along the way. Although we only overlapped for a year, I am grateful to Matt Kelley for helping me learn the basic THz-TDS setup and paving the way for all the experiments on the Legend laser system. During my first couple years in the group, Dan Holland helped me immensely with understanding the intricacies of the ASOPS system, microwave electronics, and THz spectroscopy. I am also thankful for the work he did on the ASOPS system, which would lead to the development of the THz frequency comb (Chapter 5) and indirectly to the DDS microwave spectrometer (Chapter 2).

Marco Allodi was crucial for all of the work in Part III of this thesis. In my first few years at Caltech he taught me how to use and, more importantly, fix the Legend and Mantis lasers and align the THz and near-infrared optics. He also taught me about *ab initio* simulations of clusters. We spent several years working together on various nonlinear and 2D alignments, most of which were unsuccessful. This process was sometimes frustrating, but we ended up picking up a lot of nonlinear spectroscopy along the way. I always enjoyed our chats in the office and working through various problems on the whiteboard. And when we finally detected our first TKE signals it was very exciting!

After getting the 2D experiment up and running, we started a very productive

collaboration with Ralph Welsch and Tom Miller. During this collaboration, Ralph taught me a great deal about simulation, fitting, and programming. Our meetings with Tom and Ralph were always informative, and I appreciate their attention to detail in the analysis of the 2D-TTR spectra. Ralph wrote the final version of the RDM code that was used extensively in Chapter 7 and 8.

Brandon Carroll has been my officemate and labmate for all of my time at Caltech. Whenever I had technical problems on the microwave and THz experiments, Brandon was an excellent resource. He made many contributions to the projects in Part II of this thesis, particularly with the microwave electronics, cluster spectroscopy, and implementation of the frequency comb. He also introduced me to quasioptics, which were crucial for the THz designs in Part III.

After Dan graduated, Jacob Good took the lead on the ASOPS system. During my fourth year we worked together on the THz frequency comb experiments presented in Chapter 5. His contributions were essential to this project. We also spent many hours discussing and sketching out the various signals and time/frequency domain representations of the experiment while waiting for the lasers to stabilize. In the end it really payed off! Through it all, I really enjoyed our conversations in the lab and office and ended up learning a bit about solar energy conversion too.

I would also like to acknowledge the many other people that I worked with in the Blake group over the years, including Brett McGuire, Sergio Ioppolo, Xander de Vries, Olivier Auriacombe, Griffin Mead, Xiaolin Xu, Catherine Alvarez, Kewei Xu, Oliver Chen, Daniel Guth, Jerry Feng, David Feng, Avinash Agrawal, and Brennan Ashwood as well as the astronomers — Coco Zhang, Nathan Crockett, Alex Lockwood, Dana Anderson, Masha Kleshcheva, Danielle Piskorz, and Katherine Kaufman. Thanks also to the incoming students (and postdoc) – Tony Karam, Alex Froebel, Olivia Wilkins, and Cam Buzard. I shared the amplified laser system with Brett and Sergio for several years, and enjoyed our many conversations about astrochemistry, ice spectroscopy, and THz alignments. Brett, along with Marie-Aline Martin-Drumel and Mike McCarthy, also made significant contributions to the ethanol-water dimer measurements presented in Chapter 3. Griffin, Xiaolin, and Ioan have taken the reins on the 2D-TTR work and I am excited to see what they discover in the coming years. Griffin also upgraded the CP-FTMW instrument, which we used for the analysis of the ethanol-methanol dimer in Chapter 4.

Outside of the Blake group I would like to acknowledge my friends – Nick Broten, Nat Kadunce, Julia Hammond, Linhan Chen, Katie Kirby, Ingmar Saberi, Kate

Rodriguez, and Trenton Salk – and my physical chemistry TA group during first year – Linhan Chen, Baoqing Zhou, and Laura Mertens.

If it were not for the encouragement and support of Steve Shipman, my undergraduate advisor, I would not have gone to graduate school. He taught me most of what I know about microwave spectroscopy, and first inspired me to pursue physical chemistry when I was a second year at New College of Florida.

I am also grateful to my parents, Shane and Tina, for encouraging me to follow my interest in science from an early age. It was also fun to take breaks to visit them in Arizona, Mexico, and Tonga!

Finally, I would like to thank my wife, Laura, for her love and support. I have really enjoyed our time together in Southern California and I appreciate her feedback on papers and presentations, and for listening to me rant about broken lasers for so many years. I look forward to reading her thesis in a few months and starting our new life together in Colorado!

ABSTRACT

The microwave (MW, 0.3-100 GHz) and terahertz (THz, 0.1-10 THz) regions of the electromagnetic spectrum are replete with a rich set of molecular motions, including soft inter- and intramolecular vibrations, torsions, and rotations. At room temperature these motions are well populated, and play an active role in condensed-phase chemistry on Earth. This work details the development of one MW and two THz spectrometers along with their application to the study of liquids and hydrogen-bonded clusters.

In the first section, we cover the design and construction of a chirped pulse Fourier transform microwave (CP-FTMW) spectrometer. The instrument relies on a compact, inexpensive direct digital synthesis board to generate 2 GHz, 1 microsecond chirped pulses that, after amplification, polarize the rotational states of gas-phase molecules in a pulsed supersonic jet. In an initial demonstration, the CP-FTMW instrument is used to collect the 8-18 GHz rotational spectra of the ethanol-water and ethanol-methanol dimers. These data reveal evidence of quantum tunneling, and a complicated interplay between weak and strong hydrogen-bonds in both dimers.

Next, we describe the ongoing development of a decade spanning high precision THz frequency comb, using THz time-domain spectroscopy. The instrument is capable of generating ~ 28000 comb teeth from 0.15-2.4 THz with a fractional precision of 1.8×10^{-9} and a Doppler-limited accuracy of 6.1×10^{-8} . Further prospects for studies of intermolecular interactions in jet-cooled molecular clusters are also discussed.

In the last section, we move to condensed-phase studies of THz orientational and vibrational motions of liquids. The liquids are excited with one or two intense time-delayed ultrafast THz pulses and probed with a non-resonant 40 fs Raman pulse. Initially, we use this approach to measure the picosecond molecular orientational alignment and decay timescales in several aromatic liquids. By adding a second THz pulse to the experiment and adjusting the delays between the three pulses, we control the orientational alignment of the molecules, and acquire phase-coherent 2D-THz-THz-Raman spectra in the time domain. The 2D responses of liquid CHBr_3 , CCl_4 , and CCl_2Br_2 show off-diagonal peaks from coupling between thermally-populated vibrational modes. In an extended bandwidth measurement, we observe photon-echo signals from liquid CHBr_3 and a complicated pattern of dipole forbidden transitions. The molecular origins of the forbidden transitions are still under investigation, but

are likely due to nonlinearities in the condensed-phase dipole moment surface. Coherence transfer, vibrational anharmonicity, and intermolecular coupling are also considered in this analysis.

PUBLISHED CONTENT AND CONTRIBUTIONS

1. Finneran, I. A., Holland, D. B., Carroll, P. B. & Blake, G. A. A direct digital synthesis chirped pulse Fourier transform microwave spectrometer. *Review of Scientific Instruments* **84**, 083104 (2013).
DOI: 10.1063/1.4818137
I.A.F. designed and built the instrument, collected and analyzed the data, wrote the article, prepared figures and diagrams, and revised the article.
2. Finneran, I. A., Good, J. T., Holland, D. B., Carroll, P. B., Allodi, M. A. & Blake, G. A. Decade-spanning high-precision terahertz frequency comb. *Physical Review Letters* **114**, 163902 (2015).
DOI: 10.1103/PhysRevLett.114.163902
I.A.F. designed the comb implementation, assisted in modifying the instrument, assisted in collecting and analyzing the data, wrote the article, prepared figures and diagrams, and revised the article.
3. Good, J. T., Holland, D. B., Finneran, I. A., Carroll, P. B., Kelley, M. J. & Blake, G. A. A decade-spanning high-resolution asynchronous optical sampling terahertz time-domain and frequency comb spectrometer. *Review of Scientific Instruments* **86**, 103107 (2015).
DOI: 10.1063/1.4932567
I.A.F. assisted in modifications to the instrument and software used to collect the data, and revised the article.
4. Finneran, I. A., Carroll, P. B., Allodi, M. A. & Blake, G. A. Hydrogen bonding in the ethanol–water dimer. *Physical Chemistry Chemical Physics* **17**, 24210–24214 (2015).
DOI: 10.1039/C5CP03589A
I.A.F. collected and analyzed the data, wrote the article, prepared figures and diagrams, and revised the article.
5. Seifert, N. A., Finneran, I. A., Perez, C., Zaleski, D. P., Neill, J. L., Steber, A. L., Suenram, R. D., Lesarri, A., Shipman, S. T. & Pate, B. H. AUTOFIT, an automated fitting tool for broadband rotational spectra, and applications to 1-hexanal. *Journal of Molecular Spectroscopy* **312**, 13–21 (2015).
DOI: 10.1016/j.jms.2015.02.003
I.A.F. wrote python code for the AUTOFIT program, prepared a figure, and revised the article.
6. Allodi, M. A., Finneran, I. A. & Blake, G. A. Nonlinear terahertz coherent excitation of vibrational modes of liquids. *The Journal of Chemical Physics* **143**, 234204 (2015).
DOI: 10.1063/1.4938165
I.A.F. assisted in designing and building the instrument, assisted in collecting

and analyzing the data, modeled the data, prepared figures and diagrams, and revised the article.

7. McGuire, B. A., Carroll, P. B., Loomis, R. A., Finneran, I. A., Jewell, P. R., Remijan, A. J. & Blake, G. A. Discovery of the interstellar chiral molecule propylene oxide (CH₃CHCH₂O). *Science* **352**, 1449–1452 (2016).
DOI: 10.1126/science.aae0328
I.A.F. assisted in the collection and analysis of the laboratory data, and revised the article.
8. Finneran, I. A., Welsch, R., Allodi, M. A., Miller, T. F. & Blake, G. A. Coherent two-dimensional terahertz-terahertz-Raman spectroscopy. *Proceedings of the National Academy of Sciences* **113**, 6857–6861 (2016).
DOI: 10.1073/pnas.1605631113
I.A.F. designed and built the instrument, collected and analyzed the data, assisted in modeling the data, wrote the article, prepared figures and diagrams, and revised the article.
9. Finneran, I. A., Carroll, P. B., Mead, G. J. & Blake, G. A. Hydrogen bond competition in the ethanol–methanol dimer. *Physical Chemistry Chemical Physics* **18**, 22565–22572 (2016).
DOI: 10.1039/C6CP03980D
I.A.F. collected and analyzed the data, wrote the article, prepared figures and diagrams, and revised the article.
10. Finneran, I. A., Welsch, R., Allodi, M. A., Miller, T. F. & Blake, G. A. Broadband 2D THz-THz-Raman photon-echo spectroscopy of molecular vibrations in liquids. *in preparation* (2017).
I.A.F. designed and built the instrument, collected and analyzed the data, assisted in modeling the data, wrote the article, prepared figures and diagrams, and revised the article.

TABLE OF CONTENTS

Acknowledgements	iii
Abstract	vi
Published Content and Contributions	viii
Table of Contents	x
List of Illustrations	xii
List of Tables	xiv
I Introduction	1
Chapter I: Introduction	2
1.1 THz and Microwave Spectroscopy of Liquids	2
1.2 Rotational Spectroscopy of Molecular Clusters	4
1.3 Ultrafast Terahertz Spectroscopy of Liquids	6
II Rotational Spectroscopy of Molecular Clusters	11
Chapter II: A Direct Digital Synthesis Chirped Pulse Fourier Transform Mi- crowave Spectrometer	12
2.1 Introduction	13
2.2 Methods	14
2.3 Results and Discussion	18
2.4 Conclusion	23
Chapter III: The Ethanol-Water Dimer	25
3.1 Introduction	26
3.2 Methods	27
3.3 Results and Discussion	30
3.4 Conclusion	39
Chapter IV: The Ethanol-Methanol Dimer	41
4.1 Introduction	42
4.2 Methods	43
4.3 Results and Discussion	46
4.4 Conclusion	56
Chapter V: A Decade-Spanning, High-Precision Terahertz Frequency Comb	58
5.1 Introduction	59
5.2 Methods	62
5.3 Results and Discussion	62
5.4 Conclusion	65

III Ultrafast Terahertz Spectroscopy of Liquids	67
Chapter VI: Terahertz Kerr Effect Measurements of Simple Liquids	68
6.1 Introduction	69
6.2 Methods	70
6.3 Results and Discussion	72
6.4 Conclusion	77
Chapter VII: 2D THz-THz-Raman Spectroscopy of Liquids	79
7.1 Introduction	80
7.2 Results and Discussion	81
7.3 Conclusion	89
7.4 Methods	89
Chapter VIII: Broadband 2D THz-THz-Raman Analysis of Bromoform	104
8.1 Introduction	105
8.2 Results and Discussion	105
8.3 Conclusion	116
8.4 Methods	116
IV Conclusions and Future Directions	123
Chapter IX: Conclusions and Future Directions	124
V Bibliography and Appendices	129
Bibliography	130
Appendix A: Segmented Chirp Capabilities of the AD9914 DDS	146
A.1 Stepped-LO Operation	146
A.2 Details of AD9914 Implementation	149
Appendix B: Fitting and Kraitchman Analysis of the Ethanol-Water Dimer	150
Appendix C: Fitting and Kraitchman Analysis of the Ethanol-Methanol Dimer	158

LIST OF ILLUSTRATIONS

<i>Number</i>	<i>Page</i>
1.1 The electromagnetic spectrum	3
1.2 Cluster and liquid spectroscopy	5
1.3 Pulse sequences for 1D and 2D spectroscopy	8
2.1 The CP-FTMW circuit	15
2.2 The CP-FTMW pulse timing	16
2.3 DDS/AWG comparison	20
2.4 CP-FTMW phase stability	21
2.5 Microwave spectrum of acetone	22
2.6 Inset portion of acetone spectrum	23
2.7 Propylene oxide transitions	24
3.1 The AUTOFIT program	29
3.2 Calculated energies of the ethanol-water dimer	31
3.3 The spectrum of ethanol-water	34
3.4 Double resonance measurements of ethanol-water	35
3.5 Kraitchman results for ethanol-water	35
3.6 Adaptive aggregation in ethanol-water	37
3.7 Tunneling splitting in WE-t	39
3.8 Cavity measurements of ethanol-water	40
4.1 Calculated ethanol-methanol dimer energies	42
4.2 The ethanol-methanol spectrum	47
4.3 Ethanol-methanol double resonance	50
4.4 Alcohol clusters structure comparison	51
4.5 Helium and argon spectra of ethanol-methanol	52
4.6 Tunneling fit of ethanol-methanol	54
4.7 Experimental spectrum of the ethanol dimer	56
5.1 The THz frequency comb layout	60
5.2 The THz frequency comb	61
5.3 The spectrum of water vapor	64
6.1 A schematic of the TKE experiment	71
6.2 The TKE instrument response	72
6.3 A comparison of TKE signals from six different liquids	73

6.4	TKE signal from hexafluorobenzene	74
6.5	TKE signal from toluene	74
6.6	The TKE and OKE signal of hexafluorobenzene	77
6.7	TKE coherences	78
7.1	An overview of the 2D-TTR experiment	81
7.2	Representitive time domain 2D-TTR signals	83
7.3	Quantum interpretation of the 2D-TTR signals	84
7.4	Experimental and simulated 2D-TTR spectra	85
7.5	Linear THz spectrum of liquid bromoform	86
7.6	Analysis of CBr_2Cl_2	87
7.7	RDM simulations of CBr_2Cl_2	88
7.8	A diagram of the 2D-TTR experiment	91
7.9	The 1D signal rejection for 2D-TTR	92
7.10	2D-TTR polarization	93
7.11	2D-TTR electric fields	93
7.12	2D-FFTs of bromoform	97
7.13	2D pulse sequences	98
7.14	Feynman diagrams for 2D-TTR	101
7.15	2D-TTR spectrum schematic	102
8.1	Broadband 2D-TTR results	106
8.2	The 2D spectrum of bromoform	107
8.3	Analysis of the bromoform spectrum	108
8.4	Origins of forbidden transitions	111
8.5	Coherence transfer toy problem	113
8.6	The 2D-TTR response of diamond	115
8.7	Broadband 2D-TTR instrument diagram	117
8.8	2D-TTR response of bromoform	118
8.9	Fixed parameters in RDM fits	119
9.1	Proposed MW-THz double resonance instrument	125
9.2	TKE plasma response of CS_2	127
A.1	The super-Nyquist DDS output	147
A.2	DDS segmented chirped pulse	148

LIST OF TABLES

<i>Number</i>		<i>Page</i>
3.1	Calculated parameters for ethanol-water	30
3.2	Calculated tunneling parameters for ethanol-water	32
3.3	Experimental fits for ethanol-water	33
3.4	Fit parameters for WE-t	38
3.5	A comparison of tunneling parameters for WE-t	40
4.1	Calculated ethanol-methanol parameters	45
4.2	Ethanol-methanol experimental fits	49
4.3	Kraitchman analysis of ethanol-methanol	52
4.4	Tunneling fit of ethanol-methanol	53
5.1	Measured frequencies of water vapor	65
6.1	TKE/OKE comparison	72
6.2	Goodness of fit parameters	75
7.1	RDM eigenstate energies	98
7.2	RDM matrix coupling elements	99
7.3	RDM simulation parameters	100
8.1	Dipole matrix elements	121
8.2	Polarizability matrix elements	121
8.3	Eigenstates used in 2D-TTR simulations	122

Part I

Introduction

Chapter 1

INTRODUCTION

Liquids are essential to the chemical and biological processes that occur on Earth. Many of their macroscopic properties, including solubility, vapor pressure, viscosity, and the thermodynamics of mixing, are governed by thermally-populated molecular motions resonant in the terahertz (THz) and microwave portions of the electromagnetic spectrum. These motions are generally ‘soft’ and flexible, and include the concerted movement of many atoms. Typical examples are the intermolecular Van der Waals and hydrogen bond interactions, low energy bending vibrations, conformational torsions, as well as the overall rotational motions of molecules [1–4]. Yet, directly measuring and modeling these motions is often difficult due to their fast and delocalized dynamics [3, 5]. Until recently, THz measurements have also been limited by a lack of bright radiation sources and sensitive detectors [6, 7], while microwave measurements have been restricted to relatively narrow bandwidths [8, 9].

In this thesis, we apply modern advances in high-speed digital electronics and ultrafast nonlinear optics to construct one microwave and two terahertz spectrometers to measure the structure and dynamics of molecular liquids. The thesis is divided into two parts, which correspond to two complementary approaches for studying the liquid phase. The first half of the thesis is focused on the rotational spectroscopy of cold (~ 1 K) clusters of molecules in the gas phase. These precision measurements isolate specific molecular interactions of liquids in detail. In the second half we probe bulk liquid samples at room temperature with two dimensional THz-THz-Raman spectroscopy. The measured time domain responses reveal vibrational coupling and reorientational motions on ultrafast timescales.

1.1 THz and Microwave Spectroscopy of Liquids

Spectroscopy - the study of light matter interactions - can be performed over a broad range of frequencies in the electromagnetic spectrum, each resonant with a different set of molecular motions, as shown in Fig. 1.1. In the visible (430 - 770 THz) and ultraviolet (UV, 770 THz - 30 PHz) regions of the spectrum, photons are resonant with electronic excitations in molecules, while the infrared (10 - 430 THz) probes ‘stiff’ intramolecular vibrations, such as the O-H stretch of an individual

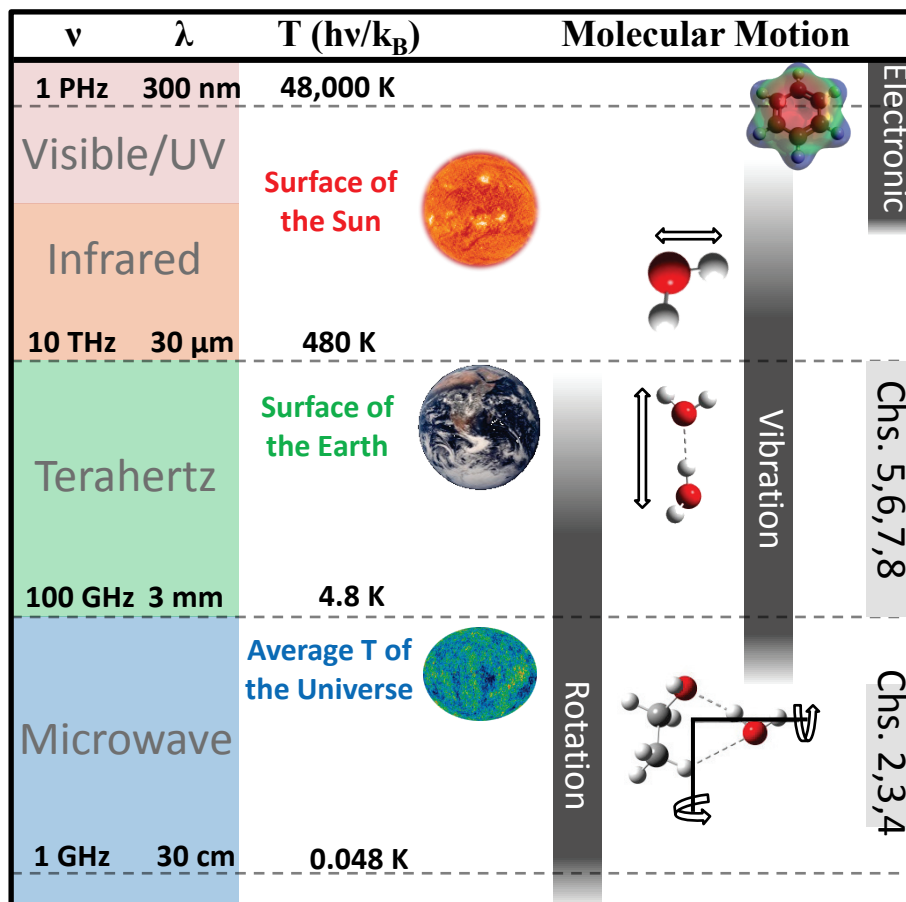


Figure 1.1: An overview of the electromagnetic spectrum in the context of molecular spectroscopy. The terahertz and microwave regions of the spectrum are the focus of this thesis and correspond to rotational and low energy vibrational motions of molecules that drive liquid phase chemistry. Image credits: NASA (Sun and Earth), WMAP Science Team (cosmic microwave background map).

water molecule. The lower frequency THz (0.1 - 10 THz) and microwave (0.3 - 100 GHz) regions of the spectrum, which are the focus of this thesis, are sensitive to overall rotations of molecules, as well as softer large amplitude vibrations, such as Van der Waals interactions, hydrogen bonds, torsions, and bending modes.

THz and microwave spectroscopy are uniquely suited to studying liquids, as they are resonant with the thermally populated motions at ambient temperatures (~ 300 K) that play an active role in chemistry [1, 3, 4]. To measure the thermally populated states at a particular temperature T requires photons of approximate energy $E = k_B T$, where k_B is Boltzmann's constant. Equivalently, the motions probed by photons of electromagnetic frequency ν are thermally excited at $T = h\nu/k_B$, where h is Planck's

constant. As shown in Fig. 1.1, the visible and UV regions of the electromagnetic spectrum correspond to thermally populated motions at $>10,000$ K, while infrared motions are significantly populated at >500 K. Most liquids on Earth lie in the 1-500 K temperature range and therefore possess thermally populated modes resonant in the THz and microwave regions.

The most direct approach for measuring microwave and THz motions of liquids is one-dimensional linear (or dielectric) spectroscopy [1]. In these experiments, the absorption and refractive index of liquids is recorded as a function of frequency, often from the MHz to the THz range [10]. Linear spectra have broad features that correspond to a combination of rotational relaxation of molecules or clusters, dipole-dipole interactions, inter- and intramolecular vibrations, and librations. Detailed analysis in the microwave and terahertz regions report directly on the internal structure and dynamics of liquids. In neat water, for example, these measurements have revealed the timescales of structural rearrangements in the hydrogen bond network and rotational relaxation [2, 10]. Linear THz measurements have also been used to measure the water of hydration around proteins and saccharides crucial to their biological function [3].

While dielectric microwave and THz spectra form the foundation of our knowledge of liquid dynamics, they are often congested and difficult to analyze. A single broad feature in a spectrum, for example, can correspond to many different environments continually interconverting on a femtosecond (10^{-15} s) to picosecond (10^{-12} s) timescale [11]. Soft, large amplitude vibrations are often highly anharmonic and delocalized, and may not obey the selection rules applicable in the infrared [12]. The rotational motions, in particular, do not form distinct peaks, as they are heavily perturbed by intermolecular interactions [2].

1.2 Rotational Spectroscopy of Molecular Clusters

The focus of Part II of this thesis is the study of molecular clusters, which isolate specific liquid phase interactions [13]. These nanoscopic aggregates only contain ~ 2 -10 molecules and are typically held at cryogenic temperatures, making their analysis much simpler than that of a bulk liquid. While cluster formation is entropically disfavored under ambient conditions, large number densities can be generated by the free jet expansion of rare gases seeded with a target molecule through a nozzle into a high vacuum ($\sim 10^{-5}$ Torr) chamber. Collisions with rare gas atoms in the dense region after the throat of the expansion rapidly cool the molecules and pro-

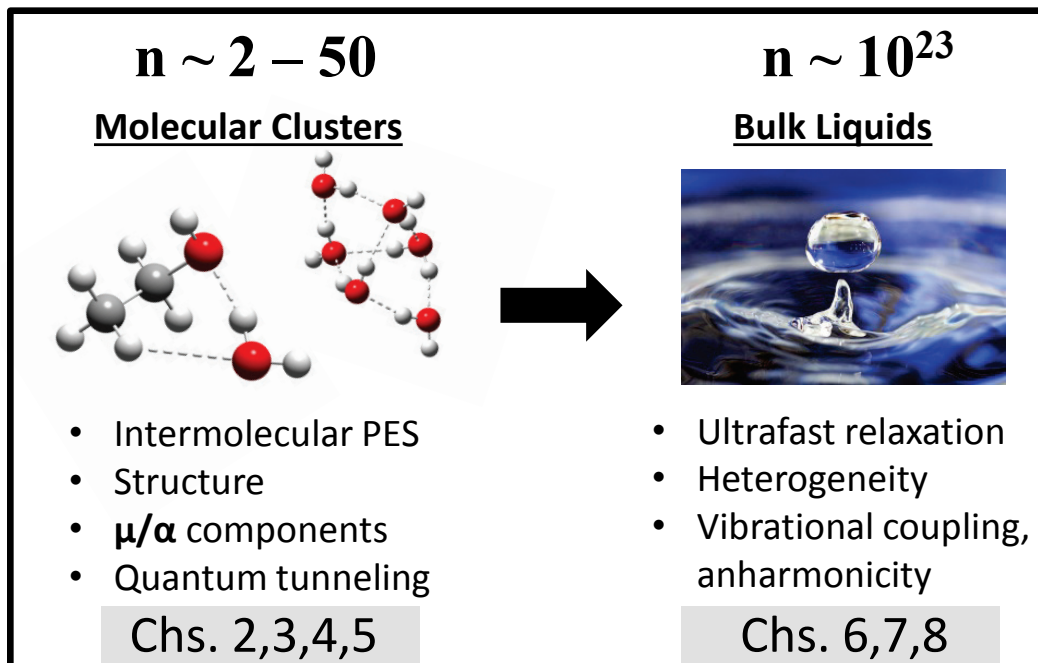


Figure 1.2: Liquids can be studied at the nanoscopic scale with molecular clusters (left) and at the macroscopic, or bulk, scale (right). Here, the number of molecules in a system is denoted by n . Data from these systems are complementary, with the nanoscopic providing detailed intermolecular potential energy surfaces (PESs), structures, and electrostatic components of small clusters, while the bulk reveals ultrafast dynamics, environment heterogeneity, and vibrational coupling and anharmonicity. The ‘intermediate’ nanometer - micron scale has also been measured with reverse micelles, revealing fascinating confinement/surface effects and acoustic phonons that are distinct from the bulk and cluster scales [16, 17]. Image credit: Wikipedia, José Manuel Suárez.

mote the formation of clusters [14]. Further past the throat, the expanding gas enters a collision-less region called the zone of silence, where they can be interrogated by microwave or THz radiation. The lack of collisions in this region allows the internally cold (~ 1 K) molecules and clusters to rotate freely for tens of microseconds, producing high-resolution rotational eigenstate-resolved spectra [15].

In the microwave region, high resolution spectra can be used to determine the moments of inertia, dipole moments, and quantum tunneling motions of clusters (Fig. 1.2). Vibrationally-averaged molecular structures can also be derived to sub-Angstrom precision with site-specific isotopic substitutions [18, 19]. The THz region, on the other hand, corresponds to low energy rovibrational transitions of clusters, from which the intermolecular potential energy surface (PES) of a cluster is

determined [20]. Spectroscopically-determined intermolecular PESs are especially important, as they can be fed directly into Monte Carlo and molecular dynamics simulations of the liquid phase [21, 22].

In Chapter 2, we detail the construction of a free jet expansion microwave spectrometer. The instrument is notably cheaper, more energy efficient, and smaller than previous designs. With this instrument, we collect the first rotational spectra of the ethanol-water and ethanol-methanol dimers in Chapters 3 and 4, respectively. These data reveal the ground state (minimum energy) structures in the two-body PESs, and a complicated interplay between weak and strong hydrogen bonds. Chapter 5 covers the development of a broadband, high resolution THz spectrometer, and a proof-of-principle measurement of water vapor at 10 mTorr. The next step is to combine the THz spectrometer with a free jet expansion to measure rovibrational spectra of hydrogen-bonded clusters, including the ethanol-water and ethanol-methanol dimers. Altogether, the microwave and THz instruments are capable of determining the structures and IPESs of moderately sized clusters ($n \sim 2-6$) to high precision.

Although rotational spectra of clusters provide precise measurements of few body intermolecular interactions and molecular structure, they do not fully capture the dynamics of the condensed phase. This is in part due to the low temperatures of free jet expansions (< 5 K), which effectively freeze the THz motions of clusters. In other words, clusters in free jet expansions are not liquid droplets, but nanoscopic ice crystals. The size of clusters accessible to rotational spectroscopy is also limited by their partition function. To date, some of the largest clusters measured by rotational spectroscopy include pioneering work on the water nonamer ($n=9$) and decamer ($n=10$) [23]. Extending these measurements to even larger clusters is exceedingly difficult, as their spectra become weaker and more complex, due to the many rotational states and isomers populated in a free jet expansion. Liquid dynamics, however, can involve the nonadditive interactions of thousands of molecules near 300 K. Thus, direct measurements of bulk liquids remain invaluable.

1.3 Ultrafast Terahertz Spectroscopy of Liquids

In Part III, we shift to direct measurements of the THz dynamics of liquids at room temperature (~ 300 K). In general, liquids containing small molecules, such as water [2], have ‘ultrafast’ dynamical timescales covering 100 femtoseconds (fs) - 1 nanosecond (ns). Longer microsecond - millisecond dynamics are also possible in aqueous biopolymers, for example, but will not be the focus of this discussion [24].

To directly measure these ultrafast motions in the time domain requires a pulse of light that is as short or shorter than the natural timescales. For this thesis, the light source for all dynamics measurements is a pulsed 40 fs amplified Titanium:Sapphire laser, which is downconverted from the near-infrared to the THz region.

A common approach for the interpretation of time resolved dynamics measurements involve time correlation functions. In a fluctuating system at thermal equilibrium, time correlation functions report on the loss of ‘memory’ of a particular variable as function of time. A simple example is the classical two point dipole correlation function $C(t_1) \propto \langle \boldsymbol{\mu}(0) \cdot \boldsymbol{\mu}(t_1) \rangle_{eq}$ [25]. This function describes the autocorrelation of the dipole moment ($\boldsymbol{\mu}$) at time $t=0$ and a later time $t=t_1$, while the brackets indicate an average over the equilibrium ensemble of molecules. The Fourier transform of this function provides the linear one-dimensional spectrum of a liquid, with rotational, vibrational, and electronic contributions. In the THz region, this can be measured by exciting a liquid with a pulse of THz light and measuring the resulting signal as a function of t_1 , as shown in Fig. 1.3. Similarly, the two point Raman autocorrelation function is $D(t_1)_{ijkl} \propto \langle \alpha_{ij}(0) \alpha_{kl}(t_1) \rangle_{eq}$, where α is the polarizability of the sample [26]. The Fourier transform of this function yields the 1D Raman spectrum, which can be measured experimentally with optical Kerr effect (OKE) spectroscopy, for example (Fig. 1.3) [27].

Now, it is important to note that the ultrafast laser experiments described above do not directly measure the equilibrium correlation function of a liquid. Instead, samples are perturbed by short pulses of light at specific times, and monitored as they return to equilibrium. However, the fluctuation-dissipation theorem states that the two correlation functions are equivalent. In other words, the thermal fluctuations of a liquid at equilibrium can be measured by recording its response after applying small perturbations from short pulses of light [28].

In general, 1D two-point correlation functions allow us to tabulate the various THz and Raman active modes present in a sample. They do not, however, directly report on the dynamics and interactions between modes. Furthermore, two-point correlation functions cannot distinguish between inhomogeneous and homogeneous broadening in a spectrum [29]. Separating the broadening mechanisms in liquids is especially important, as it reveals the distribution of molecular environments [30].

To access the underlying dynamics, mode coupling, and spectral broadening mechanisms, we must move to multidimensional three- and four-point time-correlation functions [29]. A notable example, which has been widely used in the study of

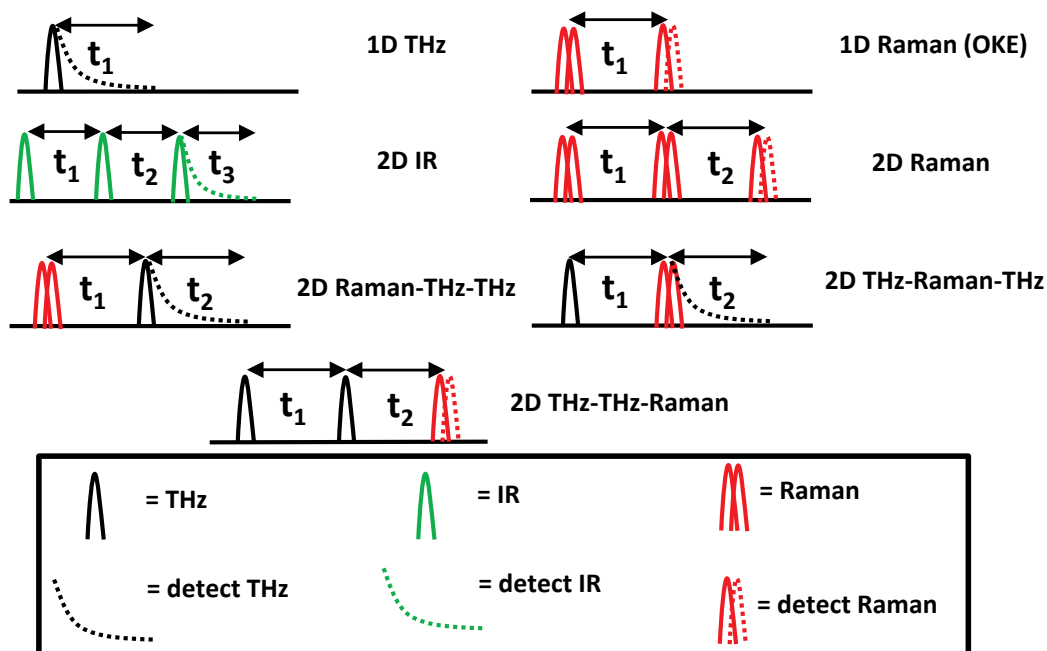


Figure 1.3: Schematics of some of the ultrafast coherent pulse sequences that have been used to measure liquids in the THz and infrared (IR) regions of the electromagnetic spectrum. Each solid ‘bump’ indicates a stimulated light-matter excitation with the sample, while the final dotted line is the detected emission. Note how the dipole allowed THz and IR excitations involve single interactions, while each Raman excitation involves two electric field interactions. The electric field scaling of each technique can be determined by counting the solid bumps. For example, 1D THz is first-order in the applied electric field, or linear, while 1D Raman and 2D IR are third-order, or nonlinear, in the field. Only odd-order techniques are allowed in bulk liquids due to their isotropic symmetry.

liquids, is 2D IR spectroscopy. A schematic of the 2D IR pulse sequence is shown Fig. 1.3, and it consists of three ultrafast pulses of IR light (as well as a fourth local oscillator detection pulse) and three time axes. Typically, the first (t_1) and last (t_3) axes are scanned to generate a 2D signal, which is Fourier transformed to produce a spectrum [31].

2D-IR spectroscopy can recover an exceptionally rich set of information on molecular liquids, not available in a traditional 1D IR spectrum [31]. For example, the distance and angle between vibrations can be determined from the intensity of off-diagonal peaks. This has been applied to structure determination [32] and folding mechanisms of proteins in solution using amide vibrations [33]. The middle time axis t_2 can also be varied to determine the spectral diffusion of a peak. This uncovers the ultrafast dynamics of vibrational population transfer between the various

modes of a molecule in a liquid. Spectral diffusion measurements on liquid water, for example, have shown surprisingly fast relaxation from the O-H stretch to bend, librational, and intermolecular modes [34]. Altogether, 2D IR has revolutionized our understanding of the liquid phase.

Developing multidimensional spectroscopies in the THz is more difficult than in the IR, because of a lack of intense ultrafast light sources and sensitive detectors. Pioneering 2D Raman experiments were carried out in the 1990s to access Raman active low energy vibrations [30]. It was soon discovered, however, that these fifth-order experiments were contaminated with cascaded third-order signals [35]. Recently, the Hamm group has demonstrated hybrid 2D Raman-THz-THz and THz-Raman-THz pulse sequences (Fig. 1.3) that overcome these difficulties [12]. In an initial demonstration Hamm and coworkers showed that there is heterogeneity in the hydrogen bond network of liquid water on a 100 fs timescale [11]. Further, the timescales of heterogeneity are perturbed in aqueous salt solutions, indicating changes to the structure of the water from ion solvation [36].

In this thesis we develop the complementary 2D THz-THz-Raman sequence (Fig. 1.3). The basis for the technique is THz Kerr effect (TKE) spectroscopy first developed by Nelson and coworkers in 2008 [37]. In Chapter 6, we build a TKE instrument, and perform proof-of-principle measurements on a series of simple liquids. The pulse sequence is equivalent to 2D THz-THz-Raman with t_1 fixed to 0. We identify a clear single exponential decay in the signal due to the reorientational decay of individual molecules, as well as a second multiexponential component likely due to intermolecular interactions. The results are compared with literature values from OKE measurements, revealing a striking difference in decay amplitudes. We attribute this to the differences in the strength of the THz and Raman coupling to the bath modes of liquids.

In Chapter 7, we implement the full 2D THz-THz-Raman spectroscopy, by adding a second time delayed THz pulse to the experiment. Varying the time delay between the two THz pulses allows us to the control of the orientational motions in several liquids on an ultrafast timescale. We also identify clear oscillations in the 2D signal, due to coupling between low energy intramolecular modes in several halomethane liquids. To investigate this coupling, we extend the bandwidth and sensitivity of the instrument in Chapter 8. This reveals many new peaks, including photon-echo contributions, and a clear trend of forbidden THz and allowed Raman transitions in the 2D spectrum. We perform a series of simulations comparing the effects of

vibrational anharmonicity, nonlinearities in the dipole and polarizability, as well as perturbations from the surrounding bath.

Finally, we discuss the overall conclusions and future directions of the thesis in Chapter 9. With modest upgrades to the existing instrumentation, we expect many exciting future applications of this work in gas- and condensed-phase chemistry.

Part II

**Rotational Spectroscopy of
Molecular Clusters**

*Chapter 2***A DIRECT DIGITAL SYNTHESIS CHIRPED PULSE FOURIER
TRANSFORM MICROWAVE SPECTROMETER**

Chirped pulse Fourier transform microwave (CP-FTMW) spectrometers have become the instrument of choice for acquiring rotational spectra, due to their high sensitivity, fast acquisition rate, and large bandwidth. In this chapter, we present the design and capabilities of a recently constructed CP-FTMW spectrometer using direct digital synthesis (DDS) as a new method for chirped pulse generation, through both a suite of extensive microwave characterizations and deep averaging of the 10-14 GHz spectrum of jet-cooled acetone. The use of DDS is more suited for *in-situ* applications of CP-FTMW spectroscopy, as it reduces the size, weight, and power consumption of the chirp generation segment of the spectrometer all by more than an order of magnitude, while matching the performance of traditional designs. The performance of the instrument was further improved by the use of a high speed digitizer with dedicated signal averaging electronics, which facilitates a data acquisition rate of 2.1 kHz. In Chapters 3 and 4, we use this instrument to collect the pure rotational spectra of the ethanol-water and ethanol-methanol dimers, respectively, formed in supersonic jet expansions.

Almost all of this chapter has been reproduced with permission from:

Finneran, I. A., Holland, D. B., Carroll, P. B. & Blake, G. A. A direct digital synthesis chirped pulse Fourier transform microwave spectrometer. *Review of Scientific Instruments* **84**, 083104 (2013).

One figure has been reproduced with permission from:

McGuire, B. A., Carroll, P. B., Loomis, R. A., Finneran, I. A., Jewell, P. R., Remijan, A. J. & Blake, G. A. Discovery of the interstellar chiral molecule propylene oxide (CH₃CHCH₂O). *Science* **352**, 1449–1452 (2016).

2.1 Introduction

Microwave spectroscopy is an invaluable tool for studying the structure [40], dynamics [41] and even the handedness [42] of gas phase species. In particular, the specificity of microwave spectroscopy has been central to the unambiguous identification of the great majority of molecules detected in the interstellar medium [43]. Applications of microwave spectroscopy to problems in physical chemistry and molecular astrophysics have been greatly accelerated by developments in laboratory techniques. One of the most significant advancements in microwave spectroscopy was the invention of pulsed microwave emission techniques in the 1950s, which provided increased sensitivity over traditional absorption experiments [44]. Further increases in sensitivity and resolution over small bandwidths were demonstrated in the 1970s and 1980s by the Flygare lab at the University of Illinois, using both waveguide and Fabry-Perot resonator spectrometers [45, 46]. In the mid-2000s the Pate lab at the University of Virginia developed a complementary Chirped Pulse Fourier Transform MicroWave (CP-FTMW) spectrometer, capable of measuring 11 GHz of bandwidth in less than 10 microseconds [9]. The bandwidth, acquisition speed, sensitivity, and relative intensity information attainable with the chirped pulse design has led to its increasingly widespread use in the molecular spectroscopy community [47–54].

There are three major components of CP-FTMW spectrometers that enable the collection of broadband spectra: high sample rate digitizers for acquisition of the microwave emission, broadband high power amplifiers (based on either solid state or traveling wave tube technology) to ensure sufficient power for sample polarization, and Arbitrary Waveform Generators (AWGs) or Arbitrary Function Generators (AFGs) for producing the chirped polarization pulse. In state-of-the-art, multi-GHz bandwidth instruments each of these major components require significant power and physical space. AFGs and AFGs, in particular, are bulky and energy-consuming, since they contain a significant amount of microwave circuitry so as to enable the generation of arbitrarily complex pulse sequences. However, for most CP-FTMW experiments (with a few notable exceptions, such as 2D MW-MW spectroscopy [55]) the waveform generator is typically only used to create pulsed linear frequency sweeps. As we will show, a simpler and more compact alternative to AFGs/AFGs is direct digital synthesis.

Direct digital synthesizers (DDSs) are Nyquist devices with good frequency agility and low phase noise. Using an external sample clock and digital control word, a DDS

generates a tunable digital signal with a numerically controlled oscillator, which is then converted into sinusoidal output with a digital-to-analog converter (DAC) [56]. Their frequency agility and low phase noise capabilities have been utilized for longer (35 μ s) broadband frequency sweeps at millimeter-wave frequencies for radar imaging applications [57], as well as slow narrowband frequency sweeps (3 MHz) in a millimeter-wave fast scan absorption spectrometer [58]. To date, however, this technology has never been used for CP-FTMW spectroscopy.

To this end, we discuss the novel use of a DDS chip to generate short ($\sim 1 \mu$ s), broadband (1.9 GHz) linear frequency sweeps for CP-FTMW spectroscopy. A second PLL board functioning as the local oscillator (LO) source further reduces the weight and size of the spectrometer. The total power requirement of the DDS and PLL boards is only 3 W, considerably less than the power draw of an AWG, 100-500 W. The DDS and PLL boards are also much smaller and lighter (1,400 cm³, 240 grams) than an AWG (42,000 cm³, 14.1 kilograms for the 4.2 GS/s Tektronix AWG710B), making it possible to use CP-FTMW spectrometers in many applications that were previously not feasible due to size, weight, or power restrictions. For this thesis, all of the components were purchased soldered into separate, and non-optimal, evaluation boards. However, the chips (DDS, PLL) used in these boards are sold individually, and could be combined into a single compact circuit board that has been optimized for the needs of the CP-FTMW spectrometer, further reducing the weight, size, and power required [59]. The current evaluation board spectrometer and future optimized circuit designs will make the CP-FTMW technique more suitable for *in-situ* applications.

2.2 Methods

Many variations on the original CP-FTMW microwave spectrometer have been described in the literature [47–54], but they are all based on the same basic theory of operation. A phase-stable broadband microwave pulse from an AWG is amplified and broadcast into a gas phase molecular sample, either in a static cell [48] or in a molecular beam expansion [9]. The coherent microwave pulse builds up a macroscopic polarization in the gas, as the molecular dipoles rotate in phase with the microwave pulse. Before the dipoles dephase, the microwave pulse ends and the molecules continue to rotate in phase, emitting a free induction decay (FID). Because the angular momentum of the molecules is quantized, they only rotate at specific frequencies that are dependent on their moments of inertia. The FID is detected in the time domain with a digitizer and Fourier transformed to recover

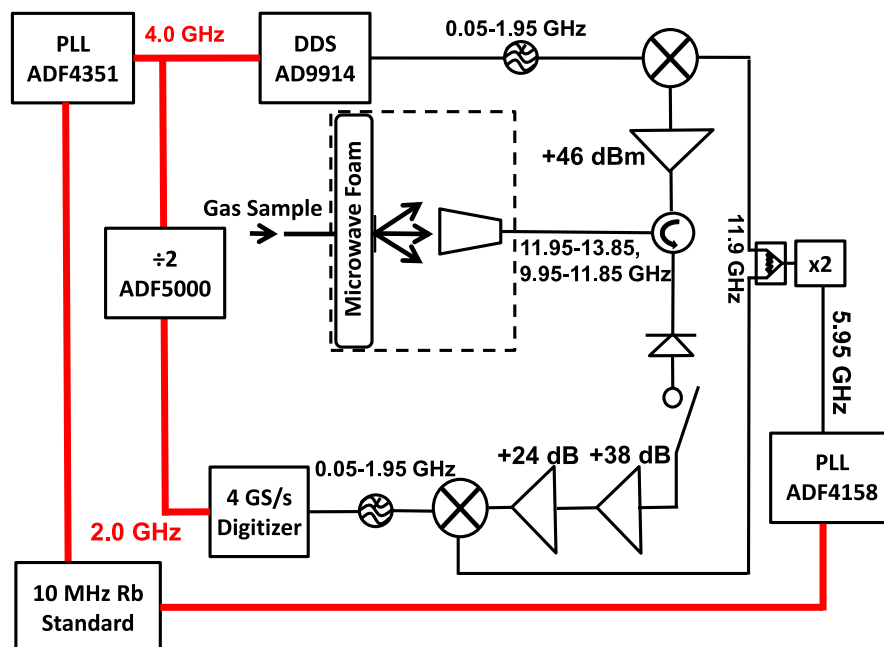


Figure 2.1: The microwave circuit of the DDS-based chirped pulse spectrometer. Microwave reference connections are highlighted in thick red lines for clarity. See text for design details.

the frequency domain spectrum. Since the frequencies that are probed with the microwave pulse are often higher than the bandwidth of the AWG and the digitizer, the chirped pulse and FID are typically heterodyned with a higher frequency signal from a microwave synthesizer or phase-locked dielectric resonant oscillator.

Our spectrometer differs from previous designs in three ways: the AWG has been replaced by a DDS board, the microwave synthesizer has been replaced by a PLL synthesizer board, and the chirp is broadcast into a coaxial expansion with one horn and microwave foam behind the pulsed valve. To utilize the full 2 GHz Nyquist bandwidth of the digitizer, we have also synchronized the DDS board and the digitizer to the same 4 GHz sample clock.

Microwave Circuit

A schematic of our spectrometer is shown in Fig. 2.1. The DDS evaluation board (Analog Devices 9914) generates a 1.9 GHz linear frequency sweep chirp in $1.2 \mu\text{s}$. The chirp is low-pass filtered (Minicircuits, VLP-24) and then upconverted by mixing with the doubled (Marki ADA-0410P) output of a PLL evaluation board (Analog Devices ADF4158) in a broadband mixer (Marki M1R-0726L), to reach

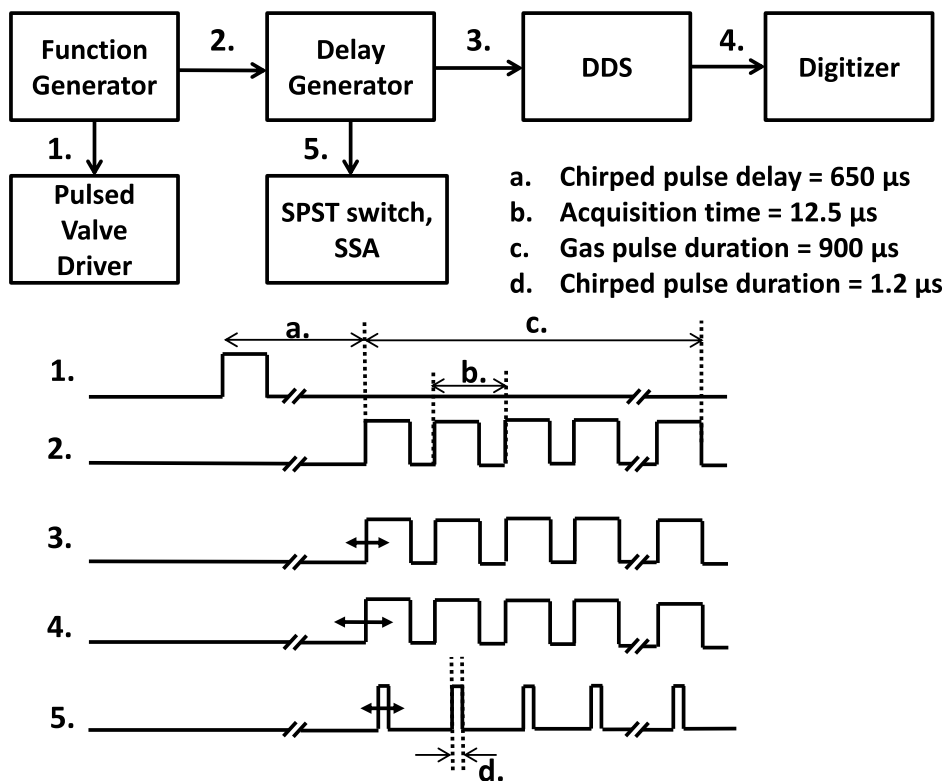


Figure 2.2: The pulse timing used for collecting multiple FIDs per gas pulse. See text for design details.

a final dual sideband bandwidth of 3.9 GHz centered at 11.9 GHz. A gap exists between 11.85-11.95 GHz. After upconversion, the chirp is amplified by a solid state 40 W amplifier (Microsemi C0618-43-T680), passed through a circulator (Teledyne C-12S63T-1), and broadcast into a vacuum chamber ($\sim 10^{-6}$ Torr) through a microwave horn (Narda model 640). The gas sample is supersonically expanded coaxially (with respect to the microwave pulse) through a pulsed nozzle (General Valve Series 9) positioned at the center of a section of microwave foam (Emerson and Cuming HR-25). Molecular sample is fed into the pulsed valve by sending argon through a gas bubbler containing the sample. While the microwave radiation is passing through the circulator, an open SPST switch (Narda S213D) prevents the pulse from damaging the detection path of the circuit, while a diode limiter (Aeroflex ACLM-4537C361K) prevents damage to the switch. The timing of the switch, the solid state amplifier, and the start of the DDS chirp are controlled by

a digital pulse delay generator (SRS DG-535). After excitation, the microwave horn collects the molecular emission, and directs it to the detection portion of the circuit through the circulator. The emission is amplified by a high-gain, low noise amplifier (Miteq AMF-5F-08001800-14-10P), downconverted by a second mixer (Marki M1R-0726L), low-pass filtered (Minicircuits, VLP-24), and sampled by a 4 GS/s digitizer (Agilent U1084A).

For the AWG tests we exchanged the DDS board with the AWG used in the original CP-FTMW paper [9] (Tektronix AWG7102, 10 GS/s, on loan from the University of Virginia). The local oscillator (LO) PLL board (ADF4158) and doubler were also replaced with a microwave synthesizer (Hittite HMC 2100) to match the conventional CP-FTMW design [9].

Instrument Triggering

A schematic of the instrument triggering is shown in Fig. 2.2. A critical design feature is the trigger signal sent directly from the DDS to the digitizer (trace 4 in Figure 2.2). When triggered, the DDS will output the chirped pulse with a random delay of up to one clock cycle, making trace 3 unusable for digitizer triggering. However, a digital high/low pin output on the DDS board does give the required precision timing for averaging waveforms on the digitizer (Appendix A).

The Agilent U1084A digitizer is capable of averaging at extremely high repetition rates using the onboard FPGA (field-programmable gate array); the only limiting factor for the repetition rate is the re-arm time of $2.7 \mu\text{s}$ between consecutive waveforms. Consequently, the maximum repetition rate for a $9 \mu\text{s}$ FID collection is 85 kHz, which could be realized in a continuous expansion or static cell experiment. Thus, our FID averaging throughput is limited by the maximum pulsed valve rate that is sustainable with our vacuum pumps. In previous CP-FTMW spectrometers multiple FIDs have been collected for each gas pulse, by outputting multiple chirped pulses from the AWG per trigger pulse [9]. The DDS board, however, generates only one chirped pulse per trigger event. To circumvent this problem we triggered the delay generator with 70 $12.5 \mu\text{s}$ square pulses from the output of a function generator (SRS DS345) that were delayed by $600 \mu\text{s}$ from the start of the synchronization signal (Figure 2.2). The synchronization signal was sent to the pulsed valve so that 70 chirped pulses were triggered per gas pulse. The pulsed valve was run at a repetition rate of 30 Hz, so that the wall clock repetition rate for the $9 \mu\text{s}$ FID collection was effectively 2.1 kHz.

We were able to further improve the performance of the instrument by using a coaxial molecular beam orientation. A similar CP-FTMW spectrometer with one horn and one focusing mirror has also been demonstrated, in perpendicular [60] and coaxial [61] arrangements. The setup presented here is similar to the last setup, except the microwave mirror has been replaced by microwave foam so that the backwards going emission is detected (Figure 2.1). This setup is more appropriate for coaxial broadband measurements, since the cavity Q is negligible. For a single nozzle setup, the overlap between the microwave radiation and the expansion is more optimal in the coaxial arrangement leading to a longer transit time for FID collection and thus a higher signal-to-noise ratio and higher spectral resolution.

2.3 Results and Discussion

To evaluate the performance of DDS-based CP-FTMW spectrometers we measured the output of the DDS board individually (with the 4 GS/s digitizer) and as part of the total microwave circuit. As an isolated component, we compared the triggering, bandwidth, and phase stability of the DDS board to the AWG. After demonstrating that the board was capable of generating a triggered, broadband, phase-stable chirped pulse, we connected it to a full CP-FTMW circuit and compared the phase stability and signal-to-noise of the new DDS/PLL-based instrument with that of the AWG/microwave synthesizer-based instrument for the FID of a transition in acetone. Phase stability of the FID is extremely important, since many data acquisition cycles must be averaged to obtain reasonable signal-to-noise ratios. Finally, we collected the full 3.8 GHz A/D bandwidth-limited spectrum of acetone with deep averaging and compared the results with predicted spectra from the literature, to demonstrate the dynamic range and relative intensity performance of the instrument.

Phase Stability and Bandwidth of the Chirped Pulse

The two main sources of phase jitter in the DDS/digitizer combination are changes in the phase of the chirped pulse output of the DDS and trigger jitter between the DDS and digitizer. Regarding the first issue, the particular DDS board (AD9914) shifts the phase of the chirp output from pulse to pulse. We took advantage of the phase-reset feature by setting the ‘Autoclear phase accumulator’ bit in the DDS chip, so that the phase was the same for every chirped pulse triggered by the delay generator [56].

Trigger jitter acts as a low pass filter in the frequency domain, limiting the bandwidth of the spectrometer when multiple time domain waveforms are co-added. We

minimized the trigger jitter by synchronizing the DDS and digitizer with the same external sample clock, the 4 GHz output of the ADF4351 PLL. The maximum external clock frequency for the digitizer is 2 GHz, so we divide the 4 GHz DDS clock by two (Analog Devices ADF5000) before it passes into the digitizer. The 2 GHz bandwidth chirped pulse output of the DDS and the AWG are shown in Figure 2.3. After averaging both waveforms up to 100,000 times no significant intensity modulations were observed in the averaged signal of the DDS, except a small dip at 1.4 GHz. A spectrogram of the waveforms indicated that both the DDS and the AWG have similar harmonic distortion, at approximately -30 dBc.

For normal operation, the bandwidth of the DDS is limited by the Nyquist frequency, or 2 GHz (using a 4 GHz sample clock). However, an inherent feature of DDS chips is low power super-Nyquist images of the fundamental [56]. These images can be filtered out of the DDS signal (as is done in this design, albeit inefficiently, as shown in Figure 2.5) or used to extend the bandwidth of the AD9914 beyond 2 GHz (as described in Appendix A).

Phase Stability and Signal-to-Noise of the FID

A common-mode rejection design (Figure 2.1) was employed to minimize LO phase jitter by splitting (Minicircuits ZX10-2-183-S+) the doubled PLL output to drive both the upconversion and downconversion mixers (as done in previous CP-FTMW circuits [47]). To evaluate the phase stability of the instrument, 10 million FIDs from the 3_{21} - 3_{12} AA transition in acetone (10762.6 MHz rest frequency, measured with 11900 MHz LO) were averaged with the DDS/PLL setup and with a conventional AWG/synthesizer circuit (Figure 2.4). The deviation from \sqrt{n} averaging is similar in both setups, indicating that the DDS spectrometer has sufficient phase stability to be used for coherent averaging in a CP-FTMW spectrometer. The total signal-to-noise at 10 million averages differed by only 4% between the AWG and DDS circuits, insignificant compared to the inherent intensity variations in CP-FTMW spectrometers [9]. The signal-to-noise of the instrument in both the DDS and AWG configurations is lower than the original Pate lab spectrometer [9], due to the polarization power available (50 W versus 2 kW), but comparable to other low power (<100 W) CP-FTMW spectrometers [47, 49, 51, 60, 62].

Full Instrument Demonstration

The spectrum of acetone between 9.95-13.85 GHz collected using the DDS CP-FTMW is shown in Figure 2.5. For this demonstration the ADF4158 PLL board

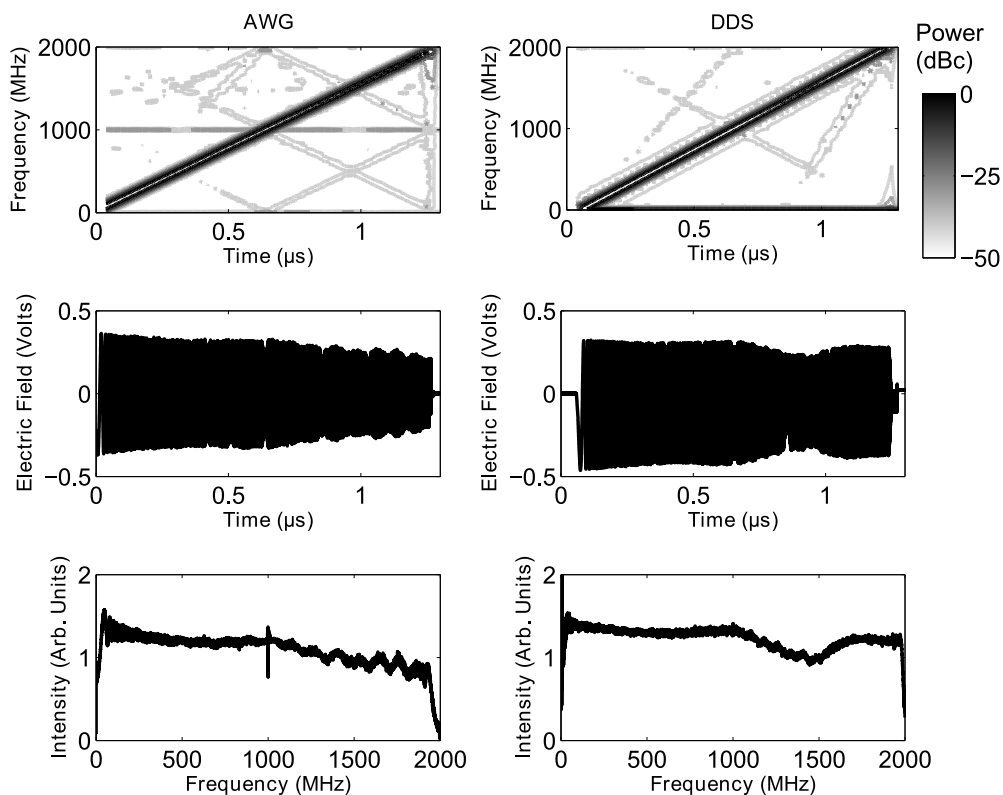


Figure 2.3: A comparison between the filtered chirped pulse outputs of an AWG (left) and a DDS (right) after 100,000 averages. The FFT of the waveforms are very similar, except for a small dip in the intensity of the DDS at 1.4 GHz. A spectrogram of the chirped pulses (top) indicates that the AWG and DDS have similar harmonic distortion in their output. The off diagonal content in the spectrogram is down by 30 dB from the main frequency sweep in both the DDS and the AWG.

was disconnected from the 10 MHz standard for improved performance. After 22 hours of averaging at a 2.1 kHz repetition rate (170 million averages) the signal-to-noise of the strongest peak was $\sim 18,000:1$. The dual sideband convolved (LO=11900 MHz) predicted spectrum of the normal species of acetone [63, 64] and the two ^{13}C substituted species [65] (scaled to 1% intensity) at 2 K are also plotted in Figure 2.5, with negative intensity. At this sensitivity, the singly substituted ^{13}C isotopologue of acetone is clearly visible in natural abundance at 160:1, as shown in the inset of Figure 2.5. Additionally, several acetone transitions above 13.9 GHz were aliased into the detection bandwidth. Although the output of the DDS and the input of the digitizer are filtered, a sufficient amount of super-Nyquist power was delivered from the DDS through the amplifiers to polarize transitions at 2-2.5 GHz offset from the

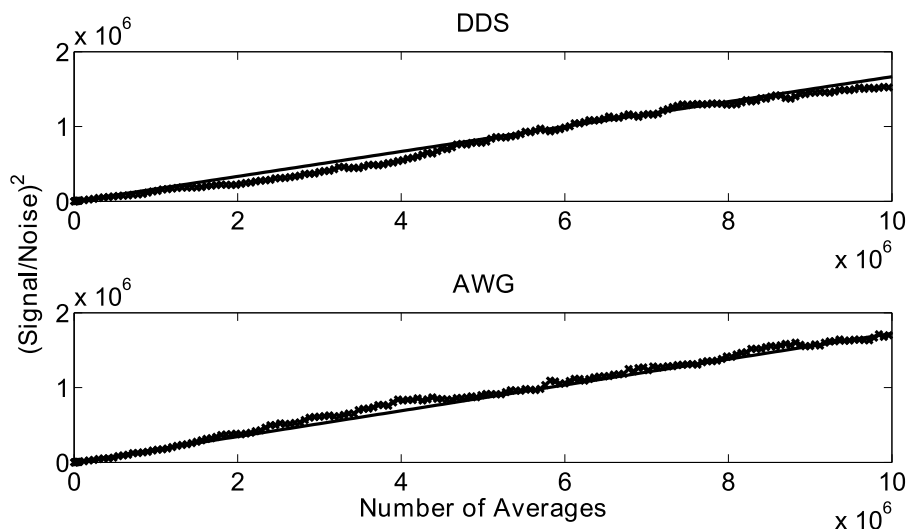


Figure 2.4: The phase stability of the DDS spectrometer was compared to that of the AWG spectrometer via emission from the $3_{21}-3_{12}$ AA transition in acetone (10762.6 MHz rest frequency, LO = 11900 MHz). Both setups show little deviation from the expected \sqrt{n} averaging.

LO frequency. This behavior can easily be removed by using higher rejection low-pass filters. Finally, the rest frequencies of the transitions were verified by shifting the LO frequency.

The relative transition strengths are greatly dependent on the response of the SSA and the coupling of the horn to free space, which causes moderate intensity variations in the measured spectrum. However, the observed relative intensity variations are comparable to those reported in the literature for conventional instruments [9].

The fast acquisition speed of the DDS CP-FTMW spectrometer is demonstrated in Figure 2.6. After 30 seconds of data collection (65,000 averages) two of the the strongest peaks of the carbonyl substituted ^{13}C isotopologue are visible at 3:1 signal-to-noise.

Finally, Doppler doublets were observed for longer ($>20 \mu\text{s}$) FID collections, as shown in Fig. 2.7. This splitting is present in both the AWG and DDS circuits. The peak splitting increases with helium backing gas, indicating that it is caused by Doppler splitting and not by the microwave circuit.

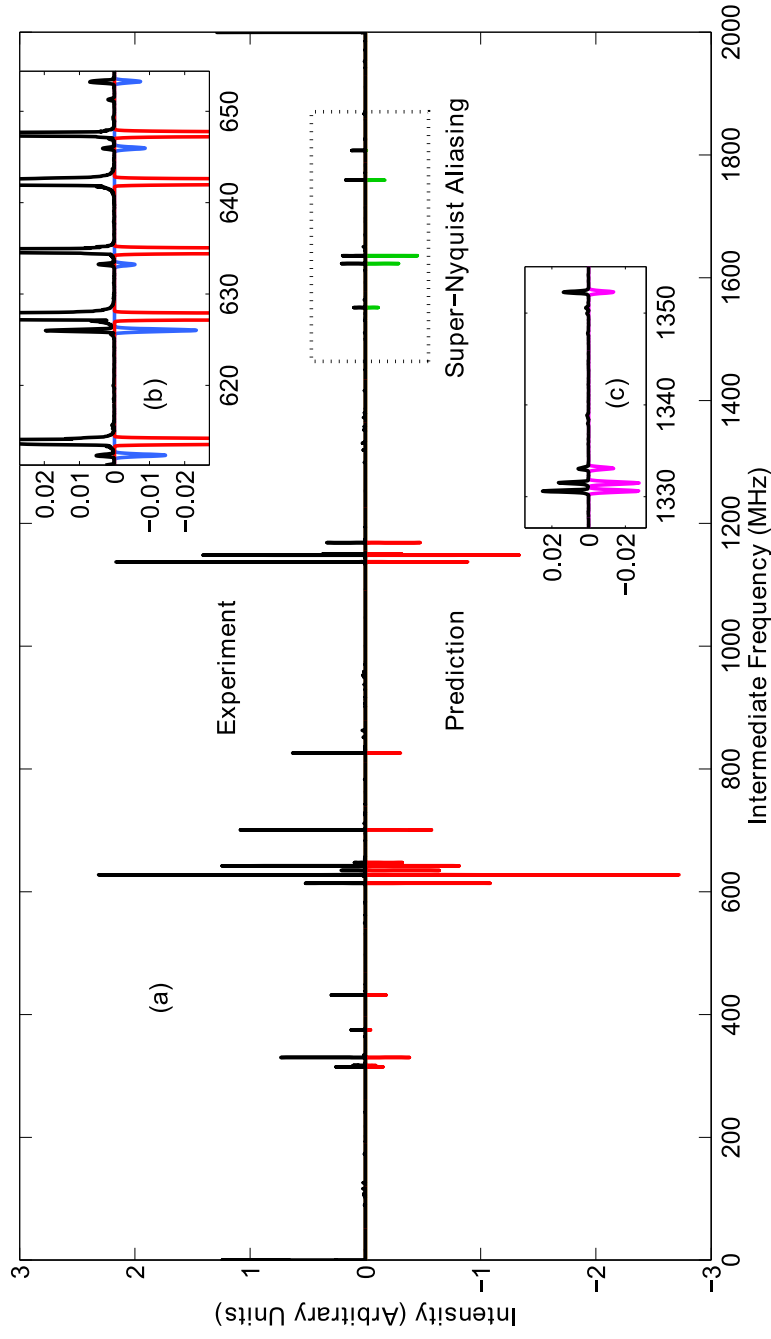


Figure 2.5: The dual sideband convolved spectrum of acetone from 9.95-13.85 GHz (LO = 11.9 GHz) after 22 hours of averaging (170 million FIDs). (a) The experimental spectrum (positive going) is plotted against a prediction of the normal species (negative intensity). The signal-to-noise is 18,000:1 on the strongest transition ($2_{11}-2_{02}$ EE). Super-Nyquist content of the normal species at 1.5-1.9 GHz is plotted with a different scaling, and highlighted in the dashed box. (b) An inset of the spectrum showing experimental and predicted $2_{11}-2_{02}$ transitions of the carbonyl ^{13}C substituted species of acetone at 2 K. (c) An inset of the methyl ^{13}C substituted species of acetone at 2 K, showing four of the $3_{21}-3_{12}$ transitions.

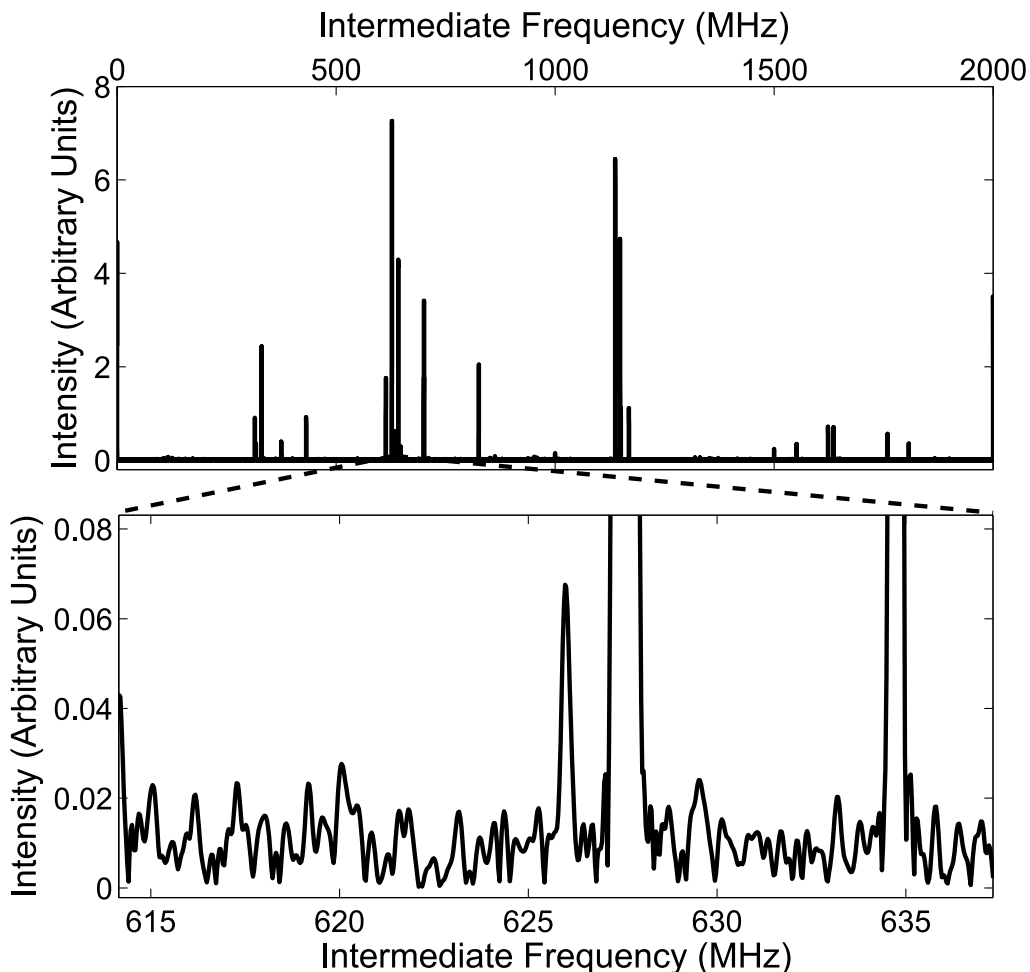


Figure 2.6: The spectrum of acetone after 30 seconds of data collection (top), with an inset showing the detection of the ^{13}C isotopologue at more than 3:1 signal-to-noise (bottom). LO = 11900 MHz

2.4 Conclusion

The utility of the CP-FTMW spectrometer for sensitive detection and characterization of gases with a permanent dipole is well established among molecular spectroscopists. With the latest bandwidth extensions in commercially available DDS chips it is now possible to generate a chirped pulse and LO signal at 12 GHz using an energy-efficient and compact design. Additionally, PLL synthesizers can be expected to increase in frequency (for example, the 18 GHz Analog Devices ADF41020 or the 6 GHz Valon 5009 synthesizer), and with sufficient multiplication the LO signal could also be supplied by the DDS. Indeed, the inherent step nature of the DDS frequency sweep matches the signal requirements for ‘stepped’ LO CP-FT mm-wave spectroscopy [66] (Appendix A). Multiplication of a DDS

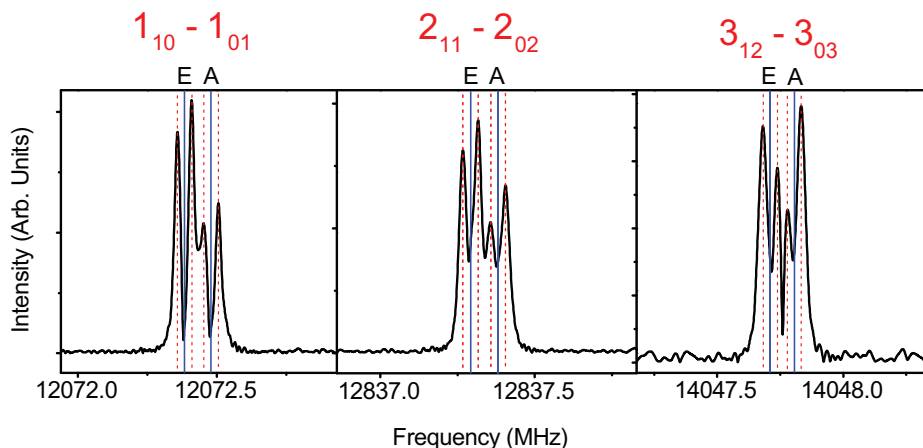


Figure 2.7: Three transitions of propylene oxide using a $130 \mu\text{s}$ FID. This long FID allows us to resolve the A-E methyl rotor splitting (solid blue lines) and Doppler splitting (dashed red lines), although it reduces the signal-to-noise ratio of the spectrum. This measurement was used in the detection of propylene oxide in the interstellar medium [39].

chirped pulse has already been demonstrated in a hybrid DDS/PLL chirped pulse synthesizer for radar applications at 675 GHz [57], and could be used to further extend the bandwidth of the instrument.

Regardless of the specific implementation, the phase stability and harmonic distortion of the DDS chirped pulses are comparable with those of the AWG for short and long averaging times, providing the required stability for coherent signal averaging. Similar advances can be expected in other areas of CP-FTMW technology as well. The complexity of FPGAs are increasing on even faster slopes than CPU architectures, and high duty cycle digitizers and averagers can therefore be expected to continue improving in capabilities well into multi-GHz bandwidth designs. For microwave studies in molecular beams where quasi-optical focusing is required, high power, high cost amplifiers will be needed, but for waveguide studies [48] or especially higher frequency applications [66] the amplifier power requirements for sample polarization drop considerably. The low cost of this new DDS-circuit design combined with these advances should allow for the widespread use of CP-FTMW spectroscopy in physical chemistry laboratories, and the capabilities outlined here open the door to truly integrated DDS/PLL single card approaches to compact, energy efficient, lightweight CP-FTMW spectrometers for *in-situ* and process monitoring applications.

Chapter 3

THE ETHANOL-WATER DIMER

In this chapter, we report the first rotational spectrum of two isomers of the ethanol-water dimer using the Caltech CP-FTMW spectrometer described in Chapter 2. With the aid of isotopic substitutions, and *ab initio* calculations, we identify the first isomer as a water-donor/ethanol-acceptor structure. Ethanol is found to be in the gauche conformation, while the monomer distances and orientations likely reflect a cooperation between the strong (O-H...O) and weak (C-H...O) hydrogen bonds that stabilizes the measured isomer. No other isomers were assigned in an argon expansion, indicating that this is the ground-state structure. This result is consistent with previous vibrationally-resolved Raman and infrared work, but sheds additional light on the structure, due to the specificity of rotational spectroscopy. In a helium-backed expansion, a higher energy water-donor/trans-ethanol-acceptor isomer was observed. This isomer exhibits a significant splitting in the measured rotational transitions, likely due to the tunneling of the water molecule between equivalent hydrogen bond acceptor sites. Followup measurements were taken with a cavity FTMW spectrometer by Brett McGuire, Marie-Aline Martin-Drumel, and Michael McCarthy at Harvard to further investigate this splitting. With a semi-empirical potential, the barrier to interconversion of the water molecule was determined to be $\sim 88 \text{ cm}^{-1}$.

Most of this chapter has been reproduced with permission from:

Finneran, I. A., Carroll, P. B., Allodi, M. A. & Blake, G. A. Hydrogen bonding in the ethanol–water dimer. *Physical Chemistry Chemical Physics* **17**, 24210–24214 (2015).

One figure in this chapter has been reproduced with permission from:

Seifert, N. A., Finneran, I. A., Perez, C., Zaleski, D. P., Neill, J. L., Steber, A. L., Suenram, R. D., Lesarri, A., Shipman, S. T. & Pate, B. H. AUTOFIT, an automated fitting tool for broadband rotational spectra, and applications to 1-hexanal. *Journal of Molecular Spectroscopy* **312**, 13–21 (2015).

3.1 Introduction

Hydrogen bonds play a critical role in many chemical and biochemical processes. In the Earth's atmosphere, hydrogen bonds control cluster formation and influence reaction rates, while in the condensed phase they guide protein folding and solvent-solute interactions. Their importance to molecular processes on Earth is due in part to their moderately low bond energies of 4-40 kcal/mol, which allow them to freely associate and dissociate under ambient conditions, as well as their directional preferences, which influence the structure of molecular assemblies [69].

Since the first descriptions of prototypical hydrogen bonds at the beginning of the 20th century a second class of "weak" hydrogen bonds has emerged. As the name suggests, weak hydrogen bonds are generally defined by interactions of <4 kcal/mol, which opens the door for many new bonding partners [70]. Structurally, all hydrogen bonds are generally defined as interactions of X-H...A, where H carries a partial positive charge, and A a partial negative charge. Weak hydrogen bonds stretch this definition to include C-H...O, O-H... π , and C-H... π interactions, among others. Although they are similar in energy to Van der Waals interactions, weak hydrogen bonds have been found to retain a distinct directional preference. In condensed phase chemistry, these weak interactions have been shown to be both ubiquitous and influential in drug-receptor recognition, molecular crystallization, and macromolecular structure [69, 71].

The ethanol-water dimer is an excellent model system for hydrogen bonding, as it exhibits both a strong O-H...O hydrogen bond, as well as a weak C-H...O hydrogen bond. The energy landscape of the dimer is thus an interplay between the relative donor/acceptor strengths of water and ethanol, as well as the gauche/trans conformations of the ethanol monomer [72]. In the condensed phase, ethanol-water mixtures have been studied extensively, due their broad applications as well as their abnormal behavior. They exhibit many thermodynamic anomalies, such as a negative entropy of mixing, for example, which are believed to originate from incomplete mixing on the microscopic scale [73]. Elucidating the structure and dynamics of hydrogen bonding of the ethanol-water clusters, especially the dimer, may inform such studies.

The Raman and infrared spectrum of the ethanol-water dimer were previously reported in the literature [74, 75]. Two ethanol acceptor isomers were identified, with the ground state corresponding to a gauche-ethanol conformation. We report a combined experimental and computational study of the ethanol-water dimer using microwave rotational spectroscopy and *ab initio* calculations. Microwave

spectroscopy is unmatched for structure determination of small hydrogen bonded clusters in the gas phase, as spectra directly reveal the moments of inertia of various species [9, 18, 76]. Indeed, microwave spectroscopy provided some of the first direct structural evidence for the O-H... π weak hydrogen bond in the benzene-water dimer [76], as well as unambiguous assignments of the relative energies of the water hexamer isomers [18].

In this chapter, we observe two isomers of the ethanol-water dimer and definitively assign the ground state structure to a water-donor structure, with ethanol in the gauche conformation. With the use of three Kraitchman substitution coordinates and *ab initio* calculations, we find evidence of cooperativity between both the strong and weak hydrogen bond interactions in this structure.

Besides structure determination, microwave spectra also provide dynamical information on motions such as quantum mechanical tunneling. Indeed, inversion tunneling was first identified in the microwave spectrum of the ammonia molecule [77]; the microwave transitions associated with this motion were later used in the first maser in 1955 by Townes et al. [78]. More recently, inversion tunneling has been identified in chiral systems such as the water trimer [79], propanediol [80], and glycerol [81], in which the tunneling motion connects a pair of enantiomers. In these cases the tunneling motions are associated with the movement of one or several hydrogen atoms. In this chapter, we identify an exceptionally massive quantum tunneling motion in the second higher energy isomer, one associated with the movement of an entire water molecule.

3.2 Methods

The spectrum of the ethanol-water dimer was collected using the Caltech chirped-pulse Fourier transform microwave (CP-FTMW) spectrometer between 8-18 GHz [38]. The mixed dimer was prepared by loading water into a reservoir pulsed valve, and flowing a backing gas (argon or helium) over a separate external reservoir containing ethanol. The mixture of ethanol, water, and 2 atmospheres of backing gas was supersonically expanded into a vacuum chamber at 10^{-5} Torr with a pulse repetition rate of 5 Hz. The CP-FTMW spectrometer circuit was the same as in Chapter 2. Double resonance measurements were carried out using a chirped pulse followed by a second single tone 0.5-1 μ s sinc pulse. Samples of ethanol (99.5% purity), ethan(ol-d) (99% purity), and D₂O (99% purity) were purchased from Sigma-Aldrich and used without further purification.

The measured spectra from the instrument are dual sideband, and so cover a total of 4 GHz for each local oscillator (LO) setting (2 GHz each in the upper and lower sideband). Thus, care must be taken in assigning molecular rest frequencies. We use a python data acquisition script to cyclically shift the LO every 3 minutes to cover 8-18 GHz and to discriminate upper versus lower sideband peaks. For every LO setting, we shift by +10 MHz and deconvolve with a separate python script.

After assigning two isomers of the dimer, targeted followup measurements were performed with a Balle-Flygare cavity FTMW spectrometer [46] at the Harvard-Smithsonian Center for Astrophysics by Brett McGuire, Marie-Aline Martin-Drumel, and Michael McCarthy. A detailed description of this instrument has been reported in the literature [82].

Spectral fitting was performed with the Watson-S Hamiltonian in SPFIT/SPCAT [83] and a newly written python graphical interface. Due to the high line density of the spectra, we used AUTOFIT, an automated broadband fitting program, to generate initial quantum number assignments and fits to the various species [68]. An overview of the AUTOFIT program is given in Fig. 3.1. Kraitchman substitution coordinates were calculated with the KRA program [84].

All *ab initio* calculations were performed using Gaussian 09 [85]. Geometry optimizations were carried out with second-order Møller-Plesset (MP2) perturbation theory [86] and the augmented-correlation consistent polarized Valence-only Triple-Zeta (aug-cc-pVTZ) basis set [87]. All optimized structures were confirmed to be true minima on the potential energy surface via harmonic frequency calculations at the same level of theory as the optimization. We subsequently performed single-point Coupled Cluster energy calculations with singles, doubles, and perturbative triples (CCSD(T)) [88] with the aug-cc-pVTZ basis set on the MP2 optimized structures. The zero point vibrational energy (ZPVE) contribution to the relative energies was evaluated from the previous harmonic frequency calculation using MP2/aug-cc-pVTZ. We computed equilibrium rotational constants (B_e) for all isomers using the molecular geometries from the MP2/aug-cc-pVTZ optimization. Next, we calculated the anharmonic cubic and semi-diagonal quartic force constants in a normal mode representation at the MP2/aug-cc-pVTZ level, and from this determined the ground state rotational constants (B_0) of the WE-g+ isomer using second-order vibrational perturbation theory [89]. We did not perform anharmonic calculations of the other isomers due to the limited computational resources available.

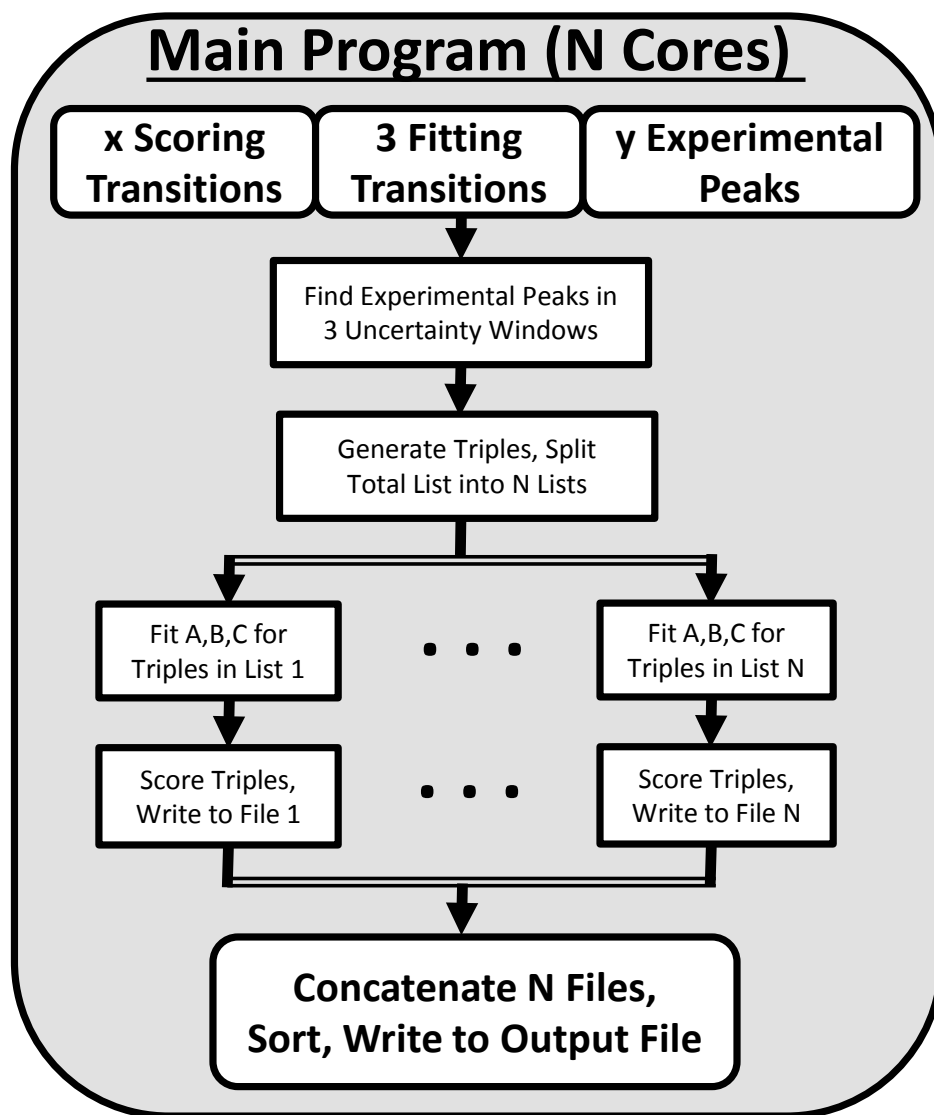


Figure 3.1: Overview of the AUTOFIT program that we developed in collaboration with the Pate lab at University of Virginia and the Shipman lab at New College of Florida. Rotational spectra are fit with a brute force algorithm that is embarrassingly parallel. The A, B, and C rotational constants for sets of three linearly independent predicted ‘fitting transitions’ are fit to all possible combinations of experimental peaks. The resulting fits are assessed and sorted with a second set of ‘scoring transitions.’ The full details of the program are reported in [68].

3.3 Results and Discussion

Computational Results

The *ab initio* energy landscape, including the zero point vibrational energy (ZPVE), of the ethanol-water dimer is shown in Fig. 3.2, and the associated equilibrium rotational constants (B_e) of each isomer are given in Table 3.1. We use nomenclature from the literature to label the various structures: WE indicates a water-donor geometry, EW a ethanol-donor motif, while -g and -t specify the hydroxyl conformation of the ethanol subunit [75]. The two hydrogen bonding sites of the WE-g isomer are further differentiated with + and -.

The strong hydrogen bond between ethanol and water makes the largest contribution to the relative energies of the structures. Since ethanol is a better hydrogen bond acceptor than donor, the water donor structures are lower in energy than the water acceptor structures [72]. The ethanol molecule can exist in the trans or gauche conformation, which dictates the position of the strong hydrogen bond.

Weaker interactions in the dimer lead to further energy separations between isomers. The lowest three isomers all exhibit water donor structures, as expected, yet the WE-g+ and WE-t isomers are significantly lower in energy than the WE-g- structure. As Fig. 3.2 shows, however, the WE-g+ and WE-t structures are both compact and exhibit a second weak C-H...O hydrogen bond interaction, while the WE-g- structure is elongated and contains no secondary interaction(s). We posit that the weak hydrogen bond stabilizes these isomers by $\sim 200 \text{ cm}^{-1}$ (0.5 kcal/mol), which is consistent with previous estimates of C-H...O binding energies [90].

	WE-g+	WE-t	WE-g-	EW-g	EW-t
A/MHz	8882	9163	22081	9772	27305
B/MHz	3676	3502	2309	3062	2071
C/MHz	2888	2799	2164	2525	1991
μ_a/D	1.8	1.7	2.5	-2.6	-2.8
μ_b/D	0.9	1.3	0.9	1.3	0.5
μ_c/D	0.4	-0.2	-0.1	0.3	0
Energy/cm⁻¹	0	22	200	291	279

Table 3.1: The calculated equilibrium *ab initio* rotational constants, dipole moments, and relative energies (including ZPVE) of the five possible isomers of the ethanol-water dimer at the MP2/aug-cc-pVTZ level of theory.

Interestingly, the predicted energies of the two water acceptor isomers do not exhibit a clear preference for compact or elongated structures. We attribute this to

barriers are close to those measured in the ethanol monomer [92] and are over 1000 cm^{-1} (Table 3.2).

We identified a second tunneling motion in the WE-t isomer (Fig. 3.2). The WE-g+ and WE-t structures both have a chiral center on the oxygen of the ethanol molecule. Interconversion between enantiomers is not feasible in the WE-g+ structure, as the hydroxyl hydrogen on ethanol blocks the path of the water molecule. However, in the EW-t isomer the hydroxyl hydrogen atom has changed position, allowing free passage of the water molecule between the ethanol acceptor sites. We identify a single transition state in this motion, resulting in a double-well potential connecting enantiomers. The energy barrier of the interconversion (66 cm^{-1} , including ZPVE) is small enough to allow quantum tunneling of the water molecule. This splits the ground vibrational state into symmetric (0+) and antisymmetric (0-) states [80].

To quantify the symmetric/antisymmetric tunneling splitting, we applied a WKB approximation of the potential [80, 93]. Using the *ab initio* energies and vibrational frequencies of the ground state and transition state, we found that the predicted splitting is $>100\times$ greater for the water tunneling than for the methyl internal rotation (Table 3.2).

	WE-t LAM	WE-t Methyl	WE-g Methyl
Barrier/ cm^{-1}	66	1078	1153
$\Delta E/\text{GHz}$	4.2	<.001	<.001

Table 3.2: The calculated energy barriers of tunneling motions in the ethanol-water dimer (including ZPVE), as well as WKB predictions for tunneling splitting of the ground vibrational state.

Experimental Results

The microwave spectrum of ethanol and water with argon as the backing gas is shown in Figure 3.3. Peaks from the ethanol dimer, water dimer, and ethanol monomer are all present, as can be seen by the predictions included from the literature [94–96]. A series of unknown strong peaks were identified when ethanol and water were present that disappeared in expansions of ethanol/argon and water/argon. Accordingly, the peaks were assumed to originate from a cluster containing both molecules.

Using AUTOFIT [68] and SPFIT [83], we fit 21 a-type and b-type transitions to a microwave rms of 14 kHz, commensurate with the line center uncertainty of the instrument (Table 3.3). The assignments were further confirmed with double

WE-g+	<i>ab initio</i>	EtOH:H ₂ O	EtOD:D ₂ O	EtOH:D ₂ O	EtOD:HOD	EtOD:H ₂ O
A/MHz	8940	9089.862(10)	8610.610(20)	9046.626(36)	8614.300(39)	8648.244(40)
B/MHz	3485	3410.8841(35)	3163.8418(85)	3191.064(14)	3203.203(17)	3381.274(13)
C/MHz	2777	2737.9705(28)	2568.4509(73)	2593.615(15)	2594.324(18)	2710.510(10)
DJ/kHz	15.0	20.33(15)	14.94(19)	16.67(83)	15.88(94)	*
DJK/kHz	-13.8	-31.35(19)	-18.50(62)	-26.9(17)	*	*
DK/kHz	48.5	137.4(25)	96.2(39)	*	*	*
d1/kHz	-4.2	-5.957(16)	-4.03(12)	*	*	*
d2/kHz	-0.40	-0.6016(46)	*	*	*	*
N		21	15	12	9	8
rms/kHz		14	15	37	41	41

Table 3.3: The *ab initio* ground state rotational and quartic distortion constants (MP2/aug-cc-pVTZ), and experimental rotational and distortion constants for the WE-g+ isomer of the ethanol-water dimer, including several deuterated species. Parameters with an asterisk (*) were fixed to the corresponding constant of the normal species, while the standard errors of the last digits are given in parentheses. All fits are from the Caltech dataset. The full list of transitions used in the fits are given in Appendix B.

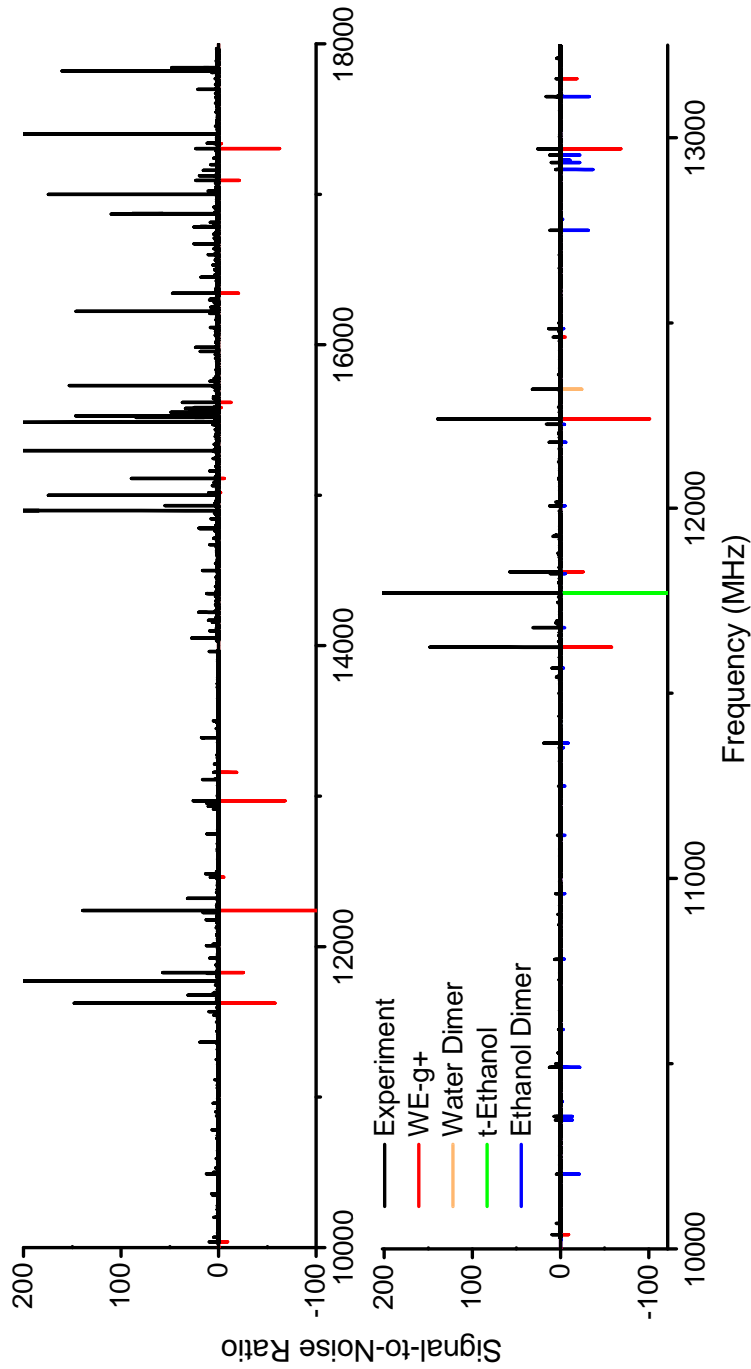


Figure 3.3: Top: The spectrum of ethanol and water in an argon expansion between 10-18 GHz (15 million averages, 40 hour acquisition at 4 LO settings). A series of strong unassigned peaks have been fit and assigned to the WE-g+ isomer of the ethanol-water dimer (red). Bottom: A 3 GHz inset of the ethanol+water expansion spectrum. Literature data for ethanol dimer [94], trans-ethanol [95], and water dimer [96] have been plotted in various colors, along with WE-g+, using a rotational temperature of 2 K. Measurements are from the Caltech instrument.

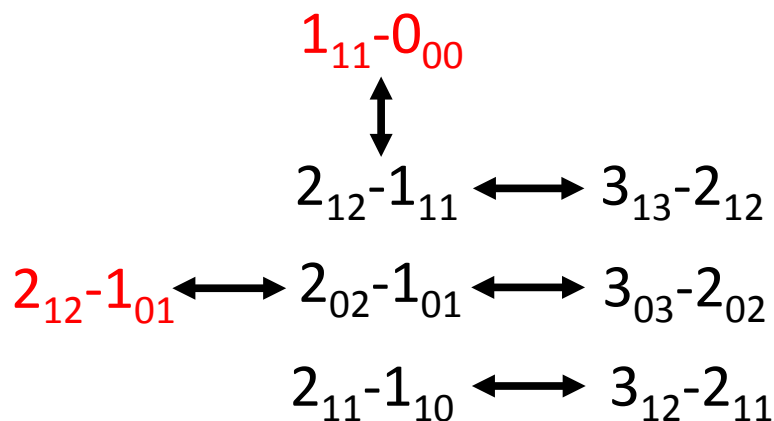


Figure 3.4: The transition connectivities confirmed with double resonance measurements (a-types in black, and b-types in red).

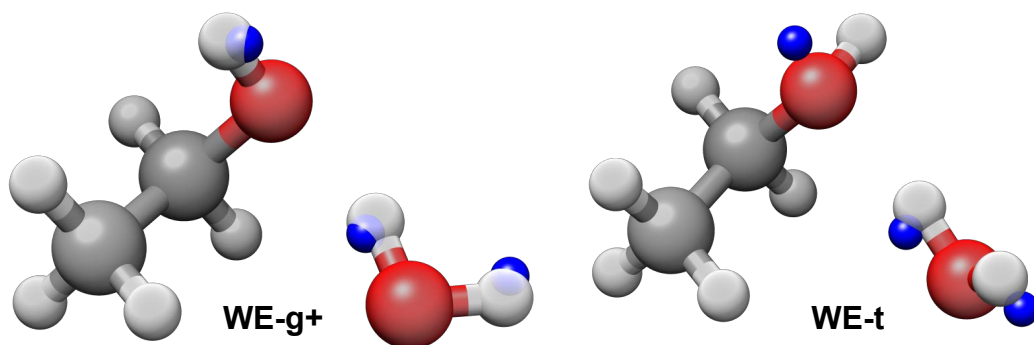


Figure 3.5: Kraitchman substitution positions of three hydrogens in the ethanol water dimer are shown as blue spheres, superimposed on the *ab initio* structures of WE-g+ (left) and WE-t (right). Based on the substitution positions, it is clear that WE-g+ is the measured isomer.

resonance measurements (Fig. 3.4). The rotational constants and dipole components ($\mu_a > \mu_b$) rule out all possible isomers except WE-t and WE-g+. Both isomers have similar structures and dipole moments; the main distinguishing feature is the orientation of the hydroxyl hydrogen of the ethanol, and the dihedral of the water molecule along the strong hydrogen bond.

To differentiate the identity of the isomer, we measured the spectra of several deuterated species of ethanol and water. Again, double resonance measurements were performed on each isotopologue to confirm assignments. The rotational constants for four isotopologues are given in Table 3.3, and the singly-substituted Kraitchman structure is shown in Fig. 3.5. The position of the hydroxyl H atom of ethanol

was calculated by substitution of EtOD:H₂O into the normal species, the outer H atom of water was calculated with substitution of EtOD:HOD into EtOD:H₂O, while the hydrogen bonded H atom was calculated with substitution of EtOD:D₂O into EtOD:HOD. We doubly confirmed the position of the ethanol hydroxyl H with substitution of EtOD:D₂O into EtOH:D₂O. For each substitution, the H-atom coordinate in the principal axis system was converted to internal coordinates and plotted on the normal species result. The deuterated spectra have lower signal-to-noise and higher spectral density than the non-deuterated spectra so definitive assignments of EtOH:HOD, EtOH:DOH, and EtOD:DOH were not possible.

The measured geometry of the dimer observed in the argon expansion is consistent with WE-g+, confirming its identity as the lowest energy isomer. This is in contrast to the ethanol monomer, which has a trans-hydroxyl ground state structure. Thus, the hydrogen bond interaction between water and ethanol stabilizes the gauche structure, an example of adaptive aggregation (Fig. 3.6). This is in agreement with previous infrared and Raman work [74, 75]. Furthermore, the measured rotational constants are consistent with the ground state rotational constants (B_0) determined in the *ab initio* anharmonic calculation. The large difference between the calculated B_0 and B_e constants indicates significant vibrational averaging of the dimer geometry even in the ground state. Large vibrational corrections to rotational constants have been reported in other hydrogen bonded clusters [18].

We hypothesize that the stabilization of the gauche conformation comes from the weak hydrogen bond of the dimer, as the strength of a C-H...O interaction is dependent on the bond angle and C-H...O distance. The Kraitchman structure in Fig. 3.5 indicates that the outer hydrogen of the water is collinear with the weak hydrogen bond, which may enable a larger overlap of the oxygen lone pair with the C-H, rather than the perpendicular H-O...C angle of the t-WE structure. Furthermore, in the *ab initio* structures the WE-g+ isomer has a C-H...O distance of 2.66 Å, while the length is 2.79 Å in WE-t. Additional microwave measurements of isotopically substituted dimers are needed to confirm the weak hydrogen bond length in WE-g+.

With helium as the backing gas, we identified a second isomer of the ethanol water dimer and fit the spectrum of the normal and EtOD:D₂O species. Extended measurements of this isomer were taken by the McCarthy group, as described in the Methods section (Fig. 3.8). The shift in the rotational constants with respect to the WE-g+ isomer suggest that the new species is WE-t. The measured a-type and b-type peaks display a doublet splitting of several MHz, which is dependent on J

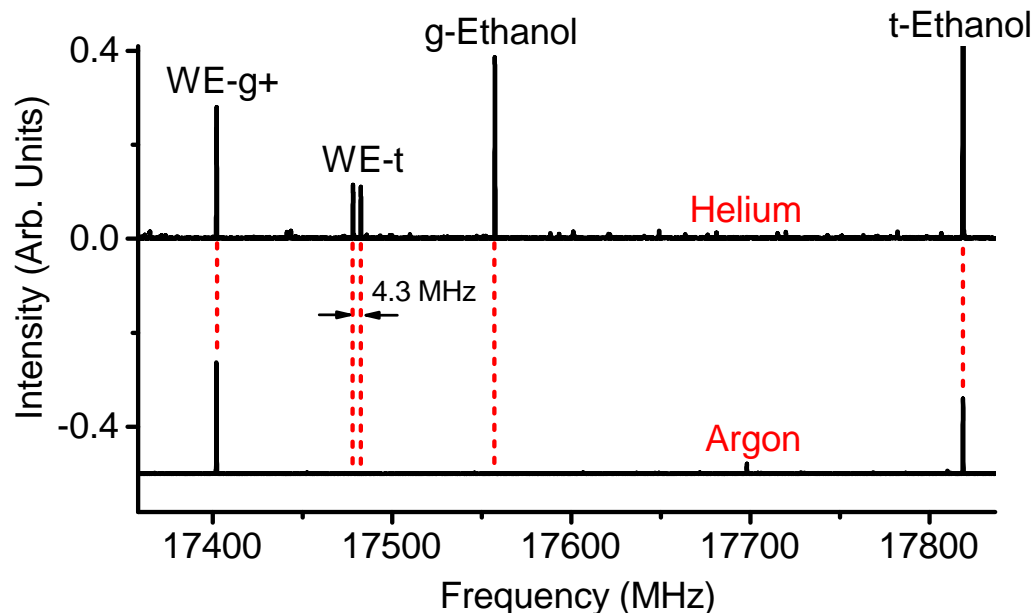


Figure 3.6: Direct spectroscopic evidence for adaptive aggregation in the ethanol water dimer. Conformational cooling in the argon expansion favors the trans orientation in the ethanol monomer and the gauche orientation in the ethanol-water dimer. Measurements are from the Caltech instrument.

and K. No c-types were observed, although we note that the predicted c-type dipole moment is exceedingly small.

Our *ab initio* results predict that the enantiomer interconversion changes the sign of the c-axis dipole moment, while preserving the sign of the a- and b-type dipole moments. Thus, selection rules dictate that c-type transitions will cross the two lowest tunneling states, here denoted $0+$ and $0-$, with a predicted splitting of 8.6 GHz. The a- and b-type transitions will stay within a single tunneling state, and will be split by a Coriolis interaction between the tunneling states. Typical Coriolis splittings are 100-1000x lower than the tunneling splitting [80].

To fit the Coriolis splitting we used the following Hamiltonian from the literature [97]:

$$H = H_{\text{rot}} + H_{\text{cd}} + H_{\text{int}} + H_{\text{tun}}. \quad (3.1)$$

The first two terms, H_{rot} and H_{cd} , are the standard rigid rotor and centrifugal distortion components, respectively, while H_{int} is the tunneling-rotation Coriolis

WE-t	<i>ab initio</i>	EtOH:H ₂ O	EtOD:D ₂ O
A+/MHz	9222.0	9358.743(55)	8671.94(82)
B+/MHz	3345.6	3272.7786(33)	3075.5359(149)
C+/MHz	2685.5	2635.704(47)	2471.8883(140)
A-/MHz		9357.966(63)	[8671.94]
B-/MHz		[3272.7786]	[3075.5359]
C-/MHz		2635.438(43)	[2471.8883]
DJ/kHz	23.6	21.3118(304)	16.66(46)
DJK/kHz	-24.2	-13.718(221)	-6.72(142)
DK/kHz	90.5	144.2(304)	[144.2]
d1/kHz	-4.76	-4.6153(77)	[-4.6153]
d2/kHz	-0.308	-0.5453(219)	[-0.5453]
F_{ca} /MHz		-319.22(45)	[-319.22]
F_{bc} /MHz		-18.461(40)	-6.91(54)
ΔE /MHz		498.48(45)	58.96(99)
N		38	14
rms/kHz		18	57

Table 3.4: Fit parameters for the WE-t isomer of the ethanol-water dimer, including several deuterated species. The normal species (EtOH:H₂O) fit is from the Harvard dataset, while the deuterated species (EtOD:D₂O) fit is from the Caltech dataset. The full list of transitions used in the fits are given in Appendix B.

interaction term:

$$\langle 0+ | H_{\text{int}} | 0- \rangle = \langle 0- | H_{\text{int}} | 0+ \rangle = F_{bc}(J_b J_c + J_c J_b) + F_{ac}(J_a J_c + J_c J_a). \quad (3.2)$$

We exclude the F_{ab} interaction term, as the tunneling motion proceeds through the *ab* plane. Finally, H_{tun} defines the energy separation, ΔE , between the 0+ and 0- states:

$$\langle 0- | H_{\text{tun}} | 0- \rangle - \langle 0+ | H_{\text{tun}} | 0+ \rangle = \Delta E. \quad (3.3)$$

With this Hamiltonian, we obtain a satisfactory fit of the measured spectrum, as shown in Table 3.4. The Coriolis coupling constant F_{ac} is moderately large, likely due to the fact that the tunneling motion proceeds mostly parallel to the *ac*-plane of the dimer. The measured energy splitting of the normal species is ~ 500 MHz, which is smaller than the *ab initio* prediction (Table 3.5). In the deuterated species, the splitting decreases considerably, as shown in Fig. 3.7, leading to an energy splitting of 50 MHz, also lower than the *ab initio* splitting of 150 MHz (Table 3.5).

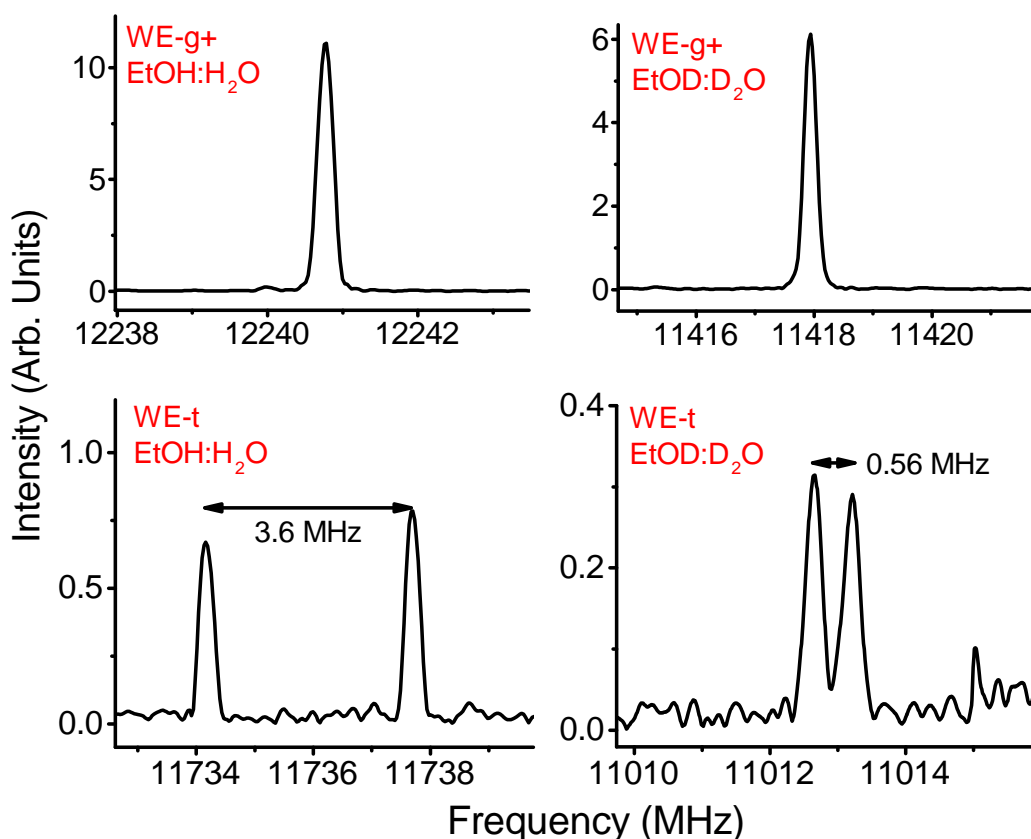


Figure 3.7: A comparison of the $2_{02} - 1_{01}$ transition in several species of the ethanol-water dimer. None of the WE-g+ isotopomers exhibit a tunneling splitting, as shown in the upper two panels. The WE-t isomer, on the other hand, shows a large splitting that is dependent on isotopic substitution (bottom two panels). Measurements are from the Caltech instrument.

The shape of the potential cannot be determined from the splitting of the lowest levels. However, we calculated a semi-empirical barrier to interconversion using the *ab initio* potential energy surface and the measured tunneling splitting. The vibrational frequencies of the ground state and transition state were held constant, while the barrier was fit to the measured energy splitting (Table 3.5). The semi-empirical barriers agree quite well with the *ab initio* barriers. Most importantly, we observe the proper scaling in the tunneling barrier with isotopic substitution.

3.4 Conclusion

We have measured the pure rotational spectrum of the ethanol-water dimer in supersonic expansions with argon and helium. Transitions from three isotopologues of one isomer were identified in the argon expansion and assigned to a compact

WE-t	ΔE_{calc} (MHz)	ΔE_{exp} (MHz)	V_{calc} (cm^{-1})	V_{exp} (cm^{-1})
EtOH:H ₂ O	4170	498	66	88
EtOD:D ₂ O	144	59	95	103

Table 3.5: A comparison of the measured and calculated tunneling splitting and derived barrier height in the WE-t isomer.

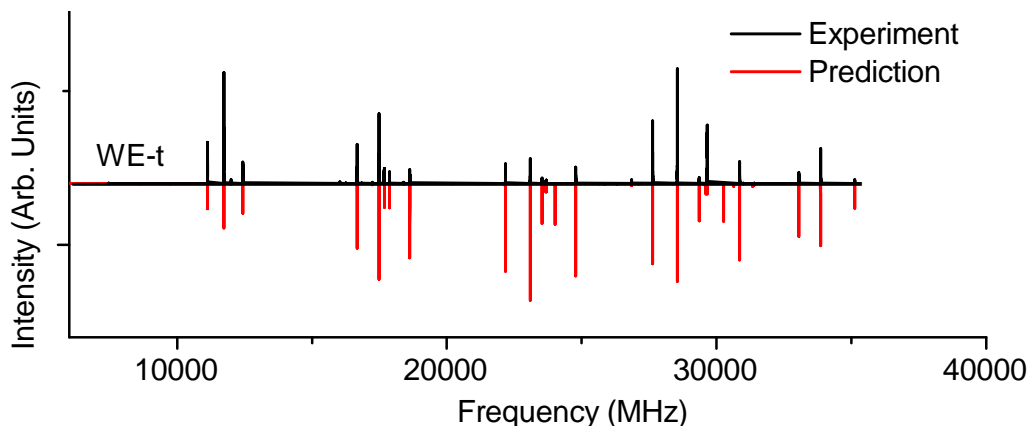


Figure 3.8: Extended measurements of the normal species of WE-t using the Harvard CfA cavity FTMW spectrometer. Data courtesy of Brett McGuire, Marie-Aline Martin-Drumel, and Michael McCarthy.

water-donor structure with ethanol in the gauche configuration. A second water-donor/trans-ethanol-acceptor isomer was observed in a helium expansion. These first rotationally-resolved measurements confirm that ethanol is a better hydrogen-bond donor than acceptor, and adaptive aggregation of ethanol, as the interaction with water stabilizes the gauche isomer relative to the trans geometry. Weak hydrogen bond interactions likely play a role in this process, as the overlap between the oxygen of the water with the C-H is more optimal in the WE-g+ isomer than the WE-t isomer.

In addition to structural information, we have also identified new dynamics in the high energy isomer. The pure rotational transitions of this isomer are split in a doublet pattern due to the quantum mechanical tunneling of water between equivalent hydrogen-bond acceptor sites.

Chapter 4

THE ETHANOL-METHANOL DIMER

Previous theoretical work on the ethanol-methanol dimer has been inconclusive in predicting the preferred hydrogen bond donor/acceptor configuration [98]. In this chapter, we report the microwave spectrum of the dimer using the Caltech CP-FTMW spectrometer from 8-18 GHz. In an argon-backed expansion, 50 transitions have been assigned to a trans-ethanol-acceptor/methanol-donor structure that is likely stabilized by a secondary weak C-H...O hydrogen bond. A higher energy isomer was observed in a helium-backed expansion and tentatively assigned to a gauche-ethanol-acceptor/methanol-donor structure. No ethanol-donor/methanol-acceptor dimers have been found, suggesting such interactions are energetically disfavored. A preliminary analysis of the A-E splitting due to the internal rotation of the methanol methyl group in the ground state species is also presented. We find evidence of the Ubbelohde effect in the measured A-E splittings of three deuterated isotopologues and the normal species of this isomer.

This chapter has been reproduced with permission from:

Finneran, I. A., Carroll, P. B., Mead, G. J. & Blake, G. A. Hydrogen bond competition in the ethanol–methanol dimer. *Physical Chemistry Chemical Physics* **18**, 22565–22572 (2016).

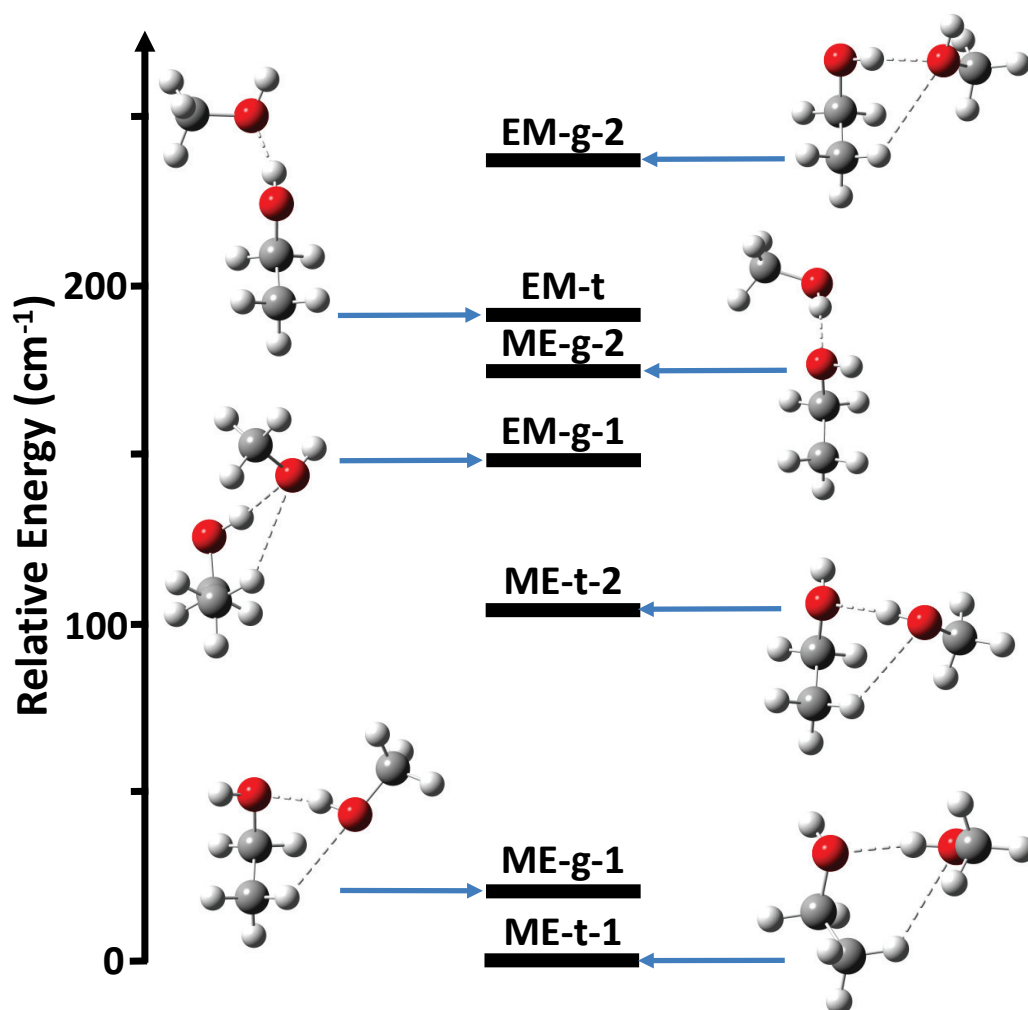


Figure 4.1: The *ab initio* relative energies, including zero point vibrational energy (ZPVE), of the various ethanol-methanol dimer isomers at the MP2/aug-cc-pVTZ level of theory. Single point energy calculations were performed using CCSD(T)/aug-cc-pVTZ.

4.1 Introduction

Structural competition between hydrogen bond donors and acceptors influences the energetics of many chemical reactions, and the structure of biological macromolecules [69, 100]. Alcohol clusters are particularly interesting systems in the study of hydrogen bond competition, as they contain a combination of stronger hydrogen bonds as well as weaker hydrophobic interactions [101]. Here, we report the microwave detection and analysis of the ethanol-methanol heterodimer, one of the simplest mixed alcohol dimers.

A fundamental question in the study of hydrogen bond competition is the donor/acceptor

preference when two molecules interact to form an isolated dimer. While the donor/acceptor strength of the two molecules is often a dominant force, weak hydrogen bonds and internal conformational preferences may also play a role. The ethanol-water, methanol-water, isopropanol- and tert-butyl alcohol-water dimers, for example, exhibit a clear preference for alcohol-acceptor/water-donor structures [67, 102–104]. For the ethanol-water dimer the most compact ethanol-acceptor/water-donor structure is favored over others, likely due to a secondary C-H...O hydrogen bond (Chapter 3) [67, 74, 102].

The structural competition in the ethanol-methanol dimer is more ambiguous than that in ethanol-water, methanol-water, isopropanol-water, and tert-butyl alcohol-water. Past theoretical work has been inconclusive in determining the ground state structure of the ethanol-methanol dimer, though the lowest energy structures of the ethanol-water and methanol-water dimers were correctly predicted [98].

In this chapter, we use the Caltech CP-FTMW spectrometer [9, 38] to identify the two lowest energy isomers of the ethanol-methanol dimer. The broad bandwidth and high-resolution of CP-FTMW spectroscopy allows for the identification and differentiation of many species in a complex mixture, while the efficient cooling in the molecular beam promotes the formation of molecular clusters. The efficiency of vibrational state cooling in the beam can also be controlled by the choice of backing gas, as we showed in Chapter 3 [105]. This has been used in larger hydrogen bonded clusters as well, such as the water hexamer, to determine the ground state structure when several isomers are close in energy [18]. We first outline the experimental and theoretical methods employed here, before turning to a discussion of the results.

4.2 Methods

The data in this chapter were taken with the Caltech CP-FTMW spectrometer, as described in Chapter 2, with several small modifications [38]. Initially, spectra were assigned in the original coaxial arrangement. The final data, however, were taken with the pulsed valve oriented perpendicular to two microwave horns. We also upgraded to a larger vacuum chamber, with the hope of increasing the repetition rate and signal-to-noise of the experiment. Unfortunately, we did not see any significant increase in the signal-to-noise ratio of the experiment with the upgraded chamber.

The carrier gas (Ar or He) was pressurized to 50 psi, sent through a bubbler containing a 1:1 mixture of ethanol and methanol, and pulsed into the vacuum chamber ($\sim 10^{-6}$ Torr) with a Parker Series 9 pulsed valve at 2-5 Hz. Ethan(ol-d) (99%) and

methan(ol-d) (99%) were purchased from Sigma-Aldrich and used without further purification. Spectra of the deuterated isotopologues were collected with 1:1 mixtures of ethan(ol-d)/methanol, ethanol/methan(ol-d), and ethan(ol-d)/methan(ol-d) in the bubbler and 50 psi of Ar as the backing gas.

Ab initio calculations were performed using Gaussian 09 [85]. Initially, the potential energy surface was explored using second-order Møller-Plesset (MP2) perturbation theory [86] and the augmented-correlation consistent polarized Valence-only Double-Zeta (aug-cc-pVDZ) basis set [106]. Structure optimizations were started from all possible donor/acceptor sites and for both trans- and gauche-ethanol. For several donor/acceptor combinations secondary minima were identified by scanning the hydrogen bond dihedral angle between the hydroxyl groups. Overall, this analysis identified 7 possible isomers, as shown in Fig. 4.1.

Next, the 7 minima were further optimized with MP2 and the augmented-correlation consistent polarized Valence-only Triple-Zeta (aug-cc-pVTZ) basis set [87] using tight convergence criteria, followed by harmonic frequency calculations at the same level of theory. The relative energies of the isomers were calculated using single-point Coupled Cluster energy calculations with singles, doubles, and perturbative triples (CCSD(T)) [88] and the aug-cc-pVTZ basis set on the MP2/aug-cc-pVTZ optimized structures. The zero point vibrational energy (ZPVE) correction was added from the MP2/aug-cc-pVTZ frequency calculation. Second-order perturbative anharmonic vibrational calculations were performed using MP2/aug-cc-pVDZ on the initially optimized (MP2/aug-cc-pVDZ) structures to determine the ground state rotational constants (B_0). Then MP2/aug-cc-pVTZ perturbative anharmonic calculations were performed on the three lowest energy MP2/aug-cc-pVTZ optimized structures [89]. We were unable to run the anharmonic calculations on all isomers using MP2/aug-cc-pVTZ with the computational resources available.

Spectral analysis of the CP-FTMW data was performed with SPFIT/SPCAT and the Watson-S Hamiltonian [83], XIAM [107], a graphical Python assignment program, and the AUTOFIT package discussed in Chapter 3 [68]. The standard errors of the SPFIT rotational constants were calculated with PIFORM, the coordinate transformation to the Principal inertia Axis System (PAS) with PMIFST, and the Kraitchman substitution coordinates with KRA [84].

Table 4.1: The *ab initio* rotational constants, dipole moments and relative energies of the seven isomers of the ethanol-methanol dimer. Columns labeled as DZ corresponds to MP2/aug-cc-pVDZ, and TZ to MP2/aug-cc-pVTZ. The relative energy (E) was determined from a CCSD(T)/aug-cc-pVTZ single point calculation on the MP2/aug-cc-pVTZ optimized structure, with a ZPVE correction from a MP2/aug-cc-pVTZ frequency calculation.

	B_e /TZ (MHz)	B_0 /DZ (MHz)	B_0 /TZ (MHz)	μ /TZ (D)	E/TZ (cm ⁻¹)
<u>ME-t-1</u>					
A	7158	7028	7195	$ \mu_a $ 2.7	0
B	2031	1964	1959	$ \mu_b $ 0.3	
C	1772	1719	1713	$ \mu_c $ 0.8	
<u>ME-g-1</u>					
A	8148	8051	8230	$ \mu_a $ 1.9	21
B	1855	1797	1799	$ \mu_b $ 0.9	
C	1633	1584	1588	$ \mu_c $ 0.3	
<u>ME-t-2</u>					
A	6634	6530	6719	$ \mu_a $ 2.5	106
B	2166	2070	2057	$ \mu_b $ 0.6	
C	1961	1884	1871	$ \mu_c $ 2.9	
<u>EM-g-1</u>					
A	7101	7005		$ \mu_a $ 2.6	148
B	2015	1939		$ \mu_b $ 1.1	
C	1787	1731		$ \mu_c $ 0.8	
<u>ME-g-2</u>					
A	12871	11030		$ \mu_a $ 3.0	175
B	1383	1478		$ \mu_b $ 0.9	
C	1381	1430		$ \mu_c $ 0.3	
<u>EM-t</u>					
A	14084	11378		$ \mu_a $ 2.7	192
B	1371	1498		$ \mu_b $ 0.7	
C	1335	1434		$ \mu_c $ 0.4	
<u>EM-g-2</u>					
A	6776	6780		$ \mu_a $ 2.7	237
B	2056	1943		$ \mu_b $ 1.2	
C	1897	1811		$ \mu_c $ 0.9	

4.3 Results and Discussion

Ab initio Results

The *ab initio* relative energies of the dimer isomers are shown in Fig. 4.1, along with their associated rotational constants and dipole moments in Table 4.1. The predicted equilibrium structures in the PAS are given in Appendix C. Each species is labeled as either ME for methanol-donor, ethanol-acceptor or EM for ethanol-donor, methanol-acceptor. The gauche and trans conformations of the ethanol subunit are labeled as g and t, respectively. Distinct isomers with the same label have been further distinguished with a -1 or -2.

Overall, the energy calculations show a clear preference for ME rather than EM structures. The three lowest energy structures have methanol as the donor, and the lowest energy ethanol-donor structure is $\sim 50 \text{ cm}^{-1}$ higher in energy than the ground state. The more elongated structures EM-t and ME-g-2, however, have a much smaller energy difference of 17 cm^{-1} . Both of these isomers have a strong hydrogen bond, but lack the weak C-H...O interactions seen in more compact structures. This may indicate that the strong hydrogen bond competition in the ethanol/methanol dimer is delicately balanced, consistent with previous theoretical work on this dimer [98].

The remaining five structures, ME-t-1, ME-g-1, ME-t-2, EM-g-1, and EM-g-2, all exhibit weak C-H...O hydrogen bonds, in addition to the strong OH...O hydrogen bond. In these species it is important to consider the non-additive properties of hydrogen bonds. Specifically, cooperative donor-acceptor or acceptor-donor interactions are generally favored over anti-cooperative donor-donor or acceptor-acceptor interactions [69]. For the three lowest energy ME structures the weak hydrogen bond is cooperative with the strong hydrogen bond, as the hydroxyl group of methanol is acting as a donor for the OH...O interaction and an acceptor for the C-H...O interaction. In the two higher energy EM structures the hydrogen bonds are anti-cooperative, with the methanol oxygen atom acting as an acceptor for both the OH...O and C-H...O interactions. Thus, the methanol-donor, ethanol-acceptor structures may be relatively stabilized by their cooperative interactions in addition to the O-H...O hydrogen bond.

Experimental Results

To isolate the ethanol-methanol dimer signal, we collected the spectrum of pure ethanol and pure methanol in an argon-backed expansion, and subtracted them from

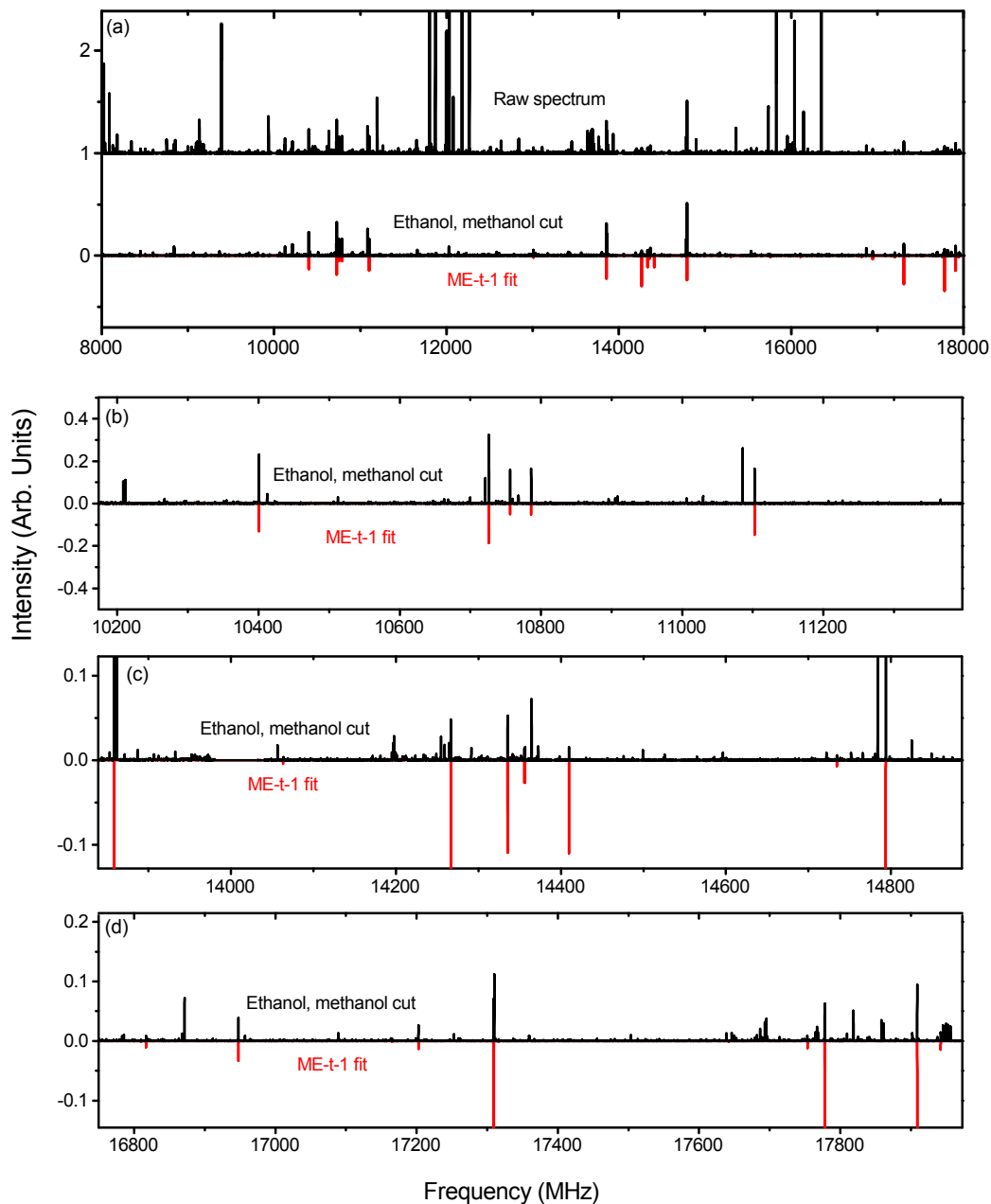


Figure 4.2: The experimental spectrum of an ethanol/methanol mixture expanded in Ar. (a) The experimental spectrum after cutting out the ethanol- and methanol-only spectra from the raw data. The ME-t-1 prediction at 2 K is shown with negative intensity in red. (b-d) Insets of portions of the experimental and predicted spectra for the ME-t-1 isomer.

the mixed ethanol-methanol spectrum (Fig. 4.2a). The strongest peaks in this subtracted spectrum (labeled ‘ethanol, methanol cut’ in Fig. 4.2a) were assigned to a series of a-type transitions. Weaker c-type and b-type transitions were also observed, yielding a total of 50 assigned transitions that were fit to an RMS of 18 kHz (Table 4.2). Several microwave-microwave double resonance measurements (Fig. 4.3(a-c)) confirmed the assignment.

The fit rotational constants (Table 4.2) are close to those calculated for several of the ethanol-methanol dimer isomers (Table 4.1). The closest match is with the ME-t-1 isomer, although they are also somewhat close to EM-g-1. However, using the relative intensity information of the experimental spectrum, we estimate the ratio between the three dipole components in the PAS to be roughly $\mu_a \approx 6\mu_b \approx 2\mu_c$. The observed μ_b/μ_c ratio is inconsistent with EM-g-1 but consistent with ME-t-1, so we assign the observed spectrum to the ME-t-1 isomer.

The spectra of two singly and one doubly deuterated species of the ME-t-1 isomer, as observed in argon expansions, were also fit (Table 4.2). The standard error on the A constant in these fits is larger than those of B and C, as only the strongest a-type transitions had sufficient signal-to-noise to be fit. For the singly substituted species, we calculated the positions of the hydrogens in the PAS using the Kraitchman single substitution equations (Table 4.3) [108]. However, caution is needed in interpreting the position of the methanol hydrogen, as the Kraitchman analysis assumes that the structure is nearly unchanged by the isotopic substitution. This is not the case for a H to D substitution in a hydrogen bond, because the vibrationally averaged deuterium bond can be shorter or longer than the hydrogen bond [109, 110]. A lengthening upon D substitution is typically seen in double minima potentials, where a proton can transfer between two equivalent positions, while shortening is observed in single well potentials, such as alcohol dimers [110, 111]. Such a change in hydrogen bond length, often called the Ubbelohde effect, has been shown to cause large errors in the substitution coordinates of hydrogen bonded clusters, e.g. $\sim 0.9 \text{ \AA}$ in the t-butylalcohol dimer [111]. Thus, the $\sim 0.6 \text{ \AA}$ difference between the *ab initio* and experimental Kraitchman $|a|$ coordinates that we observe on the methanol hydrogen, is likely due to this effect. Besides the Ubbelohde effect, the errors on the coordinates of this hydrogen are high, due to its vicinity to the center of mass [112]. The substitution coordinates of the ethanol hydrogen, however, show much better agreement with the *ab initio* results, as this hydrogen is not part of the hydrogen bond (Table 4.3). Indeed, the coordinates confirm that ethanol is the trans

Table 4.2: The experimentally fit rotational constants and centrifugal distortion constants of four isotopologues of the ME-t-1 isomer and the ME-g-1 isomer using SPFIT. Standard errors of the last digit are given in parentheses. Constants marked with an asterisk (*) were held fixed at the corresponding normal species value. The peak lists of all fits are given in the Supplementary Information.

	ME-t-1			ME-g-1	
	EtOH/MeOH	EtOD/MeOH	EtOH/MeOD	EtOD/MeOD	EtOH/MeOH
A/MHz	7278.993(8)	6911.(1)	7235.6(5)	6873.4(9)	8230.(1)
B/MHz	1909.880(1)	1900.206(5)	1908.497(2)	1898.770(4)	1770.832(3)
C/MHz	1675.696(1)	1649.315(5)	1673.907(2)	1647.678(4)	1577.648(3)
DJ/kHz	4.70(1)	*	*	*	4.43(6)
DJK/kHz	-1.18(7)	*	*	*	-22.5(6)
DK/kHz	39.(1)	*	*	*	-
d1/kHz	-0.809(6)	*	*	*	-
d2/kHz	-0.010(4)	*	*	*	-
N	50	17	17	17	13
rms/kHz	18	49	33	42	26

conformation, the lowest energy state of the isolated monomer. This is distinct from the ethanol dimer and the ethanol/water dimer, in which a gauche conformation is preferred (Fig. 4.4) [67, 102].

Next, we switched the backing gas for the expansion to helium and collected the mixed ethanol-methanol spectrum. In the helium expansion the overall signal-to-noise ratio of all the peaks is decreased, but the cooling conditions allow the population of excited conformations. We measured 13 new a-type transitions that were fit to an RMS of 26 kHz (Table 4.2), and confirmed the assignments with double resonance measurements (Fig. 4.3(d)). We assigned the new spectrum to the ME-g-1 isomer based on the values of the measured constants. The new peaks are not seen in the argon-backed expansion (Fig. 4.5), verifying that the ME-t-1 isomer is lower in energy than the ME-g-1 isomer.

Many of the peaks in the experimental spectra of ME-g-1 and ME-t-1 are split by several MHz in a doublet pattern. In our analysis, only one peak of every doublet was fit to the effective rigid-rotor Hamiltonian, while the companion peaks could not be fit to this model. As isolated monomers, both ethanol and methanol exhibit a spectral splitting due to hindered internal rotation of their methyl rotors that leads to a doublet A-E splitting pattern, where A and E are methyl torsional state symmetry labels. The three-fold barrier to internal rotation of the methyl group, V_3 , is smaller in methanol (373 cm^{-1}) than ethanol (1166 cm^{-1} for trans, 1331 cm^{-1} for gauche),

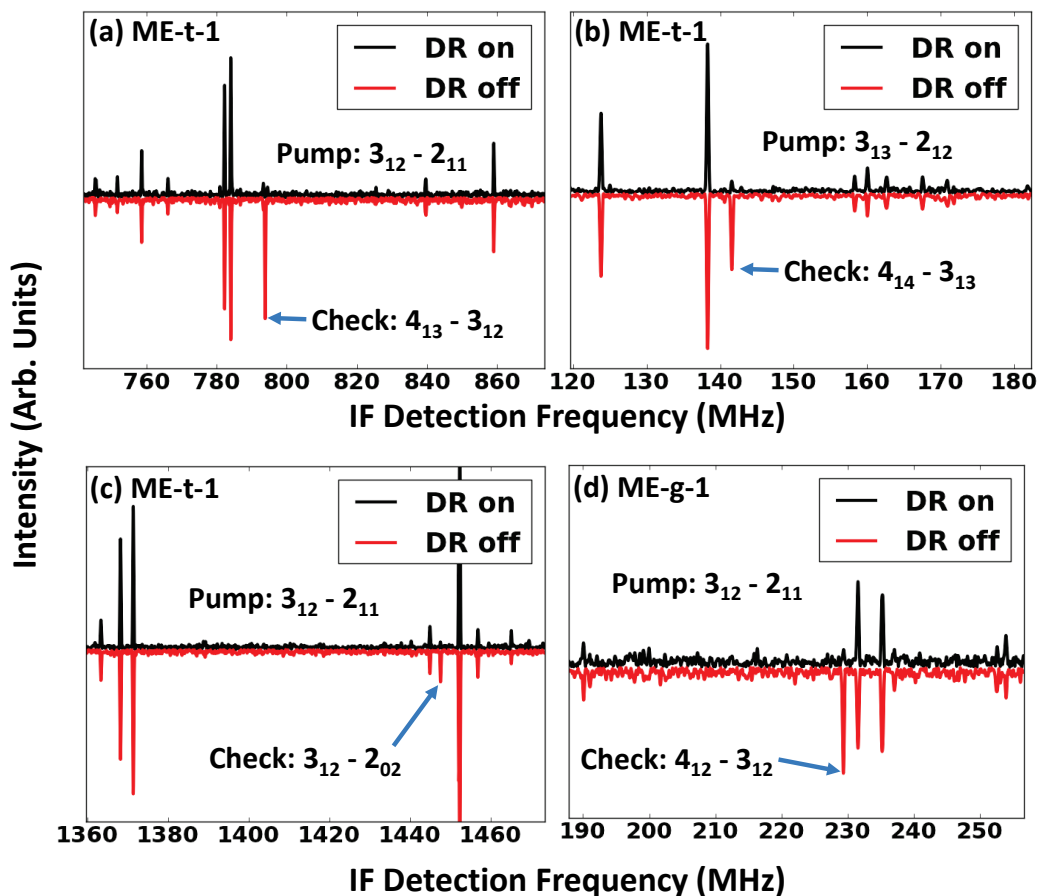


Figure 4.3: Double resonance (DR) measurements of the ME-t-1 isomer (a-c), and the ME-g-1 isomer (d). For each spectrum, a narrowband pulse was applied to the ‘pump’ transition after the standard broadband chirped pulse. Modulation was measured on the connected ‘check’ transition. Neighboring peaks to the check transition were used as a control, to make certain that there is not broad, non-resonant modulation in the spectrum.

leading to a much larger A-E splitting [92, 95, 113]. The spectrum of gauche-ethanol is further split by the tunneling of the hydroxyl hydrogen between equivalent positions, although this motion should be quenched in the ethanol-methanol dimer by the position of the methanol. Thus, we hypothesize that the splitting in the ethanol-methanol spectrum is due to internal rotation of the methyl group of methanol.

In other methanol clusters, methyl rotor tunneling splittings have also been reported, including the methanol homodimer [114], methanol-water [102], methanol-formamide [115], methanol-argon [116], methanol-CO [117], methanol-phenol [118], and methanol-sulfur dioxide [119]. Compared to the isolated monomer,

(a) ethanol:methanol

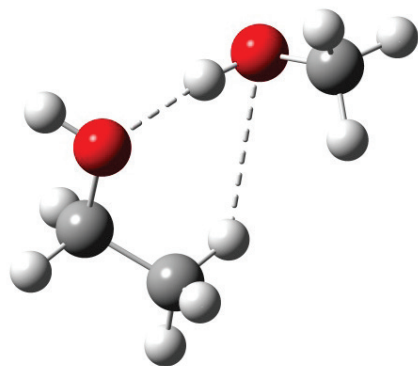
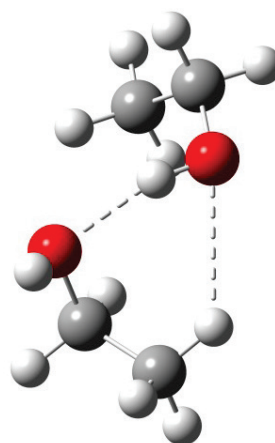
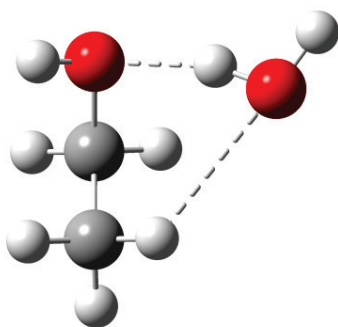
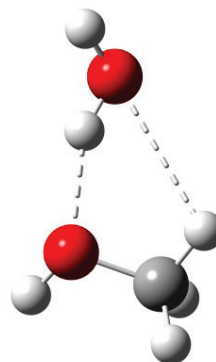
(b) ethanol:ethanol
Hearn et al. 2005(c) ethanol:water
Chapter 3(d) methanol:water
Stockman et al. 1997

Figure 4.4: The lowest energy structures of several dimers containing ethanol or methanol. The alcohols act as acceptors in the methanol-water and ethanol-water dimers, while in ethanol-methanol the ethanol is an acceptor. Interestingly, ethanol is in the trans configuration for ethanol-methanol but in the gauche configuration for ethanol-ethanol and ethanol-water.

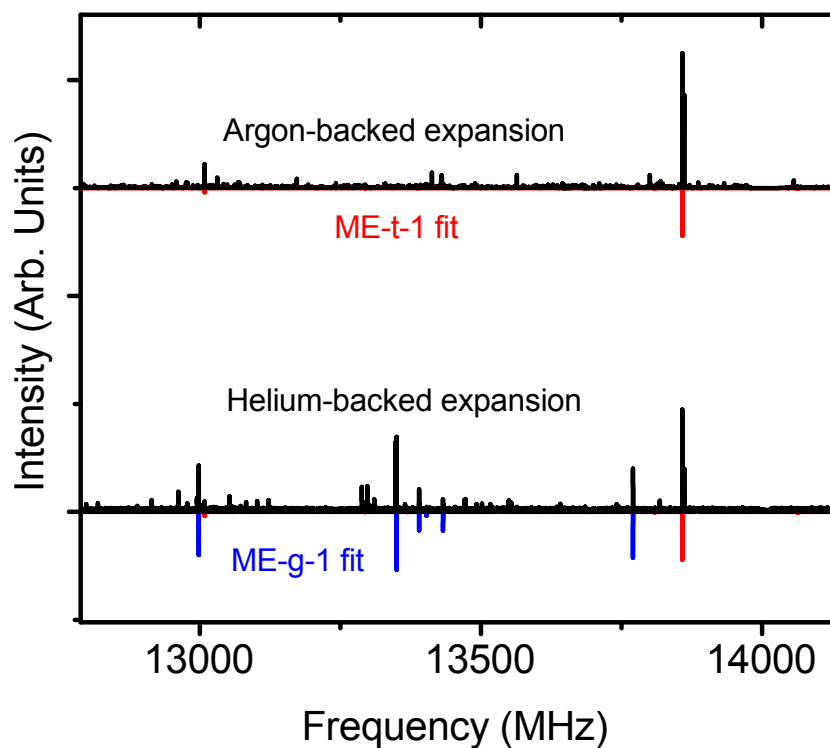


Figure 4.5: The experimental helium- and argon-backed spectra of the ethanol-methanol dimer. The ME-t-1 isomer is seen in both expansion conditions while the higher energy ME-g-1 isomer is only seen in the helium expansion. Predicted spectra are rendered at 2 K.

Table 4.3: The single-substitution Kraitchman positions of the two hydroxyl hydrogens of the ME-t-1 isomer of the ethanol-methanol dimer as compared to the vibrationally averaged *ab initio* coordinates. The propagated standard error of the experimental coordinates is on the order of 0.01 Å, although it is likely higher due to changes in the vibrationally averaged bond lengths on deuterium substitution. The detailed output of the Kraitchman calculations are given in Appendix C.

		<i>Ab initio</i>	Experiment
CH ₃ CH ₂ OH	a /Å	1.16	1.11
	b /Å	1.93	1.90
	c /Å	0.27	0.35
CH ₃ OH	a /Å	0.88	0.22
	b /Å	0.60	0.52
	c /Å	0.30	0.38

Table 4.4: A preliminary internal rotation fit of the four measured isotopologues of the ME-t-1 isomer using XIAM. Standard errors are given in parentheses, and constants marked with an asterisk(*) were fixed at the normal species value for the fit. *Ab initio* values are from the MP2/aug-cc-pVTZ level of theory for the normal species. A full list of assigned transitions and raw XIAM output is given in Appendix C.

	EtOH/MeOH	EtOD/MeOH	EtOH/MeOD	EtOD/MeOD	<i>Ab initio</i>
A/MHz	7274.75(4)	6907.(1)	7231.6(9)	6870.4(8)	7195
B/MHz	1909.610(5)	1899.947(9)	1908.279(5)	1898.559(5)	1959
C/MHz	1675.236(5)	1648.870(8)	1673.510(5)	1647.290(5)	1713
DJ/kHz	4.71(3)	*	*	*	3.7
DJK/kHz	-1.6(1)	*	*	*	1.7
DK/kHz	38.(3)	*	*	*	14.3
d1/kHz	0.81(1)	*	*	*	-0.6
d2/kHz	-0.014(6)	*	*	*	-0.04
V_3/cm^{-1}	190(1)	190.0(1)	200.0(1)	199.6(1)	257
$\epsilon/^\circ$	34.6(4)	33.8(5)	33.9(4)	33.4(4)	30.2
$\delta/^\circ$	59.9(1)	59.5(1)	59.7(1)	59.4(1)	60.3
$I_\alpha/\text{u}\text{\AA}^2$	3.38(2)	*	*	*	
N	67	32	31	31	
rms/kHz	32	58	40	44	

all of these methanol clusters have shown decreases in the fit barrier to internal rotation of $\sim 20\text{-}80\%$. In 1994, Fraser et al. noted that this drop in the fit barrier is likely unphysical, and instead due to coupling between the methyl internal rotation and large amplitude motion of the entire methanol subunit [120]. To model rotational spectra, the angle of the methyl rotor in the PAS can be fit along with the barrier to internal rotation and the moment of inertia of the methyl group, I_α . For typical organic molecules, I_α is near $3.1\text{-}3.2 \text{ u}\text{\AA}^2$. Fraser et al. note that in a dimer with methanol rigidly bound to its partner, or the strong interacting limit, the fit I_α should be close to that of a methyl group and the fit V_3 value will be physical. However, as the cluster becomes more ‘floppy’, the methanol large amplitude motion will couple to the methyl rotation, increasing the effective I_α and decreasing the fit V_3 in relation to its actual value. This is maximized in the weakly interacting limit, with free rotation of the methanol subunit in relation to its dimer partner. For a rigorous treatment of a ‘floppy’ methanol dimer, a more complex Hamiltonian with Coriolis terms must be used [120], which is beyond the scope of this work. Therefore, we will only consider a standard internal rotor model of the splitting, with an explicit awareness of its shortcomings.

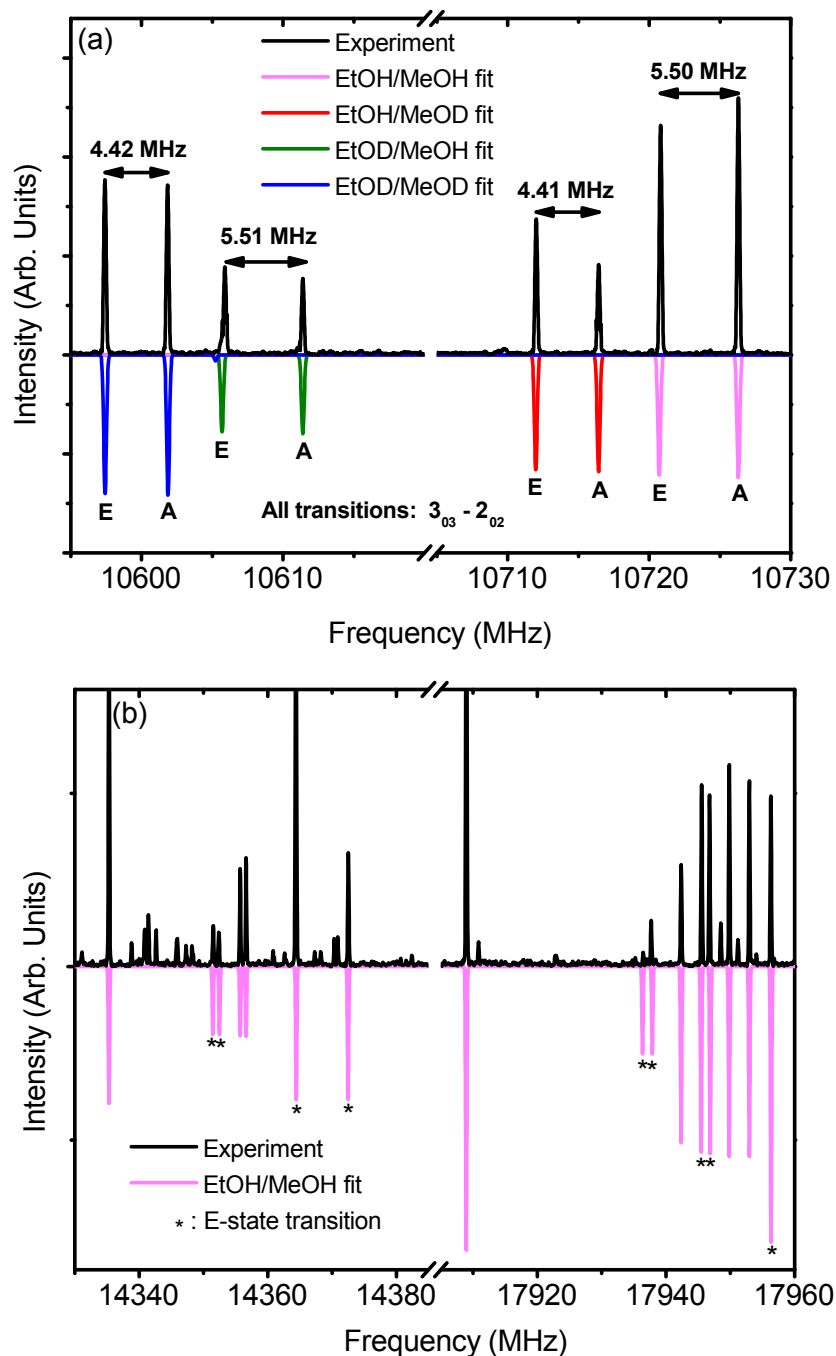


Figure 4.6: A preliminary fit of the tunneling splitting in ME-t-1. (a) A comparison of the peak splittings of the $3_{03} - 2_{02}$ transition of four isotopologues of the dimer. The experimental spectrum was measured in a deuterium enriched sample in Ar. The predicted spectra are from XIAM at 10 K, the lowest prediction temperature available in the program. (b) Other portions of the normal species fit of ME-t-1, with E-state transitions labeled with an asterisk (*). Experimental data is from a non-deuterated sample in Ar. Again, predictions are rendered at 10 K.

To model the internal rotor splitting in the ethanol-methanol dimer, we used the internal axis method Hamiltonian with the XIAM program. [107] Fits of the four isotopologues of the ME-t-1 isomer are shown in Fig. 4.6 and Table 4.4; the signal-to-noise in the helium expansion was insufficient to fit the splitting of the ME-g-1 isomer. In these fits, ϵ corresponds to the angle between the methyl group, or O-C bond of methanol, and the a-inertial axis, and δ to the angle between the c-axis and the methyl projection onto the bc-plane. The normal species fit values of $\delta=59.9^\circ$, $\epsilon=34.6^\circ$ are quite close to the *ab initio* predictions of $\delta=60.3^\circ$, $\epsilon=30.2^\circ$, confirming the orientation of methanol in the ME-t-1 isomer. We also note evidence of large amplitude motions of methanol, with the high value of $I_\alpha=3.38 \text{ u}\text{\AA}^2$, as compared to the $3.2 \text{ u}\text{\AA}^2$ expected of a methyl group. Further evidence of this motion is seen in the greatly reduced $V_3=190 \text{ cm}^{-1}$, as compared to the experimental monomer value of 373 cm^{-1} . The *ab initio* barrier, $V_3=257 \text{ cm}^{-1}$, is also much higher than the fit barrier. Thus, the fit V_3 is likely not physical, but an indicator of the flexibility of the hydrogen bond between methanol and ethanol.

In the fit parameters of the deuterated species of ME-t-1 we see further complexity arising from the donor/acceptor large amplitude motion. The species with a deuterated methanol and hence a deuterium bond, EtOH/MeOD and EtOD/MeOD, have a fit barrier of $V_3\sim 200 \text{ cm}^{-1}$, while the fit barrier of the hydrogen-bonded species EtOD/MeOH and EtOH/MeOH is $V_3\sim 190 \text{ cm}^{-1}$. Equivalently, this difference can be seen in the A-E splitting of the spectrum. In the $3_{03}\text{-}2_{02}$ transition, for example, (Fig 4.6a) the deuterium bonded dimers have a splitting of $\sim 4.4 \text{ MHz}$, while the hydrogen-bonded dimers are split by $\sim 5.5 \text{ MHz}$. Possible causes for this splitting difference could be an increase in the V_3 barrier of the methanol subunit when it is deuterated, or the Ubbelohde effect – a shortening of the hydrogen bond upon deuterium substitution. For the Ubbelohde effect, the increased rigidity of the deuterium-bonded dimer would reduce the A-E splitting. In contrast, if this change was caused by the methanol alone, we would expect to see an increase in splitting for the deuterium bonded species, as the barrier for the MeOD monomer (366 cm^{-1}) [121], is lower than the MeOH barrier (373 cm^{-1}). [113] Thus, we posit that the measured trend is due to the Ubbelohde effect, as it is inconsistent with a change in the methanol monomer barrier.

In the raw mixed ethanol-methanol spectrum (Fig. 4.2a), strong transitions from the ethanol and methanol monomers [95, 113] and homodimers [94, 114] are present as well as the methanol-argon dimer [122]. For the ethanol dimer, we have confirmed

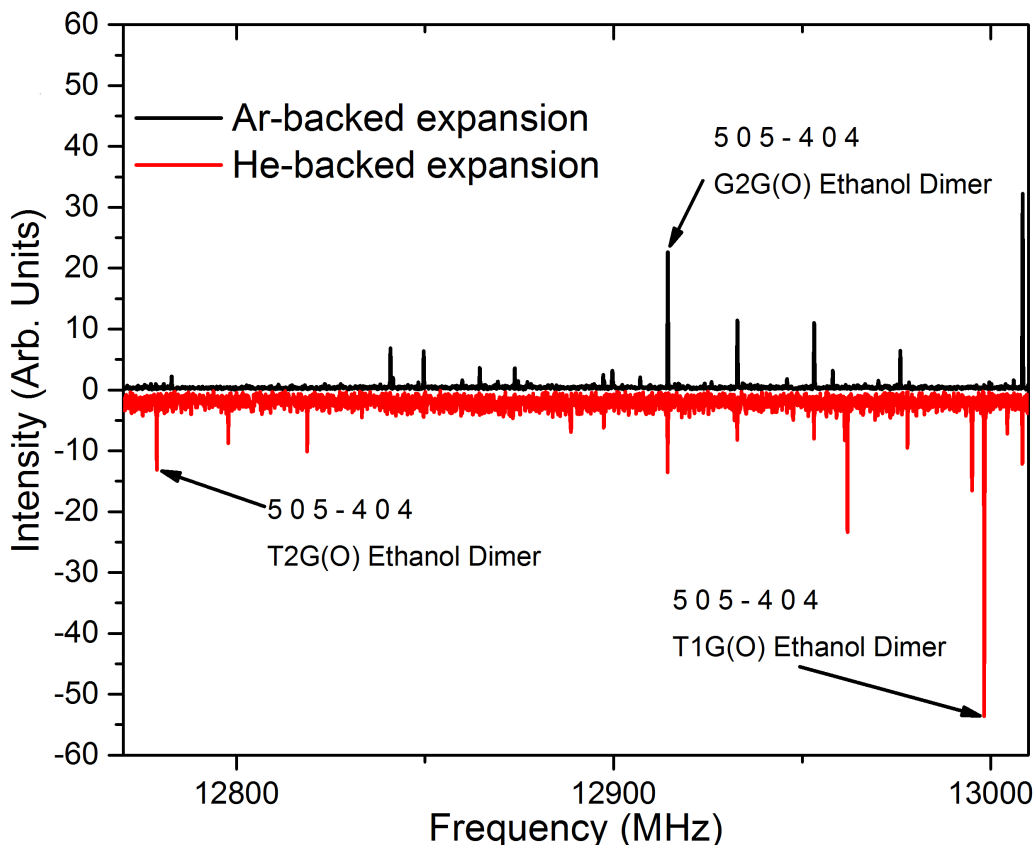


Figure 4.7: The experimental spectrum of the ethanol dimer. In the He-backed expansion all three previously measured isomers are visible, while in the Ar-backed expansion only G2G(O) is present. This indicates that G2G(O) is the ground state structure. Peak assignments are from [94].

that the G2G(O) isomer is the ground state, using transition frequencies from Hearn et al., 2005 [94]. In the helium-backed expansion all previously measured isomers are present, while cooling to the G2G(O) isomer is observed in an argon-backed expansion (Fig. 4.7).

4.4 Conclusion

Two isomers of the ethanol/methanol heterodimer have been measured and assigned to methanol-donor ethanol-acceptor configurations. In the lower energy structure ethanol is in the trans conformation, while it resides in the gauche conformation for the higher energy species. This is different than the ethanol dimer and ethanol/water dimer, both of which show an energetic preference for the gauche conformation (Fig. 4.4) [67, 102].

No ethanol-donor/methanol-acceptor isomers have been identified in the experimental data. In particular, all seven calculated isomers of the dimer have strong predicted a-type transitions in the 8-18 GHz region measured in this work, yet we could not find any EM structures with an exhaustive automated search. This strongly indicates that the measured ME-t-1 isomer is the ground state.

The A-E splitting arising from the hindered internal rotation of the methyl group of methanol was fit for the four isotopologues of the ME-t-1 isomer. The fit constants indicate that there is a significant coupling between the methyl internal rotation and a donor/acceptor large amplitude motion. This motion is more pronounced in the hydrogen-bonded species than the deuterium-bonded species, which likely arises from the Ubbelohde effect.

*Chapter 5***A DECADE-SPANNING, HIGH-PRECISION TERAHERTZ
FREQUENCY COMB**

So far, we have considered the pure rotational spectra of molecular clusters in the microwave portion of the electromagnetic spectrum. To fully determine the intermolecular potential energy surfaces of clusters, however, broadband high-resolution THz measurements are needed. Accordingly, we move to the THz region in this chapter and describe the generation and detection of a decade-spanning THz frequency comb using two Ti:Sapphire femtosecond laser oscillators and ASynchronous Optical Sampling THz Time-Domain Spectroscopy (ASOPS-THz-TDS). The comb extends from 0.15-2.4 THz, with a tooth spacing of 80 MHz, a linewidth of 3.7 kHz, and a fractional precision of 1.8×10^{-9} . With time-domain detection of the comb, we measure three transitions of water vapor at 10 mTorr between 1-2 THz with an average Doppler-limited fractional accuracy of 6.1×10^{-8} . Although the bandwidth and precision of the comb are well-suited for THz studies of clusters, the sensitivity is limited. Fortunately, there are significant improvements in sensitivity, bandwidth, and resolution that are possible with existing technologies, and that will place THz frequency combs on an equal footing with their infrared counterparts.

This chapter has been reproduced with permission from:

Finneran, I. A., Good, J. T., Holland, D. B., Carroll, P. B., Allodi, M. A. & Blake, G. A. Decade-spanning high-precision terahertz frequency comb. *Physical Review Letters* **114**, 163902 (2015).

Details of the offset lock circuit and optics used in this chapter are reported in:

Good, J. T., Holland, D. B., Finneran, I. A., Carroll, P. B., Kelley, M. J. & Blake, G. A. A decade-spanning high-resolution asynchronous optical sampling terahertz time-domain and frequency comb spectrometer. *Review of Scientific Instruments* **86**, 103107 (2015).

5.1 Introduction

The large bandwidth and high-resolution of optical frequency combs have made them an essential part of contemporary physics [125]. In metrology, visible/near-IR frequency combs have played an integral role in optical clocks and the most accurate measurements of fundamental constants [126], while in chemical physics they have been used for high-resolution molecular spectroscopy [127]. In addition, frequency combs have provided astrophysicists with a precise calibration source for radial velocity searches for Earth-sized exoplanets [128] and in measurements of the universe's expansion history [129].

Uniquely informative transitions are present in the TeraHertz (0.1-10 THz), or far-infrared, region of the electromagnetic spectrum, including molecular rotations and low-energy, large-amplitude vibrations. Various continuous wave technologies have been developed at THz frequencies, including those that potentially can be tuned over a decade of bandwidth rapidly [130], but for poorly characterized systems the search space is exceedingly large. Broadband, high-precision measurements of complex molecular spectra with THz combs will benefit fields such as molecular astrophysics [131] and atmospheric chemistry and physics [132], as precise line-centers and intensity measurements over wide spectral regions are critical for interpreting observational data. Further, THz studies of hydrogen-bonded clusters provide exacting tests of intermolecular forces [133], but particularly suffer from the need to detect narrow transitions over wide spectral windows.

Thus, extending the precision and bandwidth achievable with frequency combs into the THz region is an active area of research. The two main approaches used to date involve direct synthesis via quantum cascade lasers (QCLs) [134, 135] and down-conversion of femtosecond pulse trains from optical oscillators [136]. QCLs generally yield higher-precision, lower-bandwidth measurements, while downconversion techniques generally yield lower-precision, higher-bandwidth spectra. Alternatively, hybrid approaches with a narrowband QCL coupled with a downconverted optical oscillator [137], or electronic heterodyne detection coupled with a downconverted optical oscillator [138], have also enabled high-precision, low-bandwidth measurements. It should be emphasized that in all of these techniques there is a trade-off between the detected bandwidth and precision.

We demonstrate here the generation and coherent detection of a THz comb with both a decade-spanning bandwidth and high precision using ASynchronous Optical Sampling THz Time-Domain Spectroscopy (ASOPS-THz-TDS) [139]. The first

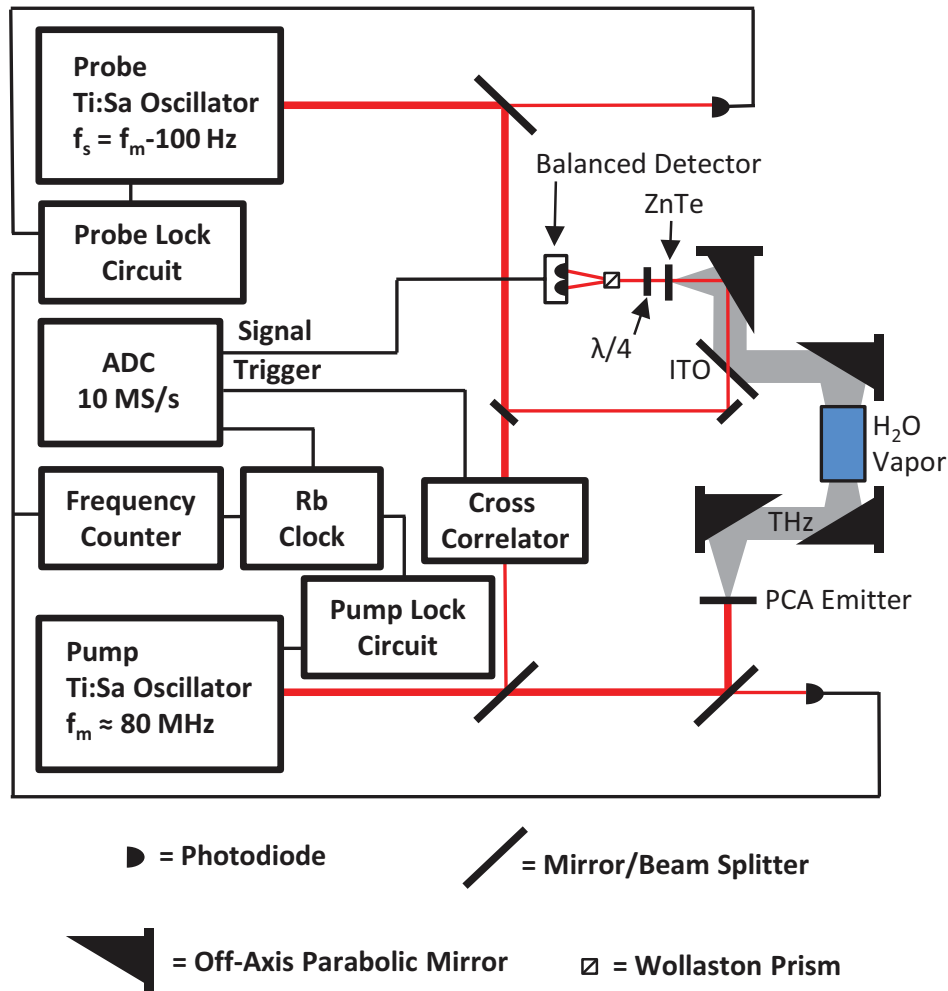


Figure 5.1: The experimental layout for the generation and detection of the THz frequency comb. See text for details.

application of this technique to THz frequency combs was demonstrated in 2014 by Hsieh et al. using two 250 MHz Er-doped fiber lasers [136], who report a fractional accuracy of 8.4×10^{-7} for two transitions of acetonitrile at 0.64 THz with a tooth width of 2.5 MHz. We have measured a 14-fold improvement in fractional accuracy and a 675-fold reduction in tooth width using a newly constructed ASOPS-THz spectrometer with two 80 MHz Ti:Sapphire femtosecond laser oscillators (Coherent Micra 5). Reaching this level of precision and accuracy is significant for THz metrology, as it is the first demonstration of broadband, Doppler-limited spectroscopy in the THz region. The Ti:Sapphire oscillators extend the bandwidth of the instrument to measure transitions between 1-2 THz, and can be further extended to 20 THz with proper optical pulse compression and THz emitter optimization, with no loss

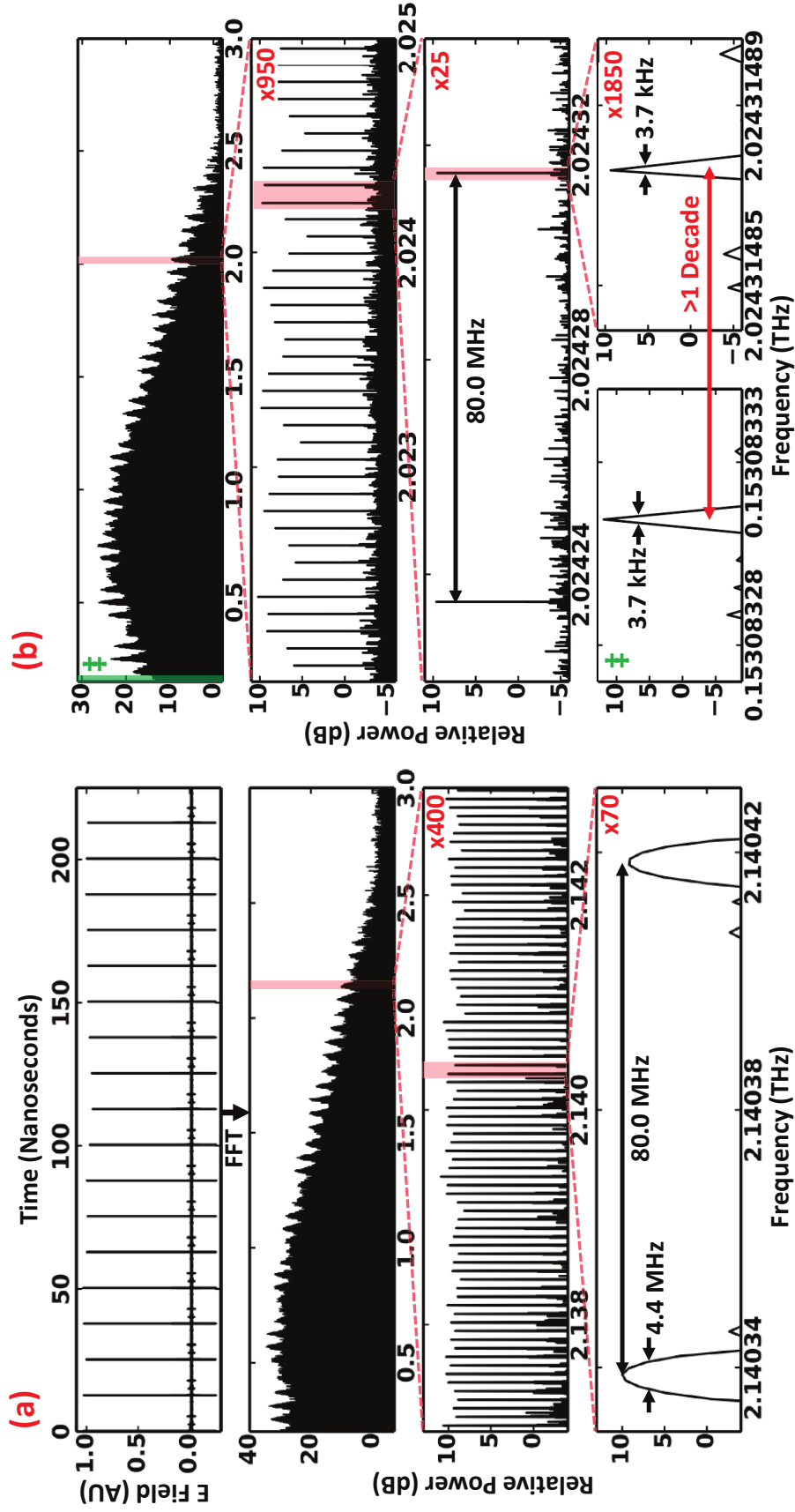


Figure 5.2: (a) The Fourier transform of a 225 ns THz pulse train in delay time yields a decade-spanning frequency comb that extends up to 2.4 THz, with a 4.4 MHz tooth width. The peak dynamic range of the comb is 30 dB after 30 minutes of integration. (b) The tooth width of the THz comb can be reduced to 3.7 kHz by extending the time domain measurement to 268 μ sec in delay time. The peak dynamic range is 20 dB after a single 107 s acquisition. Precision is preserved over the entire bandwidth of the comb, as shown in the bottom two panels.

in fractional precision [140].

5.2 Methods

An instrument schematic is shown in Fig. 5.1. A large-area interdigitated photoconductive antenna (PCA) emitter, from GigaOptics (now Laser Quantum), generates the comb. Since the downconversion process is dependent on the envelope of the optical pulse and not the phase, the THz pulses are effectively carrier-envelope-phase (CEP) stabilized, at zero CEP, without needing optical CEP stabilization. The repetition rate of the THz comb can be controlled by changing the repetition rate of the pump laser. Thus, a shift of 1 kHz in the 80 MHz pump laser corresponds to a shift of 12.5 MHz in the comb tooth at 1 THz. Here, the pump laser repetition rate is controlled by a piezo actuator and by changing the set-point temperature of the water chiller, which cools the gain medium and baseplate of the modelocked oscillator.

After generation, the THz comb is detected via electro-optic (E-O) sampling by overlapping the 800 nm pulse train of a second laser, designated the probe in Fig. 5.1, with the THz comb in a ZnTe crystal. The THz electric field, which consists of a pulse train of ~ 1 ps THz pulses, causes a transient birefringence in ZnTe, thus rotating the polarization of the 800 nm probe pulse train [141, 142]. The repetition rate of the probe laser is offset locked by 100 Hz from that of the pump, sweeping the probe pulse train through 12.5 ns of delay time (the round-trip time of the oscillator cavities) over 10 ms in the lab frame. A second lock circuit stabilizes the repetition rate of the pump laser over timescales ≥ 1 s. The full details of the lock circuits and THz optics are reported in theses by Daniel Holland and Jacob Good and in a recent publication [124, 143, 144]. The polarization of the probe light is measured by a balanced detector, and digitized.

5.3 Results and Discussion

Since the ASOPS technique ensures a repetitive phase walkout in delay time, the THz comb can be recorded in the time domain by extending the sampling window beyond the 12.5 ns interval between individual pulses. For example, the Fourier transform of a set of 18 THz pulses (covering 225 ns of delay time) yields a comb from 0.15-2.5 THz with a 4.4 MHz tooth width [30 minutes of data, Fig. 5.2(a)]. The averaging rate of the experiment is inversely proportional to the measurement window, so fewer averages are collected for longer pulse trains. However, an equivalent dynamic range is recovered in the FFT, since the dynamic range increases linearly with the length

of the measured waveform (assuming an adequate effective number of bits in the digitizer). Furthermore, since the frequency bins of the comb are much narrower than those of the isolated pulse experiment, we achieve a greater sensitivity to narrow-linewidth transitions. When measured for the same integration times, water vapor at 10 mTorr shows no clear absorptions in a high dynamic range, 12.5 ns window, while the lines are nearly saturated with a 225 ns-averaged comb, as shown in Fig. 5.3b-d.

In the frequency domain, the experiment is equivalent to heterodyne detection with dual THz combs [136]. From this viewpoint, the THz pulse train is the signal and the probe laser acts as an effective THz local oscillator. Although the probe oscillator is not a true THz comb, it acts as one via E-O sampling, as the process is dependent on the envelope of the optical field. The mixing between the THz comb and the optical pulse train generates an RF comb in the birefringence of the ZnTe with a tooth spacing equal to the offset between the lasers, and with the n th tooth of the RF comb corresponding to the n th tooth of the THz comb. Thus, for an 80 MHz pump laser repetition rate, the 12500th tooth of the signal comb at 1 THz is detected as the 12500th tooth of the RF comb at 1.25 MHz.

To test the precision of the THz comb, we extended the measurement window to 21,470 individual THz pulses, or 268 μ sec, increased the offset between the lasers to 200 Hz, and increased the sample rate of the digitizer to 20 MS/s (Fig. 5.2b). A larger laser offset lowers the ratio of lab time to delay time, such that a higher-resolution comb is acquired in an equivalent measurement time.

For short THz pulse trains, the tooth width is set by the Fourier time-frequency uncertainty relationship. However, longer pulse trains are more sensitive to various sources of jitter and drift in the system. Jitter in the offset between the pump and probe lasers, for example, will change the spacing of pulses in the time domain and thus shift the comb teeth in the frequency domain. Changes in the repetition rate of the pump laser will shift the comb teeth in the frequency domain as well. Either can broaden the teeth beyond the expected Fourier time-frequency product. For a single 107 s acquisition, we observed a transform-limited linewidth of 3.7 kHz over more than a decade of bandwidth, and thus no significant jitter in the instrument over this timescale. The tooth shown at 2.02 THz (Fig. 5.2b) demonstrates a fractional precision of $\Delta\nu/\nu = 1.8 \times 10^{-9}$.

The accuracy of our THz comb is likely limited by the lock circuit and ultimately by the Rubidium frequency reference, with a fractional uncertainty of 10^{-11} . To verify

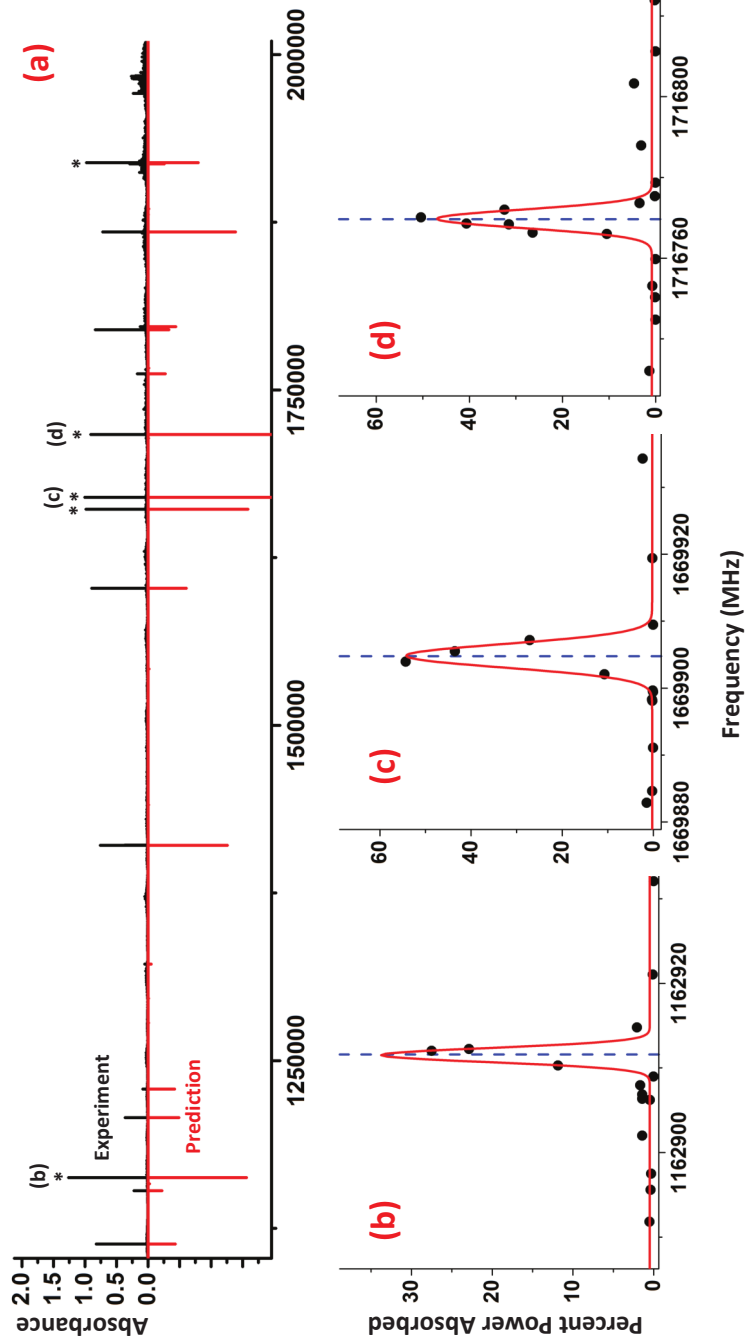


Figure 5.3: (a) The broadband spectrum of water vapor at 100 mTorr with 11 repetition rate steps. The predicted spectrum from the JPL spectral line catalog [145] is shown in red, with negative intensity. The asterisks (*) indicate saturated transitions. (b-d) The Gaussian fit (red line) to three transitions of water vapor at 10 mTorr. Line centers from the JPL catalog are indicated with vertical blue dashed lines.

the accuracy of our instrument, we tested the 225 ns comb on rotational transitions of gas-phase water in a low-pressure cell and compared our values with the JPL spectral line catalog (Fig. 5.3) [145]. Initially, we took a broadband scan of water vapor at 100 mTorr, using 11 coarse steps in repetition rate to cover the spectrum between 1-2 THz, as shown in Fig. 5.3a. The RMS of the 16 transitions analyzed was 2.0 MHz, due to the large step size. We then performed 17 fine steps on three transitions of water vapor at 10 mTorr. Here the lines are primarily Doppler-broadened and accordingly fit to a Gaussian lineshape (Fig. 5.3(b-d)). The measured RMS of the three transitions was 92 kHz, with an average accuracy of $\Delta\nu/\nu = 6.1 \times 10^{-8}$, as shown in Table 5.1. Since the measured accuracy is significantly less than the Doppler linewidth, it should be possible to improve the measured RMS by reducing the linewidths of the transitions with a molecular beam. Indeed, the number density of the cell at 10 mTorr (10^{14} molecules/cm³) and pathlength of the cell (10 cm) are similar to those achievable in molecular beams, suggesting that this comb would have sufficient sensitivity and resolution for such experiments.

Table 5.1: Measured frequencies of three water vapor transitions at 10 mTorr.

$J_{K_a K_c} - J_{K_a K_c}$	This Work (MHz)	JPL[145] (MHz)	Diff. (MHz)
$3_{21} - 3_{12}$	1162911.521	1162911.602	-0.081
$2_{12} - 1_{01}$	1669904.836	1669904.775	0.061
$3_{03} - 2_{12}$	1716769.755	1716769.633	0.122
		RMS (MHz)	0.092

5.4 Conclusion

In summary, we have generated and detected a THz comb that spans over a decade in bandwidth with a transform-limited frequency precision of 1.8×10^{-9} . The average fractional accuracy (6.1×10^{-8}) of the comb was measured on three transitions of water vapor and is Doppler-limited. Although there are several approaches to Doppler-limited, far-infrared spectroscopy, we have achieved a single measurement bandwidth of >2 THz, which is an order-of-magnitude larger than any other technique. Furthermore, we are able to generate and detect the comb with all room temperature components, while many other methods require cryogenic detectors or generators.

The applications of this comb are immense, and could include THz metrology, and measurements in support of the Hershel Space Observatory, and the Atacama Large Millimeter Array, as these observatories have complementary spectral coverage and

resolution to the THz comb. Broadband studies of vibration-rotation tunneling transitions in hydrogen-bonded water clusters are another exciting application; the water trimer and quatramer both have such transitions within the spectral range of this comb [146, 147]. The direct time-domain detection of the comb is also suitable for broad continuum measurements, such as pressure-broadened or condensed-phase samples. By implementing a commercially available pulse compressor on the pump and probe oscillators, and by employing both transmission and reflection geometries for the PCA THz emitter, the comb could also be extended to 20 THz, a century in bandwidth. A comb with these properties could measure all of the intermolecular modes of hydrogen-bonded clusters in a single experiment. Since the stability of the comb is dependent on Ti:Sapphire oscillators, many of the stabilization techniques that have been developed in optical metrology are applicable, and could improve the linewidth of the comb considerably. These improvements could open new fields of precision metrology in the THz region of the electromagnetic spectrum.

Part III

Ultrafast Terahertz Spectroscopy of Liquids

Chapter 6

TERAHERTZ KERR EFFECT MEASUREMENTS OF SIMPLE LIQUIDS

The focus of the previous four chapters has been on the precision measurements of small clusters of molecules. While these experiments reveal many of the complexities of intermolecular interactions in the condensed phase, their applications to liquids are limited by the small size and low temperature of clusters.

In this chapter, we proceed to direct measurements of liquids at room temperature using terahertz Kerr effect (TKE) spectroscopy. This relatively new technique is nonlinear in the THz electric field, which opens the door to information not attainable in a traditional linear spectrum. Here, we measure the TKE response of seven aromatic liquids at room temperature (benzene, benzene-d₆, hexafluorobenzene, bromobenzene, toluene, pyridine, and nitrobenzene) and compare our results with previous optical Kerr effect (OKE) studies. Nitrobenzene is noteworthy, as previous TKE experiments were unable to measure a response from this highly polar liquid, due to its large absorbance in the THz region. All species exhibit similar collective orientation timescales to those found in OKE spectroscopy. We identify a second intermediate exponential component, previously only seen in OKE measurements, that is separate from the electronic response and likely due to intermolecular vibrations. The TKE and OKE experiments yield different amplitudes between the two decays, suggesting distinct mechanisms of molecular excitation. We also observe time domain oscillations from the nonlinear excitation of low energy intramolecular vibrations in CCl₄ and CH₂I₂. Altogether, these measurements set the stage for 2D THz-THz-Raman spectroscopy, discussed in Chapter 7.

Two figures in this chapter were reproduced with permission from:

Allodi, M. A., Finneran, I. A. & Blake, G. A. Nonlinear terahertz coherent excitation of vibrational modes of liquids. *The Journal of Chemical Physics* **143**, 234204 (2015).

6.1 Introduction

The terahertz region of the electromagnetic spectrum (0.1-10 THz) is associated with many important motions in liquids, including inter- and intramolecular vibrations, orientational and librational motions, as well as large-amplitude conformational torsions. Since kT at room temperature corresponds to 6.2 THz (207 cm^{-1}), these motions are not spectators, but active participants in chemistry on Earth. Compared to the mid-infrared, THz motions are often delocalized over many molecules and highly anharmonic, making them difficult to model. Despite years of investigation, many questions remain about the structure and dynamics of THz motions in simple liquids [6, 11].

One experimental approach that may shed light on these motions is nonlinear spectroscopy. Indeed, nonlinear spectroscopy in the infrared and optical has provided a rich set of information on condensed-phase chemical physics, not accessible with linear techniques, including broadening mechanisms and spectral diffusion timescales [31, 149]. Unfortunately, the extension of nonlinear spectroscopy to the THz has been difficult, due to a lack of high power THz sources, and sensitive detectors.

Recently, these difficulties have been overcome with Terahertz Kerr Effect (TKE) spectroscopy, the first approach to measure a nonlinear THz response in a molecular liquid [37]. In this technique, a high-power THz pulse is used to excite a transient birefringence in a sample, that is subsequently read out by a time-delayed optical probe pulse whose polarization is oriented at 45 degrees with respect to the THz pulse. For centrosymmetric media, such as molecular liquids, the lowest-order polarization that is measured by the probe pulse is given by [37]:

$$P^{(3)}(t) = E_j^{Pr}(t - \tau) \int_0^\infty d\tau' R_{ijkl}^{(3)}(\tau') E_k^{Pu*}(t - \tau') E_l^{Pu}(t - \tau'), \quad (6.1)$$

where $P^{(3)}(t)$ is the third order polarization, E^{Pr} is the field of the probe pulse, E^{Pu} is the field of the THz pump pulse, and $R^{(3)}$ is the response function of the liquid. In this implementation, the linear THz signal is forbidden by symmetry, allowing for a background-less detection of a nonlinear THz response. The broad applicability of the technique is yet unknown, as previous work has suggested it is not feasible in polar liquids, due to the strong THz absorptions [37].

To understand the molecular interpretation of TKE spectroscopy it is useful to consider the well-established sister technique Optical Kerr Effect (OKE) spectroscopy. The implementation of OKE spectroscopy is similar to TKE, except an optical pump

pulse, typically at 375 THz (800 nm), is used, rather than a THz pulse. In both techniques the measured signal consists of an instantaneous electronic response to the applied field, followed by a long exponential tail due to the collective orientation decay of the molecules in the sample after alignment/orientation by the pump pulse [27]. A third “intermediate” quasi-exponential response is often seen in OKE signals, although it has not been reported using TKE spectroscopy [27, 37]. The origins of the intermediate response are not fully understood, but have been attributed to the decay of dissipative intermolecular vibrational oscillations. Furthermore, correlations between the intermediate and orientational responses suggest that these responses may be motionally narrowed by the orientational fluctuations in the liquid [27].

Previous theoretical work has indicated that the terms that contribute to the vibrational and orientational excitation in TKE are different than in OKE [150, 151]. The leading order contributions to the orientational signal in TKE are $\propto \alpha\alpha$ and $\propto \alpha\mu\mu$, where α is the molecular polarizability, and μ is the permanent dipole moment. The resonant dipole interaction is unique to the THz excitation frequency of TKE, as the nonresonant excitation in OKE leads to a signal only dependent on the molecular polarizability. Similarly, for vibrational excitation, the leading terms are $\propto \alpha'\alpha'$, $\alpha'\mu'\mu'$, $\alpha'\mu''\mu'$, and $\alpha''\mu'\mu'$ in TKE, while nonresonant OKE only retains the first term. The extra dipole terms in the TKE response provide complementary information to the OKE measurement. They also allow for a third order 2D THz-THz-Raman spectroscopy if two time delayed THz excitation pulses are used, as we show in Chapter 7. This is in contrast to OKE spectroscopy, where the 2D realization is a fifth order spectroscopy. The third-order measurement is advantageous, because the fifth-order signal is overwhelmed by cascaded third-order processes in all but a few select liquids [30, 35].

In this chapter, we compare TKE and OKE spectroscopy on a series of aromatic compounds that vary in polarity and orientational timescales. We find the first evidence for an intermediate decay in TKE that may shed light on intermolecular vibrations in liquids.

6.2 Methods

Our experimental TKE setup has been described in Marco Allodi’s thesis and a previous publication [148], so only a brief overview will be given here. The liquid sample is held in a fused quartz (Suprasil) cuvette with a 1 mm pathlength. To

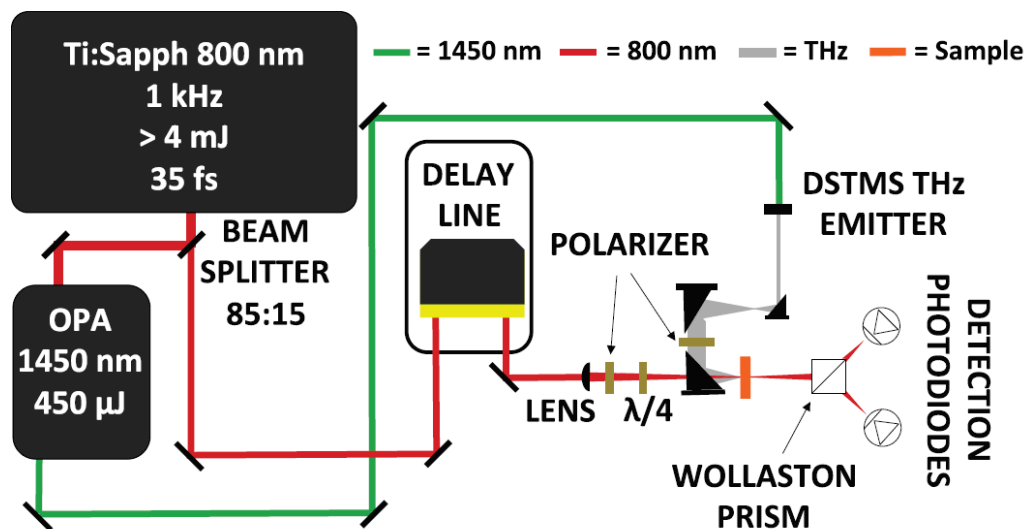


Figure 6.1: A schematic of the TKE experiment. An intense THz pulse is focused onto a liquid sample and the resulting birefringence is probed with a time-delayed 800 nm probe pulse. Heterodyne detection increases the sensitivity and enables the determination of the phase of the measurement.

generate coherent THz light we use $450 \mu\text{J}$, $1.45 \mu\text{m}$, 45 fs pulses from an optical parametric amplifier to pump a 3 mm aperture organic stillbazolium-based crystal (DSTMS), as shown in Fig. 6.1. The crystal emits $\sim 160 \text{ nJ}$ THz pulses centered at 2 THz, which we send through an optical beam block and a Gaussian telescope (magnification factor = 7.5) to focus on the sample. The bandwidth of the THz pulses is limited by the transmission through the front window of the Suprasil cuvette that holds the liquid sample. The field strength at the sample is approximately 300 kV/cm.

We detect the transient birefringence in the sample with a weak probe pulse ($\sim 2 \mu\text{J}$, 800 nm, 40 fs) from the regenerative amplifier that pumps the optical parametric amplifier. The probe beam is focused, passed through a polarizer and a $\lambda/4$ waveplate, combined with the THz beam on the sample, after which the polarization is measured with a Wollaston prism and two balanced photodiodes. To increase the sensitivity of the measurement, we employ a heterodyne detection scheme, by precisely crossing the polarization of the polarizer and Wollaston prism. The angle of the polarizer is then offset ~ 5 degrees to allow a small portion of local oscillator power on the p-polarized detection photodiode. This increases the sensitivity, makes the measurement linear in signal, and enables the determination of the phase of the response.

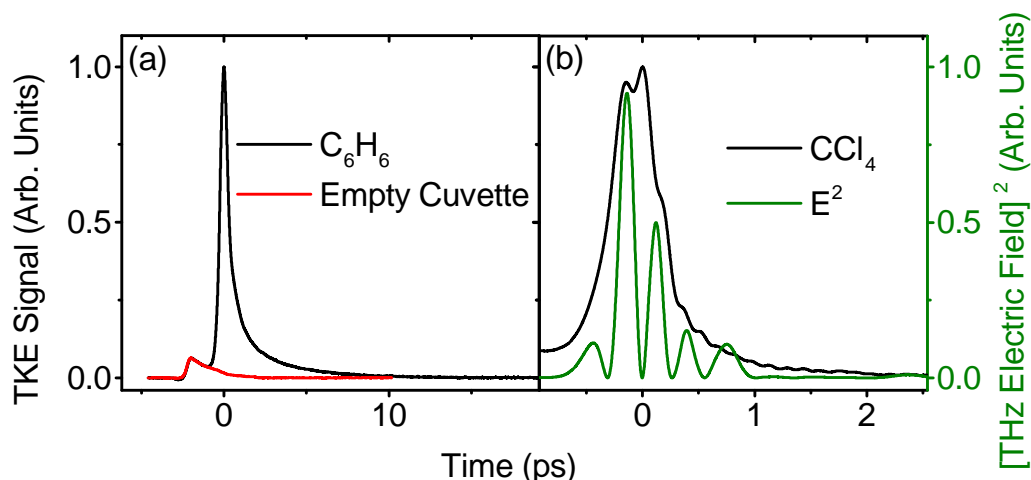


Figure 6.2: (a) The TKE response from benzene, and the empty fused quartz cuvette. The cuvette signal is much weaker and 2 ps before the liquid signal due to the index mismatch between the THz light and 800 nm light in quartz. (b) The response from CCl_4 shows no orientational contributions, and follows the square of the THz field.

Table 6.1: A comparison of our TKE results to OKE data from the literature.

Species	TKE (this work)			OKE [27, 152–154]		
	τ_1	τ_2	A	τ_1	τ_2	A
C_6H_6	3.0(2)	0.95(9)	0.40(2)	2.8(1)	1.10(8)	0.69
C_6D_6	3.3(2)	1.0(1)	0.39(2)	3.0(1)	1.14(9)	0.67
C_6F_6	14.2(5)	2.9(2)	0.58(3)	13.3(5)	2.9(2)	0.88
$\text{C}_5\text{H}_5\text{N}$	4.3(2)	1.3(1)	0.65(3)	4.1(3)	1.5(3)	0.73
$\text{C}_6\text{H}_5\text{CH}_3$	5.3(3)	1.2(1)	0.50(2)	4.80(5)	-	-
$\text{C}_6\text{H}_5\text{NO}_3$	37.7(8)	2.5(2)	0.57(3)	35(3)	1.9(2)	0.72(7)
$\text{C}_6\text{H}_5\text{Br}$	10.7(3)	2.0(2)	0.54(3)	10.9(2)	2.4(1)	-

6.3 Results and Discussion

The TKE signal of benzene is shown in Fig. 6.2(a). The electronic response at $t=0$ ps is clearly visible, as well as the long decay due to collective orientation in the liquid. All samples, including benzene, also show an early feature in the signal, due to the response from the fused quartz cuvette. Fortunately, the feature is shifted backward in time due to the index mismatch between the THz and optical light and reaches zero signal at $t=0$.

To determine the instrument response, we measured the THz field using electro-optic sampling and a 100 μm thick GaP crystal placed at the sample position. We then measured the TKE response of the spherical top CCl_4 , which shows no orientational

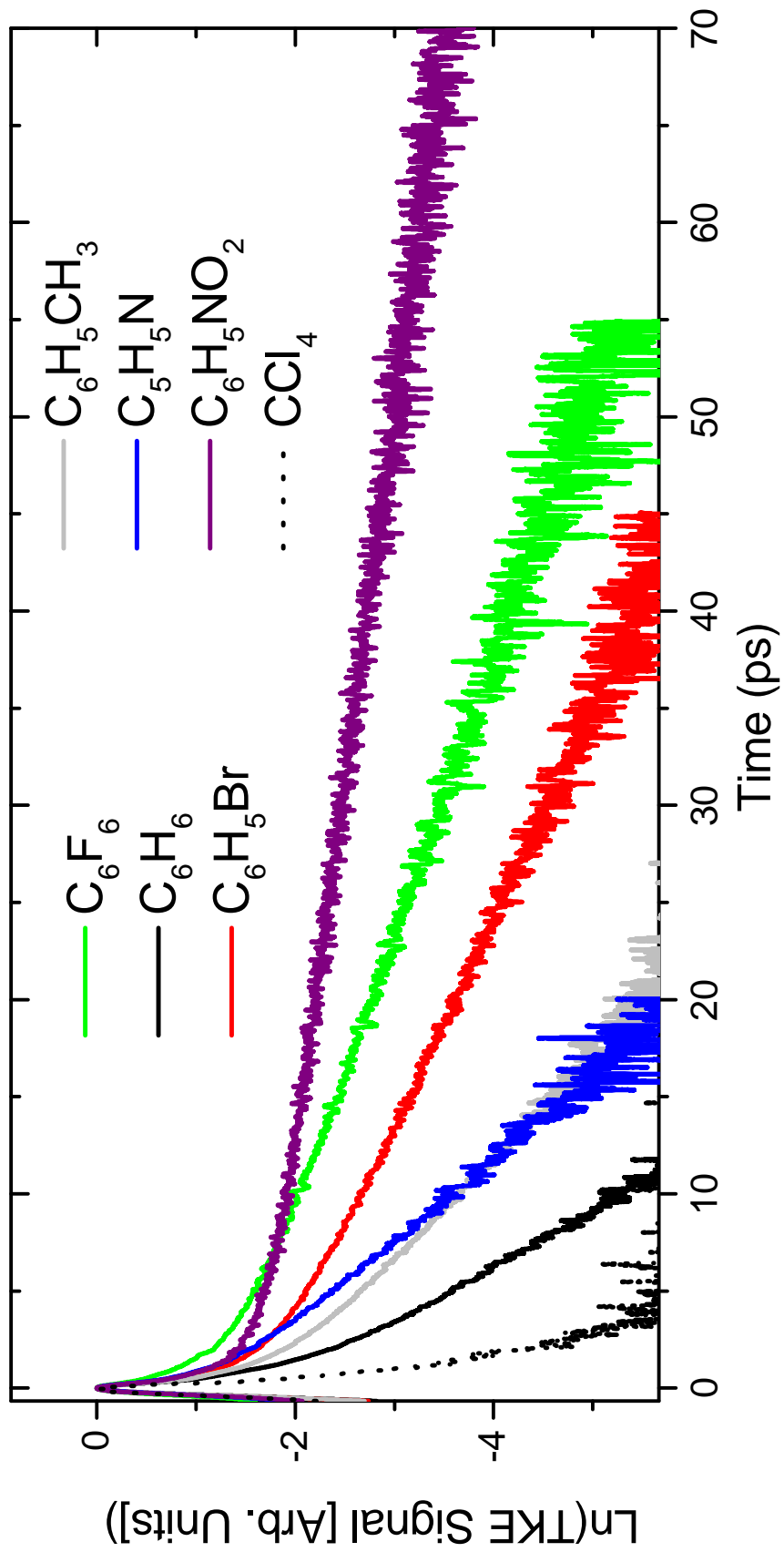


Figure 6.3: Measured TKE signals for six aromatic compounds and CCl_4 plotted on a natural log scale. All species decay linearly at long times, indicating single exponential behavior, but are curved near 5-10 ps. The CCl_4 decay serves as an instrument response function, due to the symmetry of this molecule.

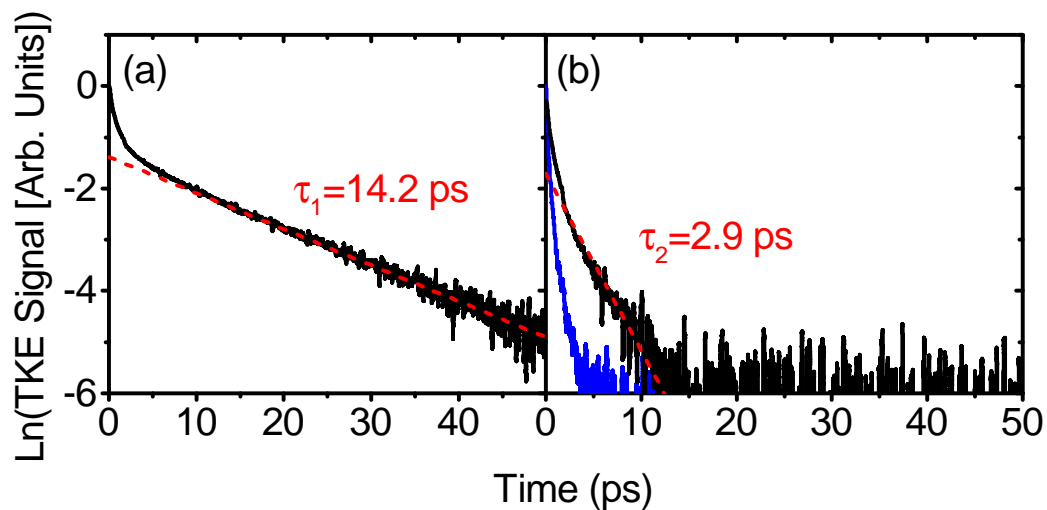


Figure 6.4: (a) The collective orientational decay of hexafluorobenzene, with the fit shown as a dashed red line. (b) The fit residual reveals a second exponential component beyond the electronic response. The CCl_4 decay is plotted in blue.

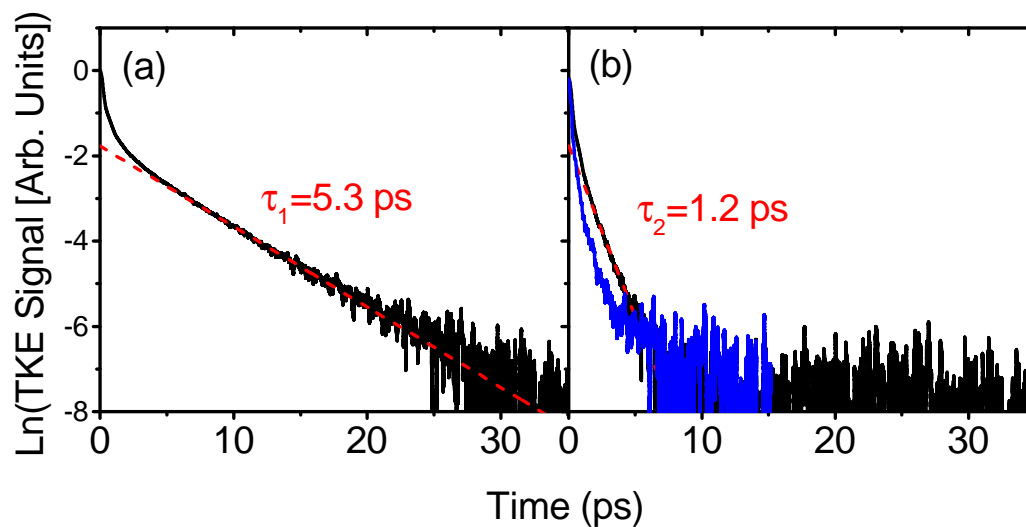


Figure 6.5: (a) The collective orientational decay of toluene. (b) The fit residual is near, but distinct from the electronic response. The CCl_4 decay is plotted in blue.

Table 6.2: Goodness of fit parameters for the biexponential fit ($b - \chi_{\text{red}}^2$) and the exponential fit ($e - \chi_{\text{red}}^2$).

Species	$b - \chi_{\text{red}}^2$	$e - \chi_{\text{red}}^2$
C ₆ H ₆	1.2	4.3
C ₆ D ₆	1.8	6.7
C ₆ F ₆	1.0	6.6
C ₅ H ₅ N	1.0	2.0
C ₆ H ₅ CH ₃	1.2	7.2
C ₆ H ₅ NO ₃	1.0	3.4
C ₆ H ₅ Br	1.2	16.4

response and follows the THz field squared (Fig. 6.2(b)). The decay constant of the electronic response is ~ 250 fs, although it is not a purely single exponential decay. Based on these traces we fit the experimental data >2 ps after the peak, to avoid the electronic responses of the samples.

The full data set is shown in Fig. 6.3, and the parameters used to fit the data are shown in Table 6.1. Benzene-d6 has been excluded from Fig. 6.3 as it is indistinguishable from benzene on this scale. With the increased sensitivity of the heterodyne detection and slower orientational timescales of the measured samples, we are able to measure TKE signals up to 70 ps of delay.

Initially, all samples were fit to a single exponential decay, as was done in previous work [37]. The goodness of fit for each decay was evaluated using the χ_{red}^2 , and found to be relatively high (at 2-16, Table 6.2). Next, we fit the decays with a biexponential function of the form:

$$B[Ae^{t/\tau_1} + (1 - A)e^{t/\tau_2}], \quad (6.2)$$

where B serves as an arbitrary scale factor and is not included in the analysis. The χ_{red}^2 for the biexponential fits vary from 1-2 (Table 6.2), indicating a better fit to the data. The biexponential behavior is illustrated for hexafluorobenzene and toluene in Fig. 6.4 and 6.5, respectively. For both molecules, the long exponential collective orientational decay is linear on a natural log scale (Fig. 6.4a, Fig. 6.5a). Once this component has been subtracted, a second exponential is visible with a shorter time constant, distinct from the electronic response of CCl₄ (Fig. 6.4(b), Fig. 6.5(b)).

For the symmetric top, nonpolar species benzene, benzene-d6, and hexafluorobenzene the collective orientational decay occurs as a single exponential decay that is

dependent on the polarizability, as these species lack a permanent dipole moment. There are no other intramolecular THz active motions in these liquids, so any residual signal is due to intermolecular motions, as has been shown in previous OKE experiments [152]. Given these constraints, we assign the 1 ps decay in benzene, benzene-d6 and the 2.9 ps decay in hexafluorobenzene to overdamped intermolecular motions excited by the THz pulse. This is the first evidence of nonlinear excitation of intramolecular motions in a liquid by a THz pulse. Although the measured time constants agree well with OKE results from the literature [152], the relative amplitudes are significantly changed. For all three species, the A constant is smaller, indicating a larger intermediate response relative to the orientational response. To further illustrate this point, we have overlaid the TKE and OKE response from hexafluorobenzene in Fig. 6.6. The OKE data was taken from the literature [155] and scaled to match the peak TKE signal and zero signal level before the arrival of the pump pulse. We attribute the larger TKE intermediate response to the additional TKE dipole terms $\propto \alpha' \mu' \mu'$, $\alpha'' \mu' \mu'$, and $\alpha' \mu'' \mu'$ that are not present in the OKE measurement.

Next, we consider the asymmetric top species pyridine, toluene, nitrobenzene, and bromobenzene. For these molecules the collective orientational signal includes terms $\propto \alpha\alpha$ and $\alpha\mu\mu$, since they all contain a permanent dipole moment. The intermediate OKE response has only been measured for nitrobenzene, pyridine, and bromobenzene and is believed to originate from intermolecular interactions, although the interpretation is more complex than in the symmetric top species [27, 153, 154]. With TKE we measure collective orientation and intermediate timescales similar to the values measured in OKE experiments, while our A constants are consistently smaller. One trend that emerges in the TKE A constants is a dependence on dipole moment. For benzene, benzene-d6, and hexafluorobenzene we see A constants that are 59%, 58%, and 66% of the OKE values. Pyridine and nitrobenzene are considerably larger, at 86% and 76%. We posit that this is due to the increased role of the permanent dipole moment in the orientational signal of these species, although further modeling is needed.

In addition to orientational and intermediate responses, many OKE signals have oscillatory components due to the excitation of intramolecular vibrational modes [27]. These features have never been observed in TKE experiments, although most small molecule liquids do not have intramolecular vibrations in the region covered by typical pulsed THz sources. To determine if such features exist in TKE, we

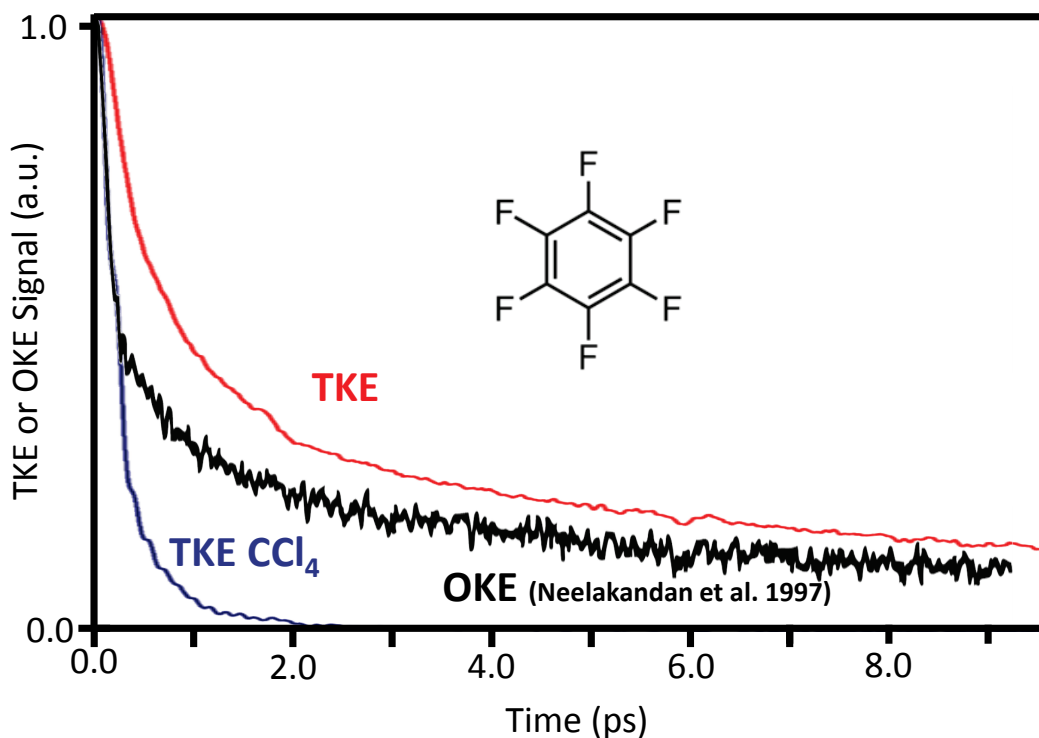


Figure 6.6: A comparison of the TKE and OKE responses of hexafluorobenzene, scaled to match the same peak signal and pre-pump pulse zero signal level. The approximate instrument response function is illustrated with the TKE response of CCl_4 . The OKE data is from [155].

compared the responses of CCl_4 , CS_2 , and CH_2I_2 (Fig. 6.7). In CCl_4 and CH_2I_2 we observed time domain oscillations consistent with excitation of the low energy ν_2 and ν_4 modes, respectively. In CS_2 , we did not observe any oscillations, as there are no intramolecular modes of this molecule in the spectral region covered by our THz pulses. The exact mechanisms of vibrational excitation in CCl_4 and CH_2I_2 are unclear from this 1D data, since the TKE experiment involves two light-matter interactions with the first THz pulse. In the next chapter (Chapter 7), we will explore the origins of these signals in more detail by adding a second THz pump pulse to the experiment.

6.4 Conclusion

In summary, we have measured the TKE responses of six aromatic compounds, including the highly polar species nitrobenzene and pyridine. All decays were fit to a biexponential function, yielding two decay constants. The longer of the two constants corresponds to the collective orientational decay in these liquids, and

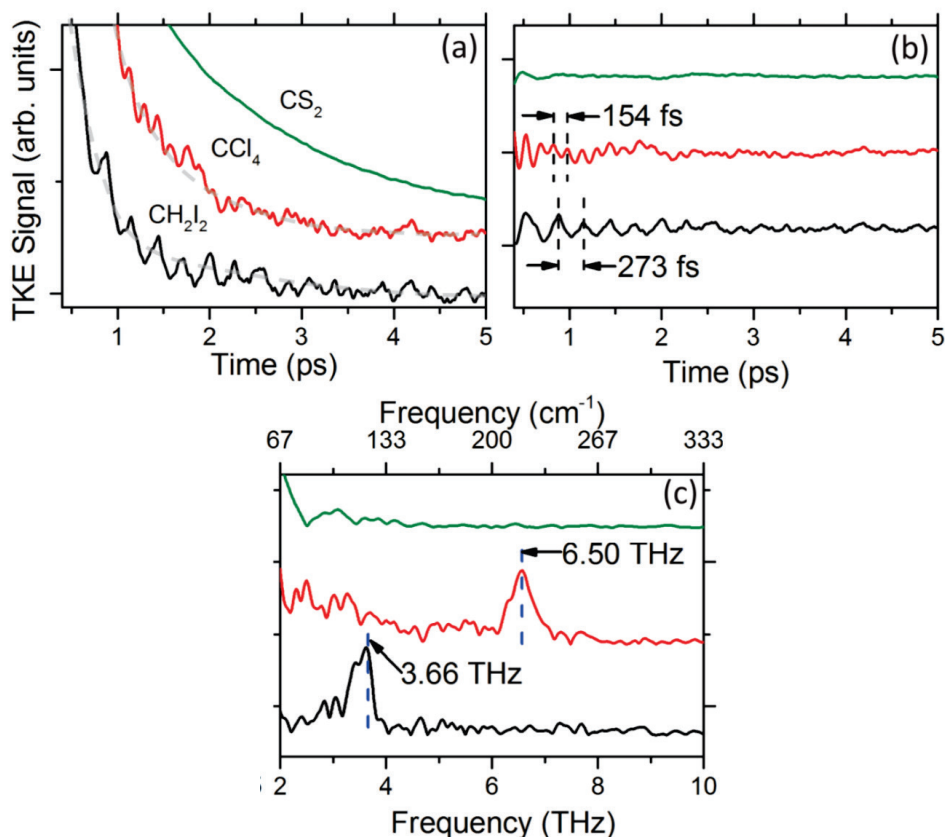


Figure 6.7: (a) In several liquids with low frequency intramolecular modes, including CCl₄ and CH₂I₂, we have observed vibrational coherences convoluted with the orientational decay. (b) Detrending the orientational response isolates the coherences more clearly in the time domain. (c) The Fourier transform of the time domain traces reveals the frequencies of the oscillations. The 6.50 THz peak in CCl₄ matches the ν_2 mode, while the 3.66 THz peak in CH₂I₂ matches the ν_4 mode.

agrees quite well with previous OKE experiments. The timescale of the second decay is close to the intermediate decay observed in OKE spectroscopy, and is likely due to overdamped intermolecular vibrations in the liquid. Although the timescales of TKE and OKE are similar, their relative amplitudes differ greatly, suggesting the influence of dipole terms in the TKE experiment. We have also observed underdamped oscillations in CCl₄ and CH₂I₂, due to the nonlinear THz excitation of intramolecular modes.

*Chapter 7***2D THZ-THZ-RAMAN SPECTROSCOPY OF LIQUIDS**

After observing nonlinear THz signals from liquids in Chapter 6, we now implement 2D THz-THz-Raman spectroscopy by adding a second THz pump pulse to the experiment. This hybrid approach isolates nonlinear signatures in isotropic media, and is sensitive to the coupling and anharmonicity of thermally activated THz modes that play a central role in liquid-phase chemistry. More generally, it is the first technique to interrogate a liquid with multiple pulses of THz light. By varying the timing between two intense THz pulses, we control the orientational alignment of molecules in a liquid, and nonlinearly excite vibrational coherences. A comparison of experimental and simulated 2D-TTR spectra of bromoform (CHBr_3), carbon tetrachloride (CCl_4), and dibromodichloromethane (CBr_2Cl_2) show previously unobserved off-diagonal anharmonic coupling between thermally populated vibrational modes. The simulations presented in this chapter were done in collaboration with Dr. Ralph Welsch and Professor Thomas Miller III.

This Chapter has been reproduced with permission from:

Finneran, I. A., Welsch, R., Allodi, M. A., Miller, T. F. & Blake, G. A. Coherent two-dimensional terahertz-terahertz-Raman spectroscopy. *Proceedings of the National Academy of Sciences* **113**, 6857–6861 (2016).

7.1 Introduction

Detailed molecular pictures of the structure and dynamics of liquids drive our understanding of chemistry and biology. Nonlinear two dimensional (2D)-infrared and -nuclear magnetic resonance (NMR) spectroscopies have revealed many specifics of liquid behavior, monitoring the coupling, spectral diffusion, and homogeneous linewidths of intramolecular vibrations and nuclear spins [34, 157]. However, the motions that directly participate in solvation and chemical reactivity are manifest in the terahertz (THz) region of the spectrum, making 2D-THz studies especially valuable. To date, no 2D technique has been demonstrated that incorporates multiple terahertz interactions with a liquid.

Recent advances in pulsed, high power THz sources with electric fields exceeding 100 kV/cm have enabled a new generation of *nonlinear* THz spectroscopy, in which THz radiation is used to both manipulate and record the response of matter [158]. It is now possible, for example, to control the alignment of gas-phase molecules [159] and antiferromagnetic spin waves [160], drive an insulator-to-metal transition in oxides such as VO₂ [161], and break up Cooper pairs in a superconductor with intense THz pulses [162]. Nonlinear THz interactions have also enabled the first demonstrations of 2D-THz spectroscopy in a double quantum well system and graphene [163, 164].

With weak transition dipole moments, yet high THz absorptivity, liquids present many challenges with respect to the development of 2D-THz spectroscopy. Initial successes with 2D-Raman spectroscopy were later shown to suffer from the interference of cascaded processes [29, 30, 165], but new schemes using optical pulse shaping have eliminated the cascaded contributions [166]. An alternative approach is resonant 2D-THz spectroscopy, analogous to 2D-IR spectroscopy. However, this method is hindered by a lack of THz directional phase-matching, leading to signals that can be easily overwhelmed by a strong linear background.

In the last few years, hybrid optical-THz techniques that circumvent these challenges have emerged, including 2D-Raman-THz spectroscopy and THz Kerr effect spectroscopy (Chapter 6) [11, 37, 148]. Here, we present the complementary 2D-TTR spectroscopy, a natural extension of these hybrid techniques, that was described theoretically by Cho in 1999 [29, 167, 168]. 2D-TTR is the first 2D-experimental technique applicable to liquids that is nonlinear in the THz field, and it is sensitive to the anharmonicity of molecular vibrations and the molecular orientational alignment. In these first experiments, the power of this technique to explore molecular

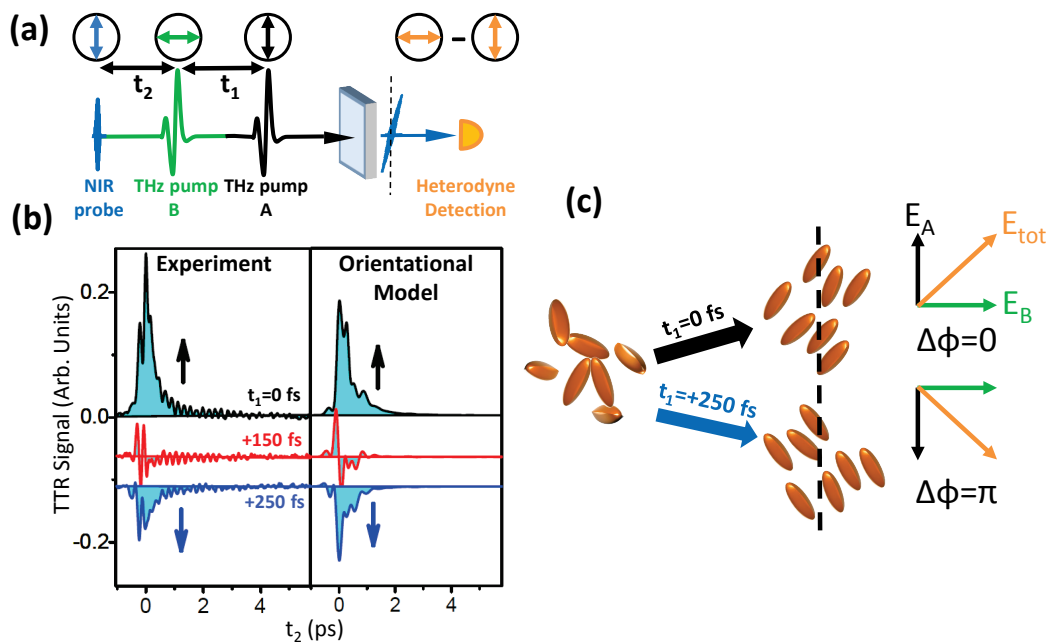


Figure 7.1: An overview of the 2D-TTR experiment. (a) The pulse sequence used in this work includes two intense THz pulses separated by time delay t_1 , followed by a weak NIR probe pulse at delay t_2 . The signal is measured as a birefringence of the NIR probe pulse, and is sensitive to changes in molecular polarizability. The polarizations of the light fields are shown in the circles above the pulses. (b) By controlling the phase overlap of two high-field THz pulses in liquid CHBr_3 , a positive ($t_1=0$ fs) or negative ($t_1=250$ fs) signal corresponding to the birefringence can be generated. Multiexponential contributions from intermolecular vibrations and librations are present near $t_2=1$ ps. At other times ($t_1=150$) the orientational birefringence is dampened. (c) The proposed molecular mechanism causing a sign change in the birefringence is due to control of the electronic polarizability and orientational alignment of the molecules in the sample.

dynamics and interactions is demonstrated in simple halogenated liquids. With modest improvements in sensitivity, 2D-TTR should be suitable for studies of inter- and intramolecular vibrational heterogeneity in biological macromolecules, amorphous solids, and hydrogen-bonded liquids.

7.2 Results and Discussion

The 2D-TTR experiment (Fig. 7.1a) uses two intense carrier-envelope-phase (CEP) stable THz pump pulses followed by a weak 40 fs near-infrared (NIR) probe pulse. By adjusting the delay t_1 between THz pulses, we control the phase of the THz radiation at the sample, while maintaining a constant power. The heterodyne-detected transient birefringence is measured along the t_2 axis with the NIR probe

pulse from the same laser system. By Fourier transforming over the t_1 and t_2 times, one can generate 2D plots in the frequency domain. In an isotropic medium, such as a liquid, the lowest order contribution to the measured nonlinear polarization is given by [37, 149]:

$$P^{(3)}(t) = \iint dt_1 dt_2 R^{(3)}(t_1, t_2) E_B(t - t_2) E_A(t - t_1 - t_2) E_{\text{nir}}(t), \quad (7.1)$$

where $R^{(3)}(t_1, t_2)$ is the third-order response function of the liquid, and $E_A(t - t_1 - t_2)$ and $E_B(t - t_2)$ are the two THz pulses and $E_{\text{nir}}(t)$ is the NIR probe pulse. Weaker single-pulse third-order responses are removed by differential chopping, as shown in the Methods section.

We illustrate the principal components of a 2D-TTR response function with the birefringent signal from liquid bromoform at 295 K (Fig. 7.1 (lhs), Fig. 7.2a). For the $t_1=0$ fs trace (Fig. 7.1b (lhs), black line), the electronic response is visible as a sharp peak near $t_2=0$ ps, which follows the $(E\text{-field})^2$ (including phase) of the THz radiation [37]. An exponential decay extending to $t_2=2$ ps results from the rotational diffusion of the molecules in the liquid as they reorient after aligning with the THz field [37]. Nonlinear vibrational coherences from the excitation of the ν_6 mode are visible as a damped oscillation out to $t_2=4$ ps [148]. As t_1 is shifted to 150 fs (red line), the transient birefringence is attenuated, while at 250 fs (blue line) the response becomes negative. A full 2D scan of this t_1 -dependent THz electric field-driven control is shown in Fig. 7.2a.

To understand the observed birefringence control, we return to the 2D-TTR pulse sequence (Fig. 7.1a). The polarizations of the THz pump pulses are orthogonal (shown in the black circles) and CEP stable. By changing the phase offset ($\Delta\phi$) between the pulses, or t_1 , we change the polarization of the total THz field (E_{tot}) when the pulses are overlapped in time (Fig. 7.1c). At $t_1 = 0$ fs, $\Delta\phi=0$, and E_{tot} is oriented at +45 degrees with respect to the probe, while at $t_1 = 250$ fs, $\Delta\phi=\pi$ and E_{tot} is oriented at +135 degrees with respect to the probe.

The electronic and nuclear alignment of the molecules follows the polarization of the THz radiation, as shown in Chapter 6 [37, 148]. Thus, we posit that the change in the measured birefringence as a function of t_1 is due to angular control of the molecular alignment induced by the THz polarization (Fig. 7.1c). A simple orientational model of this behavior using the measured THz electric fields is shown in Fig. 7.1b (rhs). The parameters of the model are given in the Methods section.

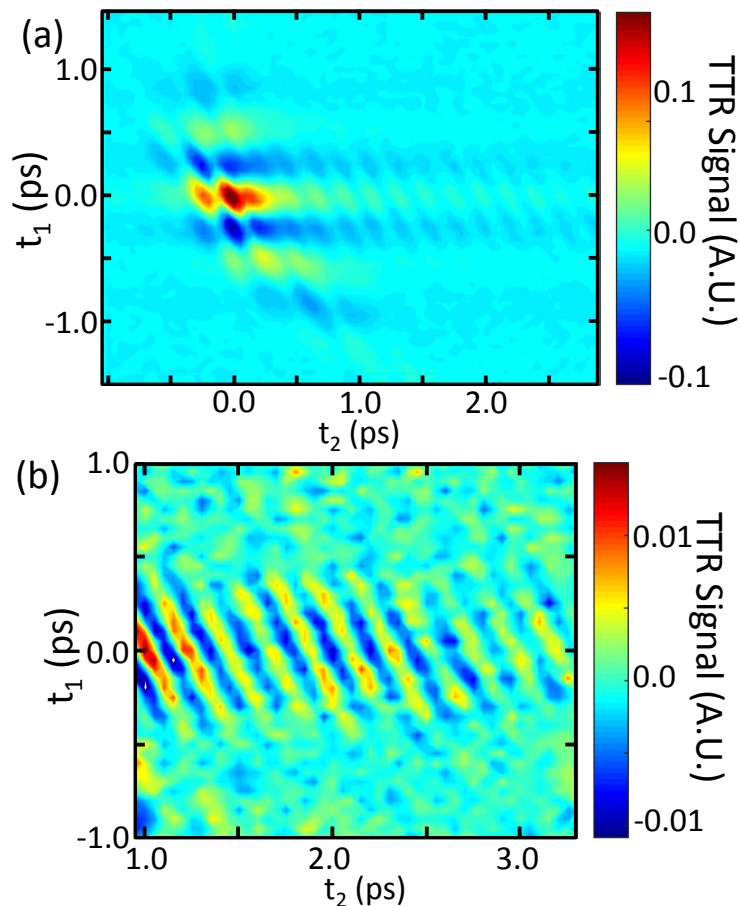


Figure 7.2: Representative time domain 2D-TTR signals. (a) The 2D time domain response of liquid bromoform (b) Cutting the response in (a) beyond $t_2=1$ ps and detrending fits isolate the vibrational coherences.

The orientational model correctly predicts the sign changes and zero crossings of the birefringence, although it does not account for the nonlinear vibrational coherences. Thus, by varying the phase of the THz polarization at the sample, one can control the orientation of molecules in a liquid.

We now consider the damped oscillation shown in Fig. 7.1b (lhs) and Fig. 7.2a. This component is due to the excitation of intramolecular vibrational coherences, and provides information on the coupling and anharmonicity of vibrations in the liquid. It is best visualized with a 2D Fourier transform along the t_1 and t_2 axes starting at $t_2=1$ ps, after detrending the orientational response with a single exponential fit for each t_2 scan (Fig. 7.2b).

The origins of the 2D-TTR signatures can be derived using third-order perturbation theory on a three-level system, yielding 24 rephasing and non-rephasing Liouville

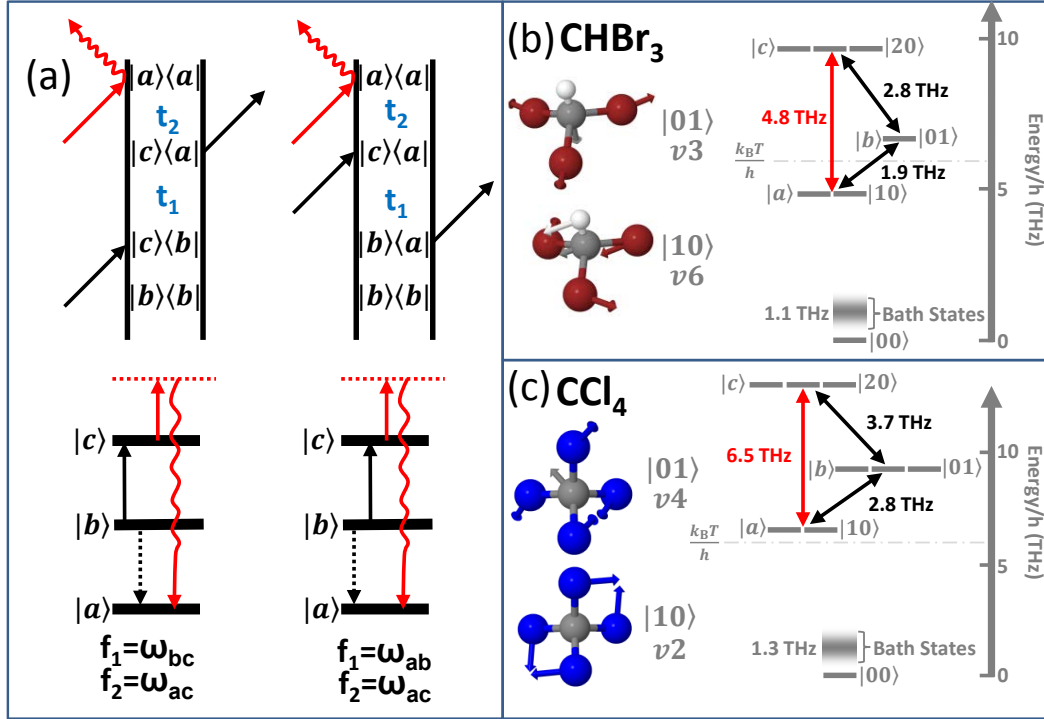


Figure 7.3: A quantum mechanical description of the measured signals. (a) 2 of 24 Liouville pathways in the 2D-TTR experiment for generalized eigenstates $|a\rangle$, $|b\rangle$, and $|c\rangle$. (b) The energy levels and observed couplings in CHBr_3 , and for CCl_4 in (c). THz excitations are shown in black, Raman in red.

pathways, as shown in Figs. 7.14 and 7.15 in the Methods section. With phase-sensitive heterodyne detection, rephasing and non-rephasing Liouville pathways are differentiated in a 2D Fourier transform. Signals in the first quadrant ($f_1 = \pm, f_2 = \pm$) are non-rephasing, while signals in the second quadrant ($f_1 = \pm, f_2 = \mp$) arise from rephasing pathways [149, 163]. The bandwidth (0.5-4 THz) of the THz pulses restricts the experiment to 8 of the 24 pathways, all non-rephasing, 2 of which are shown in Fig.7.3. The sum of the 8 pathways yields a response function $R^{(3)}(t_1, t_2)$ given by:

$$R^{(3)}(t_1, t_2) \propto \mu_{ab}\mu_{bc}\Pi_{ac}(p_{ab}e^{-i\omega_{ab}t_1}e^{-i\omega_{ac}t_2} - p_{bc}e^{-i\omega_{bc}t_1}e^{-i\omega_{ac}t_2}). \quad (7.2)$$

Here dipole and polarizability couplings are labeled as μ_{xy} and Π_{xy} , and the equilibrium population differences between states y and x as p_{xy} for the generalized three-level system. Thus, each peak in a 2D-THz-THz-Raman spectrum results from a closed-loop between three molecular eigenstates, hereafter denoted $|a\rangle$, $|b\rangle$, $|c\rangle$. Coherences are initiated by THz pump A and seen on the t_1 time- or f_1

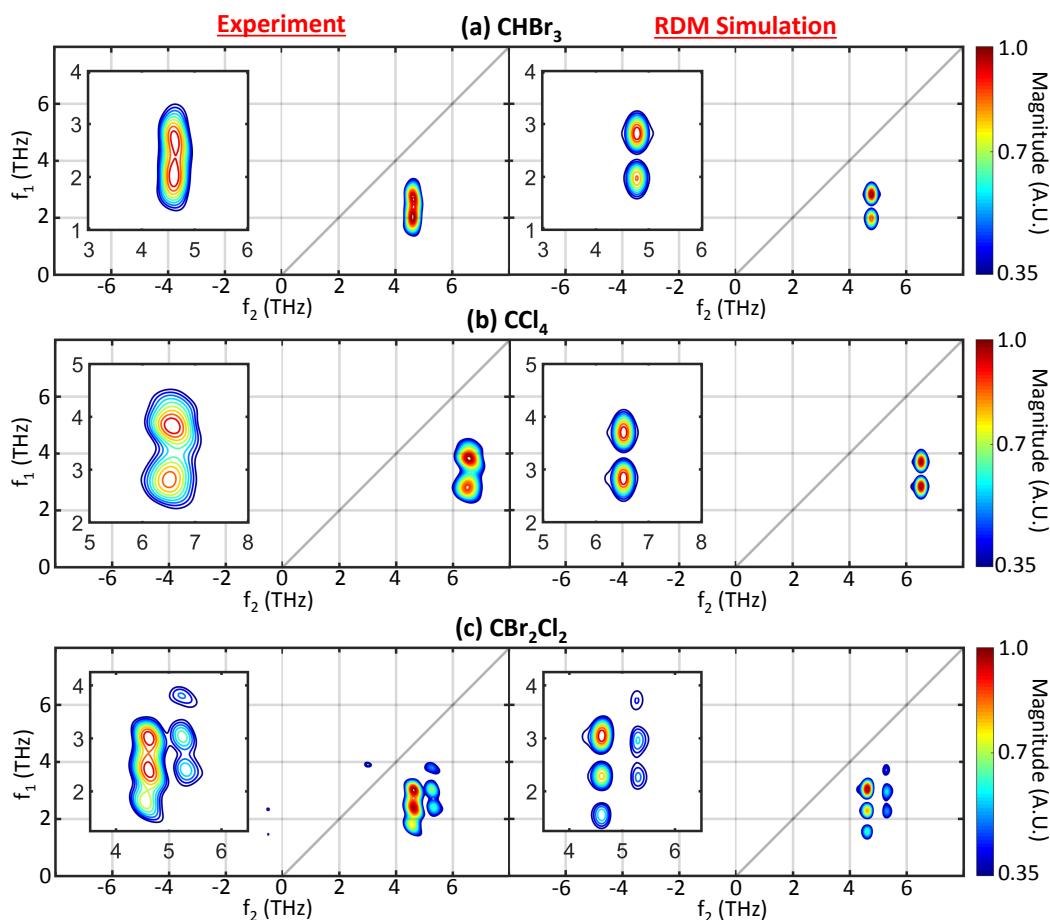


Figure 7.4: Experimental and RDM simulated 2D-TTR spectra of CHBr_3 (a), CCl_4 (b) and CBr_2Cl_2 (c). The f_1 axis corresponds to the THz pump, while the f_2 axis corresponds to the optical Raman probe.

frequency-axis. THz pump B moves these coherences to a new eigenstate, analogous to a coherence transfer pulse in 2D-NMR. The loop is closed with a $|c\rangle \rightarrow |a\rangle$ or $|a\rangle \rightarrow |c\rangle$ Raman transition on the t_2 time, or f_2 frequency, axis. Similar to 2D-Raman and 2D-Raman-THz spectroscopy, every closed-loop contains one or more transitions *forbidden in the harmonic approximation*, allowing us to directly measure the molecular anharmonicity [12, 30].

In Fig. 7.4, we demonstrate the capabilities of 2D-TTR in measuring vibrational anharmonicities with the spectra of bromoform (CHBr_3 , 295 K), carbon tetrachloride (CCl_4 , 295 K), and dibromodichloromethane (CBr_2Cl_2 , 313 K). For all three liquids, we observe peaks on the f_2 Raman axis that match the known lowest energy intramolecular vibrations: ν_6 in CHBr_3 (Fig. 7.5); ν_2 in CCl_4 [169, 170]; ν_4 and ν_5 for CBr_2Cl_2 [171]. Returning to the closed-loop picture, the $|c\rangle \leftrightarrow |a\rangle$ Raman

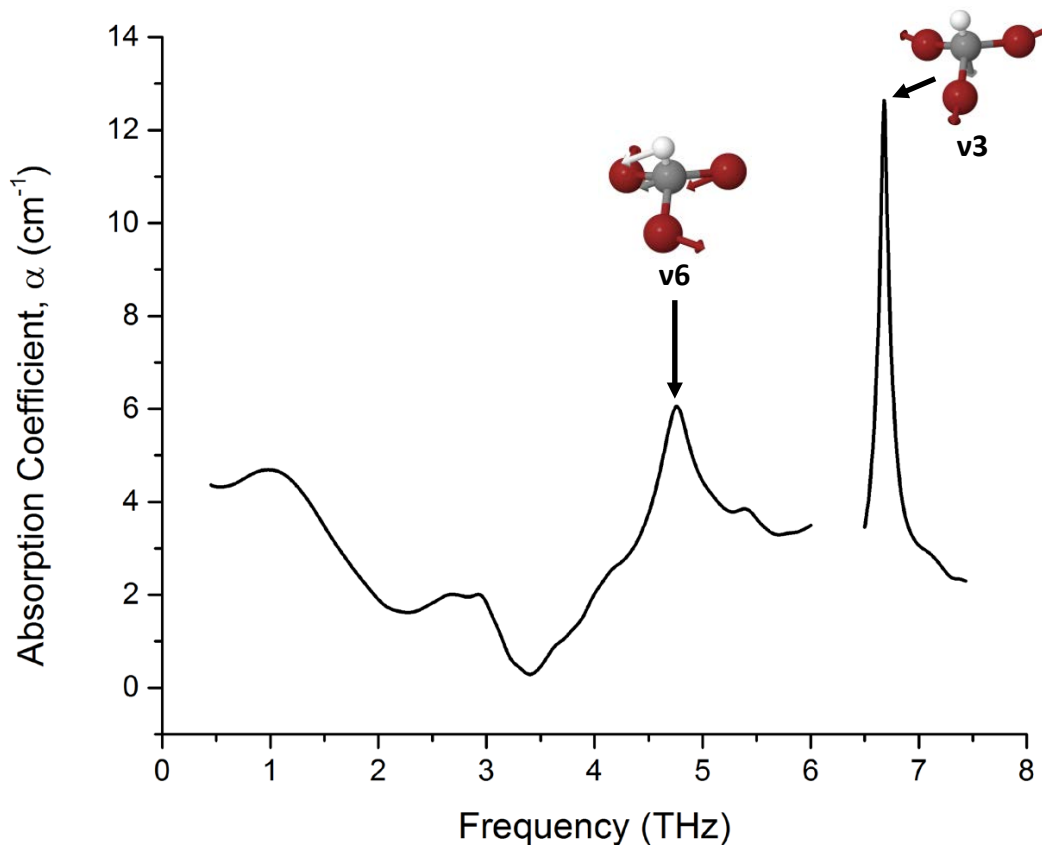


Figure 7.5: The linear spectrum of bromoform, taken with a plasma filamentation THz source, and a 200 micron thick GaP crystal for EO detection.

transition is clearly assigned to changes of one quantum in each of these low energy modes. The remaining mystery is the identity of the intermediate state $|b\rangle$ in the closed-loop, which can be determined by examining the f_1 positions of the peaks.

At ~ 300 K ($k_B T/h = 6.2$ THz) there is significant population in the low energy vibrational and bath states of these liquids. Using linear Raman and THz spectra and Eq. 7.2, we can predict the precise peak positions for coupling to different $|b\rangle$ states. For CHBr_3 , we observe a doublet f_1 peak that is consistent with anharmonic coupling between ν_6 and ν_3 , but not with anharmonic coupling of ν_6 to bath modes (Fig. 7.3b, Fig. 7.4a). CCl_4 exhibits a similar doublet on the f_1 axis that matches a ν_2 - ν_4 coupling (Fig. 7.3c, 7.4b). Simulated spectra from a reduced density matrix (RDM) method (see Methods section) show good agreement with the experimental results (Fig. 7.4a,b, rhs).

The thermally populated vibrational manifolds of CBr_2Cl_2 (Fig. 7.6) are more complicated than those of CCl_4 and CHBr_3 , which leads to further possibilities for

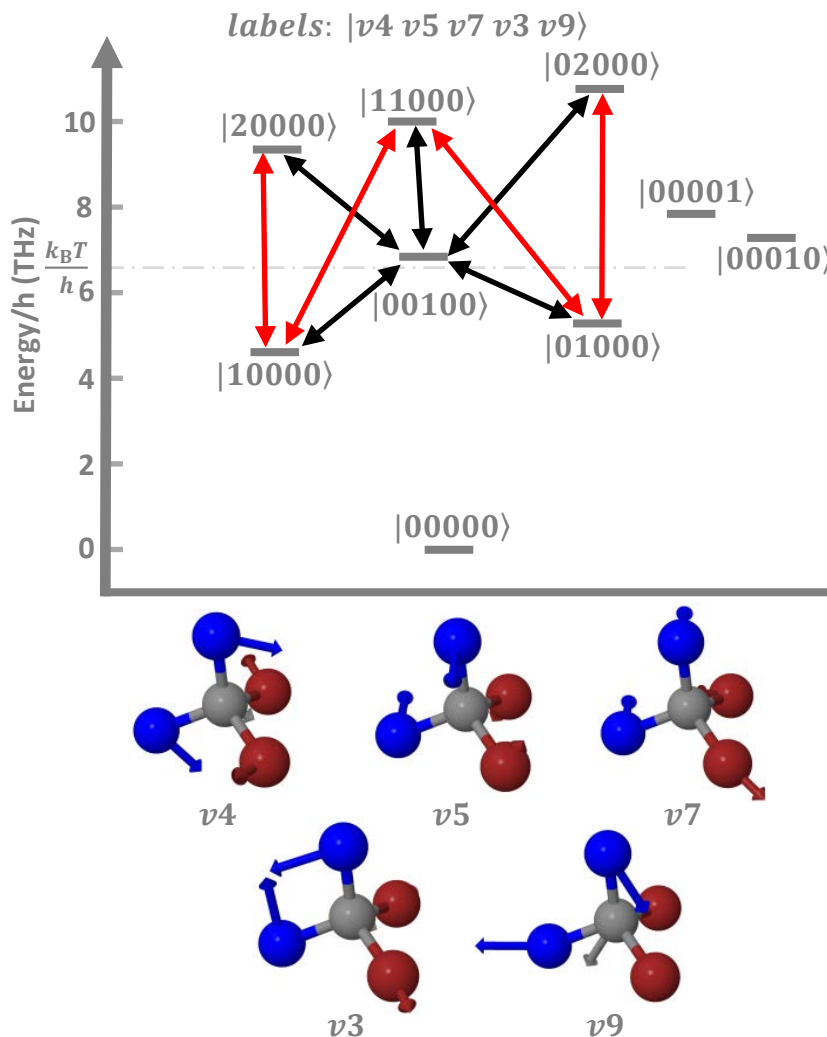


Figure 7.6: The vibrational energy levels of CBr_2Cl_2 . Observed THz excitations are shown as black arrows, those for Raman excitations in red.

vibrational coupling. However, a simple RDM simulation with eigenstates from the linear Raman spectrum and weak anharmonic $v_4 \leftrightarrow v_7$ and $v_5 \leftrightarrow v_7$ coupling reproduces all of the observed peaks (Fig. 7.4), and gives us insight into the relative coupling strengths in this liquid. Specifically, we see that the two lowest energy vibrational modes v_4 and v_5 are more strongly coupled to v_7 than v_3 and v_9 .

To test the robustness of the CBr_2Cl_2 simulations, we have plotted the RDM predicted spectra for several different coupling schemes in Fig. 7.7. With v_3 , v_9 , or $v_7/v_9/v_3$ coupling, the RDM spectra are qualitatively different than the experimental spectrum, while there is good agreement with only v_7 coupling.

We can further differentiate the v_3 coupling schemes by considering the symmetry

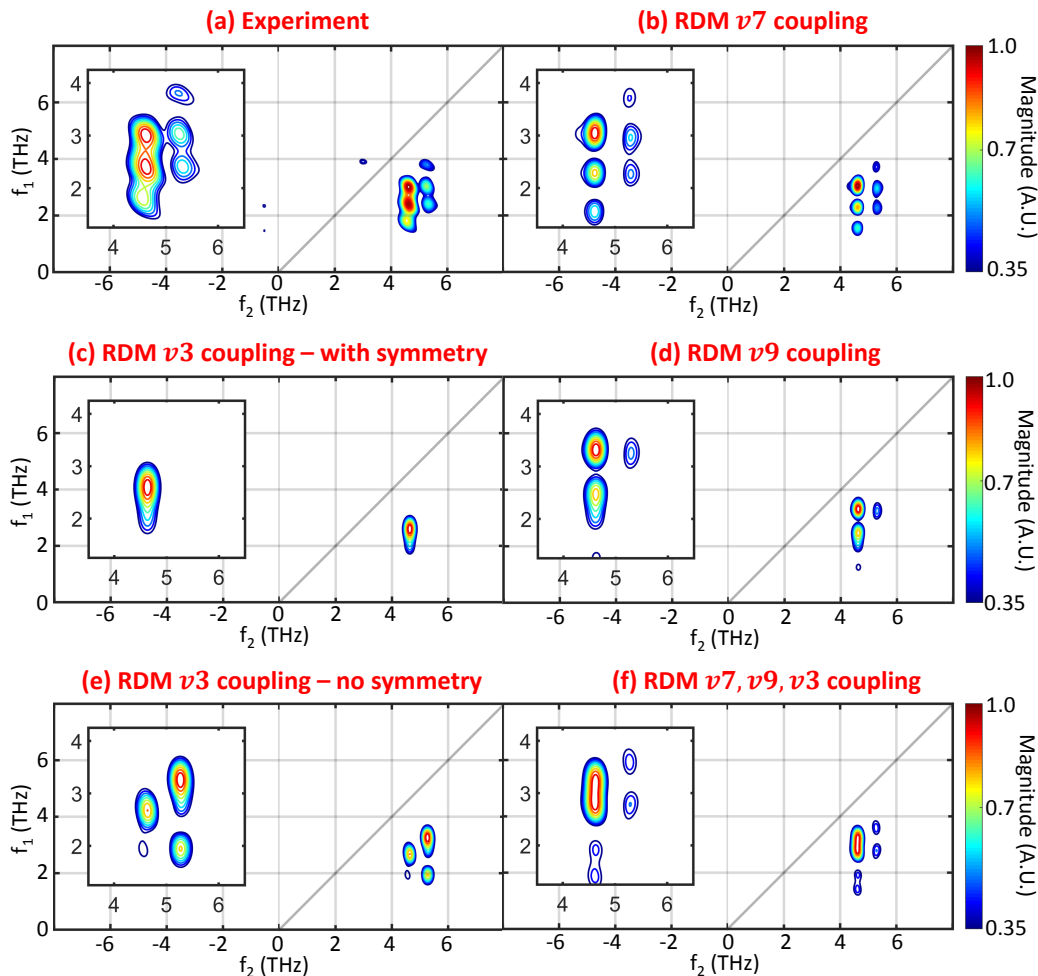


Figure 7.7: The experimental and RDM simulated spectra for various couplings in CBr_2Cl_2 .

of the modes. For any transition dipole matrix element to be non-zero, the following must be true

$$\langle \Psi_a | \hat{\mu} | \Psi_b \rangle \neq 0 \Leftrightarrow \Gamma_a \otimes \Gamma_\mu \otimes \Gamma_b \supset A_1,$$

where Ψ_j are vibrational eigenstates, $\hat{\mu}$ is the dipole operator, Γ_i denotes the irreducible representation and A_1 refers to the totally symmetric representation. The point group of CBr_2Cl_2 is C_{2v} , with irreducible representations of the dipole operator A_1 , B_1 , and B_2 . Thus, the transition between $|01000\rangle$ (A_2 symmetry) and $|00010\rangle$ (A_1 symmetry) in Fig. 7.6 is forbidden, while all others are allowed. In Fig. 7.7c we set this forbidden coupling to zero, but still do not see good agreement with the experimental spectrum. Finally, we also performed this analysis on CCl_4 and CHBr_3 , but found no symmetry forbidden transitions.

7.3 Conclusion

In summary, we have demonstrated the first 2D spectroscopy of liquids that is nonlinear in the THz field. With two time-delayed THz pulses and a NIR probe pulse, we can control the orientational alignment of molecules in a liquid and generate 2D-THz-THz-Raman spectra that are sensitive to anharmonic vibrational coupling. We measure significant coupling in the lowest frequency intramolecular modes of liquid CHBr_3 , CCl_4 , and CBr_2Cl_2 .

The off-diagonal peaks measured in the 2D-TTR spectra provide new information that is not present in a 1D linear spectrum. Specifically, the linear THz peaks of a liquid reveal the energies of its molecular eigenstates, while the off-diagonal 2D-TTR peaks show the coupling between these eigenstates. The features measured here are by definition cross peaks, since they correlate a frequency on the pump axis to a different frequency on the probe axis. This allows us, for example, to show that in CBr_2Cl_2 ν_4 and ν_5 are most strongly coupled to ν_7 – information unobtainable in a linear spectrum. These off-diagonal peaks also allow us to determine individual components of an inhomogeneously broadened feature in the linear spectrum. This is the case in CHBr_3 and CCl_4 , which show an inhomogeneously broadened absorption from 0.1-3.5 THz (Fig. 7.5) [169, 170]. It is impossible to resolve the components of these features with a linear measurement, as the broadening is intrinsic to the liquids. The 2D-TTR spectra, however, reveal several distinct components due to difference band transitions between intramolecular modes.

Although limited in these first experiments, we expect 2D-TTR sensitivity improvements of $\times 100$ using existing technologies [172, 173]. Such improvements should enable studies of intermolecular vibrations in isotropic molecular solids and hydrogen-bonded liquids. The importance of THz-active motions in biochemistry is well documented [174], and 2D-TTR studies could ultimately provide new insights on processes such as protein folding and DNA internal conversion. In the next chapter we extend the bandwidth of the THz pulses to reveal photon echo signals and further investigate the molecular origins of the forbidden transitions in bromoform.

7.4 Methods

Experiment

A schematic of the 2D-TTR experiment is shown in Fig. 7.8a. The heart of the system is a 38 fs Coherent Legend Elite USP Ti:Sa regenerative amplifier seeded by a 80 MHz Coherent Mantis oscillator. The 3.6 mJ, 800 nm pulses from the

amplifier are sent into an optical parametric amplifier (OPA, Light Conversion Ltd) and downconverted to 1450 nm (signal, 500 μJ) and 1780 nm (idler, 330 μJ). The OPA signal beam is routed through a second delay line (t_1 , Fig. 7.8(a)) and used to drive a 3 mm aperture DSTMS (4-N,N-dimethylamino-4-N-methyl-stilbazolium 2,4,6-trimethylbenzenesulfonate) THz generation crystal (Rainbow Photonics). The OPA idler output is sent directly to a second 3 mm aperture DSTMS crystal. The DSTMS crystals are optimized for THz generation phase matching near 1450 nm, but we achieve a roughly equivalent THz power near 1700 nm. The 1450 nm signal/1780 nm OPA setting was chosen to optimize the THz power of both beams, taking into account the wavelength dependent conversion efficiency of the OPA and the DSTMS efficiency.

The two separate THz pulses (3 mm beam diameter) from the signal and idler OPA beams are combined on a knife edge prism mirror, and residual optical light is blocked with a thin layer of black polyethylene and a roughened TOPAS plate. The THz pulses are run through a Gaussian telescope with $7.5\times$ magnification (22.5 mm THz beam diameter) and then focused onto the sample with a 2 inch Effective Focal Length (EFL) 90 degree off axis parabolic mirror. Both pulses have a peak field strength of ~ 300 kV/cm at the sample. Liquids are held in a 1 mm path length Suprasil quartz cuvette. The transient birefringence in the sample is probed with a small portion of the 800 nm light (1 mW) that is split off from the amplifier and sent down a mechanical delay line (t_2 , Fig. 7.8a). As described in Chapter 6, we have implemented heterodyne detection of the transient birefringence using a $10^5:1$ optical polarizer, an 800 nm $\lambda/4$ plate, a Wollaston prism, and a pair of silicon photodiodes[148]. No nonlinear signal was detected from the empty quartz cuvette in the 2D-TR experiment. This is likely due to the fact that the focusing and beam overlap was optimized inside the cuvette with CS_2 rather than on the cuvette walls.

To isolate the two-pulse 2D-TTR signal we chop the signal beam at $f_{rep}/6$ and the idler beam at $f_{rep}/4$, where $f_{rep} = 1$ kHz, the repetition rate of the laser. We detect the birefringence on a lock-in amplifier at $f_{rep}/12=83.3$ Hz. The 1 pulse rejection of the experiment on CS_2 is shown in Fig. 7.9. When either the signal or idler is blocked there is no detectable interference from the single pulse signals, confirming that the experiment is exclusively sensitive to the two pulse signal. Next, we measured the single pulse signals and compared their intensity with the two pulse signal (Fig. 7.9b). The two pulse signal is $2\times$ stronger than the idler response and $4\times$ stronger than the signal response.

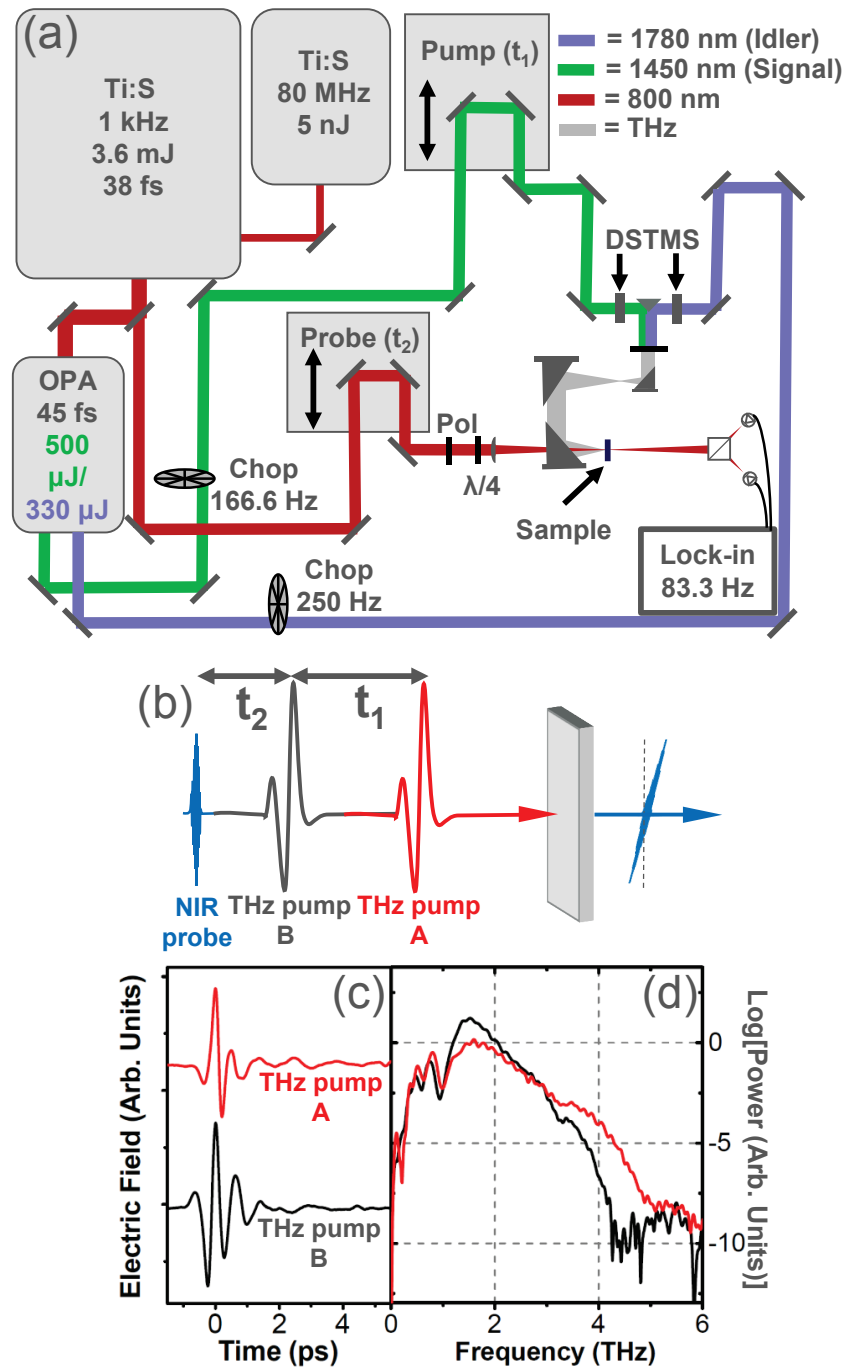


Figure 7.8: (a) A diagram of the 2D-TTR experiment. See text for details. (b) The pulse sequence used in 2D-TTR spectroscopy. (c) The measured time domain traces of the THz pulses using electro-optic sampling in a 200 micron thick GaP crystal. (d) The FFTs of the traces shown in (c).

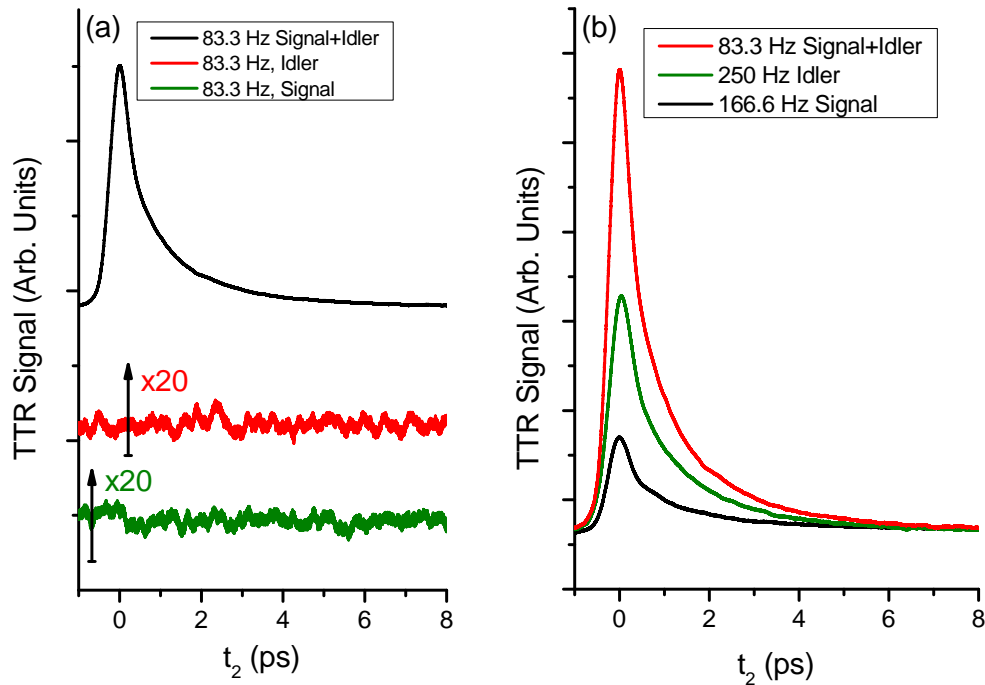


Figure 7.9: (a) The measured single pulse rejection of the 2D-TTR experiment. No interference from single pulse signals could be detected. (b) The 2- and 1-pulse responses of liquid CS_2 . The 2-pulse signal is stronger than either 1-pulse response.

The THz fields from both the signal- and idler-driven DSTMS emitters were measured with electro-optic detection using a 200 micron thick GaP crystal placed at the sample position (Fig. 7.8c). The bandwidth of the signal pulse extends from 0.5-5 THz, while that from the idler extends over 0.5-4 THz. The polarization purity of the THz pulses were measured with a wiregrid polarizer and a Gentec-EO inc. QS3-IL broadband pyroelectric detector mounted in a QS-I-TEST box at the sample position. The signal THz pulse has a polarization purity of 80%, while the idler THz pulse has a polarization purity of 90%. Finally, the peak field strength of both THz fields are ~ 300 kV/cm measured with the same pyroelectric detector and the EO traces. The details of the THz field strength measurement are given in Marco Allodi's thesis and a recent publication [148].

Orientational Model for 2D-TTR Spectra

A schematic of the light polarizations used in the 2D-TTR experiment is shown in Fig. 7.10. THz pulse A is polarized vertically, or along the \hat{y} unit vector, while THz

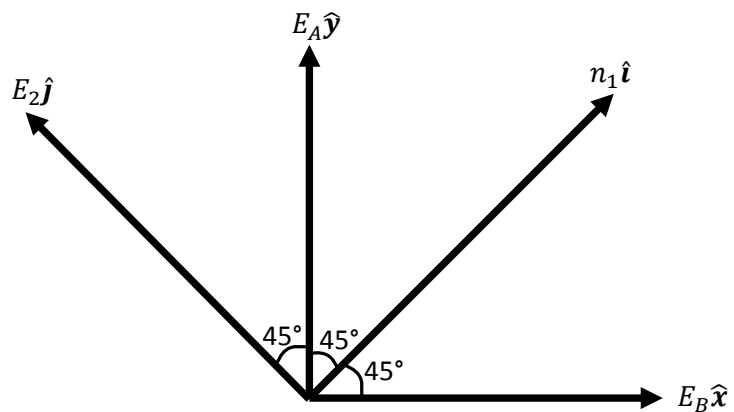


Figure 7.10: Polarization directions relevant to the 2D-TTR experiment.

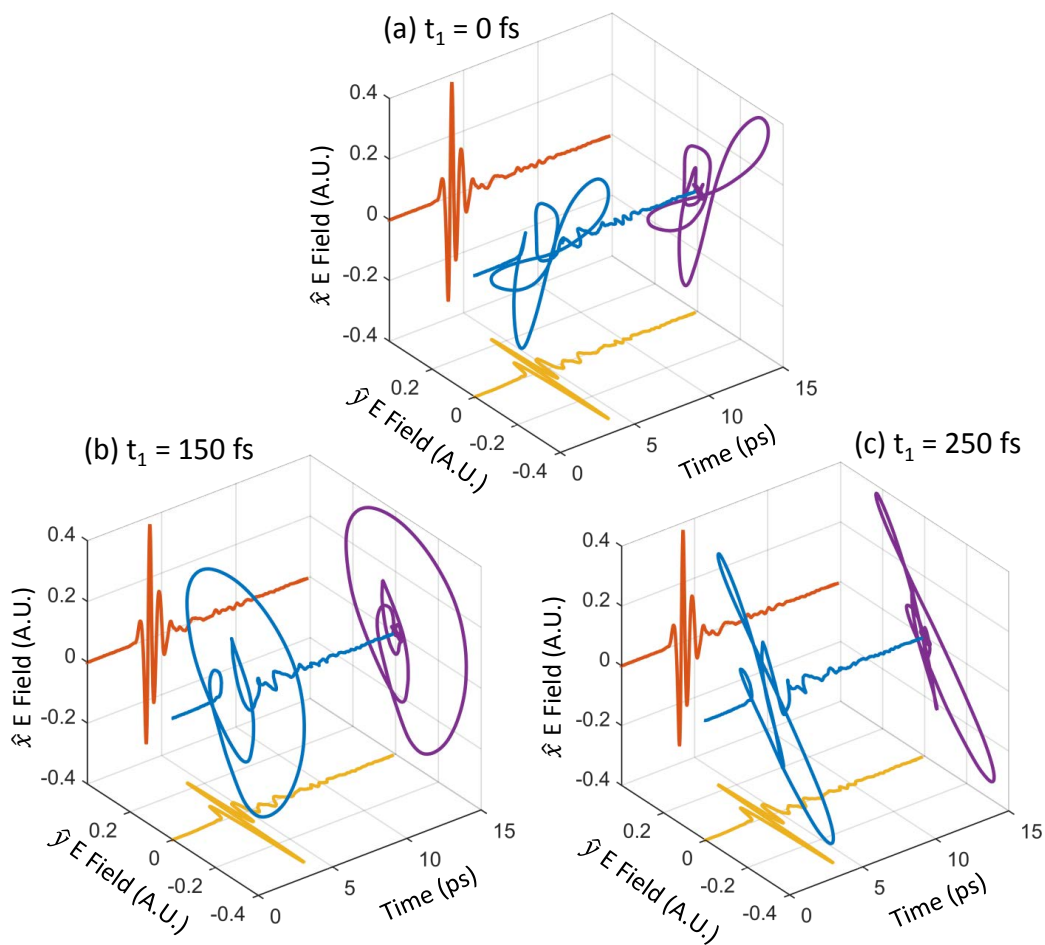


Figure 7.11: Time domain traces of the total THz electric field, including polarization at (a) $t_1=0$ fs, (b) $t_1=150$ fs, and (c) $t_1=250$ fs.

pulse b is polarized horizontally, or along the \hat{x} unit vector. When the THz pulses are overlapped in time, the polarization of the total field is dependent on t_1 . For example, at $t_1 = 0$ fs the field is rotated roughly toward the \hat{i} direction (Fig. 7.11a), while at $t_1=250$ fs the \hat{j} direction (Fig. 7.11c). At $t_1=150$ fs the field is roughly circular, with equal components along the \hat{i} and \hat{j} directions (Fig. 7.11b). The NIR probe pulse is oriented along the \hat{y} direction and the balanced detection is sensitive to the difference in the change of refractive index oriented along \hat{i} (n_1) and along \hat{j} (n_2): $S \propto \Delta n(t) = n_1(t) - n_2(t)$. In the absence of an excitation field in an isotropic liquid $n_1 = n_2$ so $\Delta n = 0$. When a THz pulse is applied in the \hat{i} direction, this leads to a signal given by

$$\Delta n_i(t) = \int dt_2 R(t_2) E_1^2(t - t_2), \quad (7.3)$$

where R is the response function of the liquid and E_1 is the field oriented in the \hat{i} direction. For an isotropic medium, excitation along the \hat{j} direction causes a sign change in Δn

$$\Delta n_j(t) = - \int dt_2 R(t_2) E_2^2(t - t_2), \quad (7.4)$$

where E_2 is the field oriented in the \hat{j} direction. The total signal is thus

$$\Delta n_{tot}(t) = \Delta n_i(t) + \Delta n_j(t). \quad (7.5)$$

The total THz field is given by $E_{tot} = E_A \hat{x} + E_B \hat{y}$. Alternatively, we can express this in the \hat{i}, \hat{j} coordinate system

$$E_{tot} = \frac{\sqrt{2}}{2} (E_A + E_B) \hat{i} + \frac{\sqrt{2}}{2} (E_B - E_A) \hat{j} = E_1 \hat{i} + E_2 \hat{j}, \quad (7.6)$$

$$\Delta n_{tot}(t) = \int dt_2 R(t_2) E_1^2(t - t_2) - \int dt_2 R(t_2) E_2^2(t - t_2). \quad (7.7)$$

Plugging in our values for E_1 and E_2 we get (for a given value of t_1)

$$\Delta n_{tot}(t) = 2 \int dt_2 R(t_2) E_A(t - t_2) E_B(t - t_2). \quad (7.8)$$

Now, using the model from our previous work we break the response function into two components: an instantaneous electronic response and a single exponential orientational response [148]. We use the measured electric fields to calculate the electronic portion of the signal, or

$$S_e(t_1, t_2) = E_A(t_2 + t_1)E_B(t_2). \quad (7.9)$$

We then calculate the orientational portion of the signal, S_o , with the discrete time step equation

$$S_o(t_1, t_2 + \Delta t_2) = S_o(t) + [E_A(t_2 + \Delta t_2 + t_1)E_B(t_2 + \Delta t_2) - S_o(t_2)/\tau]\Delta t_2, \quad (7.10)$$

where τ is the orientational decay constant [148].

Reduced Density Matrix (RDM) Simulation

Spectra are simulated using a reduced density matrix method [31, 149] in this chapter. The time evolution of the density matrix ρ is determined by the Liouville-Von Neumann equation

$$i\hbar \frac{\partial \rho}{\partial t} = [\mathbf{H}, \rho], \quad (7.11)$$

where \mathbf{H} is the Hamiltonian operator. We use a second-order differencing technique [175] to numerically calculate the time evolution of the density matrix:

$$\rho(t + \Delta t) = \rho(t) - \frac{i}{\hbar} [\mathbf{H}(t), \rho(t)] \Delta t - 2\Gamma \Delta t, \quad (7.12)$$

where $\Gamma_{i,j} = (1 - \delta_{i,j})\frac{1}{\tau_{i,j}}$ is the dephasing rate with an associated time-constant $\tau_{i,j}$ [31, 149].

The Hamiltonian $\mathbf{H}(t)$ consists of time-independent \mathbf{H}^0 and time-dependent $\mathbf{H}^L(t)$ terms, which describe the molecular system, and its interaction with the THz pulses, respectively:

$$H_{i,j}^0 = E_i \delta_{i,j}, \quad (7.13)$$

$$H_{i,j}^L(t) = \mu_{i,j} F(t). \quad (7.14)$$

Here, E_i is the energy of the i -th system eigenstate, $\mu_{i,j}$ is the dipole coupling element between state i and j and the THz electric field $F(t)$ is given as

$$F(t) = A \sum_{i=1,2} e^{\frac{-(t-\tau_i)^2}{2\sigma_i^2}} \cos(\omega_i(t - \tau_i)), \quad (7.15)$$

where τ_i , σ_i , and ω_i are the temporal delay, the temporal width, and center frequency of the i -th THz pulse, respectively and A is the THz electric field strength of both pulses.

The nonlinear molecular polarization corresponding to the measured signal is given by

$$P(t) = \text{tr}(\mathbf{D} \rho(t)) - \sum_{j=1,2} \text{tr}(\mathbf{D} \rho_j(t)), \quad (7.16)$$

where the matrix \mathbf{D} contains coupling elements for the final Raman interaction and $\rho_j(t)$ was propagated with only the j -th THz pulse. We subtract the single pulse responses from the total response to isolate the two pulse nonlinear response of the system. In the experiment, this is accomplished with differential chopping of the two THz beams. To generate the 2D response, the first THz pulse is fixed at $\tau_1 = 0.0$ fs, the second pulse is scanned as $t_1 = -\tau_2$, and the Raman readout delay is given as $t_2 = t$. 2D spectra were generated by applying a 2D FFT to the resulting 2D response. Simulations were only run for $\tau_2 > \sigma_1$, since this model does not properly describe the system response when the THz pulses are fully overlapped in the time domain. We tested the validity of this point by comparing the FFTs of the experimental data for different time windows (see Fig. 7.12). The different spectra are in qualitative agreement, although the signal-to-noise ratio and resolution are somewhat degraded.

A full list of the eigenstate energies used in the simulations is given in Table 7.1, Raman and dipole coupling elements in Table 7.2, and general simulation parameters are in Table 7.3. THz (dipole) couplings greater than 4 THz were set to zero, due to the limited bandwidth of the experiment. The eigenstates were populated at 300 K and propagated from time t_s to time t_e . Overtone and combination state energies were calculated from the fundamental energies, assuming no anharmonic shift.

Perturbative Density Matrix Derivation for 2D-TTR

The 2D-TTR experiment consists of two THz pulses followed by one Raman pulse. If we assume a third order interaction (the leading order contribution) this limits us to signals that originate from the interaction of light with a three-level system (triad) and at least one transition that is forbidden in the harmonic representation (Fig. 7.13). To understand the measured signals we start with the nonlinear polarization

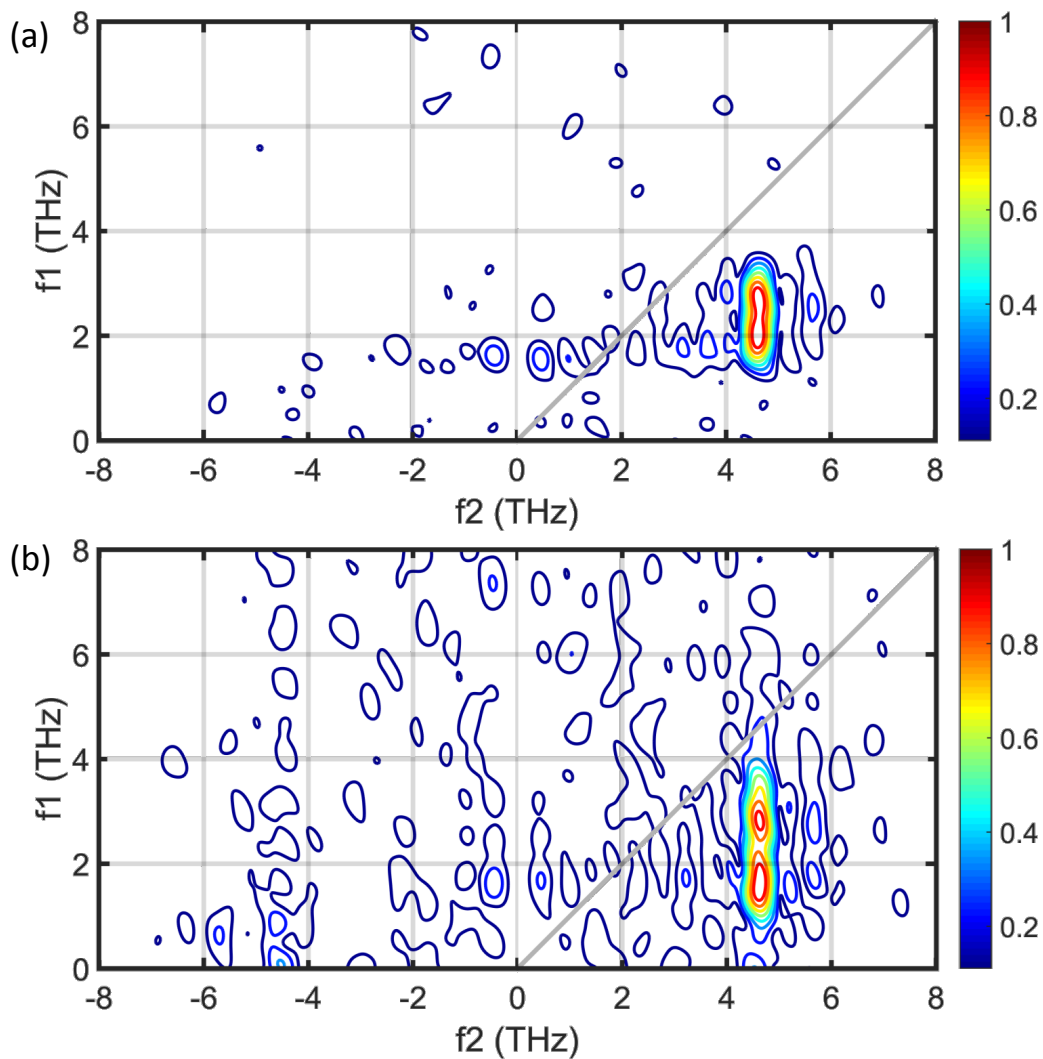


Figure 7.12: (a) The 2D-TTR spectrum of bromoform, with time domain data acquired from $-0.85 \text{ ps} < t_1 < 1.55 \text{ ps}$. (b) The 2D-TTR spectrum of bromoform, here the time window is $0.3 \text{ ps} < t_1 < 1.55 \text{ ps}$. The resolution and sensitivity are accordingly lower, but the doublet is still present.

CHBr ₃		CCl ₄		CBr ₂ Cl ₂	
State	E	State	E	State	E
$ 00\rangle, A_1$	0.0	$ 00\rangle, A_1$	0.0	$ 00000\rangle, A_1$	0.0
$ 10\rangle, E$	4.76	$ 10\rangle, E$	6.51	$ 10000\rangle, A_1$	4.62
$ 01\rangle, A_1$	6.68	$ 01\rangle, F_2$	9.29	$ 01000\rangle, A_2$	5.25
$ 20\rangle, A_1 + A_2 + E$	9.52	$ 20\rangle, A_1 + A_2 + E$	13.0	$ 00100\rangle, B_1$	6.87
—	—	—	—	$ 00010\rangle, A_1$	7.25
—	—	—	—	$ 00001\rangle, B_2$	7.85
—	—	—	—	$ 20000\rangle, A_1$	9.24
—	—	—	—	$ 11000\rangle, A_2$	9.86
—	—	—	—	$ 02000\rangle, A_1$	10.5

Table 7.1: Eigenstate energies used in the calculations, in THz. (Fig. 7.5, [169–171]) The notation is taken from the main text and symmetry labels are given for all states.

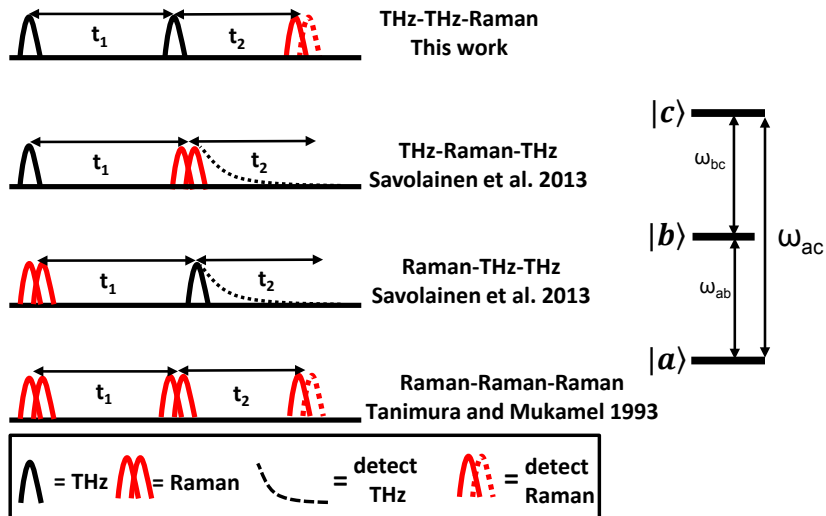


Figure 7.13: A comparison of the various 2D pulse sequences that have been used to study low energy modes of liquids via interactions with a three level system[11, 29, 30]. The signals from these techniques provide different information and are thus complementary[168].

CHBr ₃			CCl ₄			CBr ₂ Cl ₂		
i, j	$\mu_{i,j}$	i, j	$\mu_{i,j}$	i, j	$D_{i,j}$	$\mu_{i,j}$	i, j	$D_{i,j}$
$ 10\rangle, 01\rangle$	0.01	$ 00\rangle, 10\rangle$	0.01	$ 00\rangle, 10\rangle$	1.0	0.01	$ 00000\rangle, 10000\rangle$	1.0
$ 01\rangle, 02\rangle$	0.01	$ 00\rangle, 01\rangle$	0.01	$ 00\rangle, 01\rangle$	1.0	0.01	$ 00000\rangle, 01000\rangle$	0.5
—	—	$ 10\rangle, 20\rangle$	—	$ 10\rangle, 20\rangle$	1.0	0.01	$ 00000\rangle, 00100\rangle$	1.0
—	—	—	—	—	—	0.01	$ 00000\rangle, 00010\rangle$	1.0
—	—	—	—	—	—	0.01	$ 00000\rangle, 00001\rangle$	1.0
—	—	—	—	—	—	—	$ 10000\rangle, 20000\rangle$	1.0
—	—	—	—	—	—	—	$ 10000\rangle, 11000\rangle$	0.5
—	—	—	—	—	—	—	$ 01000\rangle, 11000\rangle$	1.0
—	—	—	—	—	—	—	$ 01000\rangle, 02000\rangle$	0.5

Table 7.2: Non-zero matrix elements for the dipole transition matrices, in Debye.

τ_1 in fs	0.0
τ_2 in fs	-300 – -2000
$\Delta\tau_2$ in fs	50
σ_1 in fs	250
σ_2 in fs	250
ω_1 in THz	3.0
ω_2 in THz	2.5
A in MV/cm	0.3
$\tau_{i,j}$ in fs	1500
t_s in fs	-4000
t_e in fs	4000
Δt in fs	1.0

Table 7.3: Summary of general parameters used in the density matrix propagation.

[31, 149]

$$P^{(3)}(t) = \iint dt_1 dt_2 R^{(3)}(t_1, t_2) E_B(t - t_2) E_A(t - t_1 - t_2) E_{\text{nir}}(t), \quad (7.17)$$

and the third order response function [31, 149]

$$R^{(3)}(t_1, t_2) = -\frac{1}{\hbar^2} \text{tr} \langle \Pi(t_1 + t_2) [\mu(t_1) [\mu(0), \rho_{\text{eq}}]] \rangle, \quad (7.18)$$

where ρ_{eq} is the equilibrium density matrix. Expanding commutators yields:

$$\begin{aligned} R^{(3)}(t_1, t_2) = & -\frac{1}{\hbar^2} \text{tr} \langle \Pi(t_1 + t_2) \mu(t_1) \mu(0) \rho_{\text{eq}} - \Pi(t_1 + t_2) \mu(t_1) \rho_{\text{eq}} \mu(0) \\ & + \Pi(t_1 + t_2) \rho_{\text{eq}} \mu(0) \mu(t_1) - \Pi(t_1 + t_2) \mu(0) \rho_{\text{eq}} \mu(t_1) \rangle. \end{aligned} \quad (7.19)$$

For shorthand, we now designate $\Pi(t_1 + t_2)$ as Π , $\mu(0)$ as μ_0 , and $\mu(t_1)$ as μ_1 . Any TTR signal must come from one of four interactions

$$\text{tr} \langle \Pi \mu_1 \mu_0 \rho_{\text{eq}} \rangle; \quad \text{tr} \langle \Pi \mu_1 \rho_{\text{eq}} \mu_0 \rangle; \quad \text{tr} \langle \Pi \rho_{\text{eq}} \mu_0 \mu_1 \rangle; \quad \text{tr} \langle \Pi \mu_0 \rho_{\text{eq}} \mu_1 \rangle. \quad (7.20)$$

This leads to 24 possible interactions plus their complex conjugates, all of which are shown in Fig. 7.14 with double-sided Feynman diagrams. From this point forward, we will, by convention, only consider the 24 terms in Fig. 7.14 and not their complex conjugates, as the conjugate terms do not carry any extra information. Adding the 24 terms together yields 12 distinct terms plus their complex conjugates:

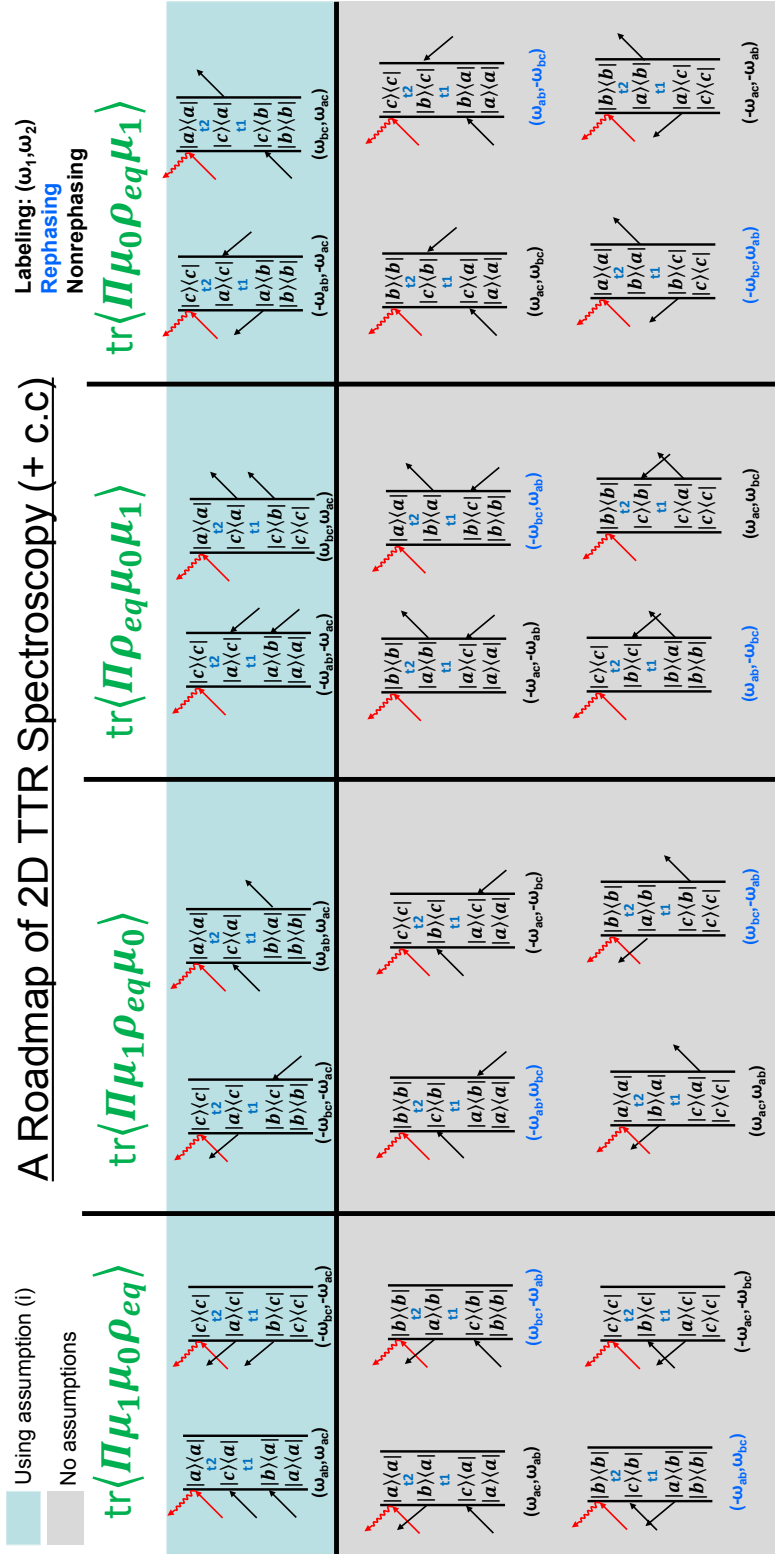


Figure 7.14: Possible third-order interactions in 2D-TTR spectroscopy.

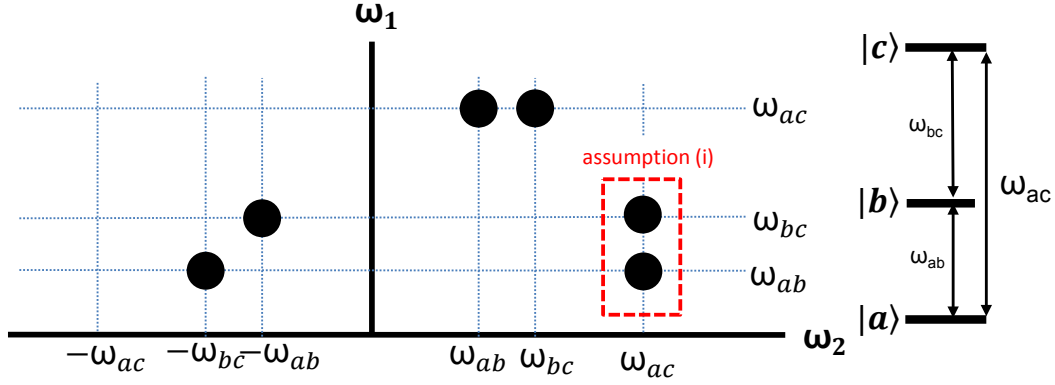


Figure 7.15: The 2D-TTR spectra possible in the interaction with a three-level system.

$$\begin{aligned}
 R^{(3)}(t_1, t_2) \propto & \mu_{ab}\mu_{bc}\Pi_{ac}((\rho_{bb} - \rho_{aa})e^{-i\omega_{ab}t_1}e^{-i\omega_{ac}t_2} - (\rho_{cc} - \rho_{bb})e^{-i\omega_{bc}t_1}e^{-i\omega_{ac}t_2}) \\
 & + \mu_{ac}\mu_{bc}\Pi_{ab}(\rho_{cc} - \rho_{aa})e^{-i\omega_{ac}t_1}e^{-i\omega_{ab}t_2} - \mu_{ab}\mu_{ac}\Pi_{bc}(\rho_{bb} - \rho_{aa})e^{-i\omega_{ab}t_1}e^{+i\omega_{bc}t_2} \\
 & + \mu_{bc}\mu_{ac}\Pi_{ab}(\rho_{cc} - \rho_{bb})e^{-i\omega_{bc}t_1}e^{+i\omega_{ab}t_2} - \mu_{ac}\mu_{ab}\Pi_{cb}(\rho_{cc} - \rho_{aa})e^{-i\omega_{ac}t_1}e^{-i\omega_{bc}t_2} \\
 & + c.c.,
 \end{aligned} \tag{7.21}$$

where ρ_{xx} is a diagonal entry in the equilibrium density matrix corresponding to the population of state x . We now define the population, p_x , and population difference, p_{xy} ,

$$\rho_{xx} = p_x, \quad p_{xy} = p_y - p_x, \tag{7.22}$$

and plug these in the response function:

$$\begin{aligned}
 R^{(3)}(t_1, t_2) \propto & \mu_{ab}\mu_{bc}\Pi_{ac}(p_{ab}e^{-i\omega_{ab}t_1}e^{-i\omega_{ac}t_2} - p_{bc}e^{-i\omega_{bc}t_1}e^{-i\omega_{ac}t_2}) \\
 & + \mu_{ac}\mu_{bc}\Pi_{ab}p_{ac}e^{-i\omega_{ac}t_1}e^{-i\omega_{ab}t_2} - \mu_{ab}\mu_{ac}\Pi_{bc}p_{ab}e^{-i\omega_{ab}t_1}e^{+i\omega_{bc}t_2} \\
 & + \mu_{bc}\mu_{ac}\Pi_{ab}p_{bc}e^{-i\omega_{bc}t_1}e^{+i\omega_{ab}t_2} - \mu_{ac}\mu_{ab}\Pi_{cb}p_{ac}e^{-i\omega_{ac}t_1}e^{-i\omega_{bc}t_2} + c.c.
 \end{aligned} \tag{7.23}$$

The THz pulses used in this work have a modest bandwidth of 0.5-4.0 THz. This is less than the lowest energy vibration in all three molecules studied. Thus, the THz

light contains sufficient bandwidth to excite ω_{ab} and ω_{bc} , but not ω_{ac} . Including this assumption, hereafter called assumption (i), we are left with

$$R^{(3)}(t_1, t_2) \propto \mu_{ab}\mu_{bc}\Pi_{ac}(p_{ab}e^{-i\omega_{ab}t_1}e^{-i\omega_{ac}t_2} - p_{bc}e^{-i\omega_{bc}t_1}e^{-i\omega_{ac}t_2}) + c.c. \quad (7.24)$$

2D-TTR spectra for these interactions are shown in Fig. 7.15. With assumption (i) we expect two non-rephasing off-diagonal peaks for each triad, while with no assumptions we expect 4 non-rephasing and 2 rephasing peaks.

If we assume a very small angle between the two THz beams, we can determine the direction of various Liouville pathways from the Feynman diagrams. In this geometry, all three beams are in the same plane and the angle between \vec{k}_A and \vec{k}_B is bisected by \vec{k}_{nir} . For the 8 pathways observed in this work, the direction of the nonlinear signal is $\vec{k}_A + \vec{k}_B + \vec{k}_{nir}$ and $-\vec{k}_A - \vec{k}_B + \vec{k}_{nir}$. If we assume $|\vec{k}_A| = |\vec{k}_B|$ then these signals will be collinear with \vec{k}_{nir} . For the 16 remaining Liouville pathways this is not the case. They will have directions given by $\vec{k}_A - \vec{k}_B + \vec{k}_{nir}$ and $-\vec{k}_A + \vec{k}_B + \vec{k}_{nir}$. These signals would be slightly offset from \vec{k}_{nir} . However, due to the high divergence of THz light, the two THz beams will be nearly collinear at the sample and these various signals will overlap with \vec{k}_{nir} .

*Chapter 8***BROADBAND 2D THZ-THZ-RAMAN ANALYSIS OF BROMOFORM**

The initial 2D THz-THz-Raman spectrometer presented in Chapter 7 was restricted to <4 THz of bandwidth by the quartz cuvette that holds the liquid samples. Ultimately, this limited the measured signals to non-rephasing peaks with low frequency THz transitions on the f_1 axis. With perturbation theory, however, we showed that other rephasing and non-rephasing 2D-TTR peaks are possible if the THz pulses can bridge the $a \rightarrow c$ transition in the generalized three-level system (Fig. 7.15). In this chapter, we implement a diamond cuvette that extends the bandwidth at the sample to ~0.5-8.5 THz and improve the THz/800 nm pulse overlap with a polarizer beam combiner. We retake the spectrum of liquid bromoform and observe the rephasing and non-rephasing peaks predicted by perturbation theory. We assign these new features to coupling within the thermally populated ladder of intramolecular vibrational states. To the best of our knowledge, this is the first measurement of a nonlinear THz rephasing (photon-echo) signal in a liquid. We also analyze the mechanisms that cause the forbidden multi-quantum transitions in general 2D-TTR spectra, and for bromoform in particular. We show that 2D-TTR spectra are sensitive to vibrational anharmonicity, nonlinearities in the molecular dipole moment and polarizability as a function of the vibrational coordinates, coherence transfer processes with the surrounding bath, and intermolecular coupling (vibrational excitons). Finally, the two-pulse terahertz Kerr effect (quadratic electro-optic effect) in diamond is used to determine the electric field of the THz pulses and instrument response function. All simulations presented in this chapter were done in collaboration with Dr. Ralph Welsch and Professor Thomas Miller III.

A manuscript detailing the results presented in this chapter is in preparation:

Finneran, I. A., Welsch, R., Allodi, M. A., Miller, T. F. & Blake, G. A. Broadband 2D THz-THz-Raman photon-echo spectroscopy of molecular vibrations in liquids. *in preparation* (2017).

8.1 Introduction

2D infrared spectroscopy has revolutionized our understanding of liquids, revealing processes such as the structural fluctuations [177] and vibrational coupling [34] in water, and the complex pathways of amyloid (protein aggregate) formation linked to many human diseases [178]. In Chapter 7 we developed a new 2D THz-THz-Raman spectroscopy, with the goal of extending these methods to THz frequencies (0.1 - 10 THz). As we have shown in previous chapters, this region is appealing for liquid studies, as it is resonant with many of the motions that govern solvation, chemical reactivity, and liquid bulk properties.

A central feature of 2D nonlinear spectroscopies in the infrared and optical has been the analysis of rephasing (photon-echo) signals, which uncover the spectral broadening mechanisms and corresponding environmental heterogeneity of a sample [31, 149]. Rephasing signals have also been recently measured with 2D Raman-THz spectroscopy in liquid water and water-salt solutions, revealing transient (~ 100 fs) heterogeneities in the hydrogen bond network [11, 12]. In the 2D THz-THz-Raman spectra that we presented in Chapter 7, however, rephasing signals are not present, due to the limited THz bandwidth of the experiment. There are also other non-rephasing signals predicted by perturbation theory (Fig. 7.15, 7.14) above the diagonal in the first quadrant of the 2D spectra that we did not observe.

In this chapter, the THz pulse bandwidth has been extended at the sample to 0.5-8.5 THz with a diamond window on the sample cuvette. We have also employed a polarizer beam combiner to optimize the THz and Raman pulse overlap. A detailed description of this implementation is given in the Methods section, and an updated instrument schematic is shown in Fig. 8.7. This bandwidth reveals many new rephasing and non-rephasing peaks in liquid bromoform, which we analyze with the RDM model developed in Chapter 7. We also use the 2D-TTR response of the diamond window to determine the electric fields of the THz pulses and the instrument response function.

8.2 Results and Discussion

Analysis of Liquid Bromoform

With the extended bandwidth 2D-TTR experiment, we observe a complicated set of vibrational coherences on the t_1 and t_2 axes, due to excitation of the ν_6 and ν_3 vibrational modes of bromoform (Fig. 8.1c). The rephasing contribution to the total signal (Fig 8.1b, trace T-3 and Fig 8.1d) is weak, but above the noise of the

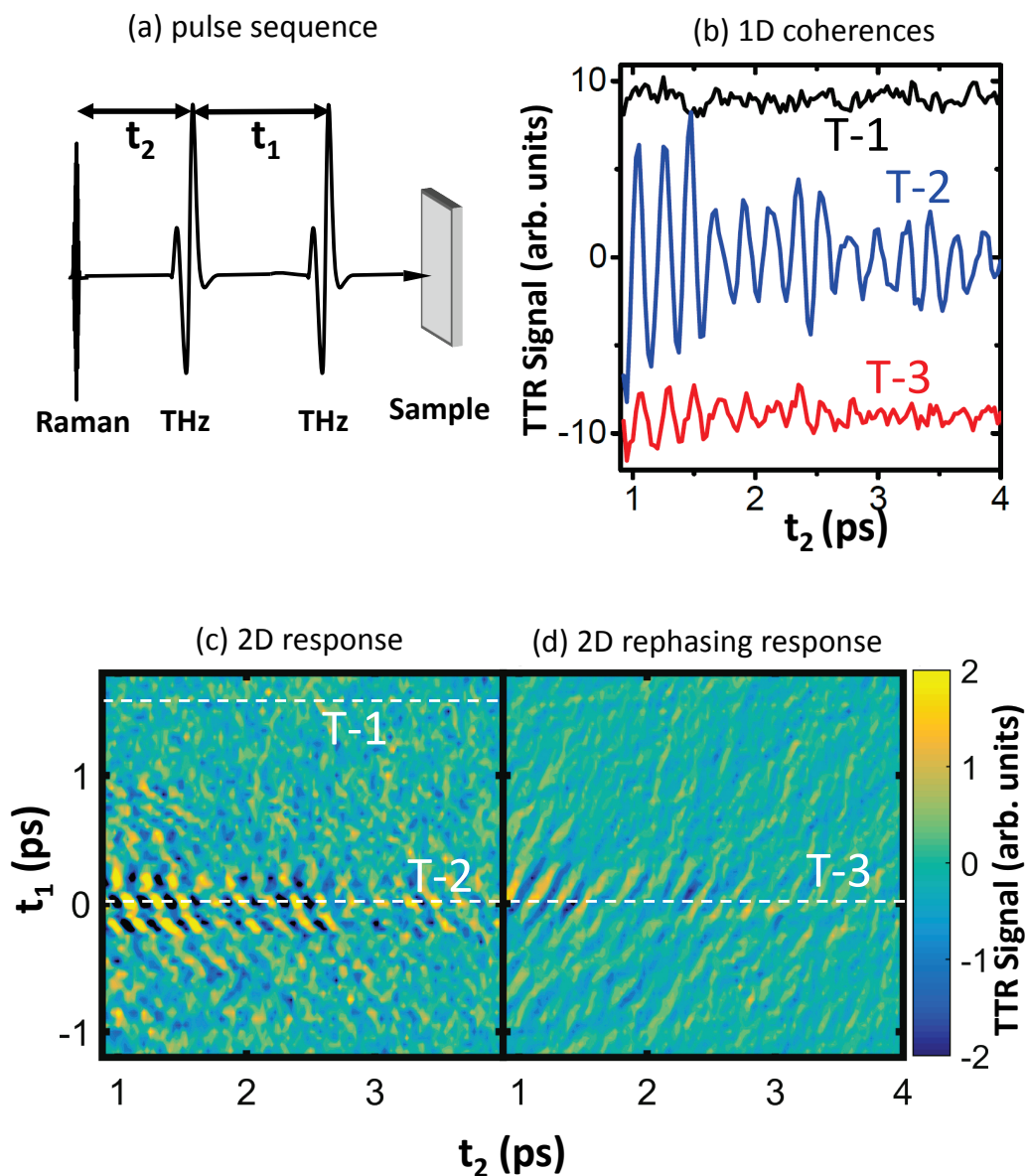


Figure 8.1: An overview of the experiment and results. (a) The 2D-TTR pulse sequence consists of two THz pulses followed by a nonresonant Raman probe pulse. (b) 1D cuts of the total signal (T-2) and rephasing signal (T-3) from liquid bromoform as compared to the noise (T-1). (c) The total 2D-TTR response of bromoform after detrending the orientational response reveals coherences on both axes. (d) The 2D-TTR rephasing response of bromoform is extracted from the total signal.

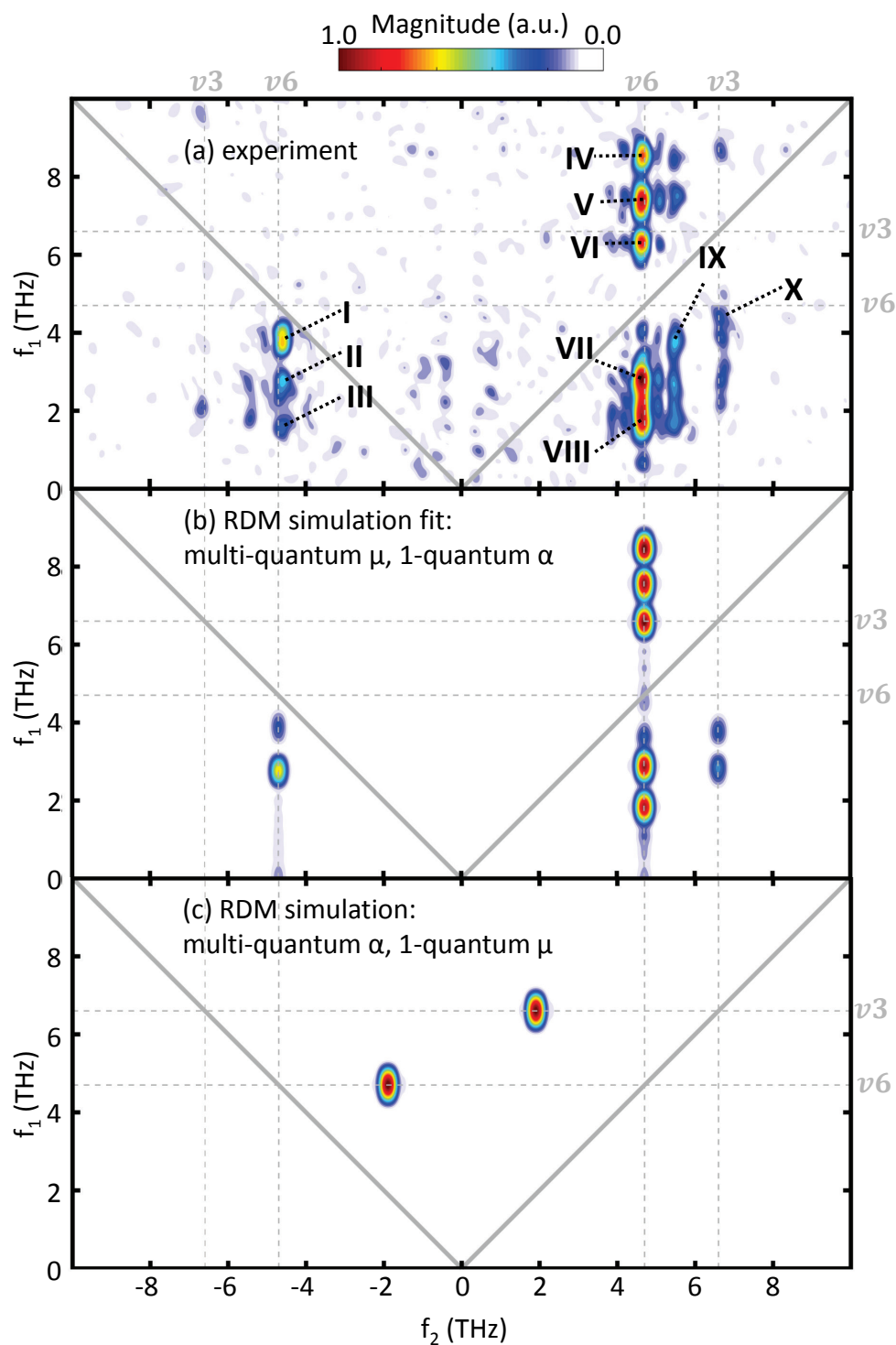


Figure 8.2: (a) The 2D FFT of the bromoform response. Several features have been labeled with Roman numerals and the 1-quantum positions of the ν_6 and ν_3 modes are indicated with dashed gray lines (b) An RDM simulation fit of the spectrum, with multi-quantum dipole couplings and 1-quantum polarizability couplings. (c) Switching the dipole and polarizability couplings in (b) leads to a qualitatively different spectrum.

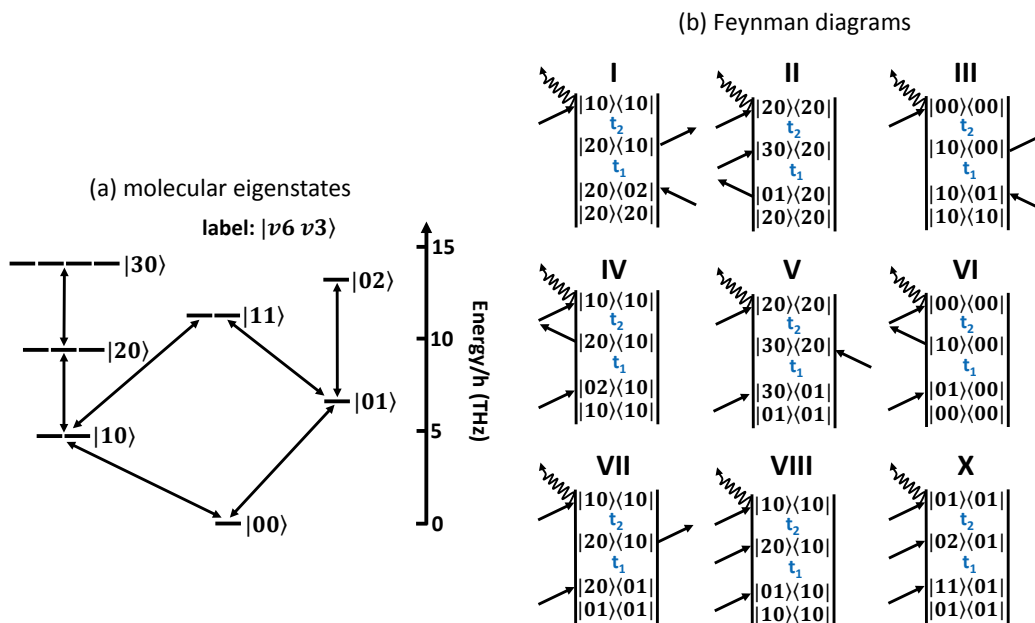


Figure 8.3: (a) Eigenstates and (b) representative Feynman diagrams that likely contribute to the labeled features of the experimental spectrum shown in Fig. 8.2a.

measurement (Fig 8.1b, trace T-1). This is the first measurement of a nonlinear THz rephasing signal in a liquid, to the best of our knowledge, and it enables the investigation of line broadening mechanisms. In this case, the dephasing rates for the rephasing and non-rephasing signals are similar, which is consistent with a homogeneously broadened sample.

The absolute value FFT of the time domain response is shown in Fig 8.2a and it reveals many off-diagonal peaks in the first and second quadrants. We note that peaks VII and VIII were observed in Chapter 7, while all other features are new. Peaks in the first quadrant, ($f_1 = \pm, f_2 = \pm$), are due to non-rephasing pathways, while peaks in the second quadrant, ($f_1 = \pm, f_2 = \mp$), arise from rephasing pathways. The frequencies of the fundamental 1-quantum transitions ν_6 and ν_3 have been marked with dashed gray lines in Fig 8.2. Qualitatively, we find that the strongest peaks align with the expected 1-quantum transitions on the f_2 axis, while the f_1 positions are distributed between 0.5-8.5 THz, likely due to multi-quantum transitions.

To interpret these results, we fit the experimental data to a RDM simulated spectrum with vibrational eigenstates up to 15 THz (Fig. 8.3a). The fundamental eigenstate energies and relative intensities were taken from the linear spectrum (Fig. 7.5), while the excited eigenstate energies and 1-quantum dipole/polarizability couplings were fixed at values consistent with a harmonic oscillator. All of the multi-quantum

dipole and polarizability couplings were fit. The parameter space was explored with a basin hopping algorithm [179] and quasi-Newton local minimizer [180]. The fitness function was calculated with an L1-norm and regularization to prevent overfitting of the data (see Methods for more details).

The resulting RDM simulated fit spectrum, Fig. 8.2b, is in moderate agreement with the experimental spectrum. A representative set of the pathways that contribute to the experimental peaks are highlighted with Feynman diagrams in Fig. 8.3b. This analysis indicates that the strongest non-rephasing peaks IV-VIII are due to multi-quantum ν_6 - ν_3 difference band transitions with the THz pulses, and 1-quantum ν_6 transitions with the Raman pulse. Each peak has a partner that shares the same set of three vibrational states (and coupling elements), but differs in the time ordering of the THz interactions, as was shown in Chapter 7 (Fig. 7.15). Examples of this behavior include peaks VII \leftrightarrow VIII, I \leftrightarrow IV, II \leftrightarrow V, and III \leftrightarrow VI. The intensity differences of the partners are dependent on the population difference of the first interaction, making peaks I-III weaker than peaks IV-VI. This comes from the population factors in the 2D-TTR response function (Equation 7.23). We note a shift in peaks VI and III not captured by the simulation that is likely due to small vibrational anharmonicities.

The simulation also shows a set of peaks near the 1-quantum ν_3 transition that matches the experimental spectrum (labeled X in Fig. 8.2a). These peaks are much weaker, since the Raman detection scheme is depolarized, while the ν_3 vibration is polarized and ν_6 is depolarized.

The off-diagonal couplings recovered from the fit confirm the differences between the THz and Raman transitions (Tables 8.1, 8.2). All of the multi-quantum polarizability couplings fit to values of near zero, while the multi-quantum dipole couplings are relatively large. Perhaps most surprising are the significant 3- and 4- quantum dipole couplings. To further illustrate this difference, a simulation with 1-quantum dipole couplings and multi-quantum polarizability couplings is shown in Fig. 8.2c. In this case, the strongest peaks are predicted at $f_2 = \pm 1.9$ THz, in complete disagreement with the experiment. Finally, a third set of peaks near $f_2 \sim 5.3$ THz (labeled IX in Fig. 8.2a) is observed in the experimental spectrum that is absent from the simulation. We do not yet know the origins of these features, but speculate that they may come from the coupling of vibrational levels above 15 THz.

Although the RDM simulations are quite useful for a phenomenological interpretation of the coherences generated in the experiment, they do not give us a direct atomistic picture. The fit shown in Fig. 8.2b, for example, indicates the presence of

forbidden THz transitions, yet is agnostic on the molecular cause of these features. Indeed, the mere existence of a 2D-TTR peak is proof of a forbidden transition, since each pathway involves at least one THz or Raman transition forbidden in the harmonic approximation [12, 30, 181].

In Fig. 8.4 we tabulate several possible molecular origins of forbidden transitions in 2D-TTR spectra. The simplest case is perhaps intramolecular vibrational anharmonicity (Fig. 8.4a) due to the shape of the potential energy surface, V , as a function of the normal mode coordinates of a molecule, q_i [30, 181]:

$$V = \frac{1}{2} \sum_i k_i q_i^2 + \frac{1}{3!} \sum_{i,j,k} g_{ijk} q_i q_j q_k + \dots \quad (8.1)$$

Here, k is the harmonic constant, g is the first anharmonic constant, and the summations are performed over the normal modes. In the harmonic case, only the first term is retained, leading to 1-quantum THz and Raman transitions ($\Delta\nu = \pm 1$) and evenly spaced eigenstates. Anharmonicity is introduced with the higher order terms, which make the eigenstates unevenly spaced and enable multi-quantum THz and Raman transitions ($\Delta\nu = \pm 1, \pm 2, \dots$). Generally, we expect larger vibrational anharmonicities in the intermolecular motions of liquids, such as hydrogen bonds, than the intramolecular modes measured in this chapter [11]. Indeed, previous combination and overtone measurements in the linear Raman spectrum of bromoform have shown that the vibrational anharmonicity is small for the ν_6 and ν_3 manifolds [182]. Thus, the stark contrast between the multi-quantum THz and 1-quantum Raman transitions seen in bromoform is likely not due to vibrational anharmonicity.

Forbidden transitions can also result from nonlinearities of the dipole moment ($\vec{\mu}$) and polarizability ($\tilde{\alpha}$) as a function of the vibrational coordinates (\mathbf{q}), which can be described with the Taylor expansions (Fig. 8.4b) [30, 181]

$$\begin{aligned} \vec{\mu} &= \vec{\mu}(\mathbf{q}_0) + \sum_i \left(\frac{\partial \vec{\mu}}{\partial q_i} \right)_{\mathbf{q}_0} q_i + \frac{1}{2} \sum_{i,j} \left(\frac{\partial^2 \vec{\mu}}{\partial q_i \partial q_j} \right)_{\mathbf{q}_0} q_i q_j + \dots \\ &= \vec{\mu}^{(0)} + \sum_i \vec{\mu}_i^{(1)} q_i + \sum_{i,j} \vec{\mu}_{ij}^{(2)} q_i q_j + \dots \end{aligned} \quad (8.2)$$

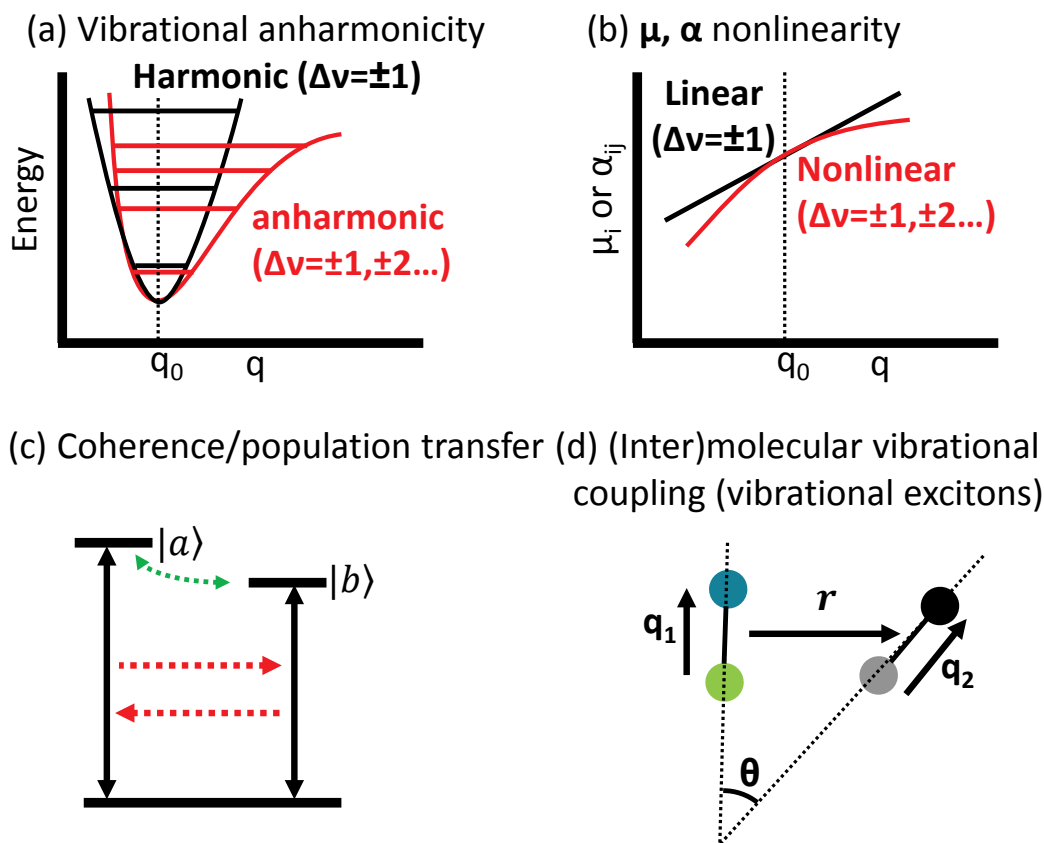


Figure 8.4: Forbidden transitions in 2D-TTR can originate from (a) intramolecular vibrational anharmonicities, (b) nonlinearities in the dipole or polarizability surfaces, (c) coherence/population transfer processes with the surrounding solvent, or (d) intermolecular coupling.

$$\begin{aligned}
 \tilde{\alpha} &= \tilde{\alpha}(\mathbf{q}_0) + \sum_i \left(\frac{\partial \tilde{\alpha}}{\partial q_i} \right)_{\mathbf{q}_0} q_i + \frac{1}{2} \sum_{i,j} \left(\frac{\partial^2 \tilde{\alpha}}{\partial q_i \partial q_j} \right)_{\mathbf{q}_0} q_i q_j + \dots \\
 &= \tilde{\alpha}^{(0)} + \sum_i \tilde{\alpha}_i^{(1)} q_i + \sum_{i,j} \tilde{\alpha}_{ij}^{(2)} q_i q_j + \dots
 \end{aligned} \tag{8.3}$$

Here, the summations are performed over the normal modes of a molecule. The zeroth order term is due to the permanent dipole moment, which produces rotational transitions, while the first order terms (linear in q_i) generate ‘allowed’ 1-quantum harmonic vibrational transitions. The nonlinear second-, third-, and fourth-order terms contribute 2-, 3- and 4- quantum transitions, respectively [30, 181]. Since the f_1 axis in a 2D-TTR spectrum is due to a THz dipole transition, a dipole nonlinearity will cause a multi-quantum f_1 transition. Similarly, multi-quantum transitions on the f_2 Raman axis are consistent with a polarizability nonlinearity. The observed

spectrum and RDM fit are therefore consistent with a dipole nonlinearity. To test this hypothesis, our collaborator, Dr. Ralph Welsch, performed a series of *ab initio* calculations on isolated bromoform molecules and found much smaller dipole nonlinearities than what was fit in the RDM simulation (Tables 8.1, 8.2). More recently, Dr. Welsch has extended the calculations to clusters of bromoform molecules to see the influence of intermolecular interactions. The preliminary results from the cluster calculations are in much better agreement with the experimental fits, with large dipole and small polarizability nonlinearities. Further analysis of the calculations is needed to confirm these exciting results.

A third possible source of forbidden transitions in 2D-TTR spectra is coherence transfer and population transfer processes (Fig. 8.4c), which have been observed in 2D infrared spectra [183]. These processes are intermolecular in nature, and result from the coupling of molecular vibrations with the surrounding solvent ‘bath’ modes of the liquid. This coupling allows for the spontaneous transfer of coherences and populations within the density matrix of the system, without the loss of phase memory. The energies of the transfers are limited to that available from the surrounding bath, or $\sim kT$, [184]. We note that these processes lead to the appearance of ‘forbidden’ multi-quantum transitions, not to their direct excitation during the light-matter interaction. This includes transitions forbidden in the harmonic approximation as well those that are symmetry forbidden. Coherence transfer is often identified with waiting time measurements, which would be possible in a 2D THz-THz-THz experiment (analogous to 2D IR) [183].

We added these processes to our phenomenological RDM simulation with the modified propagation equation [183]:

$$\frac{\partial \rho_{ab}}{\partial t} = -i\omega_{ab}\rho_{ab} + \sum_{cd} \Gamma_{ab,cd}\rho_{cd}. \quad (8.4)$$

Here, ρ is the density matrix, Γ is the (Redfield) relaxation tensor, and ω_{ab} is the transition frequency between states a and b . This entire expression is written in terms of the vibrational eigenstates of the molecular Hamiltonian (a, b, c, d). Elements in the relaxation tensor of the form $\Gamma_{ab,cd}$ correspond to coherence transfer, $\Gamma_{aa,bb}$ to population transfer, $\Gamma_{aa,aa}$ to population relaxation, and $\Gamma_{ab,ab}$ to dephasing.

Simulations of coherence transfer in a simple toy model three-level system using the updated RDM code are shown in Fig. 8.5. We found that the model is only

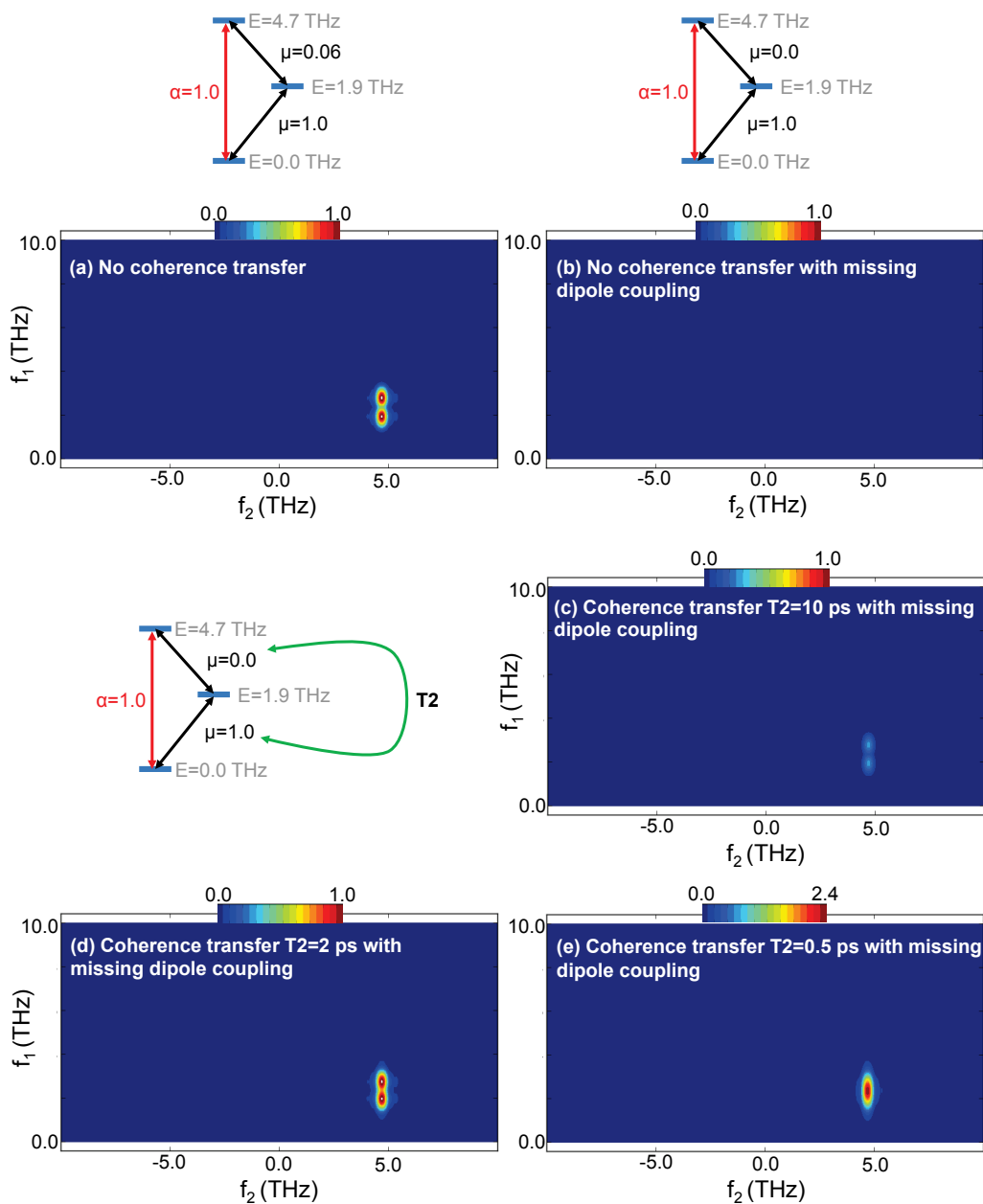


Figure 8.5: A coherence transfer toy problem using three eigenstates. (a) In a closed three level system with no coherence transfer, a doublet pattern is generated in the 2D-TTR spectrum. (b) If one of the dipole coupling elements is set to zero, then no 2D-TTR pathways are possible. (c) If a 10 ps coherence transfer is added to the system, the doublet pattern returns. (d) The doublet pattern increases in intensity for shorter coherence transfer times, but becomes motionally narrowed into a single peak (e) for times shorter than the measurement time (~ 2 ps).

sensitive to coherence transfer and not to population transfer, due to the fact that all of the intermediate states in 2D-TTR are coherences (off-diagonal in the density matrix). In Fig. 8.5a we simulated a standard three-level system that gives rise to the doublet pattern in bromoform (feature VII and VIII in Fig. 8.2). If one of the dipole couplings is set to zero (Fig. 8.5b) then no peaks are present, as expected. However, if we introduce a coherence transfer timescale $T_2=1/\Gamma_{ab,bc}$ into the system, the doublet pattern returns. The doublet intensity increases for shorter T_2 timescales, but eventually becomes motionally narrowed for timescales <1 ps and blends into a single peak. These results are quite promising, as they demonstrate how coherence transfer processes can connect a triad of eigenstates with missing or ‘forbidden’ connections. However, further simulations and fits using the full set of bromoform eigenstates were unable to reproduce the experimental spectrum. Thus, coherence transfer does not seem to be a dominant effect in the bromoform spectrum, although it may be significant in other systems.

Forbidden transitions can also result from (inter)molecular coupling (Fig. 8.4d). A detailed analysis of these effects is given in Chapter 6 of Hamm and Zanni’s book on 2D IR spectroscopy [31]. In 2D IR, these effects are often seen in the coupling of repeating functional groups in proteins, which leads to delocalized vibrons or vibrational excitons. Fundamentally, the effects are dependent on the distance and angle between the modes, as well as their intrinsic anharmonicity. Forbidden intermolecular transitions are possible in cases where the inter-mode coupling is strong and the anharmonicity is large. However, the vibrational anharmonicity is relatively small in bromoform, so we do not expect intermolecular couplings to lead to forbidden transitions.

Diamond Response

We now consider the instrument response function and bandwidth of the THz pulses used in this chapter. Traditionally, THz pulses are measured with the second-order linear electro-optic (Pockels) effect in a crystal without inversion symmetry (c.f. ZnTe, GaP), an approach that has been widely implemented for high sensitivity THz E-field detection [185]. However, the measured bandwidth is often limited by phonon absorptions and phase matching between the THz and optical light in the detection crystal [185].

In this chapter, we measure the THz electric field in diamond. With low THz dispersion, high THz transmissivity, no phonon absorptions between 0.1-15 THz, and fa-

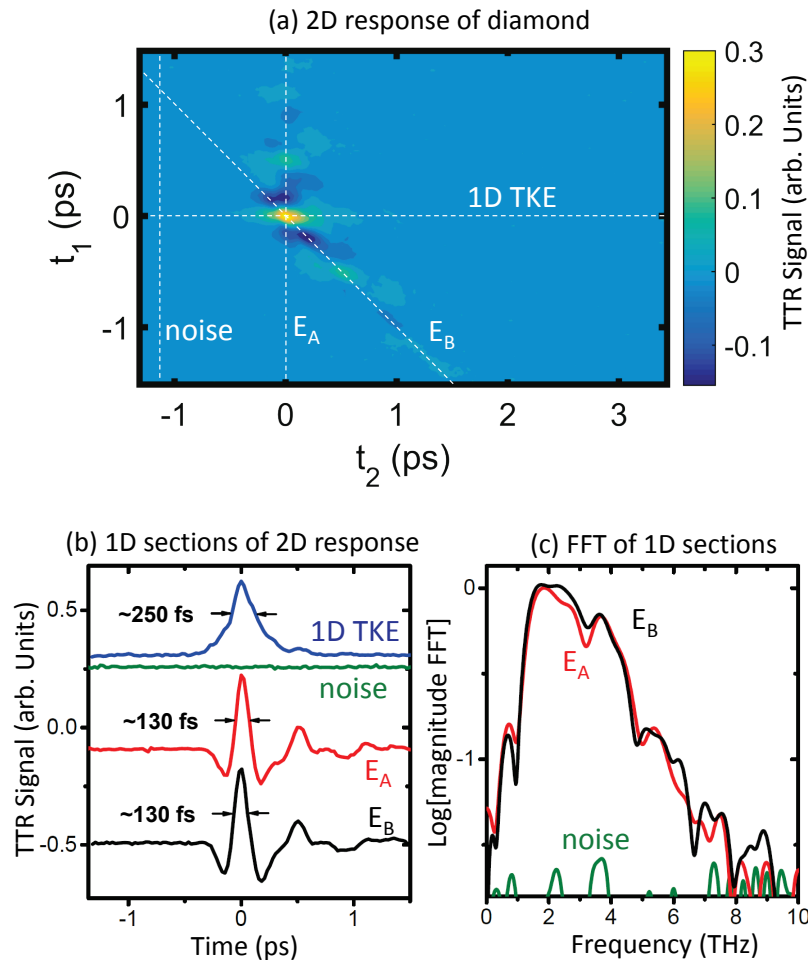


Figure 8.6: (a) The measured 2D-TTR response of diamond. (b) Several 1D sections of (a), allow us to recover the electric fields of the THz pulses. (c) Magnitude FFTs of the THz fields shown in (b).

avorable THz-800 nm phase matching, diamond is an attractive material for sampling a broadband THz field. It is centro-symmetric and exhibits no linear electro-optic response, but diamond does have a third order THz Kerr effect (quadratic electro-optic) response [37, 186]. While this third-order process is weaker than the linear electro-optic effect, it is present in all materials regardless of crystal symmetry. Furthermore, the measurement is easily implemented in the 2D-TTR experiment by shifting the diamond window into the THz focus. The measured signal is shown in Fig. 8.6a and can be described by:

$$\Delta n(t_1, t_2) = n_2 E_A(t_1 + t_2) E_B(t_2), \quad (8.5)$$

where Δn is the measured birefringence and n_2 is the nonlinear refractive index of

diamond. Several 1D sections of the 2D response are shown in Fig. 8.6b. The 1D TKE response is recovered by fixing $t_1=0$ ps and is proportional to the product of the THz fields $E_A(t_2)E_B(t_2)$. The THz field of the first pulse, E_A , is recovered by fixing $t_2=0$ ps, so the signal is proportional to $E_A(t_1)$. The field of the second THz pulse, E_B , is determined by fixing $t_1=-t_2$ with resulting signal $E_B(t_2)$. From this measurement, we find that the full width half maximum of the THz pulses in the time domain is ~ 130 fs (Fig 8.6b). We also quantify the noise of the measurement with a fourth section, far away from the diamond response. The absolute value FFT of the pulses and noise shows that the THz bandwidth extends to ~ 8.5 THz. This measurement verifies that the pulses have the necessary bandwidth to excite features I-VI in Fig. 8.2a and may be useful in future studies with intense THz pulses.

8.3 Conclusion

In conclusion, we have measured the broadband 2D-TTR spectrum of liquid bromoform. Many off-diagonal peaks are observed in the spectrum, which we have assigned to coupling between the ν_3 and ν_6 modes. A RDM fit of the measured peaks reveals allowed 1-quantum polarizability couplings and forbidden multi-quantum dipole couplings. Preliminary *ab initio* calculations indicate that these forbidden dipole couplings are due to nonlinearities in the dipole moment surface and are greatly influenced by intermolecular interactions. This unusual result highlights the importance of hybrid 2D THz-Raman studies for unraveling the complexities of low frequency molecular vibrations in liquids.

8.4 Methods

Experimental Setup

The broadband 2D THz-THz-Raman experiment is shown in Fig. 8.7, and is mostly unchanged from Chapter 7. Two THz pulses are generated from the signal and idler output of an ultrafast optical parametric amplifier (OPA) incident on two DSTMS THz emitters. The THz pulse generated by the signal is vertically polarized, while the idler THz pulse is horizontally polarized. A THz wiregrid polarizer is used to combine the two THz beams in a collinear geometry, which improves the beam overlap and co-propagation of the two THz pulses. Residual near-IR light in the THz path is blocked with a roughened TOPAS plate. The THz pulses are sent through a 7.5:1 Gaussian telescope, and then focused on the sample. The THz field strength at the sample is ~ 300 kV/cm [148]. The Raman probe pulse (~ 1 μ J, 38 fs, vertically polarized) is generated from the same laser system and focused on the

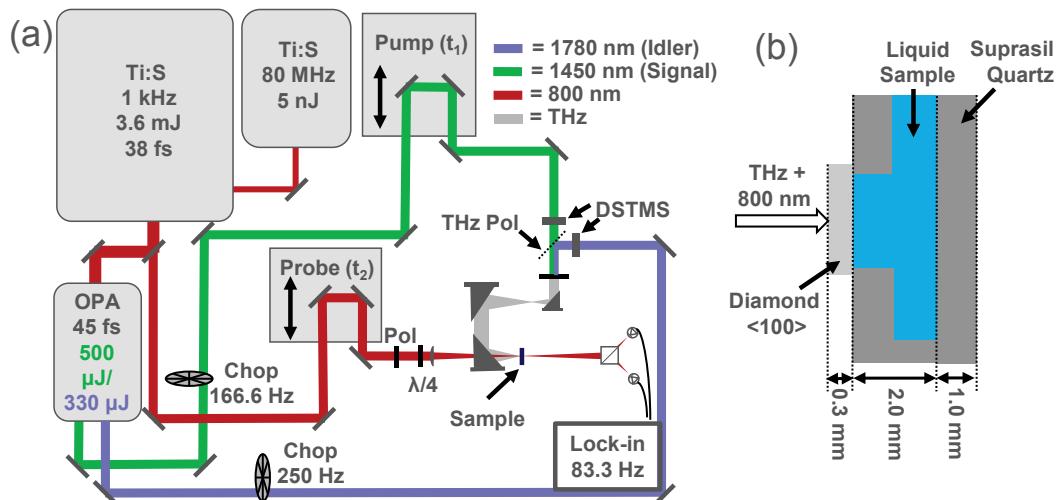


Figure 8.7: (a) A diagram of the broadband 2D-TTR experiment. A THz wiregrid polarizer (labeled ‘THz Pol’) is used to combine the THz beams. (b) Details of the sample cuvette used in the instrument. The front facing diamond window allows broadband THz transmission to the liquid sample. Both the diamond and Suprasil quartz are transparent to the 800 nm Raman probe pulse.

sample collinear to the THz beams. Heterodyne detection of the Raman probe pulse increases the signal-to-noise ratio and allows for phase-sensitive detection of the 2D-TTR response.

Liquid samples are held in a Suprasil quartz cuvette with a front facing diamond window (Fig. 8.7b). The diamond window allows broadband THz transmission to the liquid sample, while the 800 nm Raman probe passes freely through the diamond window, liquid, and back Suprasil quartz window.

Data Analysis

The raw 2D-TTR data from liquid bromoform are shown in Fig. 8.8a. The orientational response is detrended out with a single exponential fit, as demonstrated in Chapter 7. This isolates the vibrational coherences on the t_1 and t_2 axes (Fig. 8.8b). The rephasing and non-rephasing contributions to the signal are extracted with a 2D complex FFT of the total signal. The rephasing contribution is obtained by setting values in the first and third quadrant of the complex FFT to zero and then applying an inverse FFT back to the time domain (Fig 8.8c). Likewise, the non-rephasing contribution is generated by setting the second and fourth quadrant to zero and applying an inverse FFT back to the time domain (Fig. 8.8).

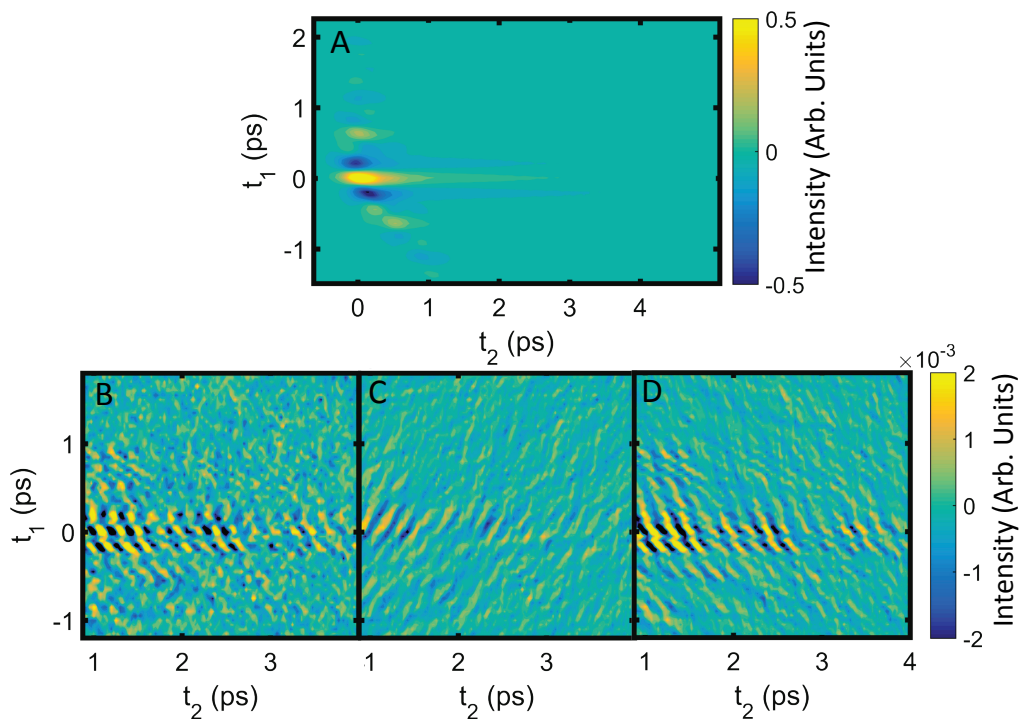


Figure 8.8: (a) The 2D-TTR response of bromoform. (b) Detrending the orientational response and shifting to larger t_2 values isolates the vibrational coherences. (c) The rephasing portion of the vibrational coherences. (d) The non-rephasing portion of the vibrational coherences.

RDM Fit Details

The simulation fits of the 2D-TTR spectrum were carried out with the third order perturbative response function and a reduced density matrix (RDM) model, based on the work in Chapter 7. The fitness of each simulated spectrum was computed with the square root of the L1-norm:

$$F = \sqrt{\sum_i (E_i - S_i)^2}, \quad (8.6)$$

where F is the fitness function, E is the experimental spectrum, S is the simulated spectrum, and the summation is performed over all points in the 2D spectrum. Each simulated and experimental spectrum was normalized to a maximum signal of 1.0 arbitrary units before this calculation. An L2-norm optimization was also tested, and it yielded nearly identical results. Regularization was also applied to the fitness

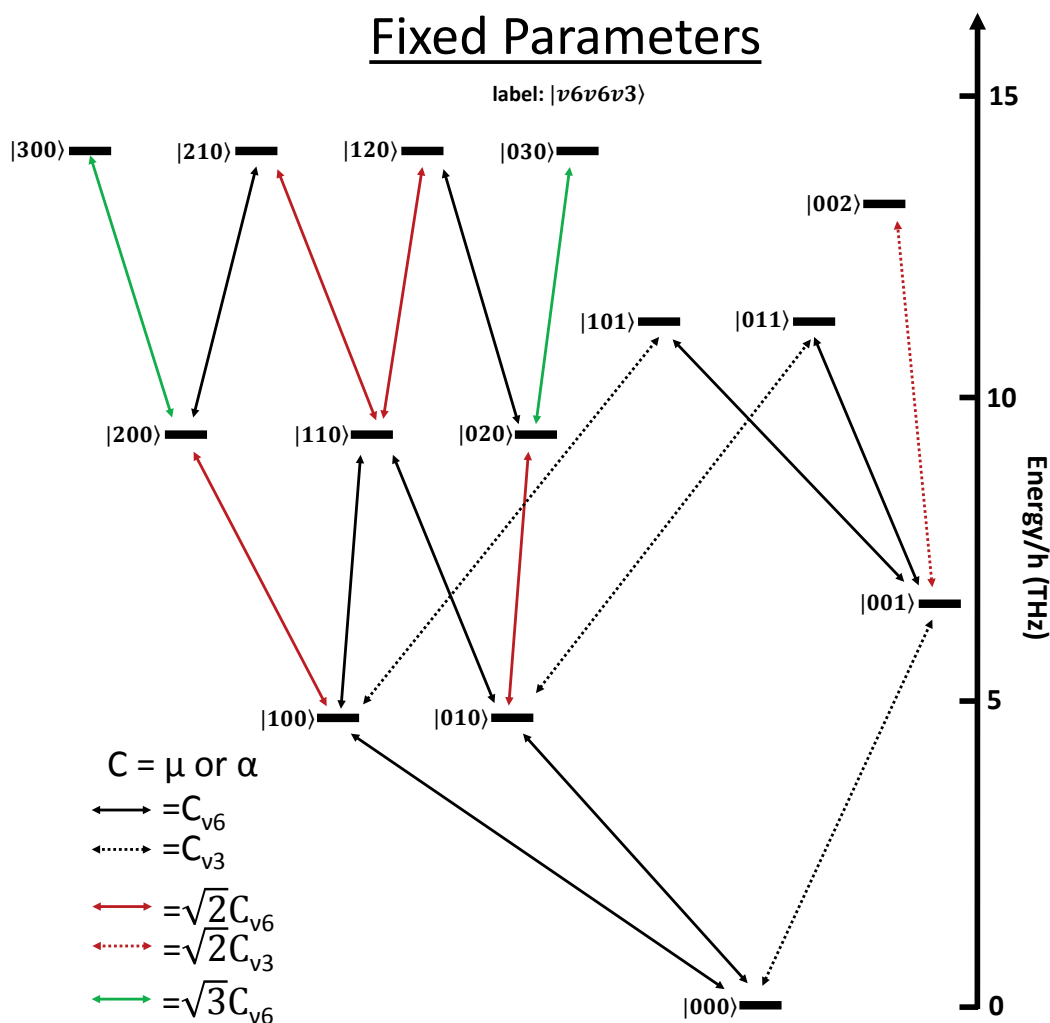


Figure 8.9: A schematic of the fixed parameters in the RDM fits.

function to prevent overfitting of the data:

$$F' = F + \alpha|\mathbf{K}|, \quad (8.7)$$

where F' is the regularized fitness function, α is the regularization parameter and \mathbf{K} is a vector containing all of the fit parameters. The value of α was maximized to penalize large fit values, without compromising the agreement between the simulated and experimental spectra. Initially, the parameter space was explored with the perturbative response function derived in Chapter 7 (Equation 7.23) and a basin-hopping algorithm [179] with a quasi-newton SLSQP local minimizer [180]. Then the couplings were further optimized with RDM simulations and the SLSQP quasi-newton minimizer [180]. RDM simulations were carried out with the same

methodology as in Chapter 7, except with a pulse duration of 150 fs and center frequency of 2.5 THz for both THz pulses.

To reduce the parameter space of the minimization, the 1-quantum couplings were fixed at values expected of a harmonic oscillator for dipole transitions: $\mu_{n-1,n} = \sqrt{n}\mu_{0,1}$ and Raman transitions: $\alpha_{n-1,n} = \sqrt{n}\alpha_{0,1}$. Here, $\mu_{0,1}$ and $\alpha_{0,1}$ are the THz and Raman coupling elements of the fundamental transitions, respectively. A full schematic of the fixed 1-quantum parameters is given in Fig. 8.9.

The relative intensities of the transition dipole moments of the ν_3 (μ_{ν_3}) and ν_6 (μ_{ν_6}) fundamentals were calculated using the ratio of the integrated absorbances of the two modes in the linear spectrum. From our previous linear data (Fig. 7.5, the ratio of the integrated absorbance is $A_{\nu_3}/A_{\nu_6} = 1.1(1)$, in agreement with the literature values [187] $A_{\nu_3}/A_{\nu_6} = 1.2$. Using our value of $A_{\nu_3}/A_{\nu_6} = 1.1$ and assuming a temperature = 295 K, the dipole coupling ratio is calculated from

$$\frac{A_{\nu_3}}{A_{\nu_6}} = \frac{\sum_{\nu_3} |n^{1/2}\mu_{\nu_3}|^2 \Delta N_n}{\sum_{\nu_6} |m^{1/2}\mu_{\nu_6}|^2 \Delta N_m} = \frac{|\mu_{\nu_3}|^2 \sum_{\nu_3} n \Delta N_n}{|\mu_{\nu_6}|^2 \sum_{\nu_6} m \Delta N_m}. \quad (8.8)$$

The sums are performed over all of the thermally populated 1-quantum transitions (including hot bands) of ν_3 and ν_6 . We truncate this sum at 15 THz of total energy. The n indices indicate the number of ν_3 quanta in the upper state and the m indices the number of ν_6 quanta in the upper state. For each transition, ΔN is the difference in population between the two states involved in each transition. We have also assumed the harmonic oscillator approximation, with the relative transition dipoles of the hot bands given by $m^{1/2}\mu_{\nu_6}$ for ν_6 and $n^{1/2}\mu_{\nu_3}$ for ν_3 , where μ_{ν_6} and μ_{ν_3} are the fundamental transition dipole moments of the two modes. Rearranging this equation we find

$$\frac{\mu_{\nu_3}}{\mu_{\nu_6}} = \left(\frac{A_{\nu_3} \sum_{\nu_6} m \Delta N_m}{A_{\nu_6} \sum_{\nu_3} n \Delta N_n} \right)^{1/2} \approx 1.6. \quad (8.9)$$

For the polarizability couplings, the ν_6 (α_{ν_6}) fundamental was fixed and the relative intensity of ν_3 (α_{ν_3}), R, was a free parameter in the fit. In this case, α_{ν_3} is expected to be smaller than α_{ν_6} , since ν_6 is depolarized, ν_3 is polarized, and the Raman probe detection is depolarized. Couplings larger than 9.5 THz were set to zero. All other multi-quantum polarizability and dipole couplings were initialized to random values between 0.0-1.0 arbitrary units and constrained to this same range in the fit. The basin-hopping minimization was run 10 times with the random initialization to

States	Quanta	HF	MP2	CCSD	Fits
$ 0\ 0\ 0\rangle, 1\ 0\ 0\rangle$	1	1.00	1.00	1.00	1.00 (fixed)
$ 0\ 0\ 0\rangle, 0\ 0\ 1\rangle$	1	1.34	1.00	1.01	1.60 (fixed)
$ 1\ 0\ 0\rangle, 0\ 0\ 1\rangle$	2	0.04	0.03	0.04	0.01
$ 2\ 0\ 0\rangle, 1\ 0\ 1\rangle$	2	0.06	0.04	0.06	0.00
$ 1\ 0\ 1\rangle, 0\ 0\ 2\rangle$	2	0.06	0.04	0.06	0.00
$ 1\ 0\ 0\rangle, 0\ 0\ 2\rangle$	3	0.00	0.00	0.00	0.22
$ 0\ 0\ 1\rangle, 2\ 0\ 0\rangle$	3	0.01	0.02	0.01	0.43
$ 1\ 0\ 1\rangle, 3\ 0\ 0\rangle$	3	0.01	0.03	0.02	0.12
$ 0\ 0\ 1\rangle, 3\ 0\ 0\rangle$	4	-	-	-	0.04
$ 2\ 0\ 0\rangle, 0\ 0\ 2\rangle$	4	-	-	-	0.22

Table 8.1: Calculated and fit dipole matrix elements relative to $\mu_{|000\rangle,|100\rangle}$. Calculations were performed by Dr. Ralph Welsch. The basis set employed is always aug-cc-pVTZ and all results are for isolated bromoform monomers. In the experimental fits, all couplings that connect states of the same energy and change in quanta were constrained to the same value (e.g. $\mu_{|001\rangle,|200\rangle}$, $\mu_{|001\rangle,|110\rangle}$, $\mu_{|001\rangle,|020\rangle}$).

States	Quanta	HF	MP2	CCSD (num.)	Fits
$ 0\ 0\ 0\rangle, 1\ 0\ 0\rangle$	1	1.00	1.00	1.00	1.00 (fixed)
$ 0\ 0\ 0\rangle, 0\ 0\ 1\rangle$	1	0.92	0.80	0.84	0.06
$ 1\ 0\ 0\rangle, 0\ 0\ 1\rangle$	2	0.02	0.02	0.02	0.00
$ 2\ 0\ 0\rangle, 1\ 0\ 1\rangle$	2	0.03	0.03	0.03	0.00
$ 1\ 0\ 1\rangle, 0\ 0\ 2\rangle$	2	0.03	0.03	0.03	0.00
$ 1\ 0\ 0\rangle, 0\ 0\ 2\rangle$	3	0.00	0.00	0.03	0.00
$ 0\ 0\ 1\rangle, 2\ 0\ 0\rangle$	3	0.00	0.00	0.01	0.03
$ 1\ 0\ 1\rangle, 3\ 0\ 0\rangle$	3	0.00	0.00	0.01	0.00
$ 0\ 0\ 1\rangle, 3\ 0\ 0\rangle$	4	-	-	-	0.00
$ 2\ 0\ 0\rangle, 0\ 0\ 2\rangle$	4	-	-	-	0.00

Table 8.2: Calculated and fit polarizability matrix elements relative to $\alpha_{|000\rangle,|100\rangle}$. Calculations performed by Dr. Ralph Welsch. The basis set employed is always aug-cc-pVTZ and all results are for isolated bromoform monomers. CCSD polarizabilities are obtained by numerical differentiating the dipole moments with respect to an external electric field. In the experimental fits, all couplings that connect states of the same energy and change in quanta were constrained to the same value (e.g. $\alpha_{|001\rangle,|200\rangle}$, $\alpha_{|001\rangle,|110\rangle}$, $\alpha_{|001\rangle,|020\rangle}$).

check the robustness of the fit. A ‘temperature’ parameter of 0.1 and 10 total basin hopping iterations were used in each run. The final coupling fit is shown in Tables 8.1, 8.2. To confirm that the fit had converged, we calculated the Hessian of the fitness function and verified that there were no negative eigenvalues.

The eigenstate energies were initialized from our previous linear spectrum with

State	E (THz)	g
00⟩	0.0	1
10⟩	4.7	2
01⟩	6.6	1
20⟩	9.4	3
11⟩	11.3	2
02⟩	13.2	1
30⟩	14.1	4

Table 8.3: Eigenstate energies (E), and degeneracies (g) used in the calculations.

$\nu_6=4.76$ and $\nu_3=6.68$ and manually varied by the experimental error of ± 0.1 THz. All combination, overtone, and difference band transitions were determined assuming zero vibrational anharmonicity (equal spacing between eigenstates in a particular manifold). The resulting best fit is shown in Table 8.3.

Part IV

Conclusions and Future Directions

Chapter 9

CONCLUSIONS AND FUTURE DIRECTIONS

Altogether, this thesis has outlined a two-pronged approach to study liquids, including precision measurements of intermolecular interactions of jet-cooled clusters, and ultrafast nonlinear THz experiments on the dynamics and vibrational coupling in the condensed phase. These two methods provide complementary data sets that can be directly compared with *ab initio* and molecular dynamics simulations. In the first half, we presented initial results on the ethanol-water and ethanol-methanol dimers that reveal an interplay between weak and strong hydrogen bonding in these clusters, while in the second half, we studied the low energy vibrational coupling and reorientational dynamics of halomethane liquids.

During the course of this work, we have developed several new instruments. The Blake lab is now equipped with a free jet expansion chirped pulse Fourier transform microwave spectrometer that can collect the pure rotational spectra of gas phase molecules and clusters of molecules. Many more experiments are possible with this spectrometer beyond the initial measurements of the ethanol-water and ethanol-methanol dimers. Currently, the sample delivery system in the instrument is limited to molecules that are in the gas or liquid phase at STP with a moderate to high vapor pressure (>1 Torr). With the addition of a laser ablation source, this could be extended to molecular solids as well [54]. The spectral coverage of the instrument (8-18 GHz) is also optimized for moderately-sized clusters and molecules (~10-20 atoms). Extending the microwave electronics to lower and higher frequency will enable investigations of larger and smaller species, respectively [23, 188].

We have also implemented a decade spanning THz frequency comb using the asynchronous optical sampling (ASOPS) instrument originally built by Daniel Holland. The ~4 kHz resolution and ~2.4 THz bandwidth of the spectrometer are sufficient for vibration-rotation tunneling studies of many hydrogen bonded clusters. Unfortunately, the THz power of the instrument (~10 μW) is low, which limits the instrument sensitivity. We have recently started a collaboration with the Jarrahi group at UCLA to improve the power and sensitivity of the instrument by 10-100 \times with plasmonically-enhanced THz emitters [189]. Further improvements in the emitted THz bandwidth are possible with 800 nm pulse compression and a

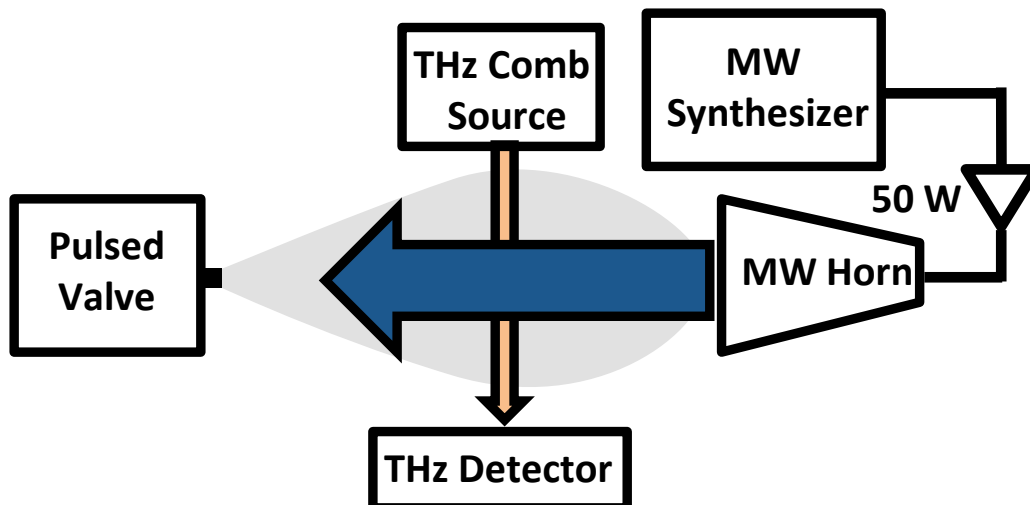


Figure 9.1: Instrument schematic of the proposed MW-THz double resonance instrument. Rotational states of molecular clusters are pumped with a continuous wave microwave source and monitored with the THz frequency comb.

reflection geometry alignment of the THz emitter [140].

While the long time-domain records presented in Chapter 5 were key to demonstrating the precision of the THz dual comb, they are not needed for normal measurements of molecular spectra. Recently, it has been shown that the full resolution of a Fourier transform infrared comb spectrometer can be extracted by detecting a single time domain ‘center-burst’ synchronized to the comb repetition rate [190]. For the ASOPS spectrometer, this is equivalent to detecting a single THz pulse record with the digitizer sample clock and total record length synchronized to the repetition rate *offset* frequency of the lasers. Interestingly, the digitizer does not need to be synchronized to the repetition rate of the lasers themselves, due to the zero phase CEP of the THz comb. If the CEP phase were non-zero, however, the digitizer would need to be synchronized to the laser repetition rate. Initial data has been collected on the THz comb instrument to confirm this functionality. Overall, this detection scheme will greatly simplify the comb spectrometer, and filter out low frequency sources of noise in the measurements.

Once the THz frequency comb spectrometer has been fully optimized in sensitivity and bandwidth, we hope to combine it with a free jet expansion for studies of molecular clusters. The analysis of vibration-rotational tunneling spectra of clusters can be challenging. For a particular set of beam conditions, multiple cluster species are often present, each with hundreds to thousands of rovibrational transitions in the

THz range. The assignment of pure rotational transitions in the microwave region are generally easier, however, because there are many fewer eigenstates to consider. To aid in the THz assignment process, we propose a MW-THz double resonance instrument, as shown in Fig. 9.1. In this approach, a continuous wave microwave source is used to pump pure rotational transitions already assigned in the CP-FTMW spectrometer. For each microwave pump frequency, the THz spectrum is collected with the frequency comb, and modulations in peak intensities are monitored. This will allow specific clusters to be ‘tagged’ with the microwave source, and greatly assist in the quantum number assignments of a THz transition. For nonpolar and dynamically averaged symmetric clusters that do not have pure rotational transitions (e.g. water trimer, tetramer, and pentamer), the microwave source could be replaced with a mid-infrared laser for IR-THz double resonance tagging.

In addition to the cluster-related instruments, we also built a 2D THz-THz-Raman spectrometer. In its present form, the instrument is capable of collecting the 2D responses of liquids and amorphous solids that are transparent to 800 nm light. Data acquisition on this instrument is quite slow, usually requiring 10 hours or more of integration to reach a sufficient signal-to-noise ratio. With the addition of a single-shot detection system, we expect an acquisition rate increase of $\sim 20\times$ [172]. Furthermore, wavefront shaping optics on the near-infrared pump beams and larger aperture DSTMS THz emitters will increase the THz field strength at the sample by at least $10\times$ [173]. Due to the *quadratic* signal scaling as a function of the THz field, this will increase the signal-to-noise ratio of the experiment by $\sim 100\times$. The field strength could be further improved with a second stage Ti:Sapphire amplifier (e.g. [173]), which would increase the near-infrared pump and corresponding THz pulse energy, but lower the laser and data acquisition repetition rate. This is advantageous for 2D-TTR, though, as the signal-to-noise ratio only scales as the *square root* of the data acquisition rate. With sufficient pulse energy and tunability (e.g. [191, 192]) the experiment could also be used for studies of vibrational ladder climbing and the coherent control of liquids and clusters.

We foresee many promising science targets with the 2D THz-THz-Raman spectrometer in the coming years. So far, the instrument has revealed vibrational coupling in pure halomethane liquids. To further disentangle the intra- and intermolecular contributions to the 2D spectra, measurements of binary mixtures would be especially informative. Nonadditive and additive features in the spectra should be indicative of inter- and intra-molecular coupling, respectively [30]. With the laser

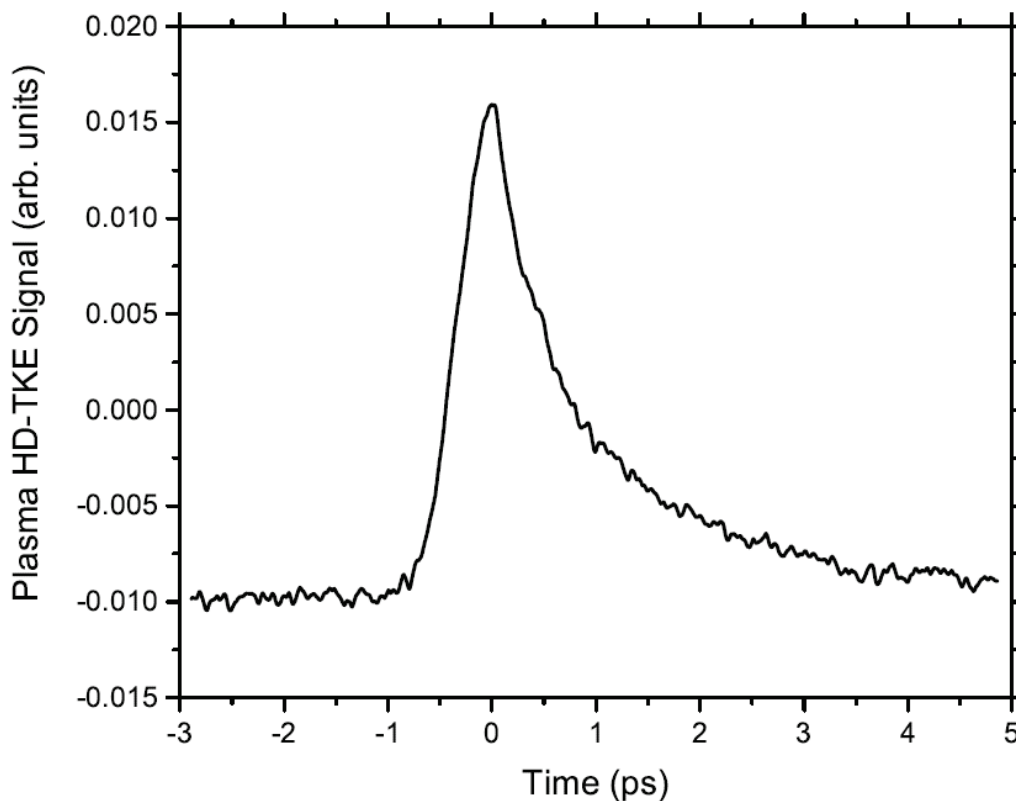


Figure 9.2: The TKE response of CS_2 measured with a two-color plasma filamentation THz source [193].

systems currently running in the Blake group, it should also be possible to align a 1D-OKE and 2D Raman-THz-THz spectrometer. A 2D THz-THz-THz instrument for waiting time measurements would also be invaluable, but more technically challenging. These data, along with temperature controlled studies, will provide a more detailed description of the off-diagonal features in the 2D-TTR spectra observed in this thesis.

A central goal of the 2D THz-THz-Raman project is to measure hydrogen-bonded liquids. The ~ 8 THz bandwidth of the instrument covers both the bending and stretching motions of hydrogen bonds and could be extended to 15 THz with HMQ-TMS organic crystal emitters [191]. However, the multi-cycle temporal profile of the THz pulses generated with these organic crystal emitters limits the time resolution. In the 2D Raman-THz-THz response of water, for example, most of the dynamics occur in the first 400 fs after excitation [11]. A possible alternative to DSTMS is two-color plasma filamentation in air, which can produce THz pulses near the ~ 50 fs transform limit of the OPA [194]. We performed initial TKE measurements with

a plasma source on liquid CS₂, and found that the signal-to-noise ratio was >10× lower than with DSTMS (Fig. 9.2). Electro-optic detection of THz pulses from both sources confirmed that the plasma peak THz electric field was ~3-4× smaller than that of DSTMS. Nevertheless, with proper optimization of the plasma source and THz focusing, it should be possible to reach 4 MV/cm with our laser system [194], which would be ideal for 2D-TTR spectroscopy.

A possible first target in 2D-TTR studies of hydrogen-bonding is acetic acid, which is thought to form dimers in the liquid phase. Previous OKE work on this species has revealed long-lived hydrogen bond coherences at room temperature that will be easily observed in a 2D-TTR spectrum [195]. Binary mixtures of alcohols and water are another intriguing target, due to the anomalous thermodynamic properties discussed in Chapter 3 [73]. And more long-term, we hope to measure the water of hydration around biopolymers that governs their reactivity and macromolecular structure [3].

Part V

Bibliography and Appendices

BIBLIOGRAPHY

1. Kindt, J. & Schmuttenmaer, C. Far-infrared dielectric properties of polar liquids probed by femtosecond terahertz pulse spectroscopy. *The Journal of Physical Chemistry* **100**, 10373–10379 (1996).
2. Yada, H., Nagai, M. & Tanaka, K. Origin of the fast relaxation component of water and heavy water revealed by terahertz time-domain attenuated total reflection spectroscopy. *Chemical Physics Letters* **464**, 166–170 (2008).
3. Leitner, D. M., Gruebele, M. & Havenith, M. Solvation dynamics of biomolecules: modeling and terahertz experiments. *HFSP Journal* **2**, 314–323 (2008).
4. Beevers, M., Crossley, J., Garrington, D. & Williams, G. Consideration of dielectric relaxation and the Kerr-effect relaxation in relation to the reorientational motions of molecules. *Journal of the Chemical Society, Faraday Transactions 2: Molecular and Chemical Physics* **72**, 1482–1493 (1976).
5. Turton, D. A., Senn, H. M., Harwood, T., Laphorn, A. J., Ellis, E. M. & Wynne, K. Terahertz underdamped vibrational motion governs protein-ligand binding in solution. *Nature Communications* **5** (2014).
6. Schmuttenmaer, C. A. Exploring dynamics in the far-infrared with terahertz spectroscopy. *Chemical Reviews* **104**, 1759–1780 (2004).
7. Cossel, K. C., Waxman, E. M., Finneran, I. A., Blake, G. A., Ye, J. & Newbury, N. R. Gas-phase broadband spectroscopy using active sources: progress, status, and applications [Invited]. *Journal of the Optical Society of America B* **34**, 104–129 (2017).
8. Park, G. B. & Field, R. W. Perspective: The first ten years of broadband chirped pulse Fourier transform microwave spectroscopy. *The Journal of Chemical Physics* **144**, 200901 (2016).
9. Brown, G. G., Dian, B. C., Douglass, K. O., Geyer, S. M., Shipman, S. T. & Pate, B. H. A broadband Fourier transform microwave spectrometer based on chirped pulse excitation. *Review of Scientific Instruments* **79**, 053103 (2008).
10. Vij, J., Simpson, D. & Panarina, O. Far infrared spectroscopy of water at different temperatures: GHz to THz dielectric spectroscopy of water. *Journal of Molecular Liquids* **112**, 125–135 (2004).
11. Savolainen, J., Ahmed, S. & Hamm, P. Two-dimensional Raman-terahertz spectroscopy of water. *Proceedings of the National Academy of Sciences* **110**, 20402–20407 (2013).
12. Hamm, P. & Savolainen, J. Two-dimensional-Raman-terahertz spectroscopy of water: Theory. *The Journal of Chemical Physics* **136**, 094516 (2012).

13. Keutsch, F. N. & Saykally, R. J. Water clusters: untangling the mysteries of the liquid, one molecule at a time. *Proceedings of the National Academy of Sciences* **98**, 10533–10540 (2001).
14. Hagena, O. F. Nucleation and growth of clusters in expanding nozzle flows. *Surface Science* **106**, 101–116 (1981).
15. Xu*, Y., Wijngaarden, J. V. & Jäger*, W. Microwave spectroscopy of ternary and quaternary van der Waals clusters. *International Reviews in Physical Chemistry* **24**, 301–338 (2005).
16. Boyd, R. W. *Nonlinear Optics* (Academic press, 2002).
17. Levinger, N. E. & Swafford, L. A. Ultrafast dynamics in reverse micelles. *Annual Review of Physical Chemistry* **60**, 385–406 (2009).
18. Pérez, C., Muckle, M. T., Zaleski, D. P., Seifert, N. A., Temelso, B., Shields, G. C., Kisiel, Z. & Pate, B. H. Structures of cage, prism, and book isomers of water hexamer from broadband rotational spectroscopy. *Science* **336**, 897–901 (2012).
19. Richardson, J. O., Pérez, C., Lobsiger, S., Reid, A. A., Temelso, B., Shields, G. C., Kisiel, Z., Wales, D. J., Pate, B. H. & Althorpe, S. C. Concerted hydrogen-bond breaking by quantum tunneling in the water hexamer prism. *Science* **351**, 1310–1313 (2016).
20. Fellers, R. S., Leforestier, C., Braly, L., Brown, M. & Saykally, R. Spectroscopic determination of the water pair potential. *Science* **284**, 945–948 (1999).
21. Goldman, N., Fellers, R., Brown, M., Braly, L., Keoshian, C., Leforestier, C. & Saykally, R. Spectroscopic determination of the water dimer intermolecular potential-energy surface. *The Journal of Chemical Physics* **116**, 10148–10163 (2002).
22. Goldman, N., Leforestier, C. & Saykally, R. A ‘first principles’ potential energy surface for liquid water from VRT spectroscopy of water clusters. *Philosophical Transactions of the Royal Society of London A: Mathematical, Physical and Engineering Sciences* **363**, 493–508 (2005).
23. Pérez, C., Zaleski, D. P., Seifert, N. A., Temelso, B., Shields, G. C., Kisiel, Z. & Pate, B. H. Hydrogen Bond Cooperativity and the Three-Dimensional Structures of Water Nonamers and Decamers. *Angewandte Chemie* **126**, 14596–14600 (2014).
24. Otsu, T., Ishii, K. & Tahara, T. Microsecond protein dynamics observed at the single-molecule level. *Nature Communications* **6** (2015).
25. Shimizu, H. Time-Correlation Function of Molecular Random Motion and Shape of Spectral Bands. *The Journal of Chemical Physics* **43**, 2453–2465 (1965).

26. Bagchi, B. *Molecular Relaxation in Liquids* (OUP USA, 2012).
27. Zhong, Q. & Fourkas, J. T. Optical Kerr Effect Spectroscopy of Simple Liquids†. *The Journal of Physical Chemistry B* **112**, 15529–15539 (2008).
28. Kubo, R. The fluctuation-dissipation theorem. *Reports on Progress in Physics* **29**, 255 (1966).
29. Tanimura, Y. & Mukamel, S. Two-dimensional femtosecond vibrational spectroscopy of liquids. *The Journal of Chemical Physics* **99**, 9496–9511 (1993).
30. Tokmakoff, A., Lang, M., Larsen, D., Fleming, G., Chernyak, V. & Mukamel, S. Two-dimensional Raman spectroscopy of vibrational interactions in liquids. *Physical Review Letters* **79**, 2702 (1997).
31. Hamm, P. & Zanni, M. *Concepts and Methods of 2D Infrared Spectroscopy* (Cambridge University Press, 2011).
32. Zanni, M. T. & Hochstrasser, R. M. Two-dimensional infrared spectroscopy: a promising new method for the time resolution of structures. *Current Opinion in Structural Biology* **11**, 516–522 (2001).
33. Buchanan, L. E., Dunkelberger, E. B., Tran, H. Q., Cheng, P.-N., Chiu, C.-C., Cao, P., Raleigh, D. P., de Pablo, J. J., Nowick, J. S. & Zanni, M. T. Mechanism of IAPP amyloid fibril formation involves an intermediate with a transient β -sheet. *Proceedings of the National Academy of Sciences* **110**, 19285–19290 (2013).
34. Ramasesha, K., De Marco, L., Mandal, A. & Tokmakoff, A. Water vibrations have strongly mixed intra-and intermolecular character. *Nature Chemistry* **5**, 935–940 (2013).
35. Blank, D. A., Kaufman, L. J. & Fleming, G. R. Fifth-order two-dimensional Raman spectra of CS₂ are dominated by third-order cascades. *The Journal of Chemical Physics* **111**, 3105–3114 (1999).
36. Shalit, A., Ahmed, S., Savolainen, J. & Hamm, P. Terahertz echoes reveal the inhomogeneity of aqueous salt solutions. *Nature Chemistry* (2016).
37. Hoffmann, M. C., Brandt, N. C., Hwang, H. Y., Yeh, K.-L. & Nelson, K. A. Terahertz Kerr effect. *Applied Physics Letters* **95**, 231105 (2009).
38. Finneran, I. A., Holland, D. B., Carroll, P. B. & Blake, G. A. A direct digital synthesis chirped pulse Fourier transform microwave spectrometer. *Review of Scientific Instruments* **84**, 083104 (2013).
39. McGuire, B. A., Carroll, P. B., Loomis, R. A., Finneran, I. A., Jewell, P. R., Remijan, A. J. & Blake, G. A. Discovery of the interstellar chiral molecule propylene oxide (CH₃CHCH₂O). *Science* **352**, 1449–1452 (2016).

40. Steber, A. L., Neill, J. L., Zaleski, D. P., Pate, B. H., Lesarri, A., Bird, R. G., Vaquero-Vara, V. & Pratt, D. W. Structural studies of biomolecules in the gas phase by chirped-pulse Fourier transform microwave spectroscopy. *Faraday Discussions* **150**, 227–242 (2011).
41. Dian, B. C., Brown, G. G., Douglass, K. O. & Pate, B. H. Measuring Picosecond Isomerization Kinetics via Broadband Microwave Spectroscopy. *Science* **320**, 924–928 (2008).
42. Patterson, D., Schnell, M. & Doyle, J. M. Enantiomer-specific detection of chiral molecules via microwave spectroscopy. *Nature* **497**, 475–478 (2013).
43. Herbst, E. & van Dishoeck, E. F. Complex Organic Interstellar Molecules. *Annual Review of Astronomy & Astrophysics* **47**, 427–480 (Sept. 2009).
44. Dicke, R. & Romer, R. Pulse techniques in microwave spectroscopy. *Review of Scientific Instruments* **26**, 915–928 (1955).
45. Ekkers, J. & Flygare, W. Pulsed microwave Fourier transform spectrometer. *Review of Scientific Instruments* **47**, 448–454 (1976).
46. Balle, T. & Flygare, W. Fabry–Perot cavity pulsed Fourier transform microwave spectrometer with a pulsed nozzle particle source. *Review of Scientific Instruments* **52**, 33–45 (1981).
47. Obenchain, D. A., Elliott, A. A., Steber, A. L., Peebles, R. A., Peebles, S. A., Wurrey, C. J. & Guirgis, G. A. Rotational spectrum of three conformers of 3, 3-difluoropentane: Construction of a 480MHz bandwidth chirped-pulse Fourier-transform microwave spectrometer. *Journal of Molecular Spectroscopy* **261**, 35–40 (2010).
48. Reinhold, B., Finneran, I. A. & Shipman, S. T. Room temperature chirped-pulse Fourier transform microwave spectroscopy of anisole. *Journal of Molecular Spectroscopy* **270**, 89–97 (2011).
49. Grubbs, G. S., Dewberry, C. T., Etchison, K. C., Kerr, K. E. & Cooke, S. A. A search accelerated correct intensity Fourier transform microwave spectrometer with pulsed laser ablation source. *Review of Scientific Instruments* **78**, 096106–096106 (2007).
50. Shirar, A. J., Wilcox, D. S., Hotopp, K. M., Storck, G. L., Kleiner, I. & Dian, B. C. Impact of Molecular Conformation on Barriers to Internal Methyl Rotation: The Rotational Spectrum of m-Methylbenzaldehyde. *The Journal of Physical Chemistry A* **114**, 12187–12194 (2010).
51. Marshall, M. D., Leung, H. O., Scheetz, B. Q., Thaler, J. E. & Muentert, J. S. A chirped pulse Fourier transform microwave study of the refrigerant alternative 2, 3, 3, 3-tetrafluoropropene. *Journal of Molecular Spectroscopy* **266**, 37–42 (2011).

52. Thomas, J., Yiu, J., Rebling, J., Jaeger, W. & Xu, Y. Chirped-Pulse and Cavity Based Fourier Transform Microwave Spectroscopy of a Chiral Epoxy Ester: Methyl Glycidate. *The Journal of Physical Chemistry A* (2013).
53. Stephens, S. L. & Walker, N. R. Determination of nuclear spin-rotation coupling constants in CF₃I by chirped-pulse Fourier-transform microwave spectroscopy. *Journal of Molecular Spectroscopy* **263**, 27–33 (2010).
54. Mata, S., Peña, I., Cabezas, C., López, J. & Alonso, J. A broadband Fourier-transform microwave spectrometer with laser ablation source: The rotational spectrum of nicotinic acid. *Journal of Molecular Spectroscopy* **280**, 91–96 (2012).
55. Wilcox, D. S., Hotopp, K. M. & Dian, B. C. Two-Dimensional Chirped-Pulse Fourier Transform Microwave Spectroscopy. *The Journal of Physical Chemistry A* **115**, 8895–8905 (2011).
56. Analog Devices. *AD9914 Data Sheet* http://www.analog.com/static/imported-files/data_sheets/AD9914.pdf. May 2013.
57. Cooper, K. B., Dengler, R. J., Llombart, N., Thomas, B., Chattopadhyay, G. & Siegel, P. H. THz imaging radar for standoff personnel screening. *IEEE Transactions on Terahertz Science and Technology* **1**, 169–182 (2011).
58. Alekseev, E., Motiyenko, R. & Margulès, L. *DDS-Based Fast Scan Spectrometer in 65th International Symposium On Molecular Spectroscopy* (2010).
59. Drouin, B. J., Tang, A., Schlecht, E., Brageot, E., Gu, Q. J., Ye, Y., Shu, R., Frank Chang, M.-c. & Kim, Y. A CMOS millimeter-wave transceiver embedded in a semi-confocal Fabry-Perot cavity for molecular spectroscopy. *The Journal of Chemical Physics* **145**, 074201 (2016).
60. Bird, R. G., Neill, J. L., Alstadt, V. J., Young, J. W., Pate, B. H. & Pratt, D. W. Ground State ¹⁴N Quadrupole Couplings in the Microwave Spectra of N, N'-Dimethylaniline and 4, 4'-Dimethylaminobenzonitrile. *The Journal of Physical Chemistry A* **115**, 9392–9398 (2011).
61. Pena, I., Daly, A. M., Cabezas, C., Mata, S., Bermudez, C., Nino, A., Lopez, J. C., Grabow, J.-U. & Alonso, J. L. Disentangling the Puzzle of Hydrogen Bonding in Vitamin C. *The Journal of Physical Chemistry Letters* (2013).
62. Jahn, M. K., Dewald, D. A., Wachsmuth, D., Grabow, J.-U. & Mehrotra, S. C. Rapid capture of large amplitude motions in 2, 6-difluorophenol: High-resolution fast-passage FT-MW technique. *Journal of Molecular Spectroscopy* **280**, 54–60 (2012).
63. Groner, P., Albert, S., Herbst, E., De Lucia, F. C., Lovas, F. J., Drouin, B. J. & Pearson, J. C. Acetone: laboratory assignments and predictions through 620 GHz for the vibrational-torsional ground state. *The Astrophysical Journal Supplement Series* **142**, 145 (2002).

64. Swalen, J. & Costain, C. Internal rotation in molecules with two internal rotors: Microwave spectrum of acetone. *The Journal of Chemical Physics* **31**, 1562 (1959).
65. Lovas, F. & Groner, P. Microwave spectra of mono-¹³C substituted acetone, (CH₃)₂CO. *Journal of Molecular Spectroscopy* **236**, 173–177 (2006).
66. Steber, A. L., Harris, B. J., Neill, J. L. & Pate, B. H. An arbitrary waveform generator based chirped pulse Fourier transform spectrometer operating from 260 to 295 GHz. *Journal of Molecular Spectroscopy* **280**, 3–10 (2012).
67. Finneran, I. A., Carroll, P. B., Allodi, M. A. & Blake, G. A. Hydrogen bonding in the ethanol–water dimer. *Physical Chemistry Chemical Physics* **17**, 24210–24214 (2015).
68. Seifert, N. A., Finneran, I. A., Perez, C., Zaleski, D. P., Neill, J. L., Steber, A. L., Suenram, R. D., Lesarri, A., Shipman, S. T. & Pate, B. H. AUTOFIT, an automated fitting tool for broadband rotational spectra, and applications to 1-hexanal. *Journal of Molecular Spectroscopy* **312**, 13–21 (2015).
69. Desiraju, G. R. & Steiner, T. *The weak hydrogen bond: in structural chemistry and biology* (Oxford University Press on Demand, 2001).
70. Steiner, T. & Desiraju, G. R. Distinction between the weak hydrogen bond and the van der Waals interaction. *Chemical Communications*, 891–892 (1998).
71. Arunan, E., Desiraju, G. R., Klein, R. A., Sadlej, J., Scheiner, S., Alkorta, I., Clary, D. C., Crabtree, R. H., Dannenberg, J. J., Hobza, P., *et al.* Definition of the hydrogen bond (IUPAC Recommendations 2011). *Pure and Applied Chemistry* **83**, 1637–1641 (2011).
72. Masella, M. & Flament, J. P. Relation between cooperative effects in cyclic water, methanol / water, and methanol trimers and hydrogen bonds in methanol / water, ethanol/water, and dimethylether / water heterodimers. *The Journal of Chemical Physics* **108**, 7141–7151 (1998).
73. Juurinen, I., Nakahara, K., Ando, N., Nishiumi, T., Seta, H., Yoshida, N., Morinaga, T., Itou, M., Ninomiya, T. & Sakurai, Y. Measurement of two solvation regimes in Water-Ethanol mixtures using X-Ray Compton scattering. *Physical Review Letters* **107**, 197401 (2011).
74. Nedić, M., Wassermann, T. N., Xue, Z., Zielke, P. & Suhm, M. A. Raman spectroscopic evidence for the most stable water/ethanol dimer and for the negative mixing energy in cold water/ethanol trimers. *Physical Chemistry Chemical Physics* **10**, 5953–5956 (2008).
75. Nedić, M., Wassermann, T. N., Larsen, R. W. & Suhm, M. A. A combined Raman-and infrared jet study of mixed methanol–water and ethanol–water clusters. *Physical Chemistry Chemical Physics* **13**, 14050–14063 (2011).

76. Suzuki, S., Green, P. G., Bumgarner, R. E., Dasgupta, S., Goddard, W. A. & Blake, G. A. Benzene forms hydrogen bonds with water. *Science* **257**, 942–945 (1992).
77. Good, W. E. The inversion spectrum of ammonia. *Physical Review* **70**, 213 (1946).
78. Gordon, J. P., Zeiger, H. J. & Townes, C. H. The maser—new type of microwave amplifier, frequency standard, and spectrometer. *Physical Review* **99**, 1264 (1955).
79. Pugliano, N. & Saykally, R. Measurement of quantum tunneling between chiral isomers of the cyclic water trimer. *Science*, 1937–1937 (1992).
80. Plusquellic, D., Lovas, F., Pate, B. H., Neill, J. L., Muckle, M. T. & Remijan, A. J. Distinguishing tunneling pathways for two chiral conformer pairs of 1, 3-propanediol from the microwave spectrum. *The Journal of Physical Chemistry A* **113**, 12911–12918 (2009).
81. Ilyushin, V., Motiyenko, R., Lovas, F. & Plusquellic, D. Microwave spectrum of glycerol: Observation of a tunneling chiral isomer. *Journal of Molecular Spectroscopy* **251**, 129–137 (2008).
82. Crabtree, K. N., Martin-Drumel, M.-A., Brown, G. G., Gaster, S. A., Hall, T. M. & McCarthy, M. C. Microwave spectral taxonomy: A semi-automated combination of chirped-pulse and cavity Fourier-transform microwave spectroscopy. *The Journal of Chemical Physics* **144**, 124201 (2016).
83. Pickett, H. M. The fitting and prediction of vibration-rotation spectra with spin interactions. *Journal of Molecular Spectroscopy* **148**, 371–377 (1991).
84. Kisiel, Z. in *Spectroscopy from Space* 91–106 (Springer, 2001).
85. Frisch, M. J., Trucks, G. W., Schlegel, H. B., Scuseria, G. E., Robb, M. A., Cheeseman, J. R., Scalmani, G., Barone, V., Mennucci, B., Petersson, G. A., Nakatsuji, H., Caricato, M., Li, X., Hratchian, H. P., Izmaylov, A. F., Bloino, J., Zheng, G., Sonnenberg, J. L., Hada, M., Ehara, M., Toyota, K., Fukuda, R., Hasegawa, J., Ishida, M., Nakajima, T., Honda, Y., Kitao, O., Nakai, H., Vreven, T., Montgomery Jr., J. A., Peralta, J. E., Ogliaro, F., Bearpark, M., Heyd, J. J., Brothers, E., Kudin, K. N., Staroverov, V. N., Kobayashi, R., Normand, J., Raghavachari, K., Rendell, A., Burant, J. C., Iyengar, S. S., Tomasi, J., Cossi, M., Rega, N., Millam, J. M., Klene, M., Knox, J. E., Cross, J. B., Bakken, V., Adamo, C., Jaramillo, J., Gomperts, R., Stratmann, R. E., Yazyev, O., Austin, A. J., Cammi, R., Pomelli, C., Ochterski, J. W., Martin, R. L., Morokuma, K., Zakrzewski, V. G., Voth, G. A., Salvador, P., Dannenberg, J. J., Dapprich, S., Daniels, A. D., Farkas, O., Foresman, J. B., Ortiz, J. V., Cioslowski, J. & Fox, D. J. *Gaussian 09 Revision D.01* Gaussian Inc. Wallingford CT 2009.
86. Møller, C. & Plesset, M. S. Note on an approximation treatment for many-electron systems. *Physical Review* **46**, 618 (1934).

87. Kendall, R. A., Dunning Jr, T. H. & Harrison, R. J. Electron affinities of the first-row atoms revisited. Systematic basis sets and wave functions. *The Journal of Chemical Physics* **96**, 6796–6806 (1992).
88. Pople, J. A., Head-Gordon, M. & Raghavachari, K. Quadratic configuration interaction. A general technique for determining electron correlation energies. *The Journal of Chemical Physics* **87**, 5968–5975 (1987).
89. Barone, V. Anharmonic vibrational properties by a fully automated second-order perturbative approach. *The Journal of Chemical Physics* **122**, 014108 (2005).
90. Debrus, G. & Steiner, T. *The Weak Hydrogen Bond in Structural Chemistry and Biology* (Oxford University Press Inc., New York, 1999).
91. Kumar, R. & Skinner, J. Water simulation model with explicit three-molecule interactions. *The Journal of Physical Chemistry B* **112**, 8311–8318 (2008).
92. Kakar, R. K. & Quade, C. R. Microwave rotational spectrum and internal rotation in gauche ethyl alcohol. *The Journal of Chemical Physics* **72**, 4300–4307 (1980).
93. Bicerano, J., Schaefer III, H. F. & Miller, W. H. Structure and tunneling dynamics of malonaldehyde. A theoretical study. *Journal of the American Chemical Society* **105**, 2550–2553 (1983).
94. Hearn, J. P. I., Copley, R. V. & Howard, B. J. High-resolution spectroscopy of induced chiral dimers: A study of the dimers of ethanol by Fourier transform microwave spectroscopy. *The Journal of Chemical Physics* **123**, 134324 (2005).
95. Lovas, F. Microwave spectra of molecules of astrophysical interest. XXI. Ethanol (C₂H₅OH) and propionitrile (C₂H₅CN). *Journal of Physical and Chemical Reference Data* **11**, 251–312 (1982).
96. Dyke, T. R. & Muentner, J. Microwave spectrum and structure of hydrogen bonded water dimer. *The Journal of Chemical Physics* **60**, 2929–2930 (1974).
97. Tanaka, K., Honjo, H., Tanaka, T., Kohguchi, H., Ohshima, Y. & Endo, Y. Determination of the proton tunneling splitting of tropolone in the ground state by microwave spectroscopy. *The Journal of Chemical Physics* **110**, 1969–1978 (1999).
98. Fileti, E. E., Chaudhuri, P. & Canuto, S. Relative strength of hydrogen bond interaction in alcohol–water complexes. *Chemical Physics Letters* **400**, 494–499 (2004).
99. Finneran, I. A., Carroll, P. B., Mead, G. J. & Blake, G. A. Hydrogen bond competition in the ethanol–methanol dimer. *Physical Chemistry Chemical Physics* **18**, 22565–22572 (2016).

100. Rose, G. D. & Wolfenden, R. Hydrogen bonding, hydrophobicity, packing, and protein folding. *Annual Review of Biophysics and Biomolecular Structure* **22**, 381–415 (1993).
101. Suhm, M. A. Hydrogen bond dynamics in alcohol clusters. *Advances in Chemical Physics* **142**, 1 (2009).
102. Stockman, P. A., Blake, G. A., Lovas, F. J. & Suenram, R. D. Microwave rotation-tunneling spectroscopy of the water–methanol dimer: Direct structural proof for the strongest bound conformation. *The Journal of Chemical Physics* **107**, 3782–3790 (1997).
103. Evangelisti, L., Gou, Q., Feng, G., Caminati, W., Mead, G. J., Finneran, I. A., Carroll, P. B. & Blake, G. A. Conformational equilibrium and internal dynamics in the iso-propanol–water dimer. *Physical Chemistry Chemical Physics* **19**, 568–573 (2017).
104. Evangelisti, L. & Caminati, W. Internal dynamics in complexes of water with organic molecules. Details of the internal motions in tert-butylalcohol–water. *Physical Chemistry Chemical Physics* **12**, 14433–14441 (2010).
105. Ruoff, R., Klots, T., Emilsson, T. & Gutowsky, H. Relaxation of conformers and isomers in seeded supersonic jets of inert gases. *The Journal of Chemical Physics* **93**, 3142–3150 (1990).
106. Dunning Jr, T. H. Gaussian basis sets for use in correlated molecular calculations. I. The atoms boron through neon and hydrogen. *The Journal of Chemical Physics* **90**, 1007–1023 (1989).
107. Hartwig, H. & Dreizler, H. The microwave spectrum of trans-2, 3-dimethyloxirane in torsional excited states. *Zeitschrift für Naturforschung A* **51**, 923–932 (1996).
108. Kraitchman, J. Determination of molecular structure from microwave spectroscopic data. *American Journal of Physics* **21**, 17–24 (1953).
109. Ubbelohde, A. & Gallagher, K. Acid-base effects in hydrogen bonds in crystals. *Acta Crystallographica* **8**, 71–83 (1955).
110. Gou, Q., Feng, G., Evangelisti, L., Loru, D., Alonso, J. L., López, J. C. & Caminati, W. Ubbelohde Effect within Weak C–H... π Hydrogen Bonds: The Rotational Spectrum of Benzene–DCF₃. *The Journal of Physical Chemistry A* **117**, 13531–13534 (2013).
111. Tang, S., Majerz, I. & Caminati, W. Sizing the Ubbelohde effect: the rotational spectrum of a tert-butylalcohol dimer. *Physical Chemistry Chemical Physics* **13**, 9137–9139 (2011).
112. Pierce, L. Note on the use of ground-state rotational constants in the determination of molecular structures. *Journal of Molecular Spectroscopy* **3**, 575–580 (1959).

113. Lees, R., Lovas, F., Kirchhoff, W. & Johnson, D. Microwave Spectra of Molecules of Astrophysical Interest: III. Methanol. *Journal of Physical and Chemical Reference Data* **2**, 205–214 (1973).
114. Lovas, F. & Hartwig, H. The Microwave Spectrum of the Methanol Dimer for $K=0$ and 1 States. *Journal of Molecular Spectroscopy* **185**, 98–109 (1997).
115. Lovas, F., Suenram, R., Fraser, G., Gillies, C. & Zozom, J. The microwave spectrum of formamide–water and formamide–methanol complexes. *The Journal of Chemical Physics* **88**, 722–729 (1988).
116. Tan, X.-Q., Sun, L. & Kuczkowski, R. L. The Methanol–Ar Complex: Apparent Reduction of the Methyl Group Internal Rotation Barrier. *Journal of Molecular Spectroscopy* **171**, 248–264 (1995).
117. Lovas, F., Belov, S., Tretyakov, M. Y., Ortigoso, J. & Suenram, R. The Microwave Spectrum and Structure of the $\text{CH}_3\text{OH}:\text{CO}$ Dimer. *Journal of Molecular Spectroscopy* **167**, 191–204 (1994).
118. Schmitt, M., Küpper, J., Spangenberg, D. & Westphal, A. Determination of the structures and barriers to hindered internal rotation of the phenol–methanol cluster in the S_0 and S_1 states. *Chemical Physics* **254**, 349–361 (2000).
119. Sun, L., Tan, X.-Q., Oh, J. J. & Kuczkowski, R. L. The microwave spectrum and structure of the methanol: SO_2 complex. *The Journal of Chemical Physics* **103**, 6440–6449 (1995).
120. Fraser, G., Lovas, F. & Suenram, R. On the apparent methyl internal-rotation barrier decrease in weakly bound methanol complexes. *Journal of Molecular Spectroscopy* **167**, 231–235 (1994).
121. Kaushik, V., Takagi, K. & Matsumura, C. Microwave spectrum of CH_3OD . *Journal of Molecular Spectroscopy* **82**, 418–426 (1980).
122. Suenram, R., Lovas, F., Fraser, G., Gillies, J., Gillies, C. & Onda, M. Microwave spectrum, structure, and electric dipole moment of $\text{Ar}-\text{CH}_3\text{OH}$. *Journal of Molecular Spectroscopy* **137**, 127–137 (1989).
123. Finneran, I. A., Good, J. T., Holland, D. B., Carroll, P. B., Allodi, M. A. & Blake, G. A. Decade-spanning high-precision terahertz frequency comb. *Physical Review Letters* **114**, 163902 (2015).
124. Good, J. T., Holland, D. B., Finneran, I. A., Carroll, P. B., Kelley, M. J. & Blake, G. A. A decade-spanning high-resolution asynchronous optical sampling terahertz time-domain and frequency comb spectrometer. *Review of Scientific Instruments* **86**, 103107 (2015).
125. Cundiff, S. T. & Ye, J. *Femtosecond optical frequency comb: Principle, Operation and Applications* (Springer, 2005).

126. Rosenband, T., Hume, D., Schmidt, P., Chou, C., Brusch, A., Lorini, L., Oskay, W., Drullinger, R., Fortier, T., Stalnaker, J., *et al.* Frequency ratio of Al⁺ and Hg⁺ single-ion optical clocks; metrology at the 17th decimal place. *Science* **319**, 1808–1812 (2008).
127. Adler, F., Thorpe, M. J., Cossel, K. C. & Ye, J. Cavity-enhanced direct frequency comb spectroscopy: technology and applications. *Annual Review of Analytical Chemistry* **3**, 175–205 (2010).
128. Li, C.-H., Benedick, A. J., Fendel, P., Glenday, A. G., Kärtner, F. X., Phillips, D. F., Sasselov, D., Szentgyorgyi, A. & Walsworth, R. L. A laser frequency comb that enables radial velocity measurements with a precision of 1 cm s⁻¹. *Nature* **452**, 610–612 (2008).
129. Steinmetz, T., Wilken, T., Araujo-Hauck, C., Holzwarth, R., Hänsch, T. W., Pasquini, L., Manescau, A., D’Odorico, S., Murphy, M. T., Kentischer, T., *et al.* Laser frequency combs for astronomical observations. *Science* **321**, 1335–1337 (2008).
130. Matsuura, S., Blake, G. A., Wyss, R. A., Pearson, J. C., Kadow, C., Jackson, A. W. & Gossard, A. C. A traveling-wave THz photomixer based on angle-tuned phase matching. *Applied Physics Letters* **74**, 2872 (May 1999).
131. Crockett, N. R., Bergin, E. A., Neill, J. L., Favre, C., Schilke, P., Lis, D. C., Bell, T. A., Blake, G., Cernicharo, J., Emprechtinger, M., Esplugues, G. B., Gupta, H., Kleshcheva, M., Lord, S., Marcelino, N., McGuire, B. A., Pearson, J., Phillips, T. G., Plume, R., van der Tak, F., Tercero, B. & Yu, S. Herschel Observations of Extraordinary Sources: Analysis of the HIFI 1.2 THz Wide Spectral Survey toward Orion KL. I. Methods. *The Astrophysical Journal* **787**, 112 (2014).
132. Waters, J. W., Froidevaux, L., Harwood, R. S., Jarnot, R. F., Pickett, H. M., Read, W. G., Siegel, P. H., Cofield, R. E., Filipiak, M. J., Flower, D. A., *et al.* The earth observing system microwave limb sounder (EOS MLS) on the Aura satellite. *IEEE Transactions on Geoscience and Remote Sensing* **44**, 1075–1092 (2006).
133. Busarow, K., Blake, G., Laughlin, K., Cohen, R., Lee, Y. & Saykally, R. Tunable far infrared laser spectroscopy of van der Waals bonds: Extended measurements on the lowest sigma bend of ArHCl. *The Journal of Chemical Physics* **89**, 1268–1276 (Aug. 1988).
134. Burghoff, D., Kao, T.-Y., Han, N., Chan, C. W. I., Cai, X., Yang, Y., Hayton, D. J., Gao, J.-R., Reno, J. L. & Hu, Q. Terahertz laser frequency combs. *Nature Photonics* **78**, 035107 (2014).
135. Rösch, M., Scalari, G., Beck, M. & Faist, J. Octave-spanning semiconductor laser. *Nature Photonics* **9**, 42–47 (2015).

136. Hsieh, Y.-D., Iyonaga, Y., Sakaguchi, Y., Yokoyama, S., Inaba, H., Minoshima, K., Hindle, F., Araki, T. & Yasui, T. Spectrally interleaved, comb-mode-resolved spectroscopy using swept dual terahertz combs. *Scientific Reports* **4**, 3816 (2014).
137. Bartalini, S., Consolino, L., Cancio, P., De Natale, P., Bartolini, P., Taschin, A., De Pas, M., Beere, H., Ritchie, D., Vitiello, M., *et al.* Frequency-Comb-Assisted Terahertz Quantum Cascade Laser Spectroscopy. *Physical Review X* **4**, 021006 (2014).
138. Skryl, A., Pavelyev, D., Tretyakov, M. & Bakunov, M. High-resolution terahertz spectroscopy with a single tunable frequency comb. *Optics Express* **22**, 32276–32281 (2014).
139. Bartels, A., Cerna, R., Kistner, C., Thoma, A., Hudert, F., Janke, C. & Dekorsy, T. Ultrafast time-domain spectroscopy based on high-speed asynchronous optical sampling. *Review of Scientific Instruments* **8**, 462 (2007).
140. Hale, P., Madeo, J., Chin, C., Dhillon, S., Mangeney, J., Tignon, J. & Dani, K. 20 THz broadband generation using semi-insulating GaAs interdigitated photoconductive antennas. *Optics Express* **22**, 26358–26364 (2014).
141. Lu, Z., Campbell, P. & Zhang, X.-C. Free-space electro-optic sampling with a high-repetition-rate regenerative amplified laser. *Applied Physics Letters* **71**, 593–595 (1997).
142. Wu, Q. & Zhang, X.-C. Free-space electro-optic sampling of terahertz beams. *Applied Physics Letters* **67**, 3523–3525 (1995).
143. Holland, D. *Design, Construction, and Applications of a High-Resolution Terahertz Time-Domain Spectrometer* (Ph.D. Thesis, California Institute of Technology, 2014).
144. Good, J. T. *Design and Applications of a Decade-Spanning Terahertz Frequency Comb Spectrometer: Doppler-limited Rotational Spectroscopy of Methanol and Methanol-OD* PhD thesis (California Institute of Technology, 2016).
145. Pickett, H., Poynter, R., Cohen, E., Delitsky, M., Pearson, J. & Müller, H. Submillimeter, millimeter, and microwave spectral line catalog. *Journal of Quantitative Spectroscopy & Radiative Transfer* **60**, 883–890 (1998).
146. Cruzan, J. D., Viant, M. R., Brown, M. G. & Saykally, R. J. Terahertz laser vibration-rotation tunneling spectroscopy of the water tetramer. *The Journal of Physical Chemistry A* **101**, 9022–9031 (1997).
147. Viant, M. R., Cruzan, J. D., Lucas, D. D., Brown, M. G., Liu, K. & Saykally, R. J. Pseudorotation in water trimer isotopomers using terahertz laser spectroscopy. *The Journal of Physical Chemistry A* **101**, 9032–9041 (1997).

148. Allodi, M. A., Finneran, I. A. & Blake, G. A. Nonlinear terahertz coherent excitation of vibrational modes of liquids. *The Journal of Chemical Physics* **143**, 234204 (2015).
149. Mukamel, S. *Principles of nonlinear optical spectroscopy* **6** (Oxford University Press, 1999).
150. Häberle, U. & Diezemann, G. Dynamic Kerr effect responses in the terahertz range. *The Journal of Chemical Physics* **122**, 184517 (2005).
151. Häberle, U. & Diezemann, G. Kerr effect as a tool for the investigation of dynamic heterogeneities. *The Journal of Chemical Physics* **124**, 044501 (2006).
152. Loughnane, B. J., Scodinu, A. & Fourkas, J. T. Temperature-dependent optical Kerr effect spectroscopy of aromatic liquids. *The Journal of Physical Chemistry B* **110**, 5708–5720 (2006).
153. Smith, N. A. & Meech, S. R. Ultrafast dynamics of polar monosubstituted benzene liquids studied by the femtosecond optical Kerr effect. *The Journal of Physical Chemistry A* **104**, 4223–4235 (2000).
154. Beard, M. C., Lotshaw, W. T., Korter, T. M., Heilweil, E. J. & McMorro, D. Comparative OHD-RIKES and THz-TDS probes of ultrafast structural dynamics in molecular liquids. *The Journal of Physical Chemistry A* **108**, 9348–9360 (2004).
155. Neelakandan, M., Pant, D. & Quitevis, E. L. Structure and intermolecular dynamics of liquids: Femtosecond optical Kerr effect measurements in nonpolar fluorinated benzenes. *The Journal of Physical Chemistry A* **101**, 2936–2945 (1997).
156. Finneran, I. A., Welsch, R., Allodi, M. A., Miller, T. F. & Blake, G. A. Coherent two-dimensional terahertz-terahertz-Raman spectroscopy. *Proceedings of the National Academy of Sciences* **113**, 6857–6861 (2016).
157. Macura, S. & Ernst, R. Elucidation of cross relaxation in liquids by two-dimensional NMR spectroscopy. *Molecular Physics* **41**, 95–117 (1980).
158. Kampfrath, T., Tanaka, K. & Nelson, K. A. Resonant and nonresonant control over matter and light by intense terahertz transients. *Nature Photonics* **7**, 680–690 (2013).
159. Fleischer, S., Field, R. W. & Nelson, K. A. Commensurate two-quantum coherences induced by time-delayed THz fields. *Physical Review Letters* **109**, 123603 (2012).
160. Kampfrath, T., Sell, A., Klatt, G., Pashkin, A., Mährlein, S., Dekorsy, T., Wolf, M., Fiebig, M., Leitenstorfer, A. & Huber, R. Coherent terahertz control of antiferromagnetic spin waves. *Nature Photonics* **5**, 31–34 (2011).

161. Liu, M., Hwang, H. Y., Tao, H., Strikwerda, A. C., Fan, K., Keiser, G. R., Sternbach, A. J., West, K. G., Kittiwatanakul, S., Lu, J., *et al.* Terahertz-field-induced insulator-to-metal transition in vanadium dioxide metamaterial. *Nature* **487**, 345–348 (2012).
162. Matsunaga, R. & Shimano, R. Nonequilibrium BCS state dynamics induced by intense terahertz pulses in a superconducting NbN film. *Physical Review Letters* **109**, 187002 (2012).
163. Woerner, M., Kuehn, W., Bowlan, P., Reimann, K. & Elsaesser, T. Ultrafast two-dimensional terahertz spectroscopy of elementary excitations in solids. *New Journal of Physics* **15**, 025039 (2013).
164. Kuehn, W., Reimann, K., Woerner, M. & Elsaesser, T. Phase-resolved two-dimensional spectroscopy based on collinear n-wave mixing in the ultrafast time domain. *The Journal of Chemical Physics* **130**, 164503 (2009).
165. Wilson, K. C., Lyons, B., Mehlenbacher, R., Sabatini, R. & McCamant, D. W. Two-dimensional femtosecond stimulated Raman spectroscopy: observation of cascading Raman signals in acetonitrile. *The Journal of Chemical Physics* **131**, 214502 (2009).
166. Frostig, H., Bayer, T., Dudovich, N., Eldar, Y. C. & Silberberg, Y. Single-beam spectrally controlled two-dimensional Raman spectroscopy. *Nature Photonics* **9**, 339–343 (2015).
167. Cho, M. Two-dimensional vibrational spectroscopy. III. Theoretical description of the coherent two-dimensional IR-Raman spectroscopy for the investigation of the coupling between both IR-and Raman-active vibrational modes. *The Journal of Chemical Physics* **111**, 4140–4147 (1999).
168. Ikeda, T., Ito, H. & Tanimura, Y. Analysis of 2D THz-Raman spectroscopy using a non-Markovian Brownian oscillator model with nonlinear system-bath interactions. *The Journal of Chemical Physics* **142**, 212421 (2015).
169. Flanders, B., Cheville, R., Grischkowsky, D. & Scherer, N. Pulsed terahertz transmission spectroscopy of liquid CHCl₃, CCl₄, and their mixtures. *The Journal of Physical Chemistry* **100**, 11824–11835 (1996).
170. Shimanouchi, T. *Tables of Molecular Vibrational Frequencies Consolidated. Volume I* tech. rep. (DTIC Document, 1972).
171. Huynh, T. & Anderson, A. Infrared and Raman Study of Solid Dibromodichloromethane. *Journal of Raman Spectroscopy* **28**, 373–377 (1997).
172. Teo, S. M., Ofori-Okai, B. K., Werley, C. A. & Nelson, K. A. Invited Article: Single-shot THz detection techniques optimized for multidimensional THz spectroscopy. *Review of Scientific Instruments* **86**, 051301 (2015).
173. Shalaby, M. & Hauri, C. P. Demonstration of a low-frequency three-dimensional terahertz bullet with extreme brightness. *Nature Communications* **6** (2015).

174. Tonouchi, M. Cutting-edge terahertz technology. *Nature Photonics* **1**, 97–105 (2007).
175. Leforestier, C., Bisseling, R., Cerjan, C., Feit, M., Friesner, R., Guldberg, A., Hammerich, A., Jolicard, G., Karrlein, W., Meyer, H.-D., Lipkin, N., Roncero, O. & Kosloff, R. A comparison of different propagation schemes for the time dependent Schrödinger equation. *Journal of Computational Physics* **94**, 59–80 (1991).
176. Finneran, I. A., Welsch, R., Allodi, M. A., Miller, T. F. & Blake, G. A. Broadband 2D THz-THz-Raman photon-echo spectroscopy of molecular vibrations in liquids. *in preparation* (2017).
177. Fecko, C., Eaves, J., Loparo, J., Tokmakoff, A. & Geissler, P. Ultrafast hydrogen-bond dynamics in the infrared spectroscopy of water. *Science* **301**, 1698–1702 (2003).
178. Shim, S.-H., Gupta, R., Ling, Y. L., Strasfeld, D. B., Raleigh, D. P. & Zanni, M. T. Two-dimensional IR spectroscopy and isotope labeling defines the pathway of amyloid formation with residue-specific resolution. *Proceedings of the National Academy of Sciences* **106**, 6614–6619 (2009).
179. Wales, D. J. & Doye, J. P. Global optimization by basin-hopping and the lowest energy structures of Lennard-Jones clusters containing up to 110 atoms. *The Journal of Physical Chemistry A* **101**, 5111–5116 (1997).
180. Perez, R. E., Jansen, P. W. & Martins, J. R. R. A. pyOpt: A Python-Based Object-Oriented Framework for Nonlinear Constrained Optimization. *Structures and Multidisciplinary Optimization* **45**, 101–118 (2012).
181. Park, K. & Cho, M. Time-and frequency-resolved coherent two-dimensional IR spectroscopy: Its complementary relationship with the coherent two-dimensional Raman scattering spectroscopy. *The Journal of Chemical Physics* **109**, 10559–10569 (1998).
182. Fernandez-Liencres, M. P., Navarro, A., Lopez, J. J., Fernandez, M., Szalay, V., de los Arcos, T., Garcia-Ramos, J. V. & Escibano, R. M. The force field of bromoform: A theoretical and experimental investigation. *The Journal of Physical Chemistry* **100**, 16058–16065 (1996).
183. Khalil, M., Demirdöven, N. & Tokmakoff, A. Vibrational coherence transfer characterized with Fourier-transform 2D IR spectroscopy. *The Journal of Chemical Physics* **121**, 362–373 (2004).
184. Baiz, C. R., Kubarych, K. J. & Geva, E. Molecular Theory and Simulation of Coherence Transfer in Metal Carbonyls and Its Signature on Multidimensional Infrared Spectra. *The Journal of Physical Chemistry B* **115**, 5322–5339 (2011).
185. Dexheimer, S. L. *Terahertz spectroscopy: principles and applications* (CRC press, 2007).

186. Sajadi, M., Wolf, M. & Kampfrath, T. Terahertz-field-induced optical birefringence in common window and substrate materials. *Optics Express* **23**, 28985–28992 (2015).
187. Ratajczak, H., Ford, T. & Orville-Thomas, W. Infrared dispersion studies: 11. Band intensities and vibrational polarizations of chloroform, bromoform and their deuterated analogues. *Journal of Molecular Structure* **14**, 281–291 (1972).
188. Zaleski, D. P., Neill, J. L., Muckle, M. T., Seifert, N. A., Carroll, P. B., Weaver, S. L. W. & Pate, B. H. A Ka-band chirped-pulse Fourier transform microwave spectrometer. *Journal of Molecular Spectroscopy* **280**, 68–76 (2012).
189. Yardimci, N. T., Yang, S.-H., Berry, C. W. & Jarrahi, M. High-power terahertz generation using large-area plasmonic photoconductive emitters. *IEEE Transactions on Terahertz Science and Technology* **5**, 223–229 (2015).
190. Maslowski, P., Lee, K. F., Johansson, A. C., Khodabakhsh, A., Kowzan, G., Rutkowski, L., Mills, A. A., Mohr, C., Jiang, J., Fermann, M. E., *et al.* Surpassing the path-limited resolution of Fourier-transform spectrometry with frequency combs. *Physical Review A* **93**, 021802 (2016).
191. Vicario, C., Monoszalai, B., Jazbinsek, M., Lee, S., Kwon, O. & Hauri, C. Intense, carrier frequency and bandwidth tunable quasi single-cycle pulses from an organic emitter covering the Terahertz frequency gap. *Scientific Reports* **5**, 14394–14394 (2014).
192. Vicario, C., Ovchinnikov, A. V., Chefonov, O. V. & Hauri, C. P. Multi-octave spectrally tunable strong-field Terahertz laser. *arXiv preprint arXiv:1608.05319* (2016).
193. Allodi, M. A. *On Ultrafast Time-Domain TeraHertz Spectroscopy in the Condensed Phase: Linear Spectroscopic Measurements of Hydrogen-Bond Dynamics of Astrochemical Ice Analogs and Nonlinear TeraHertz Kerr Effect Measurements of Vibrational Quantum Beats* PhD thesis (California Institute of Technology, 2015).
194. Clerici, M., Peccianti, M., Schmidt, B. E., Caspani, L., Shalaby, M., Giguère, M., Lotti, A., Couairon, A., Légaré, F., Ozaki, T., *et al.* Wavelength scaling of terahertz generation by gas ionization. *Physical Review Letters* **110**, 253901 (2013).
195. Heisler, I. A., Mazur, K., Yamaguchi, S., Tominaga, K. & Meech, S. R. Measuring acetic acid dimer modes by ultrafast time-domain Raman spectroscopy. *Physical Chemistry Chemical Physics* **13**, 15573–15579 (2011).
196. Analog Devices. *AD9914 Evaluation Board Circuit Schematic* http://www.analog.com/static/imported-files/eval_boards/AD9914_Schematic.pdf. May 2013.

*Appendix A***SEGMENTED CHIRP CAPABILITIES OF THE AD9914 DDS**

It is possible to extend the bandwidth of the DDS chirped pulses by utilizing the super-Nyquist images, as shown in Fig. 2.5. To explore this feature we generated a 1 GHz chirped pulse using a 2 GHz sample clock, so that the full frequency content of the pulse could be recorded with a 4 GS/s digitizer (Fig. A.1). The first image is visible in the spectrogram of the pulse at approximately -10 dBc. To test the phase stability we averaged 1000 waveforms and found no significant attenuation of the super-Nyquist content, indicating that it is both phase stable and coherent with respect to the normal pulse. Used as is, this chirped pulse could effectively polarize 1.5 GHz of bandwidth. This could possibly be extended by using an appropriate combination of filters and amplifiers operating in saturation. We also tested the bandwidth of the 2 GHz chirp with the 4 GHz sample clock using a spectrum analyzer and observed a similar frequency envelope extending to 4 GHz. The usable bandwidth of the chirped pulse in this particular example is likely ~ 3 GHz, although further tests with a high sample rate digitizer would be needed to better quantify the bandwidth. Additionally, it may be possible to extend the bandwidth to a full 4 GHz by filtering and mixing the main signal with the first image, followed by amplification.

A.1 Stepped-LO Operation

An alternate use for DDS chips in CP-FT spectroscopy, especially at higher frequencies, is for ‘stepped’ LO sources, similar to previous AWG-based stepped-LO spectrometers [9, 66]. To demonstrate this capability, we scanned the frequency of the AD9914 from 200-1800 MHz in nine $10 \mu\text{s}$ steps of 200 MHz (Fig. A.2). All spurious signals are observed at -40 dBc or less, sufficient for an LO signal in a CP-FT spectrometer. To fully implement this design, a second DDS would be needed along with a method for the generation of multiple chirped pulses per trigger pulse, or the DDS stepped-LO signal could be used in conjunction with an AFG or AWG that supplies the chirped pulse.

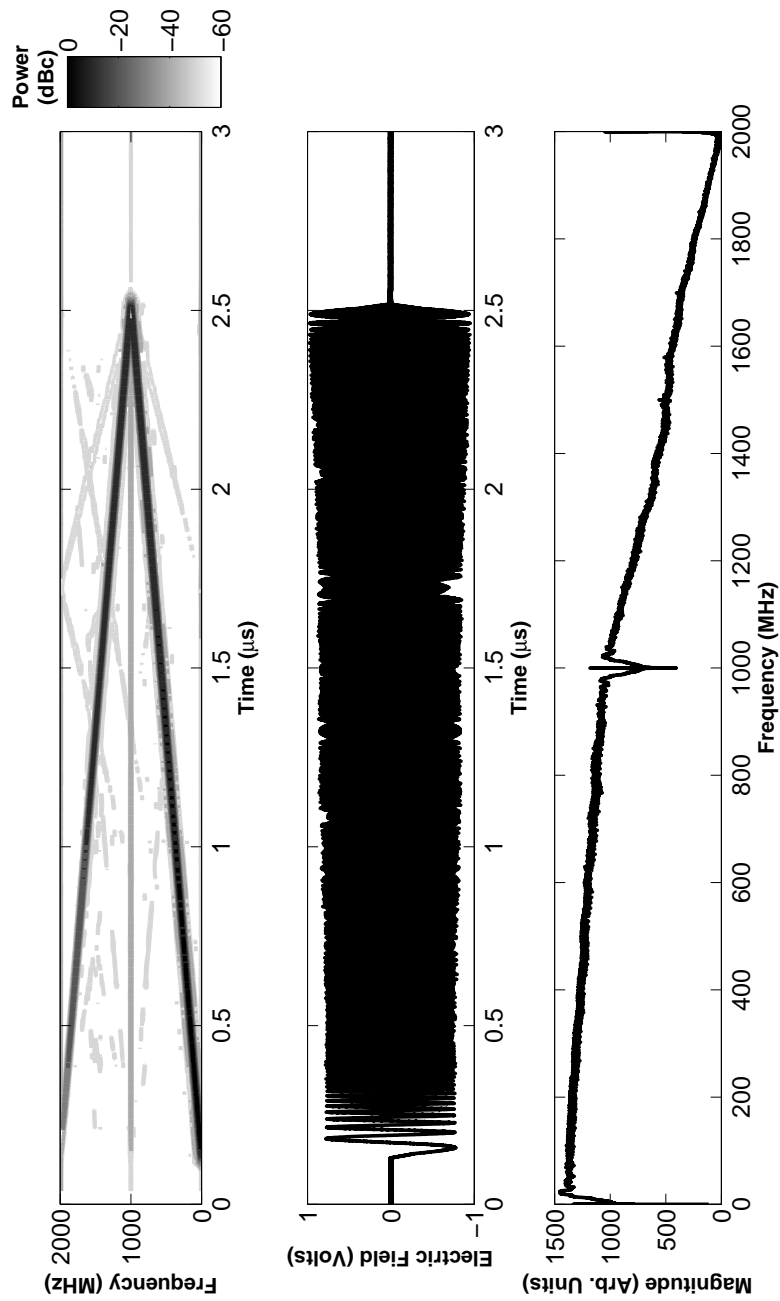


Figure A.1: The unfiltered output of the AD9914 DDS for a 1 GHz chirped pulse, using a 2 GHz sampling clock frequency, after 1000 averages. The first image of the chirp is visible between 1 GHz and 2 GHz at approximately -10 dBc.

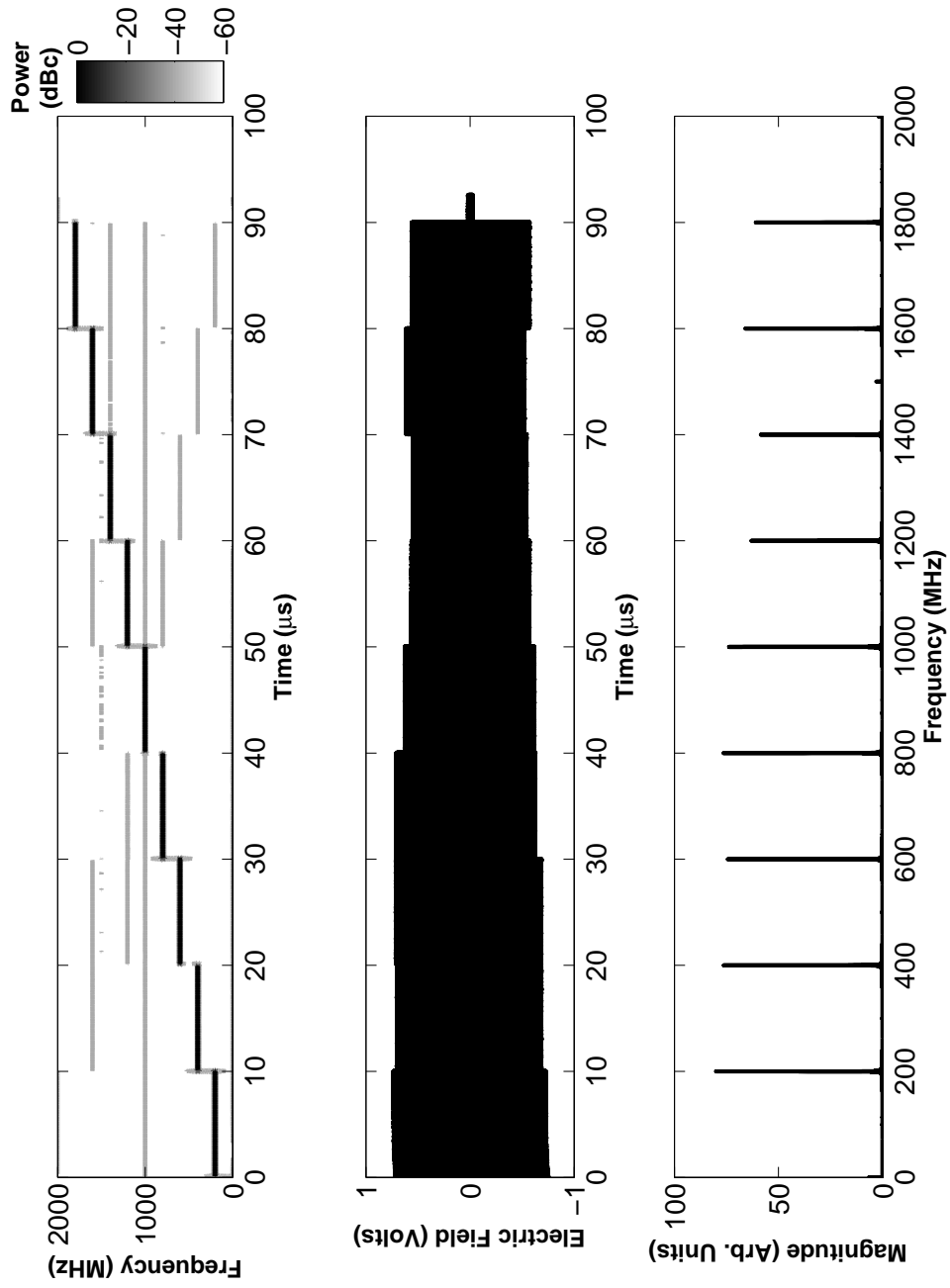


Figure A.2: A demonstration of the segmented LO capability of the AD9914. For this demonstration nine $10 \mu\text{s}$ steps of 200 MHz were taken to cover 200-1800 MHz.

A.2 Details of AD9914 Implementation

In order for the AD9914 evaluation board (AD9914/PCBZ) to generate chirped pulses it must be configured in the ‘Digital Ramp Generator’ mode within the AD9914 Evaluation Software [56]. To output a single frequency ramp without sustaining the last frequency of the ramp we set the ‘no dwell high’ pin high. Additionally, the ‘Autoclear digital ramp accumulator’ and ‘Autoclear phase accumulator’ pins are set high, so that the frequency and the phase are reset for each chirped pulse. The AD9914 is advertised with a usable sample clock frequency of up to 3.5 GHz. To extend the bandwidth of the board, we overclocked the AD9914 with a sample clock at 4 GHz, allowing chirp generation up to 2 GHz. We also increased the bandwidth of the board by attenuating the sampling clock input to -16 dBm. The cause of the bandwidth dependence on the sample clock power is currently unknown. For the 1.2 μ s, 2 GHz chirp used in this thesis, we set the sweep from 0-2000 MHz with a 10 MHz rising step size and 0.006 μ s rising sweep ramp rate in the Evaluation Software. This corresponds to stepping the DDS by 200 6 ns, 10 MHz steps for each chirp. With this configuration, the AD9914 board can be triggered from the Evaluation Software with a mouse click.

To synchronize the DDS triggering with that of the CP-FTMW spectrometer, a trigger-in signal is sent to the DRCTL-BUF (pin 63) on the AD9914 chip [196]. However, on the evaluation board this pin is also routed to the USB control chip (for software triggering), which overrides any other direct triggering. To disable the USB control, we removed the R134 0 Ohm resistor connecting the DRCTL-BUF to the USB control [196]. This allows the direct triggering of the chirp from the P102 DRCTL-BUF triple row header on the evaluation board. To achieve coherent signal averaging up to 2 GHz, the digitizer must be directly triggered from the DDS, since it can slip by up to one clock cycle when triggered. The frequency sweep trigger is obtained from the DROVR (pin 65) signal of the AD9914. On the evaluation board this signal is routed to the DROVR-BUF triple row header.

Finally, we observe a slow phase slip of the chirped pulse after many (>500) triggering events. This can be corrected by calibrating the DAC in the Evaluation Software every few seconds. Since the DAC calibration takes 133 μ s for a 4 GHz sample clock [56], this does not significantly reduce the repetition rate of the experiment. In this thesis, we performed the DAC calibration with automated mouse clicking software. Brandon Carroll has also developed Arduino software that will automatically calibrate the DAC and control the chirp parameters.

*Appendix B*FITTING AND KRAITCHMAN ANALYSIS OF THE
ETHANOL-WATER DIMER

SPECTRAL FITS FROM SPFIT

All frequencies in MHz

WE-g+ (Caltech measurements)

EtOH:H2O

J	Ka	Kc	J'	Ka'	Kc'	Measured	OMC	Error
3	1	2	3	0	3	8275.604	-0.00029	0.020
4	1	3	3	2	2	9748.674	0.01139	0.020
4	1	3	4	0	4	10038.458	0.00426	0.020
6	2	5	6	1	5	11543.455	-0.00586	0.020
2	1	2	1	1	1	11624.457	-0.00400	0.020
1	1	1	0	0	0	11827.704	0.00328	0.020
2	0	2	1	0	1	12240.769	0.01451	0.020
5	1	4	5	0	5	12461.752	-0.03144	0.020
2	1	1	1	1	0	12969.927	0.02023	0.020
3	0	3	2	1	2	13159.206	-0.01193	0.020
5	2	4	5	1	4	13273.813	0.00706	0.020
6	2	4	6	1	5	15016.412	-0.00474	0.020
5	2	3	5	1	4	15112.091	-0.00515	0.020
7	2	5	7	1	6	15485.396	0.02486	0.020
6	1	5	6	0	6	15582.996	0.01428	0.020
4	2	2	4	1	3	15617.182	-0.00255	0.020
3	2	1	3	1	2	16343.020	0.01020	0.020
8	2	6	8	1	7	16638.065	-0.01255	0.020
2	1	2	1	0	1	17303.387	-0.00146	0.020
3	1	3	2	1	2	17401.979	-0.02798	0.020
3	0	3	2	0	2	18221.856	0.00411	0.020

EtOD:D2O

J	Ka	Kc	J'	Ka'	Kc'	Measured	OMC	Error
2	1	2	1	1	1	10868.902	-0.01738	0.020
3	2	1	3	1	2	15705.990	-0.00176	0.020
2	0	2	1	0	1	11417.954	0.02356	0.020
5	1	4	5	0	5	11374.420	0.00122	0.020
1	1	1	0	0	0	11178.972	0.01445	0.020
2	1	1	1	1	0	12059.436	-0.00713	0.020
3	0	3	2	1	2	12114.742	0.00139	0.020
3	1	3	2	1	2	16274.928	0.02019	0.020
2	1	2	1	0	1	16315.628	-0.01600	0.020
2	2	0	2	1	1	16385.502	0.00158	0.020
3	0	3	2	0	2	17012.440	-0.01417	0.020
3	2	2	2	2	1	17195.792	0.02590	0.020
3	2	1	2	2	0	17378.436	-0.02480	0.020
3	1	2	2	1	1	18057.970	0.00054	0.020
4	0	4	3	1	3	18319.682	-0.00192	0.020

EtOD:H2O

J	Ka	Kc	J'	Ka'	Kc'	Measured	OMC	Error
4	1	3	3	2	2	10737.488	-0.01567	0.020
2	1	2	1	1	1	11512.420	-0.05565	0.020
1	1	1	0	0	0	11358.628	0.00942	0.020
2	0	2	1	0	1	12122.860	-0.01368	0.020
2	1	1	1	1	0	12853.550	-0.07204	0.020
2	1	2	1	0	1	16779.426	0.03751	0.020
3	1	3	2	1	2	17231.832	-0.03961	0.020
3	0	3	2	0	2	18036.290	0.05509	0.020

EtOH:D2O

J	Ka	Kc	J'	Ka'	Kc'	Measured	OMC	Error
2	1	2	1	1	1	10971.708	0.03411	0.020
2	0	2	1	0	1	11525.450	0.02983	0.020

1	1	1	0	0	0	11640.054	-0.06069	0.020
3	0	3	2	1	2	11878.428	-0.04533	0.020
2	1	1	1	1	0	12166.144	-0.04746	0.020
4	2	2	4	1	3	16200.214	-0.00539	0.020
3	1	3	2	1	2	16430.654	-0.01310	0.020
2	1	2	1	0	1	16827.208	0.03207	0.020
3	0	3	2	0	2	17180.216	-0.01309	0.020
3	2	2	2	2	1	17352.936	-0.00412	0.020
3	2	1	2	2	0	17524.824	-0.00928	0.020
3	1	2	2	1	1	18219.830	0.07278	0.020

EtOD:HOD

J	Ka	Kc	J'	Ka'	Kc'	Measured	OMC	Error
2	1	2	1	1	1	10986.010	0.02801	0.02000
1	1	1	0	0	0	11208.536	0.02710	0.02000
2	0	2	1	0	1	11546.052	0.03257	0.02000
2	1	1	1	1	0	12203.276	-0.08238	0.02000
3	0	3	2	1	2	12347.920	0.02934	0.02000
2	1	2	1	0	1	16397.028	0.00011	0.02000
3	1	3	2	1	2	16449.112	-0.06552	0.02000
3	0	3	2	0	2	17198.926	0.02688	0.02000
3	1	2	2	1	1	18272.122	0.01472	0.02000

WE-t

EtOH:H2O (Harvard+Caltech measurements)

J	Ka	Kc	v	J	Ka	Kc	v	Measured	OMC	Error
2	0	2	0	1	0	1	0	11737.71220	-0.00250	0.002
3	0	3	0	2	0	2	0	17482.59060	-0.00300	0.002
4	0	4	0	3	0	3	0	23089.35720	-0.00002	0.002
5	0	5	0	4	0	4	0	28541.04130	-0.00213	0.002
6	0	6	0	5	0	5	0	33853.84560	0.00306	0.002
7	0	7	0	6	0	6	0	39071.37610	-0.01263	0.005
3	1	3	0	2	1	2	0	16668.88610	-0.00075	0.002

4	1	4	0	3	1	3	0	22170.42920	0.00023	0.002
5	1	5	0	4	1	4	0	27631.75990	-0.00052	0.002
6	1	6	0	5	1	5	0	33050.26940	-0.00153	0.002
3	0	3	0	2	1	2	0	11987.27780	-0.00160	0.002
4	0	4	0	3	1	3	0	18407.75260	0.00283	0.002
5	0	5	0	4	1	4	0	24778.36710	0.00287	0.005
6	0	6	0	5	1	5	0	31000.45010	0.00374	0.005
7	0	7	0	6	1	6	0	37021.57150	0.00734	0.020
2	1	1	0	1	1	0	0	12441.23680	-0.00610	0.005
3	1	2	0	2	1	1	0	18629.33870	0.01595	0.005
4	1	3	0	3	1	2	0	24772.23170	0.01380	0.005
5	1	4	0	4	1	3	0	30850.67750	0.00825	0.005
6	1	5	0	5	1	4	0	36840.18040	-0.01042	0.005
2	1	2	0	1	0	1	0	17233.02430	-0.00461	0.002
3	1	3	0	2	0	2	0	22164.19720	-0.00385	0.002
4	1	4	0	3	0	3	0	26852.03880	0.00238	0.002
5	1	5	0	4	0	4	0	31394.44520	0.00559	0.002
6	1	6	0	5	0	5	0	35903.66610	-0.00102	0.002
1	1	1	0	0	0	0	0	11993.72640	0.02433	0.005
2	1	2	0	1	1	1	0	11133.37440	0.00015	0.002
2	1	2	1	1	1	1	1	11132.91600	-0.04504	0.020
2	0	2	1	1	0	1	1	11734.12000	-0.03061	0.020
2	1	1	1	1	1	0	1	12435.85000	0.01051	0.020
3	1	3	1	2	1	2	1	16667.05200	0.04139	0.020
3	0	3	1	2	0	2	1	17478.15200	-0.03494	0.020
1	1	1	1	0	0	0	1	11991.36600	0.03377	0.020
3	0	3	1	2	1	2	1	11980.14600	0.03278	0.020
3	2	2	0	2	2	1	0	17681.01040	-0.04671	0.020
4	2	3	0	3	2	2	0	23533.42360	-0.01667	0.010
6	2	5	0	5	2	4	0	35124.76690	0.00050	0.005
3	2	1	0	2	2	0	0	17876.78730	-0.00058	0.002

EtOH:D2O (Caltech measurements)

J	Ka	Kc	v	J	Ka	Kc	v	Measured	OMC	Error
2	1	2	0	1	1	1	0	10441.69400	0.03132	0.040

2	1	2	1	1	1	1	1	10441.49900	0.14626	0.040
2	0	2	1	1	0	1	1	11012.64800	-0.00217	0.040
2	0	2	0	1	0	1	0	11013.20200	-0.01656	0.040
2	1	1	0	1	1	0	0	11682.02100	-0.04245	0.040
2	1	1	1	1	1	0	1	11681.02000	-0.11640	0.040
3	1	3	0	2	1	2	0	15632.43200	-0.05982	0.020
3	1	3	1	2	1	2	1	15632.09000	0.03196	0.020
3	0	3	0	2	0	2	0	16399.29500	-0.02626	0.020
3	0	3	1	2	0	2	1	16398.62000	0.02673	0.020
3	2	2	0	2	2	1	0	16591.95600	-0.00088	0.020
3	2	2	1	2	2	1	1	16590.84400	0.00011	0.020
3	1	2	0	2	1	1	0	17490.19100	0.04116	0.020
3	1	2	1	2	1	1	1	17488.78900	-0.01301	0.020

KRAITCHMAN ANALYSIS FROM KRA, WE-g+:

The parent species: EtOH:H2O

X,	Y,	Z	=	9089.86200000	3410.88410000	2737.97050000
eX,	eY,	eZ	=	0.01000000	0.00350000	0.00280000

Mass	=	64.05242950
------	---	-------------

The isotopic species: EtOD:H2O

X,	Y,	Z	=	8648.24400000	3381.27400000	2710.51000000
eX,	eY,	eZ	=	0.04000000	0.01300000	0.01000000

Mass change	=	1.00627670
-------------	---	------------

Total mass	=	65.05870620
------------	---	-------------

M DM/(M+DM)	=	0.99071241
-------------	---	------------

KRAITCHMAN RESULTS:

	a		b		c			
0.40159	+-	0.00059	1.29274	+-	0.00018	1.09500	+-	0.00023

The parent species: EtOD:H2O

X, Y, Z = 8648.24400000 3381.27400000 2710.51000000
 eX, eY, eZ = 0.04000000 0.01300000 0.01000000

Mass = 65.05870620

The isotopic species: EtOD:HOD

X, Y, Z = 8614.30000000 3203.20300000 2594.32400000
 eX, eY, eZ = 0.03900000 0.01700000 0.01800000

Mass change = 1.00627670

Total mass = 66.06498290

M DM/(M+DM) = 0.99094948

KRAITCHMAN RESULTS:

a	b	c
2.87593 +- 0.00016	0.38597 +- 0.00133	0.31917 +- 0.00157

The parent species: EtOD:HOD

X, Y, Z = 8614.30000000 3203.20300000 2594.32400000
 eX, eY, eZ = 0.03900000 0.01700000 0.01800000

Mass = 66.06498290

The isotopic species: EtOD:D2O

X, Y, Z = 8610.61000000 3163.84180000 2568.45090000

Mass change = 1.00627670
 Total mass = 67.07125960
 M DM/(M+DM) = 0.99117943

KRAITCHMAN RESULTS:

a	b	c
1.40248 +- 0.00032	0.11251 +- 0.00403	0.11462 +- 0.00394

The parent species: EtOH:D2O

X, Y, Z = 9046.62600000 3191.06400000 2593.61500000
 eX, eY, eZ = 0.03600000 0.01400000 0.01500000

Mass = 66.06498290

The isotopic species: EtOD:D2O

X, Y, Z = 8610.61000000 3163.84180000 2568.45090000
 eX, eY, eZ = 0.02000000 0.00850000 0.00730000

Mass change = 1.00627670
 Total mass = 67.07125960
 M DM/(M+DM) = 0.99117943

KRAITCHMAN RESULTS:

a	b	c
0.46687 +- 0.00080	1.28566 +- 0.00029	1.09842 +- 0.00037

Optimized ab initio equilibrium structures in PAS

MP2/aug-cc-pVTZ, tight convergence criteria

All distances in Angstroms

Structure of WE-g+

	a	b	c
C	-1.202931	1.110411	-0.218673
H	-0.216410	1.559852	-0.314952
H	-1.641164	1.004733	-1.212248
H	-1.840466	1.781120	0.357465
C	-1.103487	-0.234312	0.470155
H	-0.655468	-0.129243	1.455714
H	-2.088501	-0.690043	0.591130
O	-0.236825	-1.139903	-0.232511
H	-0.577682	-1.238790	-1.128329
O	2.135069	0.366184	0.047997
H	2.915618	-0.142687	0.281515
H	1.439670	-0.297023	-0.096269

Structure of WE-t

	a	b	c
C	1.246354	-1.095093	-0.211887
H	0.269767	-1.575087	-0.228709
H	1.606745	-0.989247	-1.233539
H	1.938352	-1.731576	0.338078
C	1.151705	0.257251	0.452132
H	0.782679	0.156858	1.475264
H	2.128155	0.744969	0.479843
O	0.236589	1.054807	-0.320210
H	0.197295	1.933691	0.071929
O	-2.204833	-0.326287	0.132111
H	-2.797044	-0.328538	-0.624168
H	-1.441776	0.202827	-0.153975

*Appendix C*FITTING AND KRAITCHMAN ANALYSIS OF THE
ETHANOL-METHANOL DIMER

ME-t-1 Normal Species

J	Ka	Kc	J'	Ka'	Kc'	Measured	OMC	Error
3	1	3	2	1	2	10400.4460	0.0172	0.020
3	0	3	2	0	2	10726.3120	0.0082	0.020
3	2	2	2	2	1	10756.2460	-0.0047	0.020
3	2	1	2	2	0	10786.1620	-0.0043	0.020
3	1	2	2	1	1	11102.6320	-0.0255	0.020
4	1	4	3	1	3	13858.4180	0.0106	0.020
4	0	4	3	0	3	14266.6360	-0.0241	0.020
4	2	3	3	2	2	14335.3240	0.0108	0.020
4	3	2	3	3	1	14355.7120	-0.0157	0.020
4	3	1	3	3	0	14356.6280	0.0017	0.020
4	2	2	3	2	1	14409.7280	-0.0188	0.020
4	1	3	3	1	2	14793.8420	0.0095	0.020
5	1	5	4	1	4	17309.2360	-0.0263	0.020
5	0	5	4	0	4	17778.0460	-0.0073	0.020
5	2	4	4	2	3	17908.9620	0.0210	0.020
5	3	3	4	3	2	17949.8300	-0.0022	0.020
5	3	2	4	3	1	17952.9620	-0.0090	0.020
5	4	2	4	4	1	17942.3540	-0.0045	0.020
2	1	1	1	0	1	13008.4120	-0.0109	0.020
7	2	6	7	1	6	13294.4900	-0.0096	0.020
6	0	6	5	1	4	13808.9020	-0.0037	0.020
5	2	4	5	1	4	14734.6100	0.0297	0.020
4	2	3	4	1	3	15301.8480	-0.0278	0.020
8	1	7	7	2	5	15238.2080	-0.0429	0.020
3	2	2	3	1	2	15760.3960	0.0009	0.020
2	2	1	2	1	1	16106.8080	0.0060	0.020
7	0	7	6	1	5	16358.5180	0.0323	0.020

2	2	0	2	1	2	16816.7960	0.0056	0.020
3	1	2	2	0	2	16947.5700	-0.0016	0.020
3	2	1	3	1	3	17202.5120	-0.0158	0.020
6	0	6	5	1	5	17316.0280	-0.0009	0.020
3	2	2	3	1	3	17165.1200	0.0009	0.020
3	1	3	2	0	2	15542.8480	0.0003	0.020
4	2	2	4	1	3	15413.7140	-0.0042	0.020
5	2	3	5	1	4	14993.8560	-0.0127	0.020
2	1	2	1	0	1	12305.9360	0.0082	0.020
7	1	6	7	0	7	9444.8600	0.0088	0.020
4	0	4	3	1	3	9450.1280	0.0117	0.020
1	1	1	0	0	0	8954.6220	-0.0148	0.020
6	1	5	6	0	6	8338.2540	0.0458	0.020
3	2	1	3	1	2	15797.8160	0.0120	0.020
8	2	7	8	1	7	12437.1620	0.0197	0.020
9	2	8	9	1	8	11502.8360	0.0130	0.020
5	0	5	4	1	3	11029.6280	0.0148	0.020
7	1	6	6	2	4	11227.0740	0.0461	0.020
10	2	9	10	1	9	10506.3820	-0.0146	0.020
1	1	0	0	0	0	9188.8420	0.0271	0.020
4	0	4	3	1	2	8045.4000	0.0076	0.020
5	2	3	4	2	2	18056.3760	-0.0110	0.020
5	1	4	4	1	3	18476.2360	-0.0005	0.020

ME-g-1

J	Ka	Kc	J'	Ka'	Kc'	Measured	OMC	Error
3	0	3	2	0	2	10027.9080	0.0035	0.020
3	1	3	2	1	2	9752.6420	-0.0425	0.020
3	1	2	2	1	1	10332.2280	0.0526	0.020
4	1	4	3	1	3	12998.2280	-0.0108	0.020
4	0	4	3	0	3	13350.2180	-0.0145	0.020
4	2	3	3	2	2	13390.1880	0.0007	0.020
4	2	2	3	2	1	13432.7280	-0.0132	0.020
4	1	3	3	1	2	13770.6380	0.0197	0.020

5	1	5	4	1	4	16239.4340	0.0442	0.020
5	0	5	4	0	4	16655.4480	-0.0055	0.020
5	2	4	4	2	3	16731.6100	0.0085	0.020
5	2	3	4	2	2	16816.3240	-0.0036	0.020
5	1	4	4	1	3	17204.0320	-0.0373	0.020

ME-t-1 EtOD:MeOD

J	Ka	Kc	J'	Ka'	Kc'	Measured	OMC	Error
3	0	3	2	0	2	10601.8360	-0.0259	0.020
3	1	2	2	1	1	11009.4500	-0.0411	0.020
4	1	4	3	1	3	13664.7320	0.0140	0.020
4	0	4	3	0	3	14092.7120	-0.0093	0.020
4	2	3	3	2	2	14177.3840	-0.0341	0.020
4	2	2	3	2	1	14269.2500	-0.0231	0.020
4	1	3	3	1	2	14667.3700	-0.0208	0.020
5	1	5	4	1	4	17064.2320	-0.0137	0.020
5	0	5	4	0	4	17548.4520	0.0353	0.020
5	2	4	4	2	3	17709.3880	0.0277	0.020
5	3	3	4	3	2	17759.5580	-0.0687	0.020
5	3	2	4	3	1	17764.0440	-0.0570	0.020
5	2	3	4	2	2	17890.8400	0.0545	0.020
5	1	4	4	1	3	18314.4600	0.0371	0.020
3	2	2	2	2	1	10638.9260	0.0622	0.020
3	2	1	2	2	0	10675.9140	0.0796	0.020
3	1	3	2	1	2	10256.6010	-0.0023	0.020

ME-t-1 EtOH:MeOD

J	Ka	Kc	J'	Ka'	Kc'	Measured	OMC	Error
3	1	3	2	1	2	10390.2320	-0.0214	0.020
3	0	3	2	0	2	10716.4280	-0.0266	0.020
3	2	2	2	2	1	10746.6860	-0.0482	0.020
3	2	1	2	2	0	10776.9220	-0.0604	0.020

3	1	2	2	1	1	11093.6680	-0.0273	0.020
4	1	4	3	1	3	13844.7340	-0.0158	0.020
4	0	4	3	0	3	14253.1360	-0.0141	0.020
4	2	3	3	2	2	14322.5640	0.0044	0.020
4	2	2	3	2	1	14397.7980	-0.0164	0.020
4	1	3	3	1	2	14781.7520	-0.0259	0.020
5	1	5	4	1	4	17292.0500	-0.0041	0.020
5	0	5	4	0	4	17760.6020	0.0118	0.020
5	2	4	4	2	3	17892.9240	0.0293	0.020
5	3	3	4	3	2	17934.3020	0.0751	0.020
5	3	2	4	3	1	17937.4800	0.0495	0.020
5	2	3	4	2	2	18041.9380	-0.0044	0.020
5	1	4	4	1	3	18460.9980	0.0075	0.020

ME-t-1 EtOD:MeOH

J	Ka	Kc	J'	Ka'	Kc'	Measured	OMC	Error
3	0	3	2	0	2	10611.3960	-0.0034	0.020
3	2	2	2	2	1	10648.0420	-0.0415	0.020
3	2	1	2	2	0	10684.7120	-0.0244	0.020
3	1	2	2	1	1	11018.4580	-0.0042	0.020
3	1	3	2	1	2	10266.1820	0.0100	0.020
4	0	4	3	0	3	14105.7980	0.0024	0.020
4	2	3	3	2	2	14189.7480	-0.0254	0.020
4	2	2	3	2	1	14280.8580	0.0106	0.020
4	1	3	3	1	2	14679.4720	0.0180	0.020
5	1	5	4	1	4	17080.4960	0.0688	0.020
5	0	5	4	0	4	17565.3020	0.0087	0.020
5	2	4	4	2	3	17724.9120	0.0078	0.020
5	3	3	4	3	2	17774.6540	-0.0999	0.020
5	3	2	4	3	1	17779.0500	-0.1049	0.020
5	2	3	4	2	2	17904.9100	0.0902	0.020
5	1	4	4	1	3	18329.7380	0.0623	0.020
4	1	4	3	1	3	13677.5620	0.0005	0.020

Optimized ab initio equilibrium structures in PAS
 MP2/aug-cc-pVTZ, tight convergence criteria
 All distances in Angstroms

Structure of ME-t-1

	a	b	c
C	-1.418228	1.261276	-0.023401
H	-1.319410	1.454449	-1.090302
H	-0.457170	1.434296	0.457890
H	-2.146580	1.957611	0.390121
C	-1.871447	-0.160060	0.209763
H	-1.960509	-0.363708	1.279087
H	-2.840519	-0.339610	-0.260335
O	-0.884495	-1.027462	-0.373426
H	-1.157852	-1.940400	-0.234585
C	2.365334	0.354296	-0.428467
H	3.289495	0.753828	-0.018141
H	2.616511	-0.355180	-1.220455
H	1.797802	1.179063	-0.868366
O	1.663020	-0.264758	0.636341
H	0.828452	-0.602422	0.275142

Structure of ME-g-1

	a	b	c
C	-1.892196	1.056231	-0.147426
H	-2.402465	0.936010	-1.104305
H	-0.946578	1.569071	-0.313616
H	-2.521624	1.676641	0.490723
C	-1.652255	-0.288466	0.505915
H	-1.131832	-0.167801	1.453469
H	-2.592884	-0.808873	0.698091
O	-0.790176	-1.126606	-0.281823
H	-1.200975	-1.242955	-1.145721
C	2.706146	-0.089504	0.155701

H	3.443029	0.692132	0.322599
H	2.643821	-0.704150	1.056785
H	3.048571	-0.715332	-0.671749
O	1.473287	0.548717	-0.136716
H	0.80103	-0.13916	-0.266128

Structure of ME-t-2

	a	b	c
C	1.548471	-1.150780	-0.303469
H	2.020920	-0.980560	-1.269050
H	0.519334	-1.462858	-0.473918
H	2.079151	-1.952039	0.209201
C	1.588674	0.110012	0.526578
H	1.132198	-0.057365	1.505516
H	2.618714	0.438982	0.678697
O	0.857512	1.119365	-0.188241
H	0.928260	1.950433	0.292938
C	-2.099111	-0.284622	0.652952
H	-3.067807	-0.777203	0.621499
H	-1.380759	-0.972940	1.109728
H	-2.184335	0.600723	1.288730
O	-1.748118	0.046100	-0.678408
H	-0.890810	0.497252	-0.640108

Structure of M-g-1

	a	b	c
C	-1.552529	1.225313	0.013973
H	-0.624826	1.491649	0.521588
H	-1.453939	1.467287	-1.043593
H	-2.356115	1.830254	0.436055
C	-1.844097	-0.254485	0.188238
H	-2.774519	-0.519076	-0.312751
H	-1.964686	-0.489013	1.250933
O	-0.840550	-1.074889	-0.394410
H	-0.004360	-0.866601	0.051425
C	2.275310	0.394556	-0.504133

H	3.101448	1.046298	-0.221042
H	1.506993	0.984042	-0.994837
H	2.628377	-0.368012	-1.197939
O	1.659191	-0.189729	0.648161
H	2.300506	-0.763810	1.077882

Structure of ME-g-2

	a	b	c
C	-2.798686	-0.365523	-0.170291
H	-2.706028	-0.827497	-1.151253
H	-3.332276	0.579125	-0.281204
H	-3.397052	-1.015338	0.468282
C	-1.431582	-0.144109	0.440397
H	-1.513248	0.307726	1.431334
H	-0.894782	-1.084074	0.548225
O	-0.593823	0.663660	-0.399622
H	-0.997309	1.534883	-0.477946
C	2.787934	-0.383910	-0.386444
H	3.725427	-0.696855	0.066603
H	2.299509	-1.264212	-0.812036
H	3.012346	0.314827	-1.196003
O	2.006277	0.216635	0.632618
H	1.157778	0.470299	0.238057

Structure of M-t

	a	b	c
C	-2.895158	-0.251034	0.126969
H	-2.826422	-1.309013	0.374703
H	-3.222777	-0.161398	-0.907432
H	-3.641336	0.212155	0.772095
C	-1.549695	0.414585	0.305773
H	-1.623644	1.480490	0.067260
H	-1.223294	0.329826	1.347473
O	-0.624426	-0.228532	-0.561546
H	0.245938	0.178717	-0.427308
C	2.679561	-0.615227	0.238093

H	3.649659	-0.456296	0.708132
H	2.033471	-1.152874	0.924793
H	2.801405	-1.210344	-0.666604
O	2.028047	0.629188	-0.036596
H	2.549555	1.108067	-0.687679

Structure of EM-g-2

	a	b	c
C	-1.739509	1.093777	-0.287932
H	-2.303557	0.857652	-1.188802
H	-0.777158	1.510385	-0.587748
H	-2.281999	1.853098	0.276855
C	-1.539839	-0.157275	0.547948
H	-1.004730	0.090446	1.472341
H	-2.501511	-0.580357	0.835820
O	-0.859621	-1.181218	-0.164200
H	-0.014150	-0.806644	-0.457979
C	2.155471	0.282123	0.662184
H	3.139014	0.751031	0.661388
H	1.443191	0.962017	1.120576
H	2.187072	-0.640233	1.242411
O	1.689295	0.047558	-0.669844
H	2.328124	-0.515334	-1.118448

The parent species: normal species

$$\begin{aligned} X, Y, Z &= 7278.99300000 \quad 1909.88000000 \quad 1675.69600000 \\ eX, eY, eZ &= \quad 0.00800000 \quad 0.00100000 \quad 0.00100000 \end{aligned}$$

$$\text{Mass} = 78.06807956$$

The isotopic species: EHMD

$$X, Y, Z = 7235.60000000 \quad 1908.49700000 \quad 1673.90700000$$

eX, eY, eZ = 0.50000000 0.00200000 0.00200000

Mass change = 1.00627670

Total mass = 79.07435626

M DM/(M+DM) = 0.99347112

KRAITCHMAN RESULTS:

a	b	c
0.22152 +- 0.00550	0.52372 +- 0.00232	0.38070 +- 0.00323

The parent species: normal species

X, Y, Z = 7278.99300000 1909.88000000 1675.69600000

eX, eY, eZ = 0.00800000 0.00100000 0.00100000

Mass = 78.06807956

The isotopic species: EDMH

X, Y, Z = 6911.00000000 1900.20600000 1649.31500000

eX, eY, eZ = 1.00000000 0.00500000 0.00500000

Mass change = 1.00627670

Total mass = 79.07435626

M DM/(M+DM) = 0.99347112

KRAITCHMAN RESULTS:

a	b	c
1.10534 +- 0.00238	1.90330 +- 0.00142	0.34951 +- 0.00845

XIAM Fits:

Normal Species:

J	K-	K+	J	K-	K+	Sym	calc/GHz	diff/MHz	obs/GHz
3	1	3	2	1	2	S 1	10.4004294	0.0166	10.4004460
3	0	3	2	0	2	S 1	10.7263043	0.0077	10.7263120
3	2	2	2	2	1	S 1	10.7562501	-0.0041	10.7562460
3	2	1	2	2	0	S 1	10.7861652	-0.0032	10.7861620
3	1	2	2	1	1	S 1	11.1026573	-0.0253	11.1026320
4	1	4	3	1	3	S 1	13.8584070	0.0110	13.8584180
4	0	4	3	0	3	S 1	14.2666599	-0.0239	14.2666360
4	2	3	3	2	2	S 1	14.3353116	0.0124	14.3353240
4	3	2	3	3	1	S 1	14.3557234	-0.0114	14.3557120
4	3	1	3	3	0	S 1	14.3566219	0.0061	14.3566280
4	2	2	3	2	1	S 1	14.4097440	-0.0160	14.4097280
4	1	3	3	1	2	S 1	14.7938313	0.0107	14.7938420
5	1	5	4	1	4	S 1	17.3092598	-0.0238	17.3092360
5	0	5	4	0	4	S 1	17.7780513	-0.0053	17.7780460
5	2	4	4	2	3	S 1	17.9089378	0.0242	17.9089620
5	3	3	4	3	2	S 1	17.9498252	0.0048	17.9498300
5	3	2	4	3	1	S 1	17.9529638	-0.0018	17.9529620
5	4	2	4	4	1	S 1	17.9423476	0.0064	17.9423540
2	1	1	1	0	1	S 1	13.0084224	-0.0104	13.0084120
7	2	6	7	1	6	S 1	13.2944996	-0.0096	13.2944900
6	0	6	5	1	4	S 1	13.8089045	-0.0025	13.8089020
5	2	4	5	1	4	S 1	14.7345809	0.0291	14.7346100
4	2	3	4	1	3	S 1	15.3018768	-0.0288	15.3018480
8	1	7	7	2	5	S 1	15.2382509	-0.0429	15.2382080
3	2	2	3	1	2	S 1	15.7603965	-0.0005	15.7603960
2	2	1	2	1	1	S 1	16.1068037	0.0043	16.1068080
7	0	7	6	1	5	S 1	16.3584799	0.0381	16.3585180
2	2	0	2	1	2	S 1	16.8167910	0.0050	16.8167960
3	1	2	2	0	2	S 1	16.9475701	-0.0001	16.9475700
3	2	1	3	1	3	S 1	17.2025268	-0.0148	17.2025120
6	0	6	5	1	5	S 1	17.3160247	0.0033	17.3160280

3	2	2	3	1	3	S	1	17.1651186	0.0014	17.1651200
3	1	3	2	0	2	S	1	15.5428480	0.0000	15.5428480
4	2	2	4	1	3	S	1	15.4137174	-0.0034	15.4137140
5	2	3	5	1	4	S	1	14.9938651	-0.0091	14.9938560
2	1	2	1	0	1	S	1	12.3059282	0.0078	12.3059360
7	1	6	7	0	7	S	1	9.4448480	0.0120	9.4448600
4	0	4	3	1	3	S	1	9.4501162	0.0118	9.4501280
1	1	1	0	0	0	S	1	8.9546369	-0.0149	8.9546220
6	1	5	6	0	6	S	1	8.3382041	0.0499	8.3382540
3	2	1	3	1	2	S	1	15.7978047	0.0113	15.7978160
8	2	7	8	1	7	S	1	12.4371420	0.0200	12.4371620
9	2	8	9	1	8	S	1	11.5028224	0.0136	11.5028360
5	0	5	4	1	3	S	1	11.0296141	0.0139	11.0296280
7	1	6	6	2	4	S	1	11.2270267	0.0473	11.2270740
0	2	9	10	1	9	S	1	10.5063956	-0.0136	10.5063820
1	1	0	0	0	0	S	1	9.1888146	0.0274	9.1888420
4	0	4	3	1	2	S	1	8.0453941	0.0059	8.0454000
5	2	3	4	2	2	S	1	18.0563814	-0.0054	18.0563760
5	1	4	4	1	3	S	1	18.4762337	0.0023	18.4762360
4	K	-1	3	K	-1	S	2	14.7840434	0.0084	14.7840518
4	K	0	3	K	0	S	2	14.2587886	0.0836	14.2588722
4	K	1	3	K	1	S	2	13.8617020	-0.0019	13.8617002
3	K	-1	2	K	-1	S	2	11.0858756	-0.0536	11.0858220
3	K	0	2	K	0	S	2	10.7207208	0.0836	10.7208043
3	K	-2	2	K	-2	S	2	10.7683014	0.0089	10.7683103
3	K	2	2	K	2	S	2	10.7679390	-0.0799	10.7678590
3	K	1	2	K	1	S	2	10.4121486	-0.0044	10.4121442
5	K	1	4	K	1	S	2	17.3099308	-0.0059	17.3099249
5	K	0	4	K	0	S	2	17.7673451	-0.0706	17.7672745
5	K	2	4	K	2	S	2	17.9563181	-0.0193	17.9562988
4	K	-2	3	K	-2	S	2	14.3724889	0.0442	14.3725331
4	K	2	3	K	2	S	2	14.3644183	-0.0354	14.3643829
5	K	3	4	K	3	S	2	17.9468458	-0.0862	17.9467596
5	K	-3	4	K	-3	S	2	17.9454743	0.0701	17.9455444
4	K	3	3	K	3	S	2	14.3524606	-0.0695	14.3523911
4	K	-3	3	K	-3	S	2	14.3514685	0.0586	14.3515271

Lines fitted = 67
 MICROWAVE RMS = 0.032086 MHz
 RMS ERROR = 1.604313

RMS deviations (MHz), B and V sorted

B	V	n splittings	MHz	
B	V	n abs. freq.	MHz	
1	1	67	0.032086	0.037833

Parameters and Errors

BJ	1.792423199	{ 0.000001644}
BK	5.482330869	{ 0.000043047}
B-	-0.117187167	{ 0.000005099}
DJ	4.706416E-6	{ 0.030105E-6}
DJK	-1.565141E-6	{ 0.126349E-6}
DK	38.360580E-6	{ 3.176448E-6}
dj	0.809669E-6	{ 0.010591E-6}
dk	-0.014381E-6	{ 0.006856E-6}
\F	152.931591552	{ derived}
Vln	5702.490206	{ 29.809113}
\rho	0.026413563	{ derived}
\beta	0.393745679	{ derived}
\gamma	0.666631168	{ derived}
F0	149.721195297	{ 0.926732823}
epsil	0.604132007	{ 0.006630021}
delta	1.044866518	{ 0.001828002}

Standard Deviation 0.035740 MHz

----- B = 1

Rotational Constants and Errors (in GHz)

B_z	7.274754068	0.000043180
B_y	1.909610366	0.000005454
B_x	1.675236032	0.000005259

Ray's kappa -0.91629
 F0(calc) 149.721195297 0.926732823
 I_alpha 3.375467775 0.020893213
 <(i,x) <(i,y) <(i,z) 44.6206 60.5752 59.8664
 d<(i,x) d<(i,y) d<(i,z) 0.3279 0.3444 0.1047

Vln_1 2.275472 kj +/- 0.011895 kj
 190.214572 cm +/- 0.9943 cm

EtOD/MeOD

J	K-	K+	J	K-	K+	Sym	calc/GHz	diff/MHz	obs/GHz
3	0	3	2	0	2	S 1	10.6018629	-0.0269	10.6018360
3	1	2	2	1	1	S 1	11.0094883	-0.0383	11.0094500
4	1	4	3	1	3	S 1	13.6647196	0.0124	13.6647320
4	0	4	3	0	3	S 1	14.0927246	-0.0126	14.0927120
4	2	3	3	2	2	S 1	14.1774183	-0.0343	14.1773840
4	2	2	3	2	1	S 1	14.2692661	-0.0161	14.2692500
4	1	3	3	1	2	S 1	14.6673872	-0.0172	14.6673700
5	1	5	4	1	4	S 1	17.0642472	-0.0152	17.0642320
5	0	5	4	0	4	S 1	17.5484234	0.0286	17.5484520
5	2	4	4	2	3	S 1	17.7093605	0.0275	17.7093880
5	3	3	4	3	2	S 1	17.7596253	-0.0673	17.7595580
5	3	2	4	3	1	S 1	17.7640988	-0.0548	17.7640440
5	2	3	4	2	2	S 1	17.8907717	0.0683	17.8908400
5	1	4	4	1	3	S 1	18.3144185	0.0415	18.3144600
3	2	2	2	2	1	S 1	10.6388640	0.0620	10.6389260
3	2	1	2	2	0	S 1	10.6758316	0.0824	10.6759140
3	1	3	2	1	2	S 1	10.2566048	-0.0038	10.2566010
4	K	0	3	K	0	S 2	14.0863169	0.0155	14.0863324
4	K	-1	3	K	-1	S 2	14.6605028	-0.0172	14.6604856
5	K	0	4	K	0	S 2	17.5395382	-0.0037	17.5395346
3	K	0	2	K	0	S 2	10.5973807	0.0274	10.5974081
3	K	-1	2	K	-1	S 2	10.9982969	-0.0896	10.9982072
3	K	1	2	K	1	S 2	10.2635796	0.0021	10.2635817
4	K	1	3	K	1	S 2	13.6662333	0.0377	13.6662710

3 K	-2	2 K	-2	S 2	10.6555372	-0.0502	10.6554869
3 K	2	2 K	2	S 2	10.6541051	-0.0731	10.6540319
4 K	2	3 K	2	S 2	14.2119159	-0.0361	14.2118799
4 K	-2	3 K	-2	S 2	14.2281184	-0.0133	14.2281051
5 K	-3	4 K	-3	S 2	17.7570005	-0.0250	17.7569756
5 K	-2	4 K	-2	S 2	17.8342464	0.0435	17.8342899
5 K	-1	4 K	-1	S 2	18.3082676	0.0863	18.3083538

Lines fitted = 31
 MICROWAVE RMS = 0.044248 MHz
 RMS ERROR = 2.212408

RMS deviations (MHz), B and V sorted

B	V	n splittings	MHz	
B	V	n abs. freq.	MHz	
1	1	31	0.044248	0.052812

Parameters and Errors

BJ	1.772924614	{ 0.000001261}
BK	5.097481101	{ 0.000811909}
B-	-0.125634315	{ 0.000004914}
\F	152.841642697	{ derived}
Vln	5983.971429	{ 4.211286}
\rho	0.025378836	{ derived}
\beta	0.402059378	{ derived}
\gamma	0.650123203	{ derived}
epsil	0.583207412	{ 0.007392763}
delta	1.036822734	{ 0.001585476}

Standard Deviation 0.050289 MHz

----- B = 1

Rotational Constants and Errors (in GHz)

B_z	6.870405715	0.000812149
B_y	1.898558929	0.000005250

B_x	1.647290299	0.000004891
Ray's kappa	-0.90379	
F0(calc)	149.721195297	0.000000000
I_alpha	3.375467775	0.000000000
<(i,x) <(i,y) <(i,z)	44.0690 61.7031 59.4056	
d<(i,x) d<(i,y) d<(i,z)	0.3450 0.3742 0.0908	

V1n_1 2.387792 kj +/- 0.001680 kj
 199.603774 cm +/- 0.1405 cm

EtOD/MeOH

J	K-	K+	J	K-	K+	Sym	calc/GHz	diff/MHz	obs/GHz
3	0	3	2	0	2	S 1	10.6114043	-0.0083	10.6113960
3	2	2	2	2	1	S 1	10.6480860	-0.0440	10.6480420
3	2	1	2	2	0	S 1	10.6847358	-0.0238	10.6847120
3	1	2	2	1	1	S 1	11.0184452	0.0128	11.0184580
3	1	3	2	1	2	S 1	10.2661943	-0.0123	10.2661820
4	0	4	3	0	3	S 1	14.1058040	-0.0060	14.1057980
4	2	3	3	2	2	S 1	14.1897764	-0.0284	14.1897480
4	2	2	3	2	1	S 1	14.2808429	0.0151	14.2808580
4	1	3	3	1	2	S 1	14.6794313	0.0407	14.6794720
5	1	5	4	1	4	S 1	17.0804631	0.0329	17.0804960
5	0	5	4	0	4	S 1	17.5653067	-0.0047	17.5653020
5	2	4	4	2	3	S 1	17.7249076	0.0044	17.7249120
5	3	3	4	3	2	S 1	17.7747526	-0.0986	17.7746540
5	3	2	4	3	1	S 1	17.7791530	-0.1030	17.7790500
5	2	3	4	2	2	S 1	17.9048085	0.1015	17.9049100
5	1	4	4	1	3	S 1	18.3296474	0.0906	18.3297380
4	1	4	3	1	3	S 1	13.6775908	-0.0288	13.6775620
4	K	0	3	K	0	S 2	14.0977638	0.0563	14.0978201
5	K	0	4	K	0	S 2	17.5541207	-0.0270	17.5540937
3	K	0	2	K	0	S 2	10.6057886	0.0972	10.6058859
3	K	-2	2	K	-2	S 2	10.6639170	-0.0040	10.6639131
3	K	2	2	K	2	S 2	10.6629803	-0.0480	10.6629323
4	K	1	3	K	1	S 2	13.6805381	0.0245	13.6805626

4 K	2	3 K	2	S 2	14.2248643	-0.0276	14.2248367
4 K	-2	3 K	-2	S 2	14.2379574	0.0245	14.2379818
4 K	-1	3 K	-1	S 2	14.6705087	0.0380	14.6705467
3 K	1	2 K	1	S 2	10.2764018	0.0327	10.2764346
3 K	-1	2 K	-1	S 2	11.0034961	-0.0610	11.0034351
5 K	1	4 K	1	S 2	17.0815275	0.0825	17.0816100
5 K	-3	4 K	-3	S 2	17.7712229	-0.0364	17.7711865
5 K	3	4 K	3	S 2	17.7726150	-0.1607	17.7724543
5 K	-2	4 K	-2	S 2	17.8425610	0.0669	17.8426279

Lines fitted = 32
MICROWAVE RMS = 0.058285 MHz
RMS ERROR = 2.914241

RMS deviations (MHz), B and V sorted

B V n splittings MHz

B V n abs. freq. MHz

1 1 32 0.058285 0.069213

Parameters and Errors

BJ	1.774408152	{ 0.000001641}
BK	5.132687427	{ 0.001154488}
B-	-0.125538501	{ 0.000008151}
\F	152.849959365	{ derived}
Vln	5696.494665	{ 4.408302}
\rho	0.025472364	{ derived}
\beta	0.401428802	{ derived}
\gamma	0.656406096	{ derived}
epsil	0.589311721	{ 0.008853150}
delta	1.037637724	{ 0.001749882}

Standard Deviation 0.065942 MHz

----- B = 1

Rotational Constants and Errors (in GHz)

B_z	6.907095578	0.001154457
B_y	1.899946652	0.000008856
B_x	1.648869651	0.000007735
Ray's kappa	-0.90450	
F0(calc)	149.721195297	0.000000000
I_alpha	3.375467775	0.000000000
<(i,x)	<(i,y)	<(i,z)
44.2797	61.4028	59.4523
d<(i,x)	d<(i,y)	d<(i,z)
0.4096	0.4454	0.1003

Vln_1 2.273080 kj +/- 0.001759 kj
 190.014582 cm +/- 0.1470 cm

EtOH/MeOD

J	K-	K+	J	K-	K+	Sym	calc/GHz	diff/MHz	obs/GHz
3	1	3	2	1	2	S 1	10.3902516	-0.0196	10.3902320
3	0	3	2	0	2	S 1	10.7164513	-0.0233	10.7164280
3	2	2	2	2	1	S 1	10.7467340	-0.0480	10.7466860
3	2	1	2	2	0	S 1	10.7769843	-0.0623	10.7769220
3	1	2	2	1	1	S 1	11.0936949	-0.0269	11.0936680
4	1	4	3	1	3	S 1	13.8447456	-0.0116	13.8447340
4	0	4	3	0	3	S 1	14.2531419	-0.0059	14.2531360
4	2	3	3	2	2	S 1	14.3225582	0.0058	14.3225640
4	2	2	3	2	1	S 1	14.3978182	-0.0202	14.3977980
4	1	3	3	1	2	S 1	14.7817760	-0.0240	14.7817520
5	1	5	4	1	4	S 1	17.2920461	0.0039	17.2920500
5	0	5	4	0	4	S 1	17.7605740	0.0280	17.7606020
5	2	4	4	2	3	S 1	17.8928912	0.0328	17.8929240
5	3	3	4	3	2	S 1	17.9342264	0.0756	17.9343020
5	3	2	4	3	1	S 1	17.9374304	0.0496	17.9374800
5	2	3	4	2	2	S 1	18.0419489	-0.0109	18.0419380
5	1	4	4	1	3	S 1	18.4609856	0.0124	18.4609980
3	K	0	2	K	0	S 2	10.7120095	0.0115	10.7120210
4	K	1	3	K	1	S 2	13.8464832	-0.0378	13.8464454
4	K	-1	3	K	-1	S 2	14.7743007	-0.0499	14.7742508
3	K	1	2	K	1	S 2	10.3983124	-0.0543	10.3982581

5 K	0	4 K	0	S 2	17.7520613	-0.0165	17.7520448
4 K	0	3 K	0	S 2	14.2468774	0.0116	14.2468890
5 K	-2	4 K	-2	S 2	17.9888115	0.0106	17.9888220
5 K	-1	4 K	-1	S 2	18.4545366	0.0200	18.4545566
3 K	-2	2 K	-2	S 2	10.7596105	-0.0161	10.7595944
3 K	2	2 K	2	S 2	10.7588820	0.1016	10.7589836
3 K	-1	2 K	-1	S 2	11.0811893	-0.0622	11.0811271
4 K	-2	3 K	-2	S 2	14.3618651	-0.0103	14.3618548
5 K	3	4 K	3	S 2	17.9319914	-0.0513	17.9319401
5 K	-3	4 K	-3	S 2	17.9308401	0.0795	17.9309196

Lines fitted = 31
 MICROWAVE RMS = 0.040466 MHz
 RMS ERROR = 2.023301

RMS deviations (MHz), B and V sorted

B	V	n	splittings MHz	
B	V	n	abs. freq. MHz	
1	1	31	0.040466	0.048298

Parameters and Errors

BJ	1.790894660	{ 0.000001136}
BK	5.440766116	{ 0.000930768}
B-	-0.117384203	{ 0.000004926}
\F	152.928398236	{ derived}
Vln	5997.038040	{ 3.896510}
\rho	0.026354337	{ derived}
\beta	0.393089684	{ derived}
\gamma	0.653914781	{ derived}
epsil	0.591763474	{ 0.007422420}
delta	1.042556645	{ 0.001466373}

Standard Deviation 0.045990 MHz

----- B = 1

Rotational Constants and Errors (in GHz)

B _z	7.231660776	0.000930950
B _y	1.908278863	0.000005245
B _x	1.673510458	0.000004858
Ray's kappa	-0.91552	
F0(calc)	149.721195297	0.000000000
I_alpha	3.375467775	0.000000000
<(i,x)	<(i,y)	<(i,z)
44.2065	61.1975	59.7341
d<(i,x)	d<(i,y)	d<(i,z)
0.3451	0.3745	0.0840

V1n_1	2.393006	kJ +/-	0.001555	kJ
	200.039629	cm +/-	0.1300	cm